technische universität
dortmund

A Tin Story on Gold

Sn on Au(111): Structural Versatility Towards Stanene

Julian Andreas Hochhaus

2025

submitted in partial fulfillment of the requirements
for the degree of

doctor rerum naturalium
(Dr. rer. nat.)

at

Department of Physics
TU Dortmund University, Germany

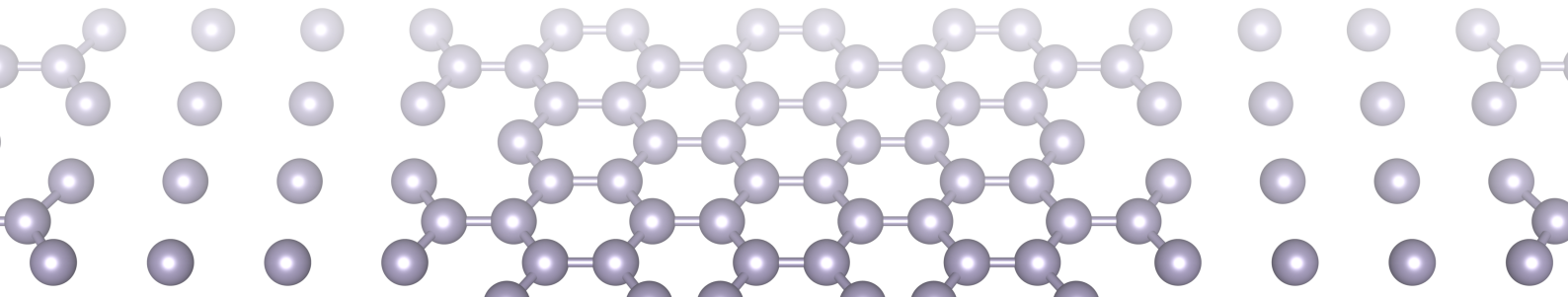

A dissertation submitted to the Department of Physics of TU Dortmund University, in partial fulfillment of the requirements for the degree of Doctor of Science.

Day of the oral examination: 04.03.2026

Examination board:
Prof. Dr. Carsten Westphal
Prof. Dr. Mirko Cinchetti
Prof. Dr. Armin Lühr
apl. Prof. Dr. Alex Greilich

Abstract

The rise of two-dimensional materials, triggered by the discovery of graphene, has sparked intense interest in *Xenes*, monoelemental 2D lattices composed of heavier group-IV elements. Among these, stanene (2D tin) is a particularly promising candidate for next-generation nanoelectronics and spintronics due to its strong spin-orbit coupling and predicted topological properties, such as the quantum spin Hall effect. However, the synthesis of high-quality stanene remains challenging, as the structural evolution of tin (Sn) is highly sensitive to the substrate and growth conditions. The Sn/Au(111) system, while promising, has been the subject of conflicting reports in the literature, with disputed structural models for the observed submonolayer Sn arrangements.

This thesis presents a comprehensive structural and chemical analysis of submonolayer Sn growth on Au(111), combining Scanning Tunneling Microscopy (STM), Low-Energy Electron Diffraction (LEED), X-ray Photoelectron Spectroscopy (XPS), and X-ray Photoelectron Diffraction (XPD). By correlating chemical state analysis with detailed structural characterization, the complex interplay between surface ordering and interface alloying is resolved. The structural evolution is categorized into two distinct regimes. At coverages below 0.33 ML, Sn adsorption is characterized by weak substrate interactions. A previously unreported, chemically freestanding (2×2) phase is identified at a coverage of 0.28 ML, representing a precursor state for buckled α-stanene. Increasing the coverage leads to the formation of a long-range-ordered Au_2Sn surface alloy. Using XPD combined with genetic algorithm optimization, this phase is definitively identified as a substitutional alloy with a $\mathrm{Rec}(26 \times \sqrt{3})$ unit cell, resolving long-standing discrepancies in its atomic structure. At higher coverages (up to 0.66 ML), the growth is driven by the interplay between the interface alloy and the Sn adlayer. This work clarifies the nature of the *X-phase*, previously interpreted as honeycomb stanene or AuSn alloy. Atomically resolved STM reveals that the X-phase is, in fact, a substrate-symmetry-breaking, square-like Sn arrangement growing atop the Au_2Sn alloy, interpreted as the onset of β-Sn(001)-like growth. Furthermore, a novel *striped phase* was discovered, featuring alternating stripes of ultraflat honeycomb stanene and the square-like Sn arrangement. These nanoribbon-like structures represent the first experimental realization of ultraflat stanene on Au(111) and the first experimental evidence of nanoribbon-like stanene structures.

Collectively, these findings provide a comprehensive framework for the submonolayer Sn/Au(111) system, demonstrating its versatility as a platform for realizing diverse low-dimensional structures and laying the groundwork for future topological investigations.

Kurzfassung

Die Entdeckung von Graphen im Jahr 2004 hat großes Forschungsinteresse an weiteren zweidimensionalen Materialien geweckt. Im Besonderen die sogenannten *Xene*, monoelementare 2D-Gitter aus den schwereren Elementen der Kohlenstoffgruppe, und ihre außergewöhnlichen Eigenschaften sind dabei in den Fokus geraten. Unter diesen gilt Stanen (2D-Zinn) aufgrund seiner starken Spin-Bahn-Kopplung und der vorhergesagten topologischen Eigenschaften, wie etwa des Quanten-Spin-Hall-Effekts, als besonders vielversprechender Kandidat für die Nanoelektronik und Spintronik der nächsten Generation. Die Synthese von hochgeordnetem Stanen bleibt jedoch eine Herausforderung, da die strukturelle Anordnung von Zinn (Sn) äußerst empfindlich gegenüber Substrat und Präparationsparametern ist. Das System Sn/Au(111) ist hierbei als besonders vielversprechend identifiziert worden.

Diese Arbeit präsentiert eine umfassende strukturelle und chemische Analyse des Wachstums von Sn auf Au(111) für Submonolagen-Bedeckungen. Unter Verwendung von Rastertunnelmikroskopie (STM), niederenergetischer Elektronenbeugung (LEED), Röntgenphotoelektronenspektroskopie (XPS) und Röntgenphotoelektronenbeugung (XPD) wird detaillierte strukturelle und chemische Charakterisierung des Sn/Au(111) Probensystems und insbesondere das komplexe Zusammenspiel zwischen Oberflächenordnung und Grenzflächenstrukturen entschlüsselt. Bei Bedeckungen unterhalb von 0.33 ML zeigt sich eine Entwicklung von chemisch schwach gebundener Sn-Struktur, hin zu einer Au_2Sn-Legierung in der obersten Probenlage. Bei einer Bedeckung von 0.28 ML wird eine chemisch entkoppelte (2×2)-Phase beobachtet, welche bisher unbekannt war. Diese wird identifiziert als Vorläufer für das Wachstum einer α-Stanen Anordnung, welche der Honigwabenanordnung der Atome im Graphene gleicht. Eine Erhöhung der Bedeckung führt zur Bildung einer langreichweitig geordneten Au_2Sn-Oberflächenlegierung. Mithilfe von XPD in Kombination mit einem genetischen Optimierungsalgorithmus wird diese Phase eindeutig als Substitutionslegierung mit einer $\mathrm{Rec}(26 \times \sqrt{3})$-Einheitszelle identifiziert, wodurch bestehende Diskrepanzen in der Literatur bezüglich ihrer atomaren Struktur eindeutig geklärt werden. Bei höheren Bedeckungen bis zu 0.66 ML wird das Wachstum durch das Zusammenspiel zwischen der Grenzflächenlegierung und der Sn-Adlage bestimmt. Für die sogenannte *X-Phase*, die zuvor in der Literatur sowohl als Honeycomb-Stanen, als auch als AuSn-Legierung interpretiert wurde, liefert diese Arbeit ein völlig neues Strukturmodell. Atomar aufgelöste STM-Messungen zeigen, dass es sich bei der X-Phase tatsächlich um eine die Substratsymmetrie brechende, quadratische Sn-Anordnung handelt, die auf der Au_2Sn-Legierung wächst und als Beginn eines β-Sn(001)-artigen Wachstums interpretiert werden kann. Darüber hinaus wurde eine neue *striped phase* entdeckt, die aus alternierenden Streifen von ultraflachem Honeycomb-Stanen und der quadratischen Sn-Anordnung besteht. Diese *Nanoribbon*-artigen Strukturen stellen sowohl den ersten experimentellen Nachweis von ultraflachem Stanen auf Au(111) dar als auch den ersten experimentellen Beleg für Stanen-Nanoribbons. Insgesamt liefern die präsentierten Ergebnisse die erste umfassende Übersicht über strukturelle Sn auf Au(111) im Submonolagenbereich. Im Besonderen kann die strukturelle Vielseitigkeit des 2D-Zinns genutzt werden zum Design komplexer zweidimensionaler Strukturen und möglicher zukünftiger topologischer Anwendungen.

Contents

List of Acronyms

ACF	autocorrelation function.
AES	Auger-Meitner electron spectroscopy.
ARPES	angle-resolved photoelectron spectroscopy.
ARXPS	angle-resolved X-ray photoelectron spectroscopy.
BL11	beamline 11.
CCD	charge-coupled device.
DELTA	Center for Synchrotron Radiation Dortmund.
DOS	density of states.
DOS	local density of states.
DS	Doniach-Šunjić.
EAL	electron attenuation lenght.
EB	electron beam heating.
EDAC	Electron Diffraction in Atomic Clusters.
EED	effective escape depth.
ESCA	electron spectroscopy for chemical analysis (ESCA).
FFT	Fast Fourier Transform.
FWHM	full width at half maximum.
HighRes	high energy-resolution XPS spectra.
ID	information depth.
IMFP	inelastic mean free path.
IV-LEED	Intensity-Voltage Low-Energy Electron Diffraction; analysis of the intensity of diffraction spots as a function of the electron energy to determine surface structure.
LEED	low-energy electron diffraction.
LINAC	linear pre-accelerator of DELTA.
LT-STM	low temperature scanning tunneling miscroscope.
MED	mean escape depth.
Miller indices	Miller indices (hkl) are used to describe the orientation of lattice planes and directions in crystallography.
ML	monolayer.
PBN	pyrolytic boron nitride.

R-factor	Pendry's reliability factor used to quantify the agreement between experimental and simulated XPD patterns.
PRNG	pseudo-random number generator.
PVD	physical vapor deposition.
QCM	quartz crystal microbalance.
QSH	quantum spin Hall.
RHEED	reflection high-energy electron diffraction.
RT-STM	room temperature scanning tunneling miscroscope.
SCW	superconducting Wiggler.
SOC	spin-orbit coupling.
STM	scanning tunneling miscroscopy.
STS	scanning tunneling spectroscopy.
TI	topological insulator.
TPP-2M	A formula derived by Tanuma, Powell, and Penn for calculating electron inelastic mean free paths.
U250	undulator 250.
U55	undulator 55.
UHV	ultra-high vacuum.
XPD	X-ray photoelectron diffraction.
XPS	X-ray photoelectron spectroscopy.

List of Symbols

a	lattice constant.
d	nearest-neighbor distance.
δ	buckling parameter of a corrugated honeycomb lattice.
E_{bin}	Binding energy.
E_{F}	The Fermi energy level is the highest energy level occupied by electrons in a material at 0 K, also used to describe the position of the Fermi edge.
E_{gap}	The energy difference between the top of the valence band and the bottom of the conduction band (band gap).
E_{kin}	Kinetic energy.
E_{pass}	Pass energy of the hemispherical energy analyzer.
E_{SOC}	Energy difference between the two peaks of a doublet, created by the spin-orbit coupling.
E_{vac}	Vacuum energy level, energy of a free electron at rest outside of any solid.
k_{B}	Boltzmann constant.
Λ_{IMFP}	Inelastic mean free path.
ν	The $\mathbb{Z}_2$ topological invariant that distinguishes trivial ($\nu = 0$) from topological ($\nu = 1$) insulators.
Φ_{A}	Work function of the analyzer.
Φ_{S}	Work function of the sample.
Φ_{T}	Work function of the tip in the STM.
v_{F}	Fermi velocity.
$\mathbb{Z}_2$	A binary topological index taking values 0 or 1 that classifies time-reversal-symmetric insulating phases as trivial or topological.

List of Figures

List of Tables

1 Introduction

I call our world Flatland, not because we call it so, but to make its nature clearer to you, my happy readers, who are privileged to live in Space.

—Edwin A. Abbott, *Flatland*

The study of structures at the atomic scale offers a unique window into a world that, like Abbott's *Flatland*, challenges our intuition. In Abbott's novella, the concept of a solid, three-dimensional object is unimaginable to the inhabitants of a strictly two-dimensional world. Conversely, we rely on advanced measurement techniques to understand the physics at the nanoscale and in low-dimensional structures. Yet, while what happens at such small scales lies beyond the reach of our senses, it is profoundly consequential for the macroscopic world we inhabit.

The development of the transistor [1] marked the beginning of the so-called Silicon Age. Silicon-based technologies have since formed the foundation of the information society, powering everything from smartphones to supercomputers. Consequently, the behavior of matter at the nanoscale has become of critical importance to our society.

However, like every era, the Silicon Age is likely approaching its end. The continued miniaturization of electronic components has long followed Moore's law, which predicts that the number of transistors on an integrated circuit doubles roughly every two years [2]. As device dimensions approach the boundary between the nanoscale and the atomic scale, fundamental physical constraints arise. In the coming years, the feature size of silicon transistors is expected to reach limits where quantum mechanical effects prevent proper device functionality [3, 4]. To sustain technological progress and ensure energy efficiency, making it sustainable as well [5], fundamentally new classes of materials must be explored, starting a technological era beyond Moore's law [6].

The rise of low-dimensional materials offers potential solutions for post-silicon electronic circuit development [7, 8]. The discovery of graphene [9], a single layer of carbon atoms arranged in a honeycomb lattice, triggered the emergence of a new research field. Graphene's exceptional electronic, mechanical, and thermal properties [10] inspired the investigation of the Flatland of 2D materials. Following graphene, other 2D counterparts from the carbon group followed: silicene [11] in 2011, germanene [12] in 2014, stanene [13] in 2015, and finally plumbene [14] in 2019.

These *Xenes* have attracted significant attention due to electronic properties similar to graphene, most notably the linear Dirac-type band dispersion [15]. Among them, the heavier elements are particularly exciting; their higher atomic number results in enhanced spin-orbit coupling (SOC), which leads to a buckled structure rather than an atomically flat arrangement, opening a bandgap. Consequently, the structural properties in these

Xenes are directly connected to their electronic properties. Stanene and plumbene, consisting of the heaviest elements of the carbon group, are especially intriguing, as their strong spin-orbit coupling introduces non-trivial topological characteristics, positioning them as promising candidates for next-generation electronic and spintronic applications [16].

Stanene, the Sn-based analogue of graphene, stands out within this family. Theoretical models predict that stanene hosts quantum spin Hall (QSH) insulating phases, possesses a large bandgap of up to 300 meV [17, 18], and may even support topological superconductivity [19]. These properties hold immense promise for room-temperature topological applications.

However, realizing stanene experimentally presents significant challenges. Bulk tin is structurally versatile, exhibiting a phase transition at 285 K between semiconducting α-Sn (diamond structure) and metallic β-Sn (body-centered tetragonal structure). While monolayer α-Sn corresponds to the honeycomb stanene phase, its thermal instability limits multilayer growth at elevated temperatures [20, 21]. Conversely, β-Sn is stable at higher temperatures and is a known superconductor ($T_c \approx 3.72$ K), with ultrathin films proposed as platforms for topological superconductivity [22].

The growth and structural arrangement of 2D Sn layers are strongly influenced by the substrate. Stanene has been synthesized on materials such as Bi_2Te_3 [13], InSb(111) [23], and various metal surfaces including Cu(111) [24], Ag(111) [25], and Pd(111) [26]. Depending on the substrate, different structural arrangements of Sn have been observed, ranging from atomically flat stanene to buckled structures.

Beyond honeycomb and hexagonal Sn arrangements, a wide range of other 2D tin allotropes have been proposed by theory. Dumbbell-like [27], staggered, layered dumbbell structures [28], as well as pentamer and tetramer arrangements, featuring rectangular unit cells [29], are predicted. Bilayer growth of β-Sn(001) with a square-lattice has been predicted by theory to be stable as well [30]. While many of these phases are expected to be topologically nontrivial, experimental realization of such non-hexagonal phases remains scarce. Typically, 2D structures grown on threefold/sixfold-symmetric (111)-surfaces adopt hexagonal geometries. Symmetry-breaking arrangements are rare, though some other elements show such symmetry-breaking 2D arrangements [31–34]. Regarding tin, β-Sn(001) layer-by-layer growth has been reported on HOPG [35], and square-like Sn monolayers have been observed on Al(111) [36]. Additionally, single-layer β-Sn has been grown on Cu(111), exhibiting a nearly freestanding electronic structure [37]. This structural versatility highlights the rich potential of 2D tin allotropes and underscores the need for detailed structural characterization.

Theoretical calculations identify Au(111) as a promising substrate for supporting planar stanene growth due to favorable lattice matching and the expected bonding behaviour [38]. Indeed, experimentally, Sn growth on Au(111) yields a wide range of structural phases. However, the existing literature presents a conflicting and often confusing picture of the Sn/Au(111) system. Reports range from descriptions of surface alloys with disputed lattice parameters [39–41] to complex incommensurate phases at higher coverages interpreted as honeycomb-like structures, zigzag chains, or AuSn alloys [41–44]. The precise atomic

arrangement, the role of alloying versus 2D layer formation, and the structural evolution depending on preparation parameters remain unresolved questions.

This thesis aims to resolve these open questions of the Sn/Au(111) system. By combining scanning tunneling miscroscopy (STM), low-energy electron diffraction (LEED), X-ray photoelectron spectroscopy (XPS), and X-ray photoelectron diffraction (XPD), a comprehensive analysis of the structural and chemical evolution of Sn on Au in the submonolayer regime is performed. This work provides the first detailed structural and chemical analysis of all phases and transitions in the submonolayer regime (below 0.66 ML), identifying several previously unknown structural arrangements. Remarkably, a chemically freestanding (2×2)-reconstruction at low coverages [45] and the first experimental realization of ultraflat honeycomb stanene on Au(111), as well as the first experimental evidence of stanene nanoribbon-like structures are reported [46]. In addition, the conflicting proposed structural models [39, 40] regarding the Au_2Sn substitutional surface alloy observed at a coverage of 0.33 ML, are resolved by a detailed XPD analysis [45]. Moreover, the so-called X-phase, which forms after depositing 0.66 ML Sn and has been interpreted either as honeycomb stanene or as AuSn alloy in the literature [41, 42]. Based on the first atomically resolved STM analysis presented here, these proposed models are revisited and challenged; instead, a substrate-symmetry-breaking square-like arrangement is identified [47].

This thesis is organized into eight chapters. Chapter 2 begins with an introduction to 2D materials, paying particular attention to their structural, electronic, and topological properties. The experimental analysis methods applied in this work are explained in Chapter 3, while the specific experimental setups are described in Chapter 4. The preparation of the Sn/Au(111) sample system is detailed in Chapter 5. This is followed by a structural analysis of low and high Sn submonolayer coverages in Chapters 6 and 7, respectively. Finally, a summary and outlook are provided in Chapter 8.

2 2D Materials

Two-dimensional materials can be visualized as a sheet of paper, but orders of magnitude thinner; they extend macroscopically in two dimensions, while the translation symmetry perpendicular to the surface is broken. The stability of 2D materials from Group 14 of the periodic table beyond graphene was predicted by Takeda and Shiraishi in 1994 [48], though their results remained essentially unnoticed until the first experimental realization of single-layer graphene by Novoselov and Geim in 2004 [9].

Materials similar to graphene, often termed *Xenes* (where X is the element), have the thickness of a single atomic monolayer (ML). They feature strong in-plane covalent bonds, while weaker van der Waals forces often dominate their interaction with a substrate. This can be explained by their valence electronic structure, which is similar across all elements in the carbon group, as illustrated by the example of graphene. In graphene's ground-state configuration, three of carbon's four valence electrons occupy sp^2-hybridized orbitals, which result from combining its $2s$ orbital with two of its $2p$ orbitals ($2p_x$, $2p_y$). These sp^2-hybridized orbitals are oriented in-plane and form strong σ-bonds with the three nearest-neighbor carbon atoms. The fourth valence electron occupies the remaining $2p_z$ orbital, oriented perpendicular to the plane, as depicted in Figure 2.1. These out-of-plane $2p_z$ orbitals form half-filled π-bonds, which host freely-moving electrons. While the strong in-plane σ-bonds grant graphene its extraordinary mechanical strength, the half-filled π-bands are responsible for its exceptionally high charge-carrier mobility [49, 50].

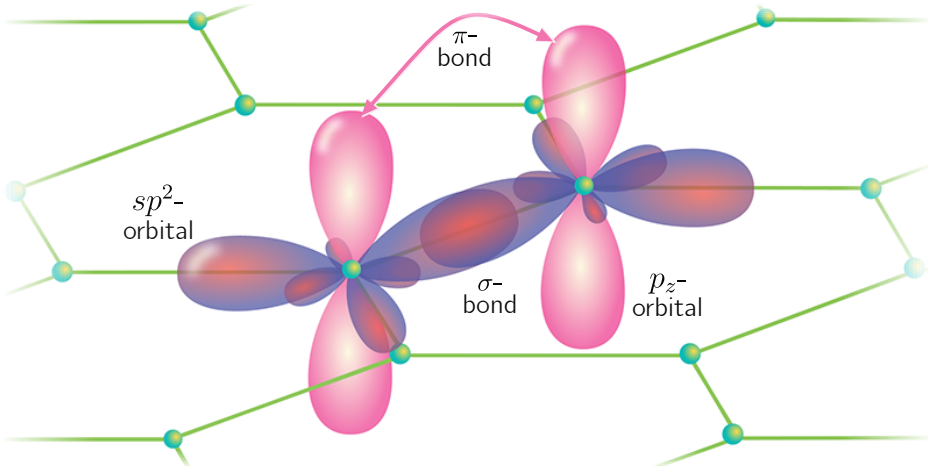

Figure 2.1: Depiction of a graphene honeycomb lattice with the out-of-plane p_z orbitals shown in light pink. Modified and reprinted with permission from [51].

However, these same π-bands are also responsible for graphene's (almost) zero band gap, which limits its application in digital electronics. The search for materials combining graphene's extraordinary properties with a tunable band gap has created interest in its heavier Group 14 analogues. The synthesis of these 2D structures has succeeded in recent

years, with silicene (silicon) in 2012 [11], germanene (germanium) in 2014 [12], stanene (tin) in 2015 [13], and finally plumbene (lead) in 2019 [14]. Some structural parameters of the Xenes of the carbon group are presented in Table 2.1.

With increasing atomic number Z, theory predicts a rapidly increasing band gap, rising from a mere 1 µeV for graphene [15] to nearly 100 meV [17] for stanene and more than 200 meV for plumbene [52].

However, experimentally realizing the predicted properties of analogues such as stanene has proven challenging, as theoretical and experimental results lack consensus. Theoretical predictions for stanene's band structure vary wildly, as different modeling approaches, structural parameters, and substrate choices yield vastly different results [17–19, 27, 28, 30, 53]. The core consensus from theory is that the substrate and structural corrugation fundamentally dictate the electronic and topological properties [15, 30, 52]. Experimentally, the situation is similarly complex. While honeycomb-like tin structures and evidence of topological states have been reported on some substrates, alloy formation is observed on others [25, 26, 40, 42, 43, 45, 54–57]. Furthermore, experimental results often contradict theoretical predictions or each other. A wide variety of superstructures are observed, and a clear understanding of all structural phases and their properties has not yet been established.

A complete treatment of the mathematical formalism behind the electronic and topological properties of stanene is beyond the scope of this experimentally focused thesis. Instead, this chapter aims to motivate how the intrinsic properties of these 2D honeycomb materials are dictated by their atomic structure. To do so, the discussion will begin with the properties of graphene and then explain the differences that arise when progressing to heavier analogues, with a focus on how structure influences electronic properties and topology.

Table 2.1: Predicted structural and electronic properties of Xenes. Here, a is the lattice constant, d is the nearest-neighbor distance, δ is the buckling height, E_{gap} is the band gap, and v_{F} is the Fermi velocity. Ranges indicate variations across different theoretical calculations.

Xene	a [Å]	d [Å]	δ [Å]	E_{gap} [meV]	v_{F} [10^5 m/s]	Ref.
C	2.46 to 2.47	1.42	0	0.001	6.3 to 10.1	[15, 58]
Si	3.82 to 3.87	2.25 to 2.28	0.44	1.5 to 2.0	5.1 to 6.5	[15, 59, 60]
Ge	4.0 to 4.06	2.34 to 2.44	0.69	23.9 to 33.0	3.8 to 6.2	[15, 60, 61]
Sn	4.67 to 4.68	2.70 to 2.83	0.85	73 to 101	4.4 to 5.5	[15, 17, 52, 61]
Pb	4.93 to 4.96	3.00	0.98	200 to 491	4.5	[52, 62]

2.1 The Honeycomb Lattice

The honeycomb lattice, common to both graphene and its heavier analogues, is not a Bravais lattice. Instead, the structure is described by a hexagonal Bravais lattice

with a two-atom basis, labeled A and B in Figure 2.2(a). The structure can also be described as two interpenetrating triangular sublattices (A and B). Atoms in sublattice A are surrounded by three nearest-neighbors from sublattice B, and vice versa. Such a lattice, where nearest-neighbors always belong to the other sublattice, is called *bipartite*. This A-B sublattice symmetry is the key to the unique electronic properties of these materials.

The fundamental structural difference between graphene and the heavier Xenes lies in the spatial arrangement of these two sublattices. In graphene, both A and B atoms are located in a single, flat plane. In the heavier analogues, the larger atomic radii weaken the π-bonding, making it energetically favorable to mix the sp^2 and sp^3 hybridizations [63, 64]. This results in a corrugated or *buckled* structure, where the A and B sublattices are vertically displaced from each other, as shown in Figure 2.2(b). This vertical separation is the buckling height, denoted by δ. The buckling height δ increases when stepping down the periodic table, reflecting the increasing sp^3 character.

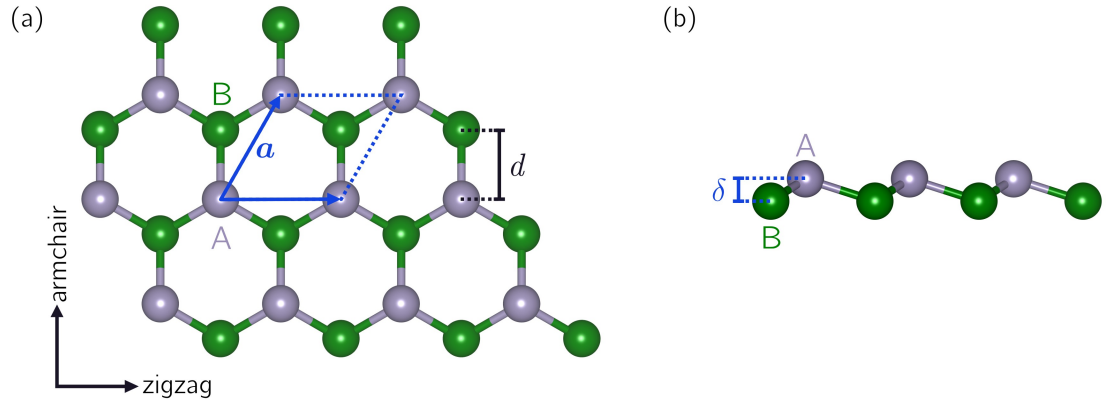

Figure 2.2: (a) Top-down view of a honeycomb lattice. The zigzag and armchair directions are indicated and named after the geometric profiles of the edges formed when the lattice is terminated along these axes. The lattice parameter is denoted by a and the nearest-neighbor distance by d.(b) Side view of a buckled structure, defining the buckling height δ as the vertical separation between the A and B sublattices.

2.2 Electronic Properties

Graphene and its heavier-element analogues are classified as Dirac materials because their low-energy excitations (excitation of states close to the Fermi level) are described by the Dirac equation, rather than the conventional Schrödinger equation [65]. The defining feature of such materials is the existence of Dirac points, where the conduction and valence bands touch linearly at the Fermi level.

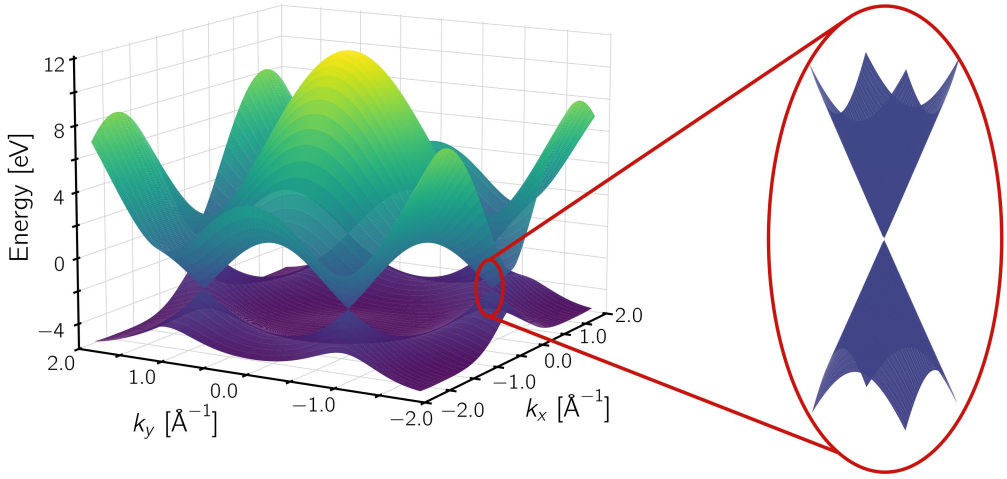

Figure 2.3: 3D plot of the band structure of graphene, showing the valence and conduction bands touching at the Dirac point in the zoomed-in inset. Nearest-neighbor and next-nearest-neighbor electron hopping were taken into account in calculating the energy bands, according to Equation D.18.

This Dirac point arises in honeycomb materials due to the equivalence of the A and B sublattices. In the nearest-neighbor tight-binding model [66], this sublattice symmetry ensures that the effective Hamiltonian is off-diagonal:

$$H(\boldsymbol{k}) = \begin{pmatrix} 0 & \xi(\boldsymbol{k}) \\ \xi^*(\boldsymbol{k}) & 0 \end{pmatrix} \tag{2.1}$$

with $\xi(\boldsymbol{k}) = -t\sum_{n=1}^{3} \exp\left(i\boldsymbol{k}\cdot\boldsymbol{\eta}_n\right)$. Here, t is the nearest-neighbor hopping energy, $\boldsymbol{\eta}_n$ are the vectors connecting an A site to its three nearest B neighbors, and $\xi^*(\boldsymbol{k})$ denotes the complex conjugate of $\xi(\boldsymbol{k})$ [67]. A detailed derivation is provided in Appendix D.

At the K and K' points of the Brillouin zone, the function $\xi(\boldsymbol{k})$ equals zero. Consequently, for small deviations $\boldsymbol{q}$ close to these points, the linearized low-energy Hamiltonian near $\pm K$ reads:

$$H_{\mathrm{D}} = \hbar v_{\mathrm{F}}\left(\sigma_x q_x \pm \sigma_y q_y\right). \tag{2.2}$$

Here, σ_x and σ_y are the Pauli matrices, $\boldsymbol{q}$ is the momentum relative to the Dirac point, and $v_{\mathrm{F}} \approx 10^6$ m/s is the Fermi velocity. The Dirac Hamiltonian H_{D} features no mass-dependent term, resulting in the characteristic gapless Dirac point responsible for graphene's semimetallic nature [67].

The corresponding eigenvalues describe a linear energy-momentum relation [64, 68]:

$$E_{\mathrm{D}} = \pm\hbar v_{\mathrm{F}}|\boldsymbol{q}|\,. \tag{2.3}$$

The Dirac Hamiltonian, as well as the linear Dirac energy momentum relation E_{D}, are mass-independent, in contrast with the conventional quadratic dispersion $E = p^2/(2m^*)$ for Schrödinger fermions, which depends on the effective mass m^*.

For the heavier elements of the carbon group, the spin-orbit coupling (SOC) alters this scenario: it effectively introduces a mass-like term into the Hamiltonian. Physically, this term opens an energy gap at the Dirac points, similar to the effect of breaking sublattice symmetry. However, rather than creating a simple potential difference between sublattices A and B, the strong SOC couples the electron's spin to its orbital motion. This results in a spin-dependent gap opening that maintains the lattice's inversion symmetry (in the absence of external fields) but lifts the degeneracy at the Dirac points K and K', given by:

$$E = \pm\sqrt{\hbar v_{\mathrm{F}}^2 |\boldsymbol{q}|^2 + \left(\frac{\Delta_{\mathrm{SO}}}{2}\right)^2} \tag{2.4}$$

where Δ_{SO} is the SOC-induced energy gap. This gap scales approximately as Z^2 with atomic number Z, becoming sufficiently large in heavier materials to enable semiconducting behavior at room temperature and to give rise to exotic states such as the quantum spin Hall (QSH) effect [64, 69–71].

2.3 Topological Properties

If materials exhibit a band gap, they are typically classified as semiconductors, with a gap of $0 \leqslant E_{\mathrm{gap}} \leqslant 4\,\mathrm{eV}$, or as insulators ($E_{\mathrm{gap}} > 4\,\mathrm{eV}$). In the following, this classification is simplified to a distinction between metallic (no energy gap) and insulating (a finite energy gap) behavior.

The formation of the SOC-induced band gap, as described above, does not simply create a trivial (normal) insulator, but rather a topologically nontrivial phase known as a QSH insulator, or a 2D topological insulator (TI). The topological nature arises from a process called band inversion: strong spin-orbit coupling causes electronic states near the Fermi level to hybridize and reorder. Consequently, states that in a conventional (trivial) insulator would contribute to the valence band maximum instead become the conduction band minimum, and vice versa. This band inversion is illustrated in Figure 2.4. For a topological insulator, orbitals normally associated with the valence band (depicted in orange) switch ordering in the energy diagram with those of the conduction band (green). This reordering of orbitals changes the electron wavefunctions' symmetry and topology, introducing a fundamentally nontrivial character to the material.

Two insulators are considered topologically equivalent if their Hamiltonians can be smoothly deformed into one another without closing the band gap. Insulators are thus classified by a topological invariant, such as the $\mathbb{Z}_2$ invariant ν, which mathematically describes the "twisting" or winding of the occupied electronic wavefunctions in momentum space. Insulators with $\nu = 1$ are topologically non-trivial, while those with $\nu = 0$ are trivial (normal). Crucially, the non-trivial state ($\nu = 1$) is protected by time-reversal symmetry. This symmetry forbids elastic backscattering of the spin-polarized edge states by nonmagnetic impurities. Because the topological invariant necessarily changes at the boundary between regions of differing topology ν (such as the boundary between a topological insulator and vacuum), the band gap must close at the interface to allow this

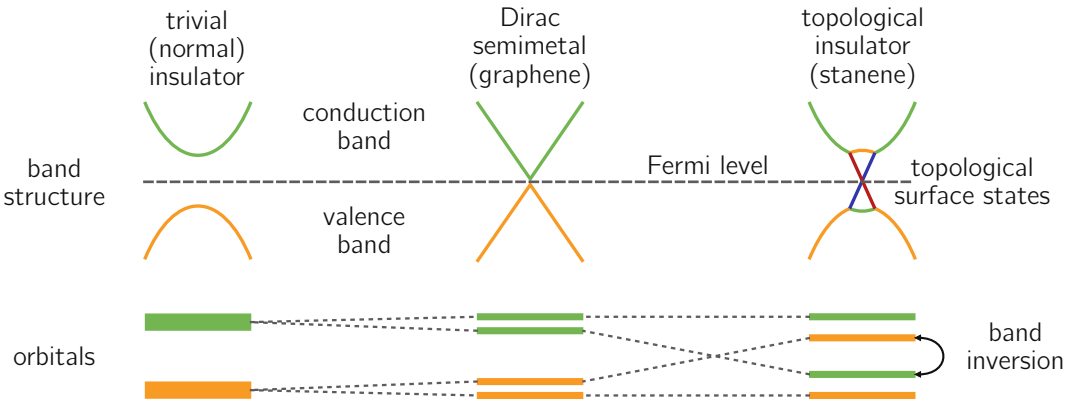

Figure 2.4: Schematic illustration of band inversion: In a normal insulator, the band gap is trivial; in Dirac semimetals like graphene, the gap closes at the Dirac point; in topological insulators (e.g., stanene), the bands invert their orbital character at the high-symmetry point. In addition, topological surface states appear in the band gap.

change. As a result, gapless conducting edge states must exist at the boundary. This principle is known as the bulk-edge correspondence. The existence of such edge states is topologically protected. As long as the system remains in its topological phase, the change in the bulk invariant at the boundary requires the presence of gapless edge states. These boundary states cannot be destroyed unless the topological phase of the insulator itself is destroyed, e.g., by closing its bulk band gap [67].

A topological insulator, therefore, has an insulating bulk but requires the existence of conducting channels along its edges (in 2D) or surfaces (in 3D). However, this topological phase can be destroyed by perturbations that close and reopen the bulk band gap, thereby changing ν. Several mechanisms can influence the band gap and induce a topological phase transition in buckled honeycomb structures, including applying a perpendicular electric field, mechanical strain, substrate interactions, or chemical functionalization. These perturbations can alter the effective SOC strength or crystal symmetry, driving the system between trivial and nontrivial phases [67].

While the terminology can be counterintuitive in two dimensions, it is crucial to note that conducting states in 2D materials appear at the one-dimensional edges rather than at surfaces. Since a 2D material is intrinsically a surface, its topological boundary is defined by its one-dimensional edge. Consequently, investigating 1D edges in 2D materials, such as those in germanene and stanene nanoribbons, is of significant importance due to the potential presence of topological edge states [72–75].

To summarize, both the electronic and topological properties of these materials are highly sensitive to the band gap. Unlike semimetallic graphene, heavier elements of the carbon group naturally exhibit band gaps due to their stronger SOC. Controlling structural parameters, such as the buckling δ, or modifying the chemical environment through substrate interactions and functionalization, enables the precise tuning of these electronic and topological properties, unlocking technological possibilities beyond graphene's semimetallic nature.

3 Theoretical Background

This chapter provides an overview of the theoretical foundations for the experimental methods used in this work. The discussion begins with the inelastic mean free path (IMFP) in Section 3.1, which is the physical basis for the surface sensitivity of electron-based techniques. Building on this framework, Section 3.2 details the principles of X-ray photoelectron spectroscopy (XPS). Subsequently, electron diffraction methods are introduced, with X-ray photoelectron diffraction (XPD) and low-energy electron diffraction (LEED) presented in Sections 3.3 and 3.4, respectively. Finally, Section 3.5 provides an introduction to scanning tunneling miscroscopy (STM).

3.1 Inelastic Mean Free Path (IMFP)

To obtain structural or chemical information from a sample using electron-based methods, electrons that retain their initial kinetic energy are of primary interest. Only elastically scattered electrons can form diffraction patterns through interference, as inelastic scattering processes destroy the phase coherence required for interference. Consequently, elastically scattered electrons are essential for diffraction methods such as LEED and XPD [76]. Similarly, in XPS, it is only possible to determine the binding energy of a core level if the emitted photoelectrons have preserved their initial kinetic energy.

Accordingly, the distance that electrons can penetrate the solid before losing part of their kinetic energy defines the probing depth of these techniques. Hence, a critical quantity is the probability of inelastic scattering of electrons within a solid, which occurs through interactions such as those with plasmons or phonons. A measure for this probability is the inelastic mean free path (IMFP), $\Lambda_{\mathrm{IMFP}}(\mathrm{E})$, defined as the average distance an electron travels between successive inelastic collisions. This corresponds to the distance over which the intensity of an electron beam is attenuated to $1/e \approx 37\,\%$ of its initial value [77, 78].

An initial electron beam of intensity I_0 traveling through a sample decays exponentially with the path length d in the solid:

$$I(d) = I_0 \exp\left(-\frac{d}{\Lambda_{\mathrm{IMFP}}(E)}\right). \tag{3.1}$$

In numerous experiments on varying materials [80–83], it has been found that $\Lambda_{\mathrm{IMFP}}(\mathrm{E})$ is largely independent of the material. As shown in Figure 3.1, $\Lambda_{\mathrm{IMFP}}(\mathrm{E})$ follows the so-called *universal curve*, which exhibits a broad minimum around 70 eV.

The IMFP becomes shorter than 1 nm in the vicinity of this minimum, which means an electron can only penetrate the first 3–4 atomic layers before being scattered inelastically.

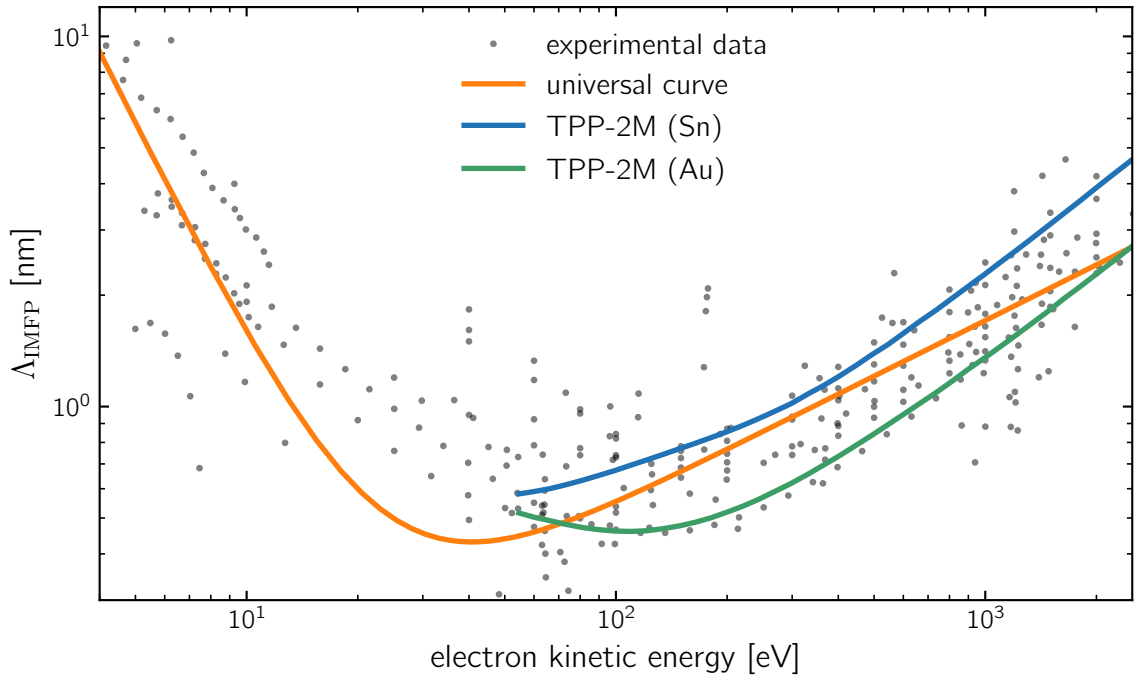

Figure 3.1: The universal curve as well as IMFPs for Sn and Au obtained using the TPP-2M formula [79] are plotted in comparison to experimental data of different elements taken from [80–83].

Therefore, the use of low-energy electrons for diffraction experiments (XPD and LEED) and for chemical analysis (XPS) makes these techniques highly surface-sensitive.

As shown in Figure 3.1, the universal curve exhibits two branches with different slopes in the double-logarithmic plot. In the low-energy region, electrons mainly lose energy by creating electron-hole pairs. The inelastic scattering probability is proportional to the density of states available for excitation, both occupied ($\propto E$) and unoccupied ($\propto E$), leading to the universal curve scaling with $\propto E^{-2}$ in this energy range [84, 85].

At higher electron energies, plasmon excitation and core-level electron ionization become the dominant loss processes. Qualitatively, the inelastic scattering cross-section σ can be assumed to be proportional to the interaction time τ, which is inversely proportional to the electron velocity ($v \propto \sqrt{E}$). Assuming the non-relativistic case, τ and thereby σ are proportional to $1/\sqrt{E}$. Since Λ_{IMFP} is inversely proportional to σ, the slope of $\Lambda_{\mathrm{IMFP}}(\mathrm{E})$ at higher kinetic energies scales with $\sqrt{E}$ [84–86]. Where the two loss mechanisms overlap, the universal IMFP curve reaches a global minimum, approximately in the range $E = 40\,\mathrm{eV}$ to $100\,\mathrm{eV}$, which defines the energy range of minimal electron escape depth for most materials [77, 87].

Seah and Dench curated a database of all IMFP data available in 1979 and found that the best-fit universal curve follows the relation [82]:

$$\Lambda_{\mathrm{uc}}(E) = \frac{143}{E^2} + 0.054\sqrt{E}\,. \tag{3.2}$$

However, as is evident from the deviations of individual data points from this curve, the universal curve provides only a general trend, and more advanced models that account for material-specific properties are required for higher precision. Such a more accurate description is given by the TPP-2M formula, especially for kinetic energies $E_{\mathrm{kin}} > 50\,\mathrm{eV}$:

$$\Lambda_{\mathrm{TPP\text{-}2M}} = \frac{E}{E_{\mathrm{p}}^2(\beta \ln(\gamma E) - (C/E) + (D/E^2))}\,. \tag{3.3}$$

The parameters E_{p}, β, γ, C, and D are material-dependent, derived from physical quantities such as the plasmon frequency, the number of valence electrons, the density, the atomic weight, and the bandgap of the material [79, 88]. The resulting curves for tin and gold, calculated using the TPP-2M formula, are also presented in Figure 3.1 [79].

In addition to the high surface sensitivity resulting from their short IMFP, low-energy electrons have de Broglie wavelengths (compare with Section 3.4) that coincide well with typical interatomic distances in a crystal of a few angstroms. Combining these two factors, a short penetration depth and well-suited wavelengths, makes low-energy electrons the perfect probe for surface chemistry, the electronic structure of surface layers, and surface structural determination. These advantages are heavily applied in this work through the use of XPS, LEED, and XPD.

3.2 X-Ray Photoelectron Spectroscopy (XPS)

The photoelectric effect describes the emission of electrons from a material when it is irradiated with electromagnetic radiation. The phenomenon was first observed by Heinrich Hertz in 1887 [89] during experiments with radio waves, where he observed that ultraviolet light promotes the sparking between metal electrodes. Shortly afterward, Wilhelm Hallwachs, Hertz's assistant, systematically analyzed the effect and demonstrated that ultraviolet light induces the loss of charge from a negatively charged metal plate, indicating the emission of negatively charged particles [90]. These findings challenged the classical wave model of light, which could not explain why electron emission depended on the frequency of the incident light rather than its intensity.

Before Einstein proposed the quantization of light in 1905 [91], it was not understood why photoelectrons were emitted with low-intensity, high-frequency light but not with high-intensity, low-frequency light. Classical theory predicted that sufficiently intense light of any frequency should eject electrons and that the kinetic energy of emitted electrons should increase with intensity, but experiments contradicted both predictions. Einstein postulated that light is composed of particles called photons, each with an energy of $h\nu$, which could be fully transferred to an electron bound in a solid to induce its emission. Here, h is Planck's constant and ν is the frequency of the light. To eject an electron, the photon's energy must be greater than the sum of the electron's binding energy and the material's work function. Therefore, the frequency of the photons, not

their number (intensity), determines whether electrons are ejected. Any remaining energy is converted into the kinetic energy of the emitted photoelectron:

$$h\nu = E_{\text{kin}} + E_{\text{bin}} + \Phi_{\text{S}} \,. \tag{3.4}$$

The material's work function Φ_{S} is given by the difference between the vacuum level E_{vac} and its Fermi level: $\Phi_{\text{S}} = E_{\text{vac}} - E_{\text{F}}$. The vacuum level is defined as the energy of a free electron at rest outside the material, serving as a reference point for the kinetic energy of emitted photoelectrons.

Einstein's equation shows that if the photon energy $h\nu$ is known, measuring the kinetic energy E_{kin} allows one to determine the binding energy of the core level from which the photoelectron was emitted. Based on this principle, Siegbahn developed the first spectrometer to measure atomic binding energies in 1956 [92–94]. He initially named the technique electron spectroscopy for chemical analysis (ESCA) (ESCA), but today, the term X-ray photoelectron spectroscopy (XPS) is more common.

The process of photoemission is depicted in Figure 3.2 and can be described as a three-step process:

1. **Photoexcitation**: A photon with energy $h\nu$, greater than the sum of an electron's binding energy E_{bin} and the sample's work function Φ_{S}, transfers its energy to a core electron, exciting it into an unoccupied electronic state with an energy above the vacuum level E_{vac}. At this point, the electron has sufficient energy to leave the solid, but it is still physically located within the solid.

2. **Transport to the Surface**: The excited electron travels towards the solid's surface. During this transport, it may undergo elastic and inelastic scattering events, potentially losing energy.

3. **Escape into Vacuum**: If the electron reaches the surface with sufficient kinetic energy, specifically, if its energy exceeds the vacuum level, it overcomes the surface potential barrier Φ_{S} and is ejected into the vacuum. Electrons that suffered inelastic scattering on their way to the surface but still escape are detected at lower kinetic energies and contribute to the background signal as secondary electrons.

To measure the photoelectron's energy with the analyzer, the electron must overcome the analyzer's work function. If the sample and the analyzer are in electrical contact, their Fermi levels align. As shown in the inset in Figure 3.2, to be detected in the analyzer, photoelectrons have to overcome the analyzer's work function Φ_{A}. Consequently, the measured kinetic energy is referenced to the analyzer's work function, and measuring the photoelectrons' kinetic energy provides no information about the sample's work function, Φ_{S}. Because the analyzer's work function is a known constant, measuring the kinetic energy of the photoelectrons allows a direct determination of the binding energy of the core level from which the electron was emitted. Einstein's equation, as applied to XPS measurements, is therefore formulated as:

$$E_{\text{kin}} = h\nu - E_{\text{bin}} - \Phi_{\text{A}} \,, \tag{3.5}$$

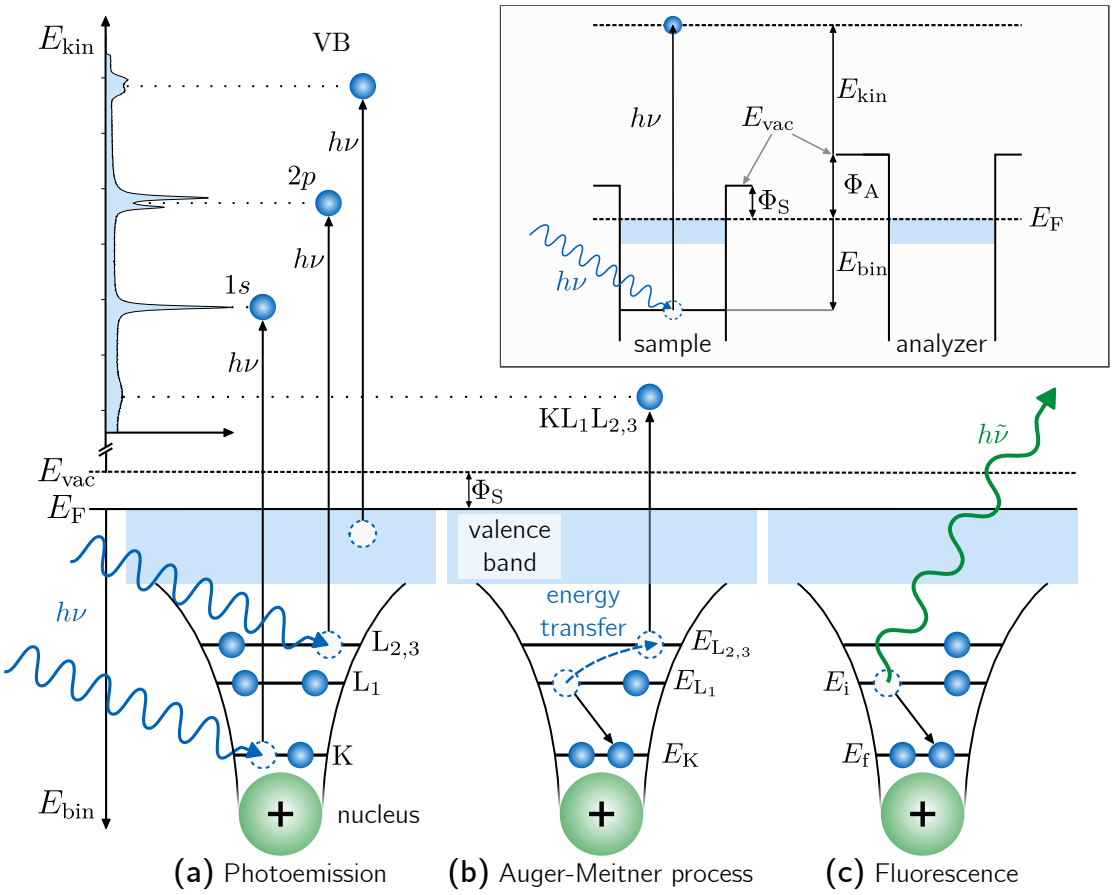

Figure 3.2: (a) Principle of photoemission. (b) Auger-Meitner effect and (c) fluorescence illustrate relaxation processes refilling the core hole. The inset illustrates Einstein's photoemission equation applied to XPS measurements in the energy diagram. Inspired by [95].

with Φ_A being the analyzer's work function. This relationship is illustrated in the energy level diagram in the inset of Figure 3.2.

The three-step model serves as a useful approximation of the photoemission process; however, the details are more complex [96, 97]. For an accurate description, additional effects must be considered. For example, the emitted electron might interact significantly with the core hole it leaves behind [98, 99]. Furthermore, the photoemission process is often described using the *sudden* or *frozen orbital approximation*. This approximation assumes that the removal of the core electron happens instantaneously compared to the relaxation time of the remaining electrons. Therefore, the other electrons are considered *frozen* in their initial orbitals during the photoemission event, and they do not have time to relax or adjust to the presence of the core hole before the photoelectron leaves the sample. This approximation essentially ignores the effect of electronic relaxation on the binding energy associated with the main photoemission peak [100–103].

As illustrated in the top left of Figure 3.2, the emitted photoelectrons generate a spectral distribution. The secondary electrons contribute to a continuous inelastic background. Additional signals, often relatively broad and less pronounced than the core-level signals, are also observed and stem from relaxation processes that refill the core hole. The

hole created by the emitted photoelectron can be refilled in two ways: Either by the Auger-Meitner effect [104, 105], depicted in Figure 3.2(b), where an electron from a higher energy level relaxes into the core hole and the excess energy is transferred to another electron, which may then be emitted and measured in the spectrum. Or by fluorescence, depicted in (c), where the excess energy is released by the emission of a photon with energy $h\tilde{\nu}$.

For the Auger-Meitner process, the kinetic energy of the emitted Auger electron $E_{\text{kin, A-M}}$ depends only on the energy differences of the contributing energy levels and is independent of the initial excitation energy. For the example depicted, the measured kinetic energy would be:

$$E_{\text{kin, A-M}} = E_{\text{K}} - E_{\text{L}_1} - E_{\text{L}_{2,3}} - \Phi_{\text{A}} \,. \tag{3.6}$$

This property makes Auger signals distinguishable from photoemission signals; when the excitation energy $h\nu$ is varied, Auger signals remain at a constant kinetic energy, while photoemission signals shift linearly with $h\nu$.

Precise energy analysis of the emitted electrons is fundamental to recording photoelectron spectra. The methods for this analysis can be classified into four main principles: resonant collision phenomena, time-of-flight experiments, dispersion by an electric or magnetic field, and retardation by a potential barrier [106, 107]. Of these, dispersion and retardation are the most commonly used in modern instrumentation. Retarding field analyzers function as a high-pass filter. While conceptually simple, they offer limited energy resolution. They are thus typically employed in techniques like LEED, where high resolution is not the primary goal (see Section 3.4). In contrast, electron spectroscopy requires higher energy resolution, for which dispersive field methods are ideal. These analyzers act as band-pass filters, selectively transmitting only electrons within a narrow energy window, allowing for a precise and direct measurement of the spectral distribution [106]. A hemispherical analyzer is often used for this task. The one used in this thesis is a CLAM IV analyzer from VG Microtech, as sketched in Figure 3.3. After being emitted from the sample, photoelectrons pass through three key components of the analyzer before detection: the lens system, the deflecting hemispheres, and the detector. The lens system consists of a series of electrostatic lenses that focus and retard the photoelectrons. These lenses define the acceptance angle and the inspected area on the sample, image the sample plane onto the hemisphere's entrance slit, and, most importantly, retard or accelerate the photoelectrons to a fixed pass energy E_{pass} before they enter the analyzer through an entry slit.

The hemispherical analyzer can be understood as a spherical capacitor in which the outer hemisphere is held at a negative potential, V_2, and the inner hemisphere at a positive potential, V_1. This arrangement creates a radial electric-field gradient that causes electrons to disperse according to their kinetic energy as they traverse the analyzer. Only electrons with a kinetic energy E_{kin} that matches a small energy window around the pass energy E_{pass} will follow the central trajectory and reach the detector. The required voltages are determined by the relationship:

$$e(V_2 - V_1) = E_{\text{pass}} \left(\frac{r_2}{r_1} - \frac{r_1}{r_2} \right) , \tag{3.7}$$

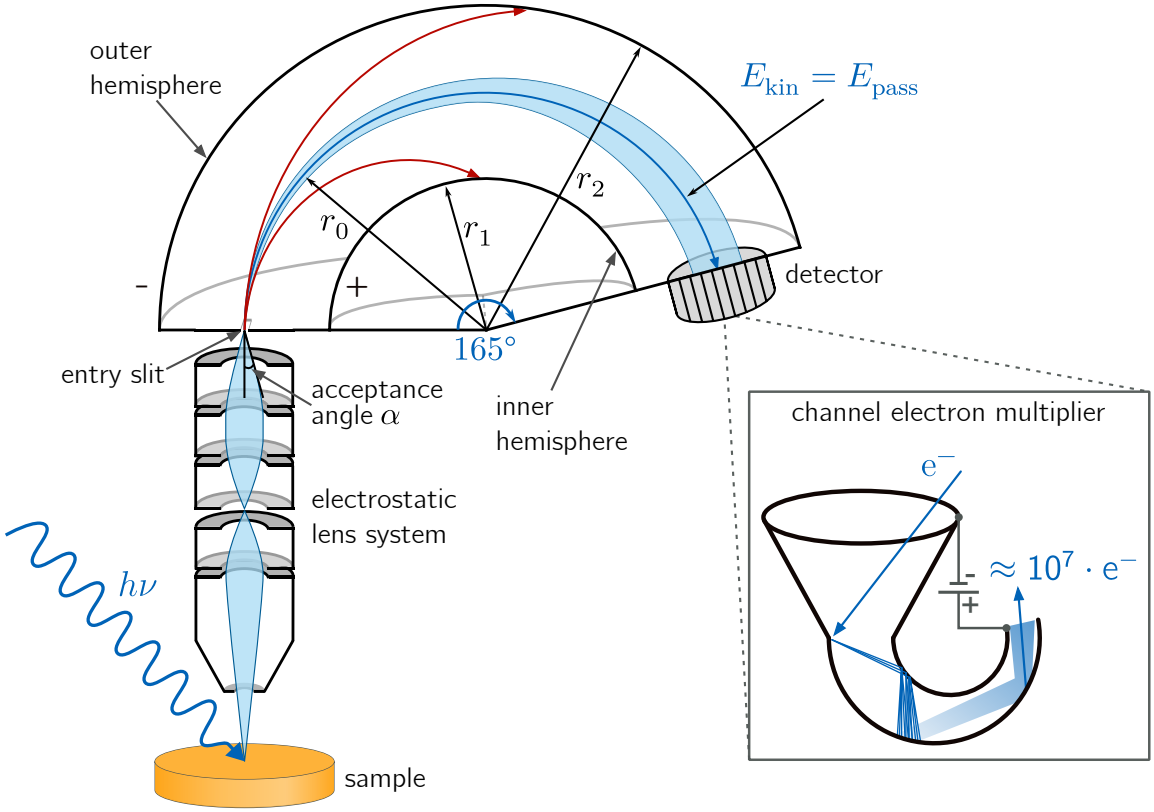

Figure 3.3: Sketch of the hemispherical analyzer installed at the experimental setup. The system consists of the lens system, the energy analyzer sphere, and the detector. Figure inspired by [108–110].

with the radius of the outer hemisphere $r_2 = 187\,\text{mm}$ and the radius of the inner hemisphere $r_1 = 113\,\text{mm}$ [111]. The mean radius of the analyzer, $r_0 = (r_1 + r_2)/2 = 150\,\text{mm}$, defines the central trajectory that electrons with kinetic energy $E_{kin} = E_{pass}$ follow. Photoelectrons whose kinetic energy does not match the pass energy window will strike either the inner or outer hemisphere, depending on whether their kinetic energy is smaller or larger than the pass energy, respectively. The analyzer thereby acts as a band-pass filter.

Due to the spherical nature of the electric field gradient, the shape of the entry slit is significant. While a curved entry slit that mimics the analyzer's focal plane will be imaged as a straight line at the exit, a straight slit will be imaged as a curved line on the detector. Consequently, a straight slit offers greater angular acceptance but compromises energy resolution. For high-resolution XPS measurements, a curved entry slit is hence the optimal choice [112].

As indicated by the blue shade in Figure 3.3, the analyzer transmits electrons within a narrow energy window, $\pm\Delta E(E_{pass})$, centered around the pass energy, E_{pass}. Accepting an energy interval rather than a single energy value allows for higher count rates. The axis parallel to the electric field gradient is therefore known as the energy-dispersive axis.

Reducing the pass energy narrows the energy window $E_{\text{pass}} \pm \Delta E(E_{\text{pass}})$, which improves the energy resolution. However, this simultaneously reduces the number of transmitted electrons, thereby lowering the signal intensity. A trade-off must therefore always be made between energy resolution and signal intensity [111]. Exit slits can also be inserted at the exit of the hemispheres to further improve energy resolution. The theoretical limit of the energy resolution of the analyzer, ΔE_{ana}, scales directly with the pass energy:

$$\Delta E_{\text{ana}} = E_{\text{pass}} \left(\frac{w_1 + w_2}{4r_0} + \frac{\alpha^2}{2} \right), \tag{3.8}$$

where w_1 and w_2 are the widths of the entry and exit slits, respectively, and α is half the acceptance angle of the electron cone at the entry slit [113–115].

To detect electrons across this energy window, the detector consists of a linear array of nine channel-electron multipliers (CEMs, often called short channeltrons) positioned along the energy-dispersive axis.

Each CEM amplifies a single incoming electron into a detectable electronic pulse, providing a signal gain of 10^6 to 10^8, which is then registered by a counting unit [116]. As shown in the inset of Figure 3.3, a channeltron consists of a horn-shaped tube coated with lead glass, a high-resistance, high-emissivity material that forms a continuous dynode. A high voltage of approximately 2 kV to 3 kV is applied between the entrance and exit of the channeltron. When an electron strikes the channeltron's inner walls, secondary electrons are emitted. These secondary electrons are then accelerated down the tube by the potential difference. The curved geometry of the channel, which is much more complex than depicted in the figure, ensures they will strike the inner wall again, initiating an electron avalanche that multiplies the number of electrons with each subsequent impact [116].

3.2.1 Angle-Resolved X-ray Photoelectron Spectroscopy (ARXPS)

As previously discussed, the IMFP determines the information depth that XPS can access. While photoelectrons with kinetic energies of only a few hundred electronvolts are already highly surface-sensitive due to their small IMFP (compare with Section 3.1), the surface sensitivity can be increased further. If the sample is rotated relative to the analyzer, as sketched in Figure 3.4, the effective escape depth (EED) from which photoelectrons can escape the sample decreases. While at normal emission the EED is on the order of the IMFP, at a grazing emission angle of $\Theta = 60°$, the EED is significantly reduced, thereby enhancing the contribution of the surface layers to the total signal [117].

Angle-resolved photoelectron spectroscopy (ARPES) is a general term that makes use of the angular dependence of photoemitted electrons in both the polar (Θ) and azimuthal (Φ) directions. Most commonly, the term ARPES refers to the study of electronic band structures, which involves mapping the electronic dispersion of the valence band in k-space. As will be discussed in Section 3.3, the angular distribution of diffracted

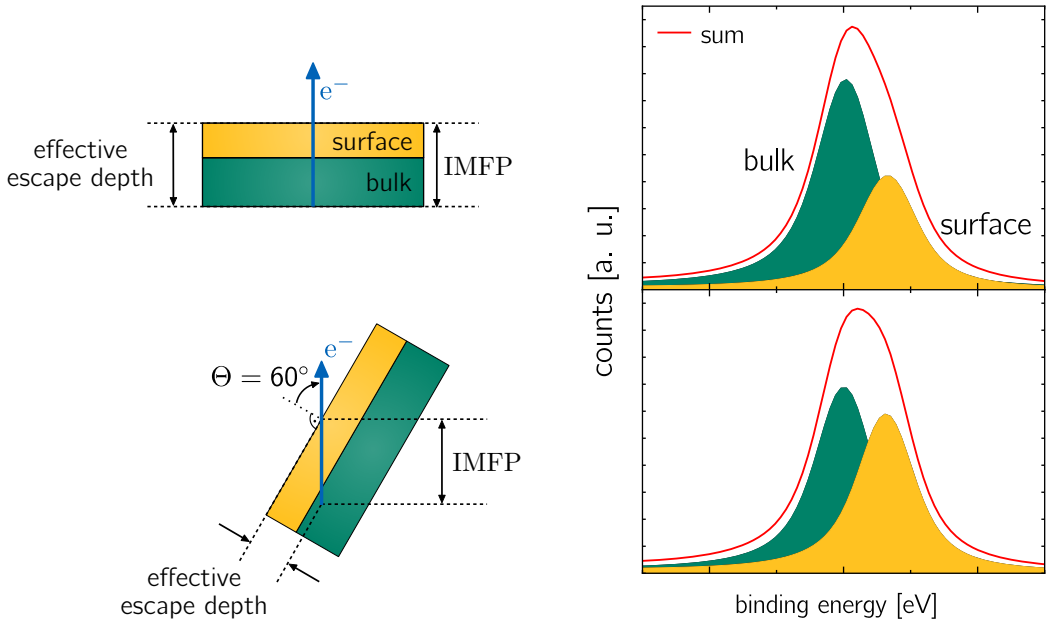

Figure 3.4: Principle of angle-resolved X-ray photoelectron spectroscopy (ARXPS). Measuring photoelectrons emitted at grazing angles effectively reduces the escape depth and increases the surface sensitivity compared to measuring at a normal emission angle.

photoelectrons is also used in XPD to analyze the local structural arrangement. In this work, ARXPS is primarily used to resolve the layer arrangement of the topmost surface and interface layers of a sample.

The EED, however, should not be confused with related concepts such as the information depth (ID), the electron attenuation lenght (EAL), or the mean escape depth (MED) [77, 78]. While all are closely related, the EED is a simplified geometric approximation that neglects diffraction effects [117]:

$$\Lambda_{\mathrm{EED}} = \cos(\Theta) \cdot \Lambda_{\mathrm{IMFP}} \,. \tag{3.9}$$

This simple relation provides a good qualitative understanding of how grazing-angle measurements increase surface sensitivity and helps in the analysis of the stacking order in layered systems, which is the main application of angle-resolved spectroscopy in this thesis [118, 119].

3.2.2 XPS Data Analysis

Quantitative analysis of XPS measurements typically involves fitting the measured spectrum to contributions from different chemical elements or a single element in different chemical environments. As sketched in Figure 3.2, spectral lines can be assigned to the electronic orbitals of the elements in the sample under investigation. For samples consisting of multiple elements, analyzing the relative intensities of these contributions enables the determination of the sample's elemental composition. Databases such as the

one provided by NIST [120] help identify the elemental contributions observed in XPS spectra.

Measured XPS spectra can be divided into two categories:

- **Survey spectra** span a wide energy range and are used for the identification of the sample's elemental composition.
- **high energy-resolution XPS spectra (HighRes)** are recorded with high energy resolution over a narrow energy range corresponding to a specific core level. These spectra enable detailed analysis of the different chemical environments in which an element exists in the sample.

Film thicknesses for thin adlayers or stacked-layer structures can be obtained from survey spectra. This is done either by using ARXPS or by analyzing the relative intensities of core levels from different elements [121–123]. These approaches are primarily based on the attenuation of photoelectron signals by the layers stacked above the emitting layer. However, this method is less precise in the monolayer or submonolayer regime, or when growth occurs in island-like rather than layer-by-layer growth. As submonolayer coverages are a primary focus of this thesis, film thicknesses were determined using Fadley's approach for submonolayer coverage [124], as summarized by Zemlyanov et al. [125]. This approach is described in detail in the Appendix C, and depends on sample-dependent parameters, such as material densities, Scofield cross-sections, and photoelectron attenuation lengths.

Spin-Orbit Coupling

As depicted in Figure 3.5, a typical high-resolution XPS spectrum of a core level with non-zero angular momentum displays a characteristic doublet structure, separated by the spin-orbit splitting energy, E_{SOC}. The details of the peak lineshapes and background contributions will be discussed later and are ignored here for simplicity. The example shown represents the Au $4f$ signal, which is investigated in detail in this thesis. Each bound electron is described by a unique set of quantum numbers, which define the stationary state in which the electron resides [126]. The states of electrons are described using two different notations: the X-ray notation (IUPAC notation) and the spectroscopic notation. The use of two different notations has historical origins; the spectroscopic notation was developed primarily by chemists, while the X-ray notation was developed by physicists [127]. Since XPS was established with significant contributions from chemistry, and Auger-Meitner electron spectroscopy (AES) was mainly developed by physicists, the X-ray notation is still commonly used to describe the Auger-Meitner process. In contrast, the spectroscopic notation is widely used to describe XPS spectra. A detailed description of these nomenclatures and how to convert between them is provided in the Appendix A.3.

The principal quantum number, n, defines the energy level (or shell) an electron occupies. It can take integer values starting from $n = 1$ for the most tightly bound electrons, with increasing values for energy levels farther from the nucleus. Each principal energy

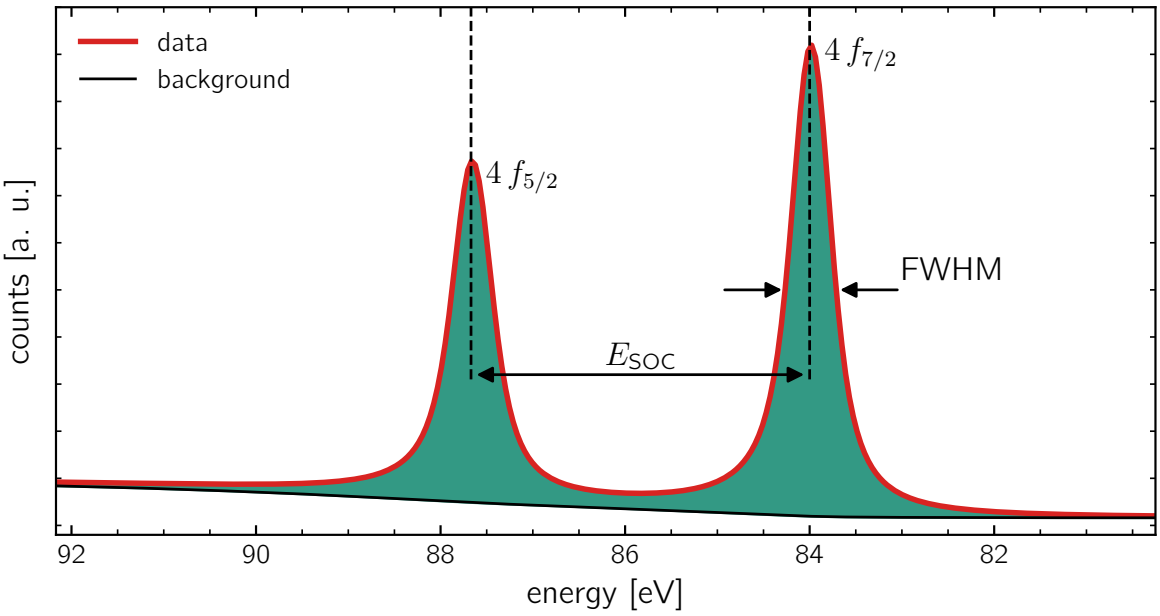

Figure 3.5: Typical XPS spectrum of the Au $4f$ signal, the two peaks of a doublet are observed.

level contains one or more subshells, which determine the shape of the electron's spatial distribution. These are characterized by the angular momentum quantum number, l, which can take integer values from 0 to $n-1$. The orientation of the orbital angular momentum vector is described by the magnetic quantum number, m_l, which specifies its projection onto a defined axis (conventionally the z-axis) and can take integer values from $-l$ to $+l$. Lastly, the orientation of the electron's spin ($s = 1/2$) is described by the spin magnetic quantum number, m_s, which can take values of $m_s = \pm 1/2$ [127, 128].

Each orbital (defined by n, l, m_l) can contain a maximum of two electrons, which must have opposing spins $m_s = \pm 1/2$. Crucially, no two electrons in the same atom can have an identical set of all four quantum numbers (n, l, m_l, m_s). This is the Pauli exclusion principle [129]. A detailed explanation of the quantum numbers is given in the Appendix A.1.

Spin-orbit splitting in XPS arises because electrons in an atomic subshell with non-zero orbital angular momentum ($l > 0$) experience an interaction between their orbital angular momentum (l) and their intrinsic spin angular momentum (s). This interaction couples the two momenta, meaning that m_l and m_s are no longer independent [130]. Consequently, a new set of quantum numbers is required to describe the electron's state, defined by the total angular momentum, j. A single energy level splits into a doublet of two states with slightly different binding energies, distinguished by their j value, which can take the values $j = l \pm s = l \pm 1/2$. The orientation of the total angular momentum vector is described by the total magnetic quantum number, m_j, which runs in integer steps from $-j$ to j. The set of quantum numbers describing an electron state under spin-orbit coupling is therefore (n, l, j, m_j).

Each of these spin-orbit split states, characterized by a specific j value, has a degeneracy of $2j + 1$. This degeneracy, which corresponds to the number of possible m_j values, is precisely the reason that the two components of a spin-orbit doublet in an XPS spectrum exhibit a distinct intensity ratio. For example, for a core hole in the Au $4f$ subshell ($l = 3$), the two possible j values are $j = 3 + 1/2 = \frac{7}{2}$ and $j = 3 - 1/2 = 5/2$. The degeneracy of the $j = 7/2$ state is $2(7/2) + 1 = 8$, while the degeneracy of the $j = 5/2$ state is $2 \cdot (5/2) + 1 = 6$. The ratio of the number of available final states, and thus the expected intensity ratio of the corresponding XPS peaks, is therefore $8 : 6$, or $4 : 3$. Further details are given in the Appendix A.2.

Chemical Shift

A key advantage of XPS is its ability to resolve the different chemical environments in which an element exists within a sample. This ability arises from slight, environment-dependent shifts in the measured binding energy, a phenomenon known as the chemical shift. This effect was discovered by Kai Siegbahn, for which he was awarded the Nobel Prize in Physics in 1981 [131].

A classic and instructive example is the C $1s$ core-level spectrum of the ethyl trifluoroacetate molecule, as displayed in Figure 3.6 [132, 133]. The molecule contains four carbon atoms, each in a distinct chemical environment. The origin of the chemical shift can be understood by considering the local electronegativity of the bonding partners. Valence electrons involved in a chemical bond are shifted towards the partner with the higher electronegativity. This displacement reduces the extent to which these valence electrons screen the nuclear charge for the remaining core electrons. Consequently, the core electrons experience a higher effective nuclear potential, which increases their binding energy, making them harder to remove.

For example, the CF_3 component is shifted by $\Delta E = 8.2\,\text{eV}$ relative to the CH_3 component. By comparing the electronegativities on the Pauling scale, where higher values indicate stronger electron attraction (C: 2.55, H: 2.2, O: 3.44, and F: 3.98), it becomes clear that the observed trend in binding energy shifts correlates with the electronegativity of the bonding partners.

While this concept often serves as a good rule of thumb, deviations exist [134, 135], especially in alloys. Au-Sn alloys, in particular, are well known for such unexpected shifts [136]. To determine core-level binding energies, the Fermi level (E_F) is the standard reference, requiring that the sample and spectrometer be in good electrical contact. Consequently, interpreting observed shifts in core-level binding energies is not simply a function of electronegativity but results from the interplay of several competing physical effects that can shift both the core levels and the alloy's Fermi level relative to the pure elements [136]. For a system like AuSn, the most important factors include:

- **Alloy Fermi Level**: An alloy forms a new, common Fermi level that is distinct from that of its pure constituents. Since all core levels are referenced to this new E_F, the entire electronic "energy ladder" shifts. Only if all core-level binding energies

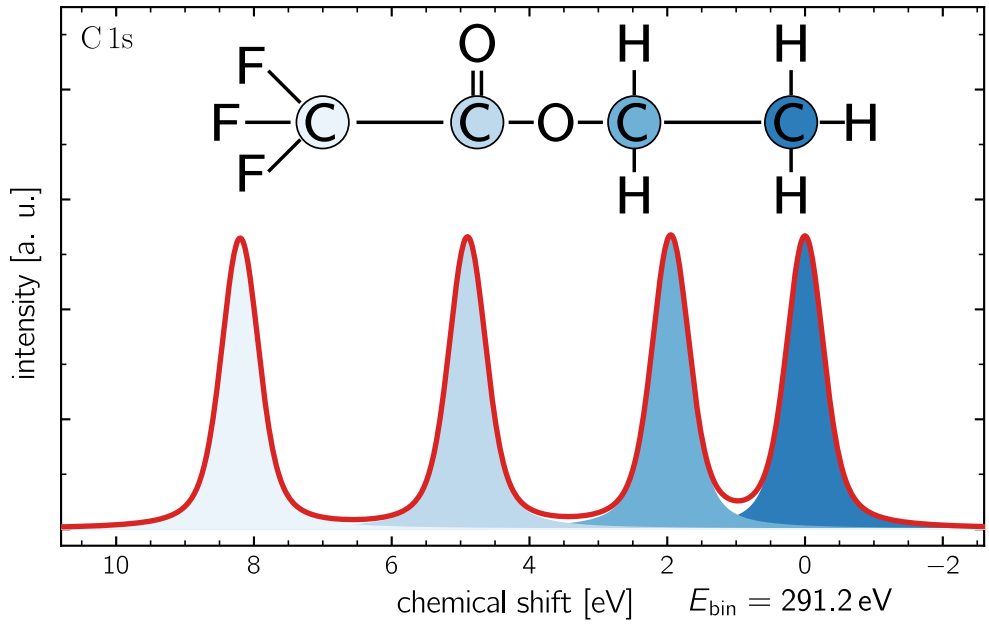

Figure 3.6: The C 1*s* core level shifts of the ethyl trifluoroacetate molecule illustrate the shift in binding energy observed for carbon atoms in different chemical environments. Reproduced from [132, 133].

are referenced to this new Fermi level is a direct comparison to the binding energies of the pure elements meaningful.

- **Inter-Atomic Charge Transfer**: If charge transfer occurs between alloying elements, it can significantly shift the Fermi level. This is especially true for metals with a low density of states (DOS) at E_F. For example, Au has a DOS of only $\approx 0.3\,\frac{\text{electrons}}{\text{atom}\cdot\text{eV}}$ close to E_F, meaning even a small charge transfer can shift its Fermi level by hundreds of meV.

- **Packing Density**: Alloying often changes the interatomic spacing. An increase in density (compression) leads to stronger interatomic core-valence repulsion, which can shift core levels to lower binding energies.

- **Final State Effects**: The measured binding energy is also affected by how efficiently the surrounding valence electrons screen the core hole created during photoemission. This screening efficiency can change dramatically upon alloying, leading to significant shifts in the binding energy.

- **Intra-Atomic Charge Transfer/Rehybridization**: The occupancy of valence levels can change upon alloying. It has been observed that for AuSn alloys, an intra-atomic charge transfer from the Au 5*d* to the 6*s* level occurs. This process increases the binding energy of the Au core levels, offsetting the expected shift to lower binding energies that would result from inter-atomic charge transfer from the less electronegative Sn (1.96) to Au (2.54).

A special case of binding energy shift, known as a surface core-level shift, is observed for atoms at the sample surface. These atoms experience a modified chemical environment due to their reduced number of bonding partners, a consequence of the broken symmetry at the surface [136, 137]. This effect was first observed for the Au $4f$ signal [138].

Background and Peak Shape

The primary analytical focus of this thesis is on HighRes XPS spectra, which are fitted to quantitative models to identify different chemical states. A significant challenge in quantitative XPS analysis is selecting appropriate peak lineshapes and background models to identify different chemical states of an element. In the following, background models and peak shapes are discussed, before the fitting procedure is explained.

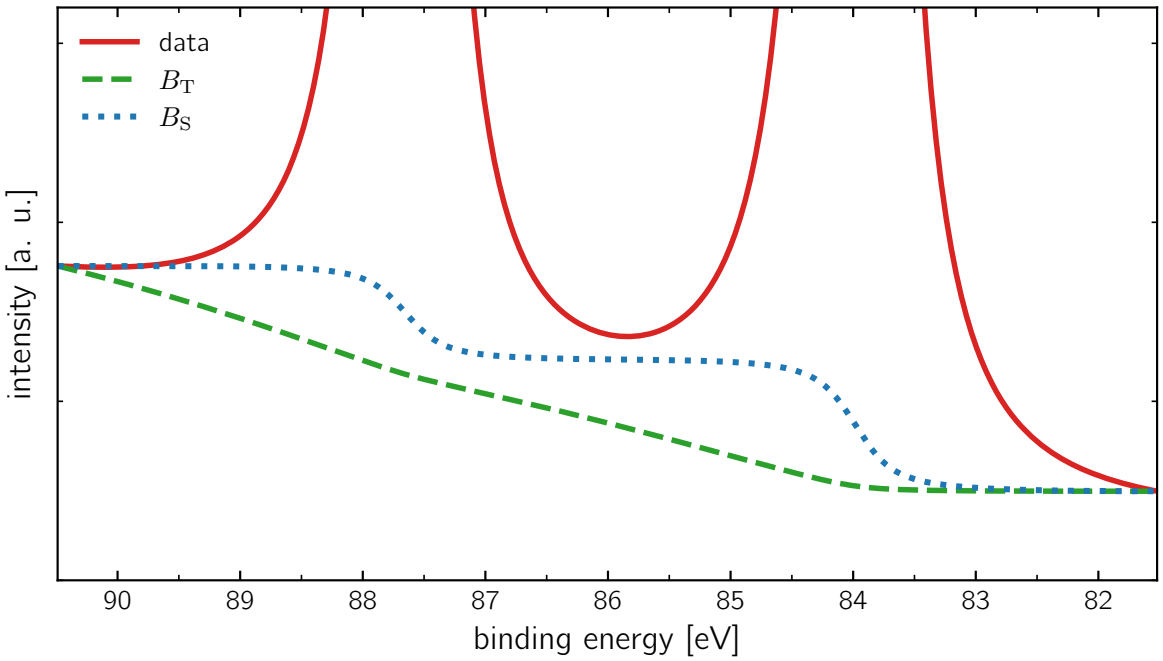

Figure 3.7: Comparison of the background shapes of the Tougaard background B_T and the Shirley background B_S.

As previously discussed in Section 3.1, during photoemission, an electron excited from a core level may undergo inelastic scattering events on its way to the solid's surface. These processes, which lead to kinetic energy losses and the creation of secondary electrons, generate a characteristic background in the measured spectrum.

To model this background, two approaches are commonly used: the empirical Shirley background and the physically motivated Tougaard background. Figure 3.7 demonstrates the different characteristics of these two models. The Shirley background (B_S), represented by the blue dotted line, exhibits a step-like behavior, obtained by integrating the measured data over a defined energy range surrounding the peak. In contrast, the Tougaard background (B_T), represented by the dashed green line, has a shape derived

from the inelastic scattering cross-section, which naturally accounts for the energy loss tail and thus allows for a more physically meaningful analysis of asymmetric peaks (details on the signal's peak shape will be discussed later).

The Shirley background is calculated as:

$$B_{\mathrm{S}}(E_1) = k \int_{E_1}^{E_2} [I(E') - I(E_2)] \, \mathrm{d}E' \ , \tag{3.10}$$

with E_1 and E_2 being the start and end points of the integration range, and $I(E')$ being the measured intensity [139]. The Shirley background assumes a uniform energy loss function and is therefore best suited for approximately symmetric peaks, where the signal is well described by a line shape that is similar on the low- and high-binding-energy sides. In contrast, many core-level spectra, especially in metals and strongly interacting systems, exhibit asymmetric peaks due to lifetime broadening and many-body effects, which lead to an extended tail on the high-binding-energy side.

The Shirley background does not approximate the sloping background behaviour of such asymmetric peaks well [140]. The Tougaard background, however, is based on the inelastic-electron scattering cross-section, providing a more physical model for the background and better accounting for the long inelastic tail underlying asymmetric core-level features:

$$B_{\mathrm{T}}(E) = \lambda(E) \int_{E}^{\infty} K(E,T) I(E') \, \mathrm{d}E' \ . \tag{3.11}$$

Here, $T = E' - E$ is the energy loss, $\lambda(E)$ is the IMFP, and $K(E,T)$ describes the probability that an electron of energy E loses energy T when traveling through the solid [141]. The product $\lambda(E)K(E,T)$ is the inelastic-electron scattering cross-section, which can be approximated using various functional forms. One common form is:

$$\lambda(E)K(E,T) = \frac{BT}{(C + C'T^2)^2 + DT^2} \ , \tag{3.12}$$

where the parameters B, C, C', and D can be obtained from electron energy loss spectroscopy (EELS) [142].

Since the Tougaard model assumes that the characteristic inelastic tail becomes negligible at kinetic energies of approximately 30 eV to 50 eV below the main peak, and the integral in Equation (3.11) extends to infinity, practical approximations must be made. Commonly, HighRes spectra are not measured over such a broad energy range. It has been shown, however, that even for these limited ranges, modifying the Tougaard background by adding a polynomial term yields reasonably good fitting results [140, 143].

Photoelectrons emitted from a well-defined energy level should ideally produce a delta function, $\delta(E - E_{\mathrm{bin}})$, in the XPS spectrum. However, as discussed in Appendix B, intrinsic and extrinsic broadening effects cause the measured peak to have a finite width and a specific peak lineshape. Mathematically, the ideal delta function is convoluted with various broadening functions to generate the final measured signal.

The broadening due to the finite core-hole lifetime has a Lorentzian shape:

$$L(E; E_0, \sigma_\mathrm{L}) = \frac{1}{\pi}\left[\frac{\sigma_\mathrm{L}}{(E-E_0)^2 + \sigma_\mathrm{L}^2}\right], \tag{3.13}$$

where E_0 is the center and $f_\mathrm{L} = 2 \cdot \sigma_\mathrm{L}$ defines the full width at half maximum (FWHM) of the Lorentzian [144]. Thermal and instrumental broadening contributions are well described by a Gaussian function:

$$G(E; E_0, \sigma_\mathrm{G}) = \frac{1}{\sigma_\mathrm{G}\sqrt{2\pi}} \cdot \exp\left(-\frac{(E-E_0)^2}{2\sigma_\mathrm{G}^2}\right), \tag{3.14}$$

with $f_\mathrm{G} = 2 \cdot \sigma_\mathrm{G}\sqrt{2\ln 2} \approx 2.355\sigma_\mathrm{G}$ being the Gaussian FWHM [144]. All Gaussian contributions can be combined into a single effective Gaussian because the convolution of two Gaussians is itself a Gaussian, with a variance equal to the sum of the individual variances: $\sigma^2_{\mathrm{G,conv}} = \sigma^2_{\mathrm{G},1} + \sigma^2_{\mathrm{G},2}$ [145]. The resulting peak shape, a convolution of a Gaussian and a Lorentzian [146], is known as a Voigt profile:

$$V(E; E_0, \sigma_\mathrm{G}, \sigma_\mathrm{L}) = \int_{-\infty}^{\infty} G(E'; 0, \sigma_\mathrm{G}) L(E - E'; E_0, \sigma_\mathrm{L})\, \mathrm{d}E' \ . \tag{3.15}$$

While there is no simple analytical solution for the Voigt integral, it can be expressed as the real part of the Faddeeva function, which can be computed numerically [147]. However, the Lorentzian used in the Voigt profile is symmetric. For metals, the interaction

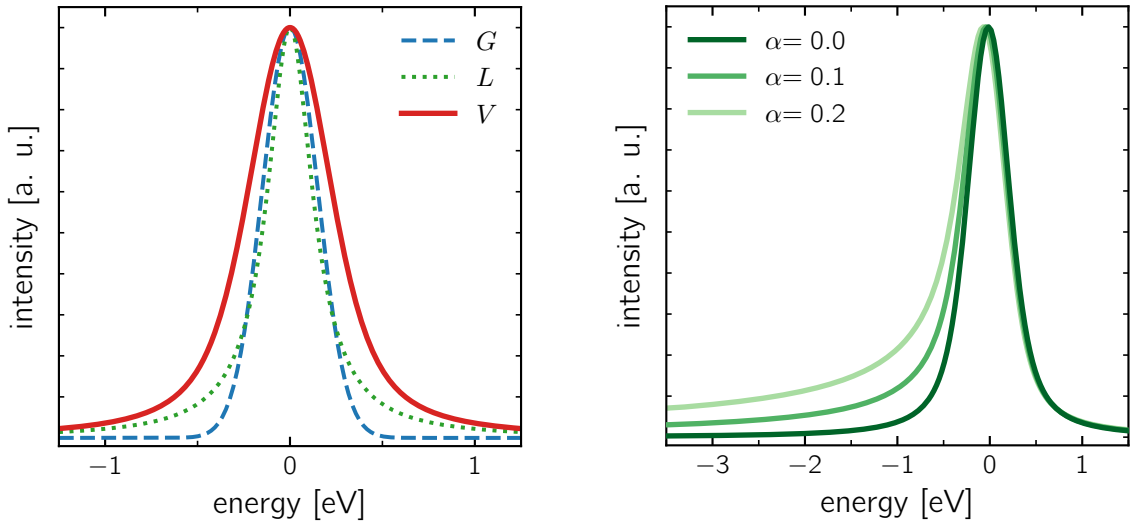

(a) Convoluted Voigt profile.

(b) Doniach-Šunjić profile.

Figure 3.8: (a) Visualization of a Voigt profile V as the convolution of a Lorentzian L and a Gaussian G. (b) The Doniach-Šunjić profile plotted for different asymmetry parameters α.

of the core hole with conduction electrons adds an asymmetry to the peak shape, creating

a tail towards lower kinetic energy (higher binding energy) [148]. This requires the use of asymmetric peak lineshapes like the Doniach-Šunjić (DS) lineshape [149]:

$$DS(E; E_0, \gamma, \alpha) = \frac{\cos\left[\frac{\pi\alpha}{2} + (1-\alpha)\cdot \arctan\left(\frac{E-E_0}{\gamma}\right)\right]}{[(E-E_0)^2+\gamma^2]^{(1-\alpha)/2}}\,. \tag{3.16}$$

Here, α is the asymmetry parameter. If $\alpha = 0$, the DS peak lineshape reduces to a Lorentzian profile, with the width parameter $\gamma = \sigma_{\mathrm{L}}$. The DS profile presents challenges, most notably that its area is mathematically infinite. Therefore, when calculating peak areas, the integration must be performed over a finite energy range.

As with the Voigt profile, its FWHM has no simple analytical solution and must be approximated. Empirically, by fitting the FWHM of DS profiles as a function of γ and the asymmetry α, it was found that:

$$f_{\mathrm{DS}} = \gamma\Big(2 + \alpha\cdot b + (\alpha\cdot c)^4\Big)\,, \tag{3.17}$$

provides a very good approximation, with $b = 2.5135$ and $c = 3.6398$, yielding an error of less than 2% for $\alpha < 0.25$. Further details are found in the `lmfitxps` documentation [150].

Since the DS profile accounts only for intrinsic broadening (lifetime and asymmetry), it must, as in the Voigt profile, be convoluted with a Gaussian to account for instrumental and thermal broadening. This convoluted Doniach-Šunjić-Gaussian profile is used to fit all HighRes core-level spectra in this thesis.

Fitting Procedure and Software

Fitting a mathematical model to experimental data requires an optimization procedure to determine the model's parameters that achieve the best possible agreement with the measured spectrum. This optimization is performed by minimizing a target function, typically based on the residual, which is the difference between the measured spectrum $I(E)$ and the model function $M(E, \boldsymbol{p})$. For XPS data, which are subject to Poisson counting statistics, the weighted residual should be minimized [151, 152]. The weighted residual $R(k)$ at each data point k is given by:

$$R(k) = \frac{I(k) - M(k, \boldsymbol{p})}{\sqrt{I(k)}}\,. \tag{3.18}$$

This weighting prevents the high-intensity peak regions from disproportionately influencing the fit. The quantity that the algorithm minimizes is χ^2, the sum of the squares of these residuals:

$$\chi^2(\boldsymbol{p}) = \sum_{k=1}^{N} [R(k)]^2 = \sum_{k=1}^{N} \frac{[I(k) - M(k, \boldsymbol{p})]^2}{I(k)}\,, \tag{3.19}$$

where N is the number of experimental data points. To assess the goodness-of-fit, the reduced chi-squared is used:

$$\chi^2_{\text{red}}(\boldsymbol{p}) = \frac{\chi^2(\boldsymbol{p})}{N - P}. \tag{3.20}$$

Typically, the number of independent parameters P is small compared to the number of data points ($N \gg P$), ensuring that $N - P \approx N$.

In this thesis, all model fitting and parameter optimization are performed using the Levenberg-Marquardt algorithm [153, 154]. While this fitting process is well defined, finding suitable software for XPS analysis is challenging. Most widely used tools are proprietary and limited to Windows operating systems, such as `CasaXPS` [155], `Thermo Avantage` [156], `Unifit` [157], and others [158–160]. Their proprietary, *black-box* nature prevents users from adapting the code or independently verifying the fitting algorithms. Key limitations in many commercial packages include the use of approximations for the Voigt and Doniach-Šunjić peak lineshapes and, crucially, a static approach to background subtraction. Typically, the background is calculated and subtracted *before* the peak fitting, which can introduce artifacts, especially for multi-component and asymmetric XPS peak signals.

To overcome these limitations, a new open-source Python package, `lmfitxps` [150], was developed as part of this thesis. It is built upon the robust `LMFIT` Python library, which implements the Levenberg-Marquardt algorithm [161]. `lmfitxps` implements the background and peak-shape models discussed above. Its critical feature is the ability to include the background model in the optimization process and to optimize all background parameters *simultaneously* with the peak parameters, avoiding the issues of static background subtraction.

Building on this package, a cross-platform graphical user interface, `LG4X-V2` [162], was also developed to streamline the analysis workflow. This work was inspired by software developed by Hideki Nakajima [163]. The development of open-source tools is continued by Gwilherm Kerherve, who developed `KherveFitting/LG4X-V3` and added significant new features to the software [164].

For all spectra fitted in this thesis, both the χ^2_{red} and a plot of the normalized residual $R(E)$ are provided. A good fit is indicated by a residual that is randomly distributed around zero and a reduced chi-squared value that approaches unity ($\chi^2_{\text{red}} \to 1$) [151, 165]. A guiding principle in spectral fitting is to always constrain parameters within physically meaningful boundaries and to avoid adding components solely to improve the fit quality without physical justification [165]. To aid in model selection, information criteria can be used to balance the goodness-of-fit against model complexity [166–168].

Referencing of Binding Energies

Determining absolute binding energies in XPS can be challenging, a topic that has been discussed extensively in the literature [169–171]. The gold standard for conductive samples that are in good electrical contact with the spectrometer is to measure the sample's Fermi edge. As long as the spectrometer's energy scale is linear, the Fermi

edge provides a robust internal reference, with its inflection point defined as zero binding energy ($E_{\mathrm{bin}} = 0\,\mathrm{eV}$).

Figure 3.9(a) shows an experimentally measured Fermi edge. In this work, the Fermi edge was measured before and after each set of HighRes spectra using identical spectrometer and excitation source settings as for the measurement itself. The binding energy scale was then calibrated by fitting the Fermi edge with a model consisting of a Fermi-Dirac distribution convoluted with a Gaussian.

The fit model is highly sensitive to the center position of the Fermi edge. This is demonstrated in Figure 3.9(b), where the reduced χ^2_{red} is plotted for different center positions of the fit model applied to the data from Figure 3.9(a). This procedure enables precise and reproducible energy referencing. In addition, the width of the Gaussian used to broaden the Fermi-Dirac function provides a direct measure of the total experimental energy resolution, as detailed in Appendix B.

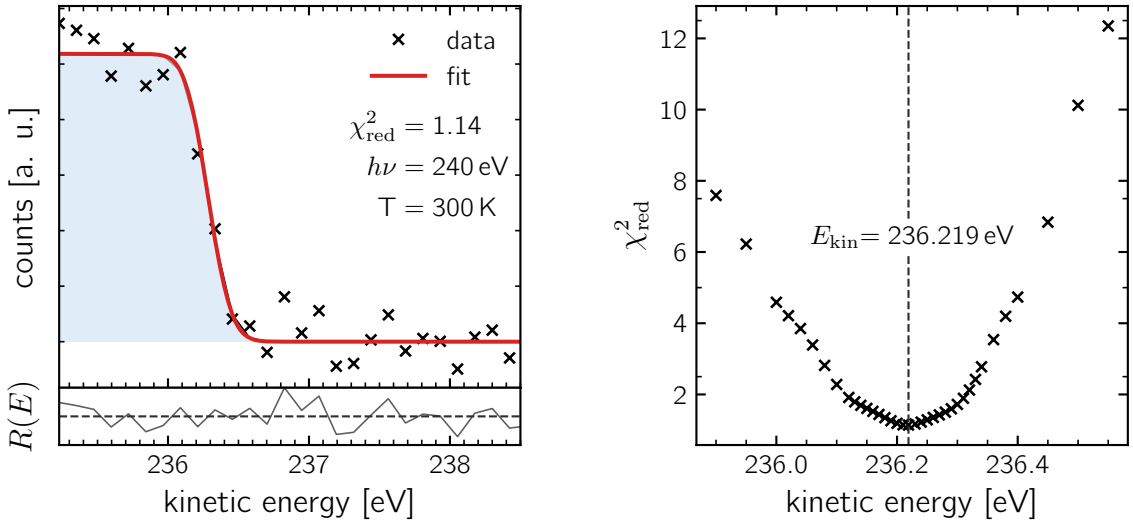

(a) Measured and fitted Fermi edge.

(b) Binding energy calibration.

Figure 3.9: (a) A measured Fermi edge is fitted with a model (red line) to precisely determine its energy position, defined as 0 eV binding energy. (b) The reduced chi-squared of the fit exhibits a parabolic shape with a minimum at the true Fermi edge position, demonstrating the high precision of the calibration method.

3.3 X-Ray Photoelectron Diffraction (XPD)

While XPS focuses on the energy and momentum of emitted photoelectrons, properties described within the particle model, XPD utilizes the particle-wave duality of electrons [172]. This concept is also central to LEED, which will be discussed in Section 3.4.

Although the basic principle is similar to X-ray photoelectron *spectroscopy*, the key difference is that X-ray photoelectron *diffraction* takes the wave characteristics of the emitted photoelectron into account. A photoelectron, emitted from a core level of a

so-called emitter atom, can scatter at the atoms surrounding the emitter, referred to as scatterers [173, 174]. This principle is illustrated in Figure 3.10(a).

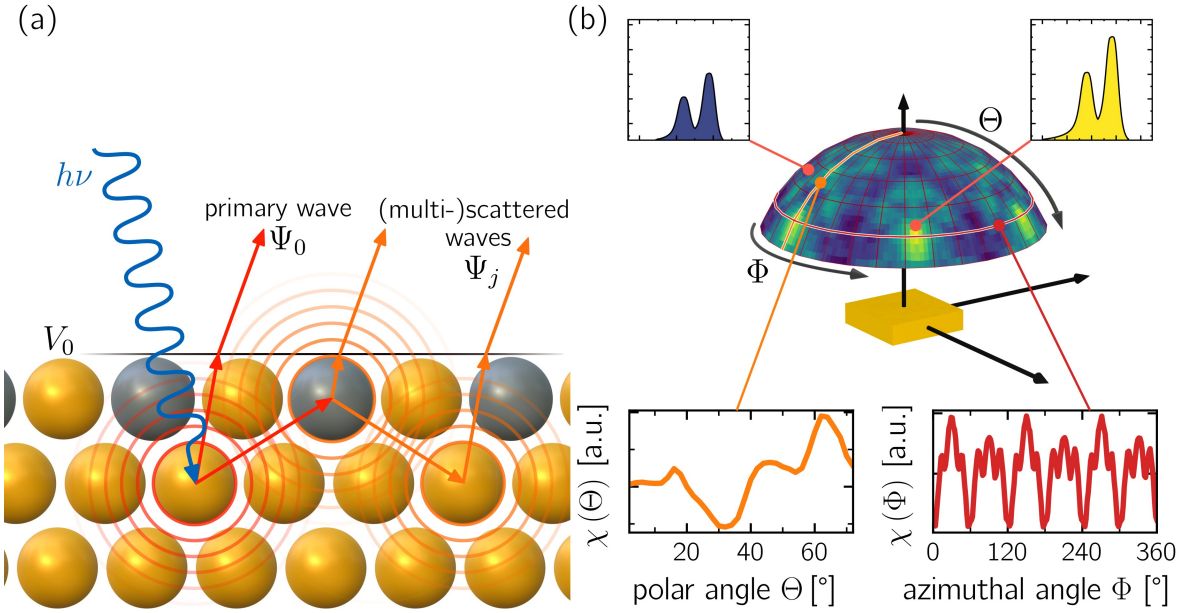

Figure 3.10: (a) Illustration of photoelectron diffraction. The primary wave Ψ_0 interferes with the (multiply) scattered waves Ψ_j, resulting in an interference pattern containing structural information about the local environment of the emitter. (b) Intensity modulation in the experimental XPD pattern is observed as a function of the polar Θ and azimuthal Φ angles; each data point on the hemisphere corresponds to a single integrated XPS spectrum. Figures inspired by [175].

Considering a single emitted photoelectron wave, the unscattered, primary photoelectron wave, Ψ_0, interferes with the photoelectron waves, Ψ_j, that have been elastically scattered at neighboring atoms. This creates a complex interference pattern that depends on the final emission direction, defined by the wavevector $\boldsymbol{k}$ (or equivalently by the angles Φ and Θ). The resulting intensity modulation recorded by the detector is the square of the total wavefunction, which is the sum of all contributing waves:

$$I(\boldsymbol{k}) = \left| \Psi_0(\boldsymbol{k}) + \sum_j \Psi_j(\boldsymbol{k}) \right|^2 . \tag{3.21}$$

The direct wave Ψ_0 is the component emitted from the source atom that travels straight to the detector. Each scattered wave Ψ_j is created by a fraction of the primary wave traveling first to a neighboring scatterer atom j and is then diffracted towards the detector [176]. The direct wave, originating from the emitter at the origin, takes the form $\Psi_0 \propto 1/r \exp(ikr)$. A wave scattered from an atom at position $\boldsymbol{r}_j$ is likewise described as a spherical wave originating from that point, $\Psi_j \propto 1/|\boldsymbol{r} - \boldsymbol{r}_j| \exp\left(ik|\boldsymbol{r} - \boldsymbol{r}_j|\right)$ [176].

The interference between Ψ_0 and Ψ_j at the detector is determined by the phase difference between them. This difference arises because the scattered wave travels a longer, different

path to the detector than the direct wave. The path-length difference depends on both the scatterer's location and the scattering angle. The resulting intensity modulations are therefore directly dependent on the interatomic distances and the geometric arrangement of the surrounding atoms. It is important to note that only elastic scattering preserves the phase coherence between Ψ_0 and Ψ_j (compare Section 3.1). In addition to the phase shift, the atomic scattering factor $f_j(\boldsymbol{k})$ defines the amplitude of scattered waves. It depends strongly on the energy, the scattering angle, and the element of the scattering atom [175, 177, 178]. Furthermore, as sketched in Figure 3.10(a), the photoelectron wave undergoes refraction at the surface when leaving the sample due to the inner potential V_0, which influences the angles at which the intensity maxima are observed [179]. Therefore, the

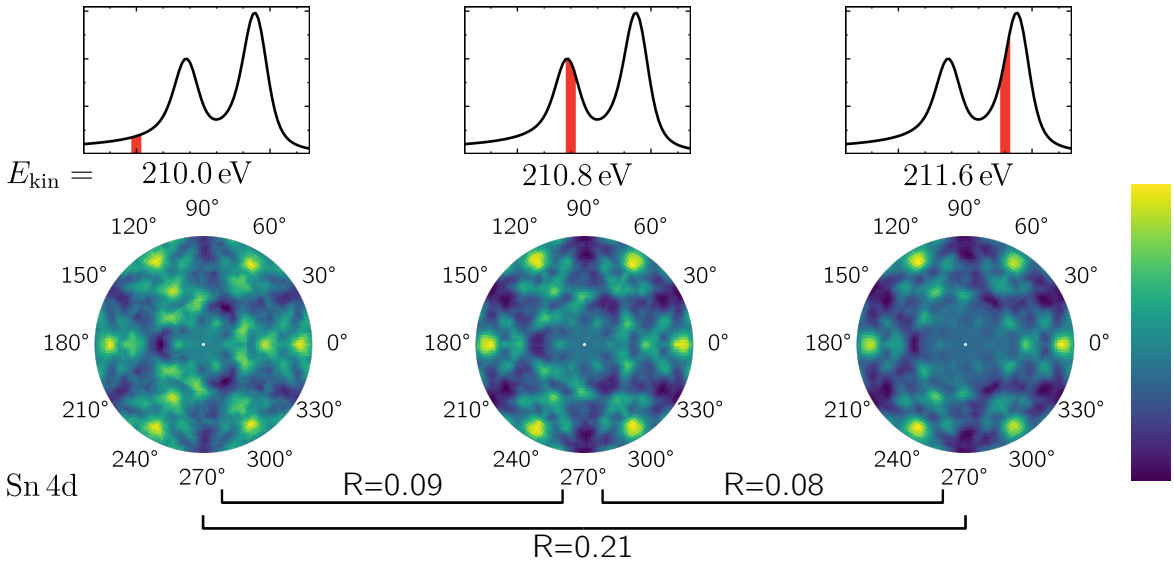

Figure 3.11: The high sensitivity of the XPD diffraction pattern to small changes in the photoelectron kinetic energy is demonstrated. In the top row, the energy range integrated to obtain the corresponding XPD pattern below is marked in red. The difference between the resulting XPD patterns is quantified by the R-factor, which is a factor of 5 larger than the agreement between experimental and simulated patterns observed in Section 6.1.4.

interference condition changes as either the measured emission angle or the photoelectron energy is varied. The latter can be achieved, for example, by measuring emission from a different core level or by changing the photon energy $h\nu$. Measuring the angular dependence of the photoemission intensity modulations allows a precise determination of the local structural environment of the emitter atom. This measurement principle is shown in Figure 3.10(b). The resulting hemisphere of intensity modulations is plotted as a function of the polar angle Θ and the azimuthal angle Φ. Each data point on the hemisphere represents an integrated HighRes spectrum.

In contrast to most other diffraction methods, XPD does not rely on long-range periodicity. Due to its high sensitivity to the local environment, it is suitable for systems with only local order, such as small atomic clusters. Furthermore, XPD offers chemical resolution. Since the diffracted photoelectron is emitted from a specific core level within the sample, rather than being generated by bombardment with an external electron beam, the technique is element-specific. This chemical sensitivity allows for determining the contribution of a

specific chemical state to the diffraction pattern, enabling a precise, element-resolved analysis of the local structure [180–182].

Figure 3.11 demonstrates the high sensitivity of the diffraction pattern to the photoelectron's kinetic energy. Although all three patterns shown have identical rotational symmetry, apparent differences are visible despite only minor differences in the integrated energy range of the measured photoelectron spectrum. To generate each pattern, the photoemission intensity was integrated over a narrow energy interval of only 120 meV centered on the stated kinetic energy. This interval is sufficiently narrow to justify calculating only a single energy step using the Electron Diffraction in Atomic Clusters (EDAC) algorithm, while averaging four experimental data points. For the XPD patterns presented in this work, the energy interval was chosen to be a narrow window of 120 meV, centered on the maximum intensity of the respective core-level peaks, namely Au $4f_{7/2}$ and Sn $4d_{5/2}$.

3.3.1 XPD Data Analysis

Acquiring XPD patterns is often time-consuming, with the duration depending on the desired angular resolution. A complete pattern, like that shown in Figure 3.10, consists of 7200 individual XPS spectra measured at different azimuthal (Φ) and polar (Θ) angles. All presented patterns were recorded using an excitation energy of $h\nu = 240\,\mathrm{eV}$. The angular resolution covered a polar angle range of $2° \leq \Theta \leq 72°$ in steps of $\Delta\Theta = 2°$ and a full azimuthal range of $0° \leq \Phi < 360°$ with increments of $\Delta\Phi = 1.8°$ for the Sn 4d XPD pattern. For the Au 4f measurement, a reduced polar angle range of $6° \leq \Theta \leq 72°$ was used due to limited beam time.

During the measurement of an XPD pattern, the incident photon flux decreases over time due to the intensity decay of the synchrotron radiation, as discussed in Section 4.3.3. Therefore, after subtracting a Shirley background from each spectrum, a normalizing anisotropy function, $\chi(\Theta, \Phi)$, was applied to the data for each polar angle Θ. More advanced background models are not implemented in the XPD software, and their effect on the resulting XPD pattern is negligible, as different backgrounds primarily generate a constant offset that is removed by the anisotropy function. This function is defined as:

$$\chi(\Theta, \Phi) = \frac{I(\Theta, \Phi) - \overline{I(\Theta)}}{\overline{I(\Theta)}}\,, \tag{3.22}$$

where $I(\Theta, \Phi)$ is the integrated intensity measured at the emission direction defined by the angles Θ and Φ, and $\overline{I(\Theta)}$ represents the mean intensity averaged over all azimuthal angles Φ for that specific polar angle Θ [183]. The anisotropy function effectively flattens the measured "ring" for each polar angle Θ of the XPD pattern. As a result, as seen in Figure 3.12(c), the diffraction pattern is already clearly visible after this normalization. However, artifacts such as cracks can sometimes appear, often attributed to poor electrical grounding of the sample at certain rotation angles. In the pattern shown, such a crack is visible at $\Phi \approx 230°$. These artifacts are removed either by applying symmetry operations to small azimuthal angle ranges where cracks appear or by normalizing the intensity

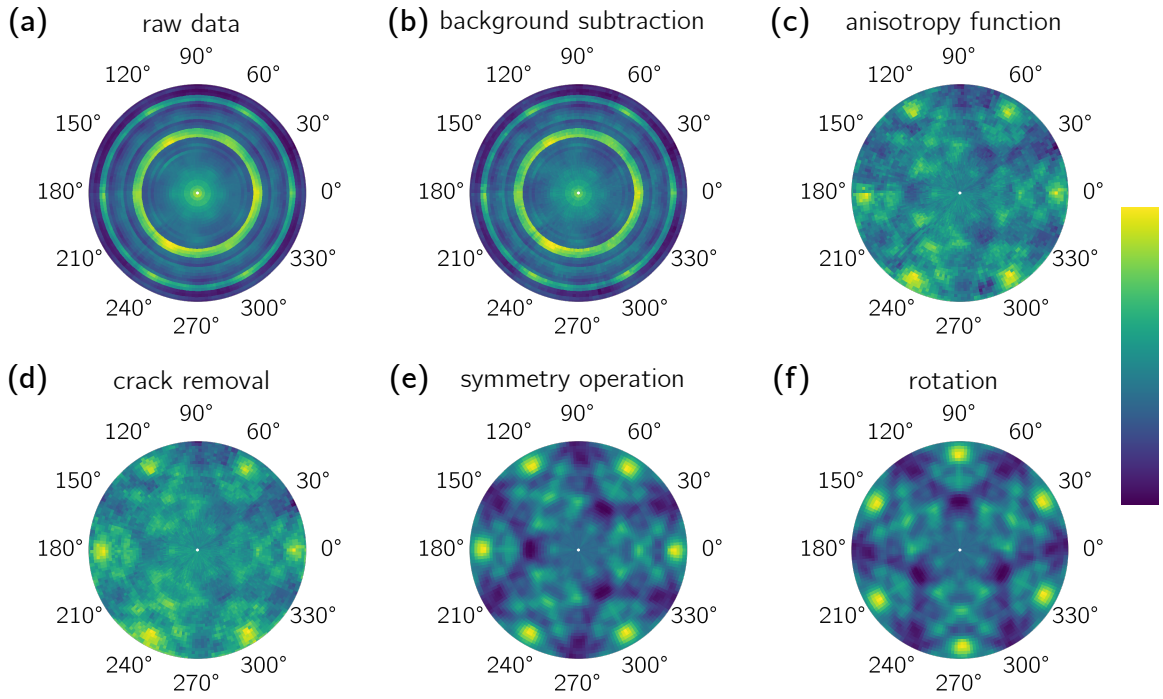

Figure 3.12: Overview of the post-processing steps from measured raw data in (a) to the presented XPD pattern in (f), demonstrated for the Sn 4d XPD pattern.

of affected individual spectra relative to their neighbors. The resulting XPD patterns are further processed by applying a threefold symmetrization operation to the entire XPD pattern. This step averages and interpolates the data based on the known surface symmetry. Finally, the pattern is often rotated to align its coordinate system with that of the simulated crystal structure for direct comparison.

Simulating XPD Patterns

A direct, analytical reconstruction of the sample's atomic structure from an XPD pattern is generally not feasible. This is because the phase information of the electron wave is lost in the intensity measurement, as $I(\boldsymbol{k})$ is the squared modulus of the total wavefunction. Therefore, a trial-and-error approach is used, in which diffraction patterns for different test structures are calculated and compared with experimental data. The agreement between the experimental and computed patterns is then evaluated to find the best match between the proposed model and the structure of the measured sample [184]. To quantify the agreement between the experimental (χ_{exp}) and simulated (χ_{sim}) patterns, Pendry's reliability factor (R-factor) is used:

$$\mathrm{R} = \frac{\sum_{\Theta,\Phi} \left[\chi_{\mathrm{exp}}(\Theta,\Phi) - \chi_{\mathrm{sim}}(\Theta,\Phi)\right]^2}{\sum_{\Theta,\Phi} \left[\chi^2_{\mathrm{exp}}(\Theta,\Phi) + \chi^2_{\mathrm{sim}}(\Theta,\Phi)\right]} \,. \tag{3.23}$$

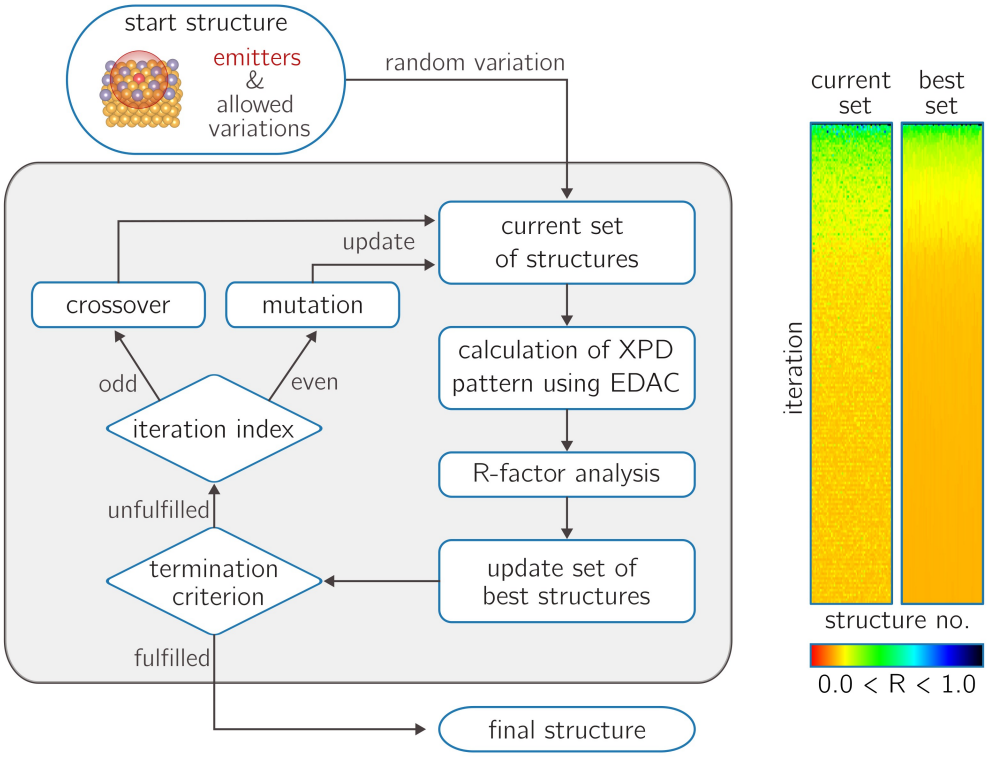

Figure 3.13: Flow chart of the genetic algorithm with the evolution of the R-factors for the best set of test structures.

The R-factor ranges from $0 \leq \mathrm{R} \leq 2$, where $\mathrm{R} = 0$ indicates perfect agreement, $\mathrm{R} = 1$ indicates no correlation, and $\mathrm{R} = 2$ corresponds to perfect anticorrelation [185]. The structural parameters of the test structure are iteratively varied to minimize the R-factor.

To simulate the XPD patterns, the EDAC algorithm was used [186]. The algorithm calculates the multiple scattering of electron waves at the atomic potentials within a cluster of atoms. These atomic potentials are approximated using a muffin-tin model [187], and the scattering is calculated up to the 20th order to take into account all significant scattered photoelectron waves Ψ_j [186]. The simulation cluster includes all atoms surrounding the emitter that are required for the calculation to converge. Specifically, it must contain all atoms for which the multiple-scattering amplitude of the photoelectron wave significantly contributes to the resulting interference pattern. The cluster size is typically defined by a radius $R_{\mathrm{max}} \approx 1.5\Lambda_{\mathrm{IMFP}}$ [186], where the inelastic mean free path (Λ_{IMFP}) is calculated using the TPP-2M formula, compare Equation (3.3). The EDAC code also allows for the use of a paraboloidal cluster for emitters near the surface. This shape is a computational optimization; it excludes atoms that are geometrically distant and cannot be reached by an electron undergoing multiple scattering processes before leaving the solid within a total path length of R_{max}. To calculate the multiple scattering of electron waves, the EDAC algorithm solves for the exact Green's function propagator iteratively. The calculation requires $\approx (10/3) \cdot N^2 \cdot (l_{\mathrm{max}} + 1)^3$ multiplications per iteration, where N is the number of atoms in the cluster and $l_{\mathrm{max}} \propto kr_{\mathrm{mt}}$ is the

maximum significant angular momentum needed for convergence, with k being the electron momentum and r_{mt} being the muffin-tin radius of the scatterers [186].

To find the optimal structure, a genetic algorithm is used to minimize the R-factor, thereby systematically improving the match between the simulated and experimental diffraction patterns [188, 189]. The principle of the genetic algorithm is illustrated in the flowchart in Figure 3.13. The process begins with an initial structural model (the start structure), which defines the atomic positions and their allowed ranges of structural variations. Each variable structural parameter of the initial structural model serves as a *gene*, while the allowed range of the parameter defines the possible *traits* for that gene.

From the initial structural model, a set of initial candidate structures is generated through random variation. For each candidate structure in the set, the corresponding XPD pattern is calculated using EDAC, and its agreement with the experimental data is quantified using the R-factor. Based on the R-factors, a subset of the best-agreement structural models is identified. As long as the termination criterion has not been met, a new generation of candidate structures is created. This is achieved either by randomly selecting pairs of best structures and combining their genes (crossover) or by randomly varying existing structures (mutation). This new set of candidate structures is then used for the next round of EDAC calculations and R-factor analysis.

The operations within the genetic algorithm (mutation, crossover, and variation) can potentially modify atomic positions in ways that violate known periodicity or rotational symmetries of the sample, e.g., as determined previously by LEED measurements. To prevent this, structural constraints must be imposed before running the algorithm. This is typically accomplished by grouping symmetry-equivalent atoms and restricting their parameters to move in unison, thereby preserving properties such as unit-cell periodicity.

3.4 Low-Energy Electron Diffraction (LEED)

Nearly every ultra-high vacuum (UHV) chamber used for surface science is equipped with a LEED system because it provides rapid insight into the surface's periodicity using a reliable, compact experimental setup. Electron diffraction is based on particle-wave duality, first postulated for massive particles by de Broglie in 1924 [172]. This was experimentally confirmed shortly thereafter by Davisson and Germer [190] and by Thomson [191] in diffraction experiments. Low-energy electrons are highly suitable for surface-sensitive measurements due to their short IMFP, especially in the energy range of 30 eV to 200 eV, as discussed in Section 3.1. The associated de Broglie wavelength:

$$\lambda = \frac{h}{\sqrt{2 m_{\mathrm{e}} E_{\mathrm{kin}}}}\,, \tag{3.24}$$

ranges from 2.2 Å to 0.9 Å, enabling the resolution of interatomic distances [76, 192]. When electrons are accelerated onto a well-ordered sample, elastically backscattered electrons interfere constructively if the 2D Laue condition is satisfied:

$$\boldsymbol{G}_{hk} = \boldsymbol{k}_f - \boldsymbol{k}_0 \,. \tag{3.25}$$

Here, $\boldsymbol{k}_0$ and $\boldsymbol{k}_f$ are the wave vectors of the incident and scattered electrons, respectively [193]. $\boldsymbol{G}_{hk}$ is a two-dimensional reciprocal lattice vector of the sample's surface lattice, given by:

$$\boldsymbol{G}_{hk} = h \cdot \boldsymbol{a}^* + k \cdot \boldsymbol{b}^* \,. \tag{3.26}$$

The vectors $\boldsymbol{a}^*$ and $\boldsymbol{b}^*$ are the reciprocal lattice vectors corresponding to the real-space lattice vectors $\boldsymbol{a}$ and $\boldsymbol{b}$, which define the sample's surface lattice in real space. h and k are the Miller indices that specify positions in reciprocal space.

The Laue condition can be visualized using the Ewald sphere construction, shown in Figure 3.14. For a two-dimensional lattice, the periodicity perpendicular to the surface is indefinitely large; this is represented by continuous lattice rods extending from the reciprocal lattice points, marked by yellow dots in Figure 3.14(a). The Ewald sphere is constructed as follows: The wavevector of the incident electrons, $\boldsymbol{k}_0$, connects the origin of the reciprocal lattice to the center of the sphere, and its length defines the sphere's radius. As the Ewald sphere is defined in reciprocal space, its radius scales inversely with the de Broglie wavelength ($|\boldsymbol{k}_0| \propto 1/\lambda$). Since only elastically scattered electrons preserve the phase coherence required for interference, LEED exclusively considers elastic scattering. Consequently, the wavevector of a scattered electron, $\boldsymbol{k}_f$, has the same length as the incident wavevector, $|\boldsymbol{k}_f| = |\boldsymbol{k}_0|$. Every intersection of the lattice rods with the Ewald sphere fulfills the Laue condition and corresponds to the position of a diffraction spot in the measured LEED pattern.

In contrast to grazing-incidence techniques such as reflection high-energy electron diffraction (RHEED), in LEED the incident electron beam is normal to the sample surface, simplifying the Ewald construction. Because the magnitude of the incident wavevector $|\boldsymbol{k}_0|$ determines the Ewald sphere's radius, adjusting the electron energy varies this radius. This, in turn, changes the number of intersections with the reciprocal lattice rods and enables higher-order spots to be observed at higher beam energies. As illustrated in Figure 3.14(b), the measured LEED pattern is a two-dimensional projection of these intersections.

Thus far, we have considered an ideal two-dimensional surface lattice with no periodicity in the direction perpendicular to the surface. In reality, the sample consists of many atomic layers; accounting for three-dimensional periodicity modifies this simple picture. Because of the short IMFP of low-energy electrons, the topmost 3 to 5 layers dominate the LEED pattern. Nevertheless, the three-dimensional periodicity of the bulk crystal produces an intensity modulation along each lattice rod. Consequently, the intensity of each diffraction spot varies with electron energy. Additionally, multiple scattering events and the atomic basis at each lattice point further contribute to this energy-dependent intensity modulation.

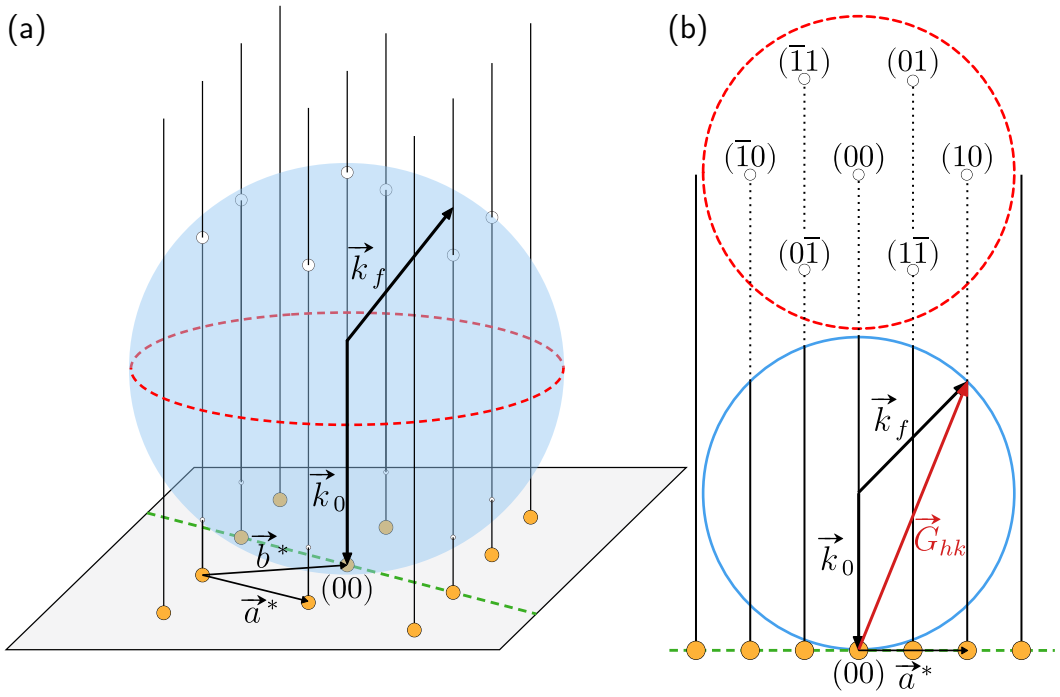

Figure 3.14: (a) The intersections of the lattice rods with the Ewald sphere can be observed as spots in the LEED pattern. (b) The two-dimensional cut along the green line in (a). In the top half, the two-dimensional projection of the Ewald sphere with the position of the rod intersections is shown. Spots in the reflection pattern are labeled using their Miller indices (hk). Adapted from [194].

Analogous to the analysis of XPD patterns described in Section 3.3, the intensity modulation of LEED spots can be used to determine the local atomic structure of the sample. This analysis, which involves recording the energy-dependent intensity of LEED spots by measuring $I(E)$ curves for each spot, is known as IV-LEED [76, 192, 193, 195].

A typical LEED setup is shown in Figure 3.15. It consists of an electron gun, in which electrons are emitted from a hot cathode, focused by a Wehnelt cylinder, and accelerated by an anode. An additional lens system provides further focusing of the electron beam. The cathode is biased at a negative voltage $-V$ relative to the sample, which is typically held at ground potential. This potential difference accelerates the electrons toward the sample, and their resulting kinetic energy upon reaching it is $E_{\text{kin}} = \text{e} \cdot V$.

A four-grid energy filter is installed in front of the fluorescence screen, with the first grid grounded so that the scattered electrons experience a field-free region as they travel from the sample towards the fluorescence screen. A suppressor voltage of $-(V - \Delta V)$ is applied to the second and third grids, which act as a high-pass energy filter, rejecting electrons that have scattered inelastically and lost kinetic energy. The fourth grid is grounded, screening the suppressor grids from the high positive voltage ($\approx 6\,\text{kV}$) applied to the fluorescent screen. The concentric, spherical geometry of the grids and screen reduces distortions in the recorded LEED pattern, providing an accurate projection of reciprocal space. For normal incidence, the (00) spot, the specularly reflected beam,

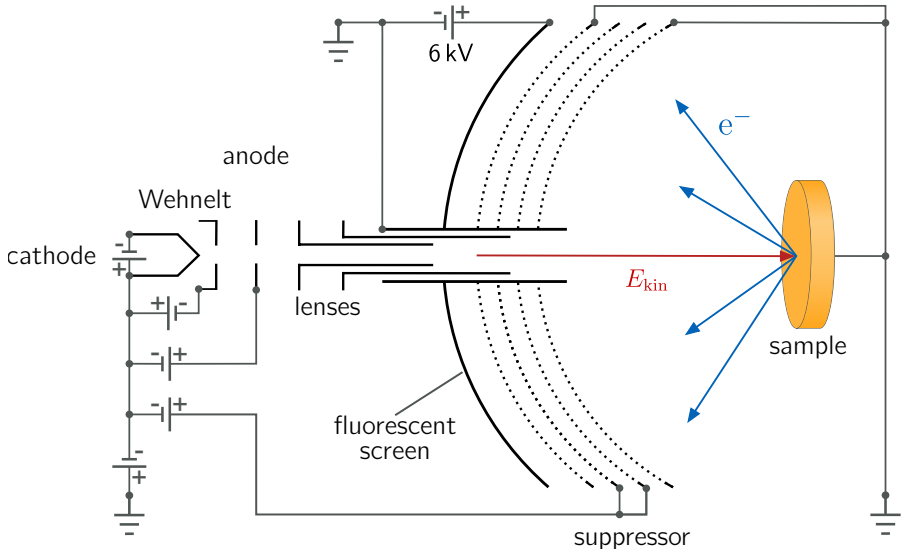

Figure 3.15: Schematic of the LEED setup, consisting of the electron gun with the focusing lenses, the four-grid energy filter system, and the fluorescent screen where the LEED pattern can be observed. Adapted from [196]

which is the most intense, is blocked by the electron gun, improving the visibility of fainter higher-order diffraction spots. LEED patterns are typically recorded with a charge-coupled device (CCD) camera that captures images of the fluorescent screen through a viewport.

3.5 Scanning Tunneling Microscopy (STM)

STM is a powerful tool for investigating the electronic and structural properties of solid-state surfaces. An STM produces topographic images of conductive sample surfaces with up to atomic resolution. The technique was developed by Gerd Binnig and Heinrich Rohrer in 1981, for which they were awarded the Nobel Prize in Physics in 1986 [197–199]. For STM measurements, a sharp metal tip is brought into close proximity to the sample surface, within 1 nm. The schematic of an STM setup is shown in Figure 3.16. This small gap represents a potential barrier for electrons. However, due to quantum-mechanical tunneling, electrons can pass through this finite barrier. Thus, despite the gap, a tunneling current I_T can be established. This tunneling current is exponentially dependent on both the potential barrier height (controlled by the bias voltage) and the barrier width (the tip-sample distance) [200, 201]. This exponential dependency makes the tunneling current highly sensitive to both parameters. The tip is mounted on a piezoelectric tube scanner that uses the inverse piezoelectric effect to control its position [202]. STM tips used in this thesis are made from tungsten wire via electrochemical etching in sodium hydroxide (NaOH), with the detailed procedure being described in [203]. To record an image, the controller moves the piezoelectric tube to raster the tip line by line across a predefined area of the sample. The measured data are then processed to generate topographic

images of the rastered area. The STM can be operated in two modes: the *constant height* and *constant current* modes. In this work, all presented data were recorded in constant-current mode. In this mode, a feedback loop adjusts the tip's z-position to maintain a constant tunneling current. The voltage applied to the piezo to change the tip height z is recorded at each raster point and then converted into an apparent height. As will be shown later, this apparent height does not necessarily correspond to the surface's geometric height.

A gain parameter regulates the feedback loop. The gain parameter must be set high enough for the controller to quickly adjust the tip's position during scanning to avoid crashing into the sample. However, if the gain is set too high, the feedback loop becomes overly sensitive, leading to high-frequency oscillations of the tip.

The STM is extremely sensitive to external vibrations and therefore requires advanced decoupling systems to prevent vibrational noise from affecting the measurements. Typically, the entire UHV chamber is decoupled from the building's foundation by a spring and damper system. Internally, an eddy-current damping system is often used to decouple the measurement stage from the UHV chamber itself.

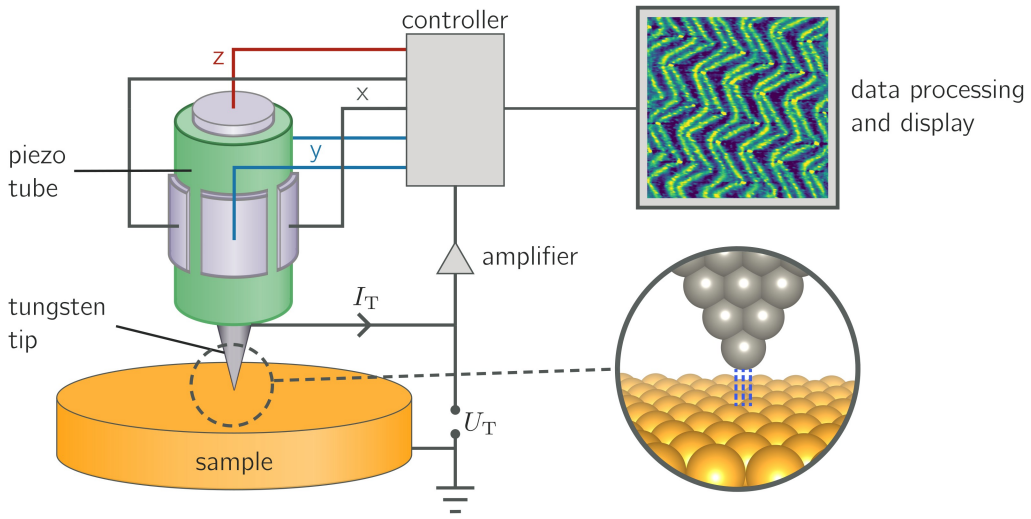

Figure 3.16: Schematic of an STM experimental setup. An atomically sharp tip, positioned by a piezoelectric tube scanner, rasters across the sample surface. The controller maintains a constant tunneling current between the tip and sample, generating a real-space topographic image of the surface.

3.5.1 Physical Phenomena in STM

The basic principle of STM operation is the quantum mechanical tunneling effect, first theoretically formalized by R.H. Fowler and L. Nordheim in 1928 [204]. They analyzed electron field emission and demonstrated that electrons have a finite probability of tunneling through a one-dimensional surface barrier, from which they derived the corresponding emission current. In the following, the basic model of the tunneling

effect through a one-dimensional barrier, as depicted in Figure 3.17, is explained, closely following the explanation given in [205]. The tunneling junction consists of three regions:

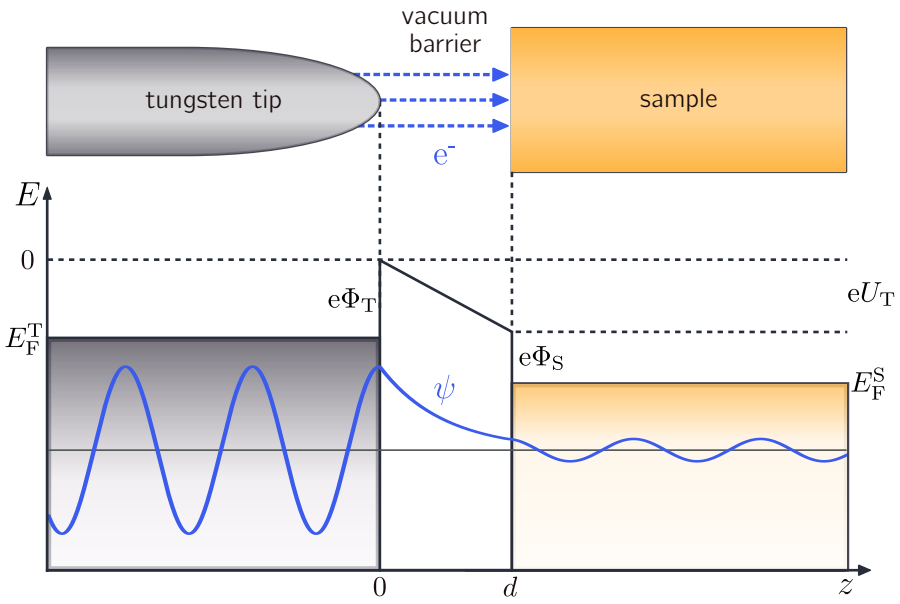

Figure 3.17: Sketch of the tunnel barrier between tip and sample. The Fermi level of the sample is shifted by the bias voltage U_T. The electron's wavefunction, depicted in blue, decays exponentially in the vacuum barrier between the tip and the sample; nevertheless, the tunneling process is considered elastic, so the electron's wavefunction frequency is conserved during transmission.

the tungsten tip, the sample, and the vacuum barrier separating them. Classically, electrons cannot cross this potential barrier from the tip to the sample or vice versa. In quantum mechanics, however, electrons have a finite probability of tunneling through the barrier. As illustrated in blue in Figure 3.17, the electron wavefunction ψ extends across all three regions, penetrating the tunneling barrier. While the tip and sample share the same vacuum energy level, they typically have different work functions (Φ_T, Φ_S) and Fermi levels (E_F^T, E_F^S). Additionally, applying a bias voltage U_T to the sample shifts its energy levels relative to the tip. By applying a positive sample bias, lowering E_F^S, tunneling from the tip's filled states to the sample's empty states is enabled. Conversely, applying a negative sample bias of $-U_\mathrm{T}$ raises E_F^S, leading to tunneling from the sample to the tip. To mathematically describe the tunneling process, it is reduced to a one-dimensional problem. Assuming identical work functions of sample and tip ($\Phi_\mathrm{T} = \Phi_\mathrm{S} = V_0$) and no applied bias voltage ($U_\mathrm{T} = 0\,\mathrm{V}$). The vacuum tunneling barrier is thereby of height V_0. Schrödinger's equation describes the problem:

$$\left[-\frac{\hbar^2}{2m}\frac{\partial^2}{\partial z^2} + V(z)\right]\psi(z) = E\psi(z)\,, \tag{3.27}$$

Because the potential is different in these three regions (tip, sample, and vacuum barrier), the Schrödinger equation must be solved separately for each region using a suitable ansatz:

$$\psi(z) = \begin{cases} Ae^{ikz} + Re^{-ikz}, & z < 0 \text{ (tip)} \\ A_{\mathrm{v}}e^{ikz} + R_{\mathrm{v}}e^{-ikz}, & 0 \leq z \leq d \text{ (vacuum barrier)} \\ Te^{ikz}, & z > d \text{ (sample)} \end{cases} \tag{3.28}$$

The constants are determined using the continuity conditions for the wavefunction and its first derivative at the boundaries of the three regions, from which the tunneling probability $T(E)$ can be derived. For a wide and high potential barrier, the tunneling probability has an exponential dependence on the barrier width d:

$$T(E) \propto \exp(-2\kappa d)\,, \tag{3.29}$$

with $\kappa \propto \sqrt{V_0 - E}$ being the inverse decay length, which depends on the barrier height V_0. The tunneling current I_{T} is proportional to this probability and therefore also decreases exponentially with increasing gap width d and barrier height V_0.

While this simple model illustrates the basic principle of quantum tunneling, it neglects that the sample and tip are typically made of different materials and that a bias voltage U_{T} is applied. Additionally, the tip and sample are not limited to a single electronic state; their electronic structures are described by their respective DOS. To accurately describe the tunneling process, advanced models of the STM tunneling contact are required. The first more accurate description was formulated by Bardeen, who discussed the tunneling between two metals with an oxide layer in between as a many-particle problem in 1961 [206]. Tersoff and Hamann later, after the invention of the STM, applied Bardeen's groundwork to the tunneling process in STM [207]. They showed that for a tip with an *s*-wave-like state at its apex, meaning the tip's electronic wavefunction is spherically symmetric and localized at its outermost atom, the tunneling current is proportional to the sample's local density of states (DOS) at the Fermi level, evaluated at the position of the tip $\boldsymbol{r}_0$:

$$I_{\mathrm{T}} \propto \sum_{\nu} |\psi_\nu(\boldsymbol{r}_0)|^2 \delta(E_F - E_\nu) \equiv \rho_S(E_F, \boldsymbol{r}_0)\,, \tag{3.30}$$

where ψ_ν are the wavefunctions of the sample [207]. The apparent height recorded in constant-current mode, therefore, does not exclusively represent the geometric topography. Instead, the feedback loop maintains a contour of constant tunneling current, which is proportional to the sample's DOS integrated over the energy range defined by the bias voltage. Thus, the *apparent height* measured in STM is a convolution of the geometric topography of the sample and its local electronic structure.

It is worth noting that the Tersoff-Hamann approximation described above is valid only for very small bias voltages and low temperatures and is not applicable, for example, to semiconductors [208]. In the literature, many other descriptions of the STM tunneling process can be found. Notably, Chen generalized the Tersoff-Hamann approach to include tip orbitals with higher angular momentum, showing that localized p_z and d_{z^2} tip orbitals are crucial for achieving true atomic resolution [209]. These orbitals are prominent in

d-band metals such as platinum, iridium, or tungsten, which explains their popularity as STM tip materials. Further theoretical descriptions are found in the literature, for example, those that use Green's functions [205], model the tip as a cluster of atoms [210], or apply molecular orbital theory to the tunneling contact [211].

3.5.2 STM Image Analysis

Preparing an atomically flat surface and aligning it perfectly with the STM's scanning plane is nearly impossible. Consequently, raw STM data typically exhibits a global tilt. Furthermore, the data are often affected by experimental artifacts, such as electronic noise, external vibrations, and distortions due to piezo creep, a slow, gradual drift in the piezoelectric scanner's position after a voltage change. A thermal drift between consecutive images is also common.

To analyze the STM data, post-processing methods such as plane subtraction, data leveling, and drift, as well as line-by-line corrections, are necessary. The Gwyddion software was used for all post-processing and for extracting quantitative results, such as lattice constants and periodicities [212].

Z-correction

To correct the sample's tilt, a plane leveling correction is applied. In the top row of Figure 3.18, the raw STM data is displayed; the height profile of the step edge clearly shows a sloping linear background. To remove the tilt, the data are leveled by subtracting a plane:

$$\tilde{z} = z - (ax + by + c)\,. \tag{3.31}$$

This method is only effective for a linear tilt of the entire image plane; it does not correct non-linear distortions between the height coordinate z and the lateral position (x, y). In addition to the global tilt of the sample, the measurement principle of STM contributes to further instrumental distortions. An STM image is recorded line by line. The tip scans horizontally in what is called the *fast-scan* axis, as marked by the red arrow in Figure 3.18. Due to the rapid scan speed along this axis, measured distances along this axis are largely unaffected by drift. Since the entire frame often requires several minutes to complete, the vertical axis used to stack the lines is consequently referred to as the *slow-scan* axis, as marked in the figure. Each line is typically scanned twice: once from left to right and again on the return path from right to left. The data from these two scans are saved as separate images, referred to as the *forward* and *backward* images, respectively. Sometimes, due to an inhomogeneous tip shape, one scan direction offers significantly better resolution and fewer scan artifacts. The entire image frame is usually scanned from bottom to top, called the *trace-up scan*, and then subsequently from top to bottom, called the *trace-down scan*. One therefore obtains four images of each scanned area: the *trace-up* and *trace-down scans*, each scanned *forward* and *backward*.

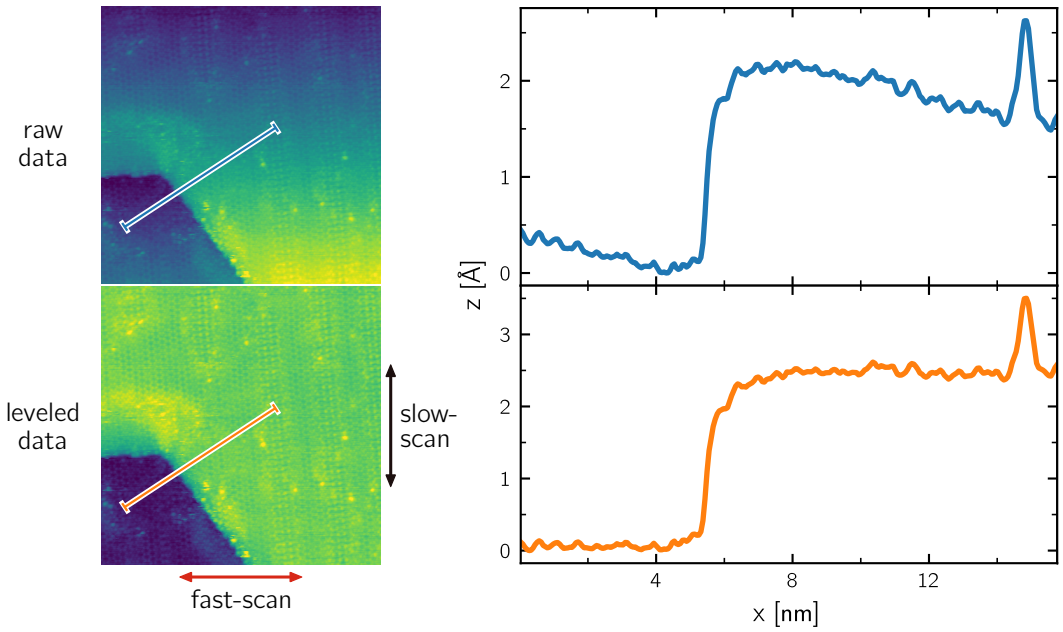

Figure 3.18: Atomically resolved STM image of a single atomic step. In the top row is the image before correction, and in the bottom row is the image after data correction via plane leveling. The extracted height profiles shown on the right indicate the improvement, going from a tilted step to a step with flat terraces after correction.

XY-correction

The obtained square STM image usually does not correspond to a square area of the sample due to instrumental drift. This becomes especially evident when comparing consecutive measurements. After scanning an up- and down-scan image of the same area, the images are not identical due to thermal and piezoelectric drift [213]. Piezo drift is most pronounced immediately after moving the tip over large distances, as illustrated by the two consecutive images in Figure 3.19. As is evident, the up-scan image in the top row differs from the subsequent down-scan image, not only in the scanned area but also in the distortion of the atomic features. Directly after changing the measurement position, one often observes non-linear piezo drift for several minutes, after which the drift becomes almost perfectly linear, as shown in Figure 3.19. If the STM tip is kept at the same position for an extended period, the drift rate often decreases significantly, sometimes becoming negligible. Drift correction can be applied by measuring a known feature, such as the lattice periodicity (known from LEED measurements), and calculating its measured distortion compared to the expectation [214]. Alternatively, if the scanner is well-calibrated, the drift vector can be calculated by tracking a distinct feature across consecutive images, though this method does not account for piezo miscalibration. In this thesis, corresponding LEED measurements were consistently available, allowing for the correction of both the drift and any small piezo miscalibrations.

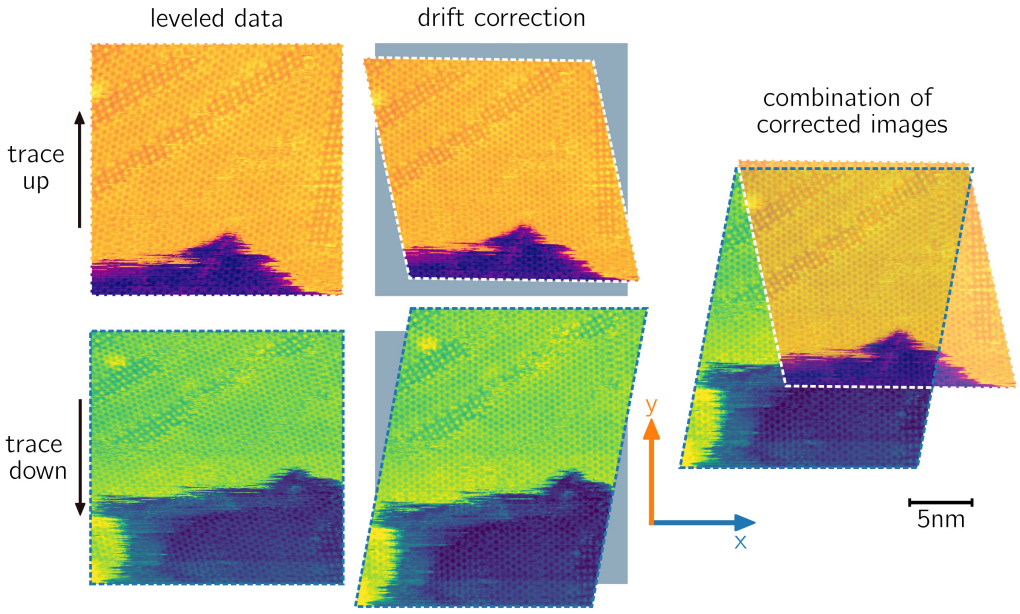

Figure 3.19: Two consecutive images of the same region are shown. Due to linear piezo drift, the inspected area shifts between and during the measurement of both images. After applying drift correction, the structural details in both images match when overlaid.

Line correction

The state of the tip apex might change during scanning, causing an abrupt vertical shift Δz between adjacent scan lines. If this change does not significantly influence the electronic states involved in the tunneling process, it simply introduces an offset in the absolute height value z of subsequent lines. To address this, STM images are often corrected using line-by-line correction methods. Various methods are used to find representative heights and slopes for each scanned line, which are then used to correct the line. Methods such as calculating the median height $\tilde{z}$ or the mode value of the height, as well as using polynomial fitting, can be applied [212]. However, great care must be taken when applying correction methods that include a slope or higher-order polynomials to avoid introducing artifacts or removing relevant details [215, 216].

Determining the atomic lattice

To determine lattice constants and periodicities from atomically resolved STM data, a combination of reciprocal-space methods is used. A 2D Fast Fourier Transform (FFT) is applied to the real-space STM image to generate a reciprocal-space image, revealing the data's primary periodicities. This allows for direct comparison with periodicities observed in LEED measurements. In addition, the autocorrelation function (ACF) and the power spectral density (PSD) function, which is the FFT of the ACF, are also used to determine lattice parameters [216].

4 Experimental Setup

This chapter briefly presents the different experimental setups used in this thesis. An overview of the instruments is provided in Table 4.1, and a short description of each experimental setup is provided at the end of this chapter. The instrumentation for the primary techniques of this thesis was already addressed in the previous chapter. This chapter presents the remaining methods, primarily focusing on sample preparation and manipulation. Additionally, a brief description of the Center for Synchrotron Radiation Dortmund (DELTA) and beamline 11 (BL11), which were used for the XPS and XPD measurements, is given.

Table 4.1: Overview of the instrumentation used in this thesis.

Chamber	Techniques	Institute/Location	P_{base} [mbar]
BL11	LEED, XPS/XPD	Beamline 11, DELTA	$< 1 \times 10^{-10}$
RT-STM	LEED, STM	AG Westphal/TU Dortmund	$< 5 \times 10^{-11}$
LT-STM	LEED, STM	AG Hövel/TU Dortmund	$< 5 \times 10^{-11}$

4.1 Ultra-High Vacuum (UHV)

A vacuum is defined as a space entirely devoid of matter. Since such a state cannot be achieved experimentally, vacuum is instead categorized into different pressure ranges. For surface science experiments, the use of UHV systems, operating at pressures in the range of 1×10^{-9} mbar to 1×10^{-12} mbar, is necessary for two main reasons [217]: Firstly, the low particle density in UHV enables the use of techniques that rely on particle transport (e.g., electrons) from the sample to the detector, thereby minimizing scattering from gas-phase particles. Secondly, surface-sensitive experiments require the sample surface to remain stable and clean for a significant duration. The low particle density in UHV minimizes interactions with residual gas molecules, thereby maintaining a contaminant-free surface for an extended period of time. Consequently, all sample preparation and data acquisition in this work are performed in UHV chambers.

4.1.1 Mean Free Path of Particles

The ideal gas law approximates the behavior of residual gas particles in UHV systems as:

$$n = \frac{N}{V} = \frac{P}{k_{\text{B}}T}. \tag{4.1}$$

Here, the particle density n, given by the number of gas particles N per unit volume V, is proportional to the pressure P and inversely proportional to the average particle's thermal energy $k_{\mathrm{B}}T$, with k_{B} being the Boltzmann constant [218].

Assuming a hard-sphere collision model, the average distance a particle travels between collisions is given by:

$$\lambda_{\mathrm{gas}} = \frac{k_{\mathrm{B}}T}{\sqrt{2}\sigma P}, \tag{4.2}$$

where λ_{gas} is the mean free path and σ is the collisional cross-section of the particles. This equation enables the calculation of the mean free path at different pressures [219]. At room temperature ($\approx 300\,\mathrm{K}$) and assuming an average particle radius of 1 Å, the mean free path at standard atmospheric pressure ($P \approx 1 \times 10^5\,\mathrm{Pa} = 1\,\mathrm{bar}$) is approximately 1 µm. For electron-based techniques such as LEED, XPS, and XPD, a long mean free path is required to prevent electron scattering by residual gas molecules. A path length exceeding tens of meters, which is achieved at pressures of $\approx 1 \times 10^{-5}$ mbar or lower, is typically sufficient.

It is important to distinguish this *gas-phase mean free path*, which describes the scattering of electrons or ions with residual gas particles in the UHV chamber, from the *IMFP* of electrons within a solid, which was discussed in Section 3.1.

4.1.2 Monolayer Formation Time

For gas particles of density n, where the average particle velocity $\overline{v}$ is determined by the Maxwell-Boltzmann distribution, the flux Γ of particles impinging on a surface is given by:

$$\Gamma = \frac{1}{4} n \overline{v}\,. \tag{4.3}$$

Using the ideal gas law (4.1) and substituting $\overline{v}$ derived from the Maxwell-Boltzmann distribution [220] yields:

$$\Gamma = \frac{1}{4} \cdot \frac{P}{k_{\mathrm{B}}T} \cdot \sqrt{\frac{8k_{\mathrm{B}}T}{\pi m}} = \frac{P}{\sqrt{2\pi m k_{\mathrm{B}}T}}. \tag{4.4}$$

In reality, only a fraction of the impinging particles adsorb onto the surface; most desorb relatively quickly back into the gas phase. This process is described by the sticking coefficient, ξ, which represents the probability that an impinging particle will adsorb. A worst-case scenario, where every impinging particle sticks ($\xi = 1$), provides a lower limit for the monolayer formation time:

$$\tau = \frac{n_{\mathrm{mono}}}{\Gamma}\,, \tag{4.5}$$

where $n_{\mathrm{mono}} \approx 1 \times 10^{15}\,\frac{\mathrm{particles}}{\mathrm{cm}^2}$ is the typical atomic density of a monolayer [221]. Using Equation 4.5, one can calculate that at room temperature and atmospheric pressure, a monolayer of a typical gas like nitrogen N_2 (molecular mass of $m \approx 28\,\mathrm{u}$) forms within

nanoseconds. In contrast, under UHV conditions, this process takes several hours or even days.

In summary, these two requirements mandate the use of UHV for all surface-sensitive experiments: a long mean free path in the gas phase for electron-based techniques (such as LEED, XPS, and XPD) and, even more importantly, a long monolayer formation time to ensure a stable, clean surface over extended time periods.

4.2 Sample Preparation

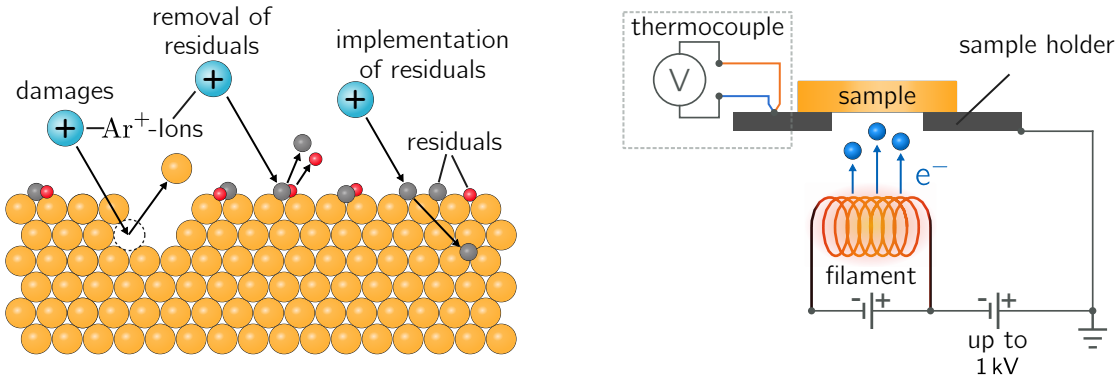

(a) Sample bombardment by Ar^+ ions.

(b) Electron beam sample heating.

Figure 4.1: (a) Visualization of the processes occurring when the sample is bombarded by Ar^+ ions. (b) Schematic of a typical setup for sample annealing by electron beam heating. In the low temperature scanning tunneling miscroscope (LT-STM) chamber, a thermocouple is mounted close to the sample to monitor its temperature.

To prepare the sample system, each UHV system used is equipped with a sputter gun, a sample-heating setup, and at least one evaporator for depositing monolayer Sn films on the Au(111) sample surface. While the specific preparation recipes will be provided in Chapter 5, the experimental techniques applied are explained below.

Typically, the substrate crystal is cleaned and prepared through repeated cycles of sputtering and annealing before monolayer films are deposited on top. To sputter the sample, a sputter gun is used. A noble gas, typically argon (Ar), is introduced into the sputter gun via a needle valve to a back pressure of $\approx 1 \times 10^{-6}$ mbar. Inside the gun, the gas is ionized by a filament; the resulting ions are then accelerated and focused onto the sample. As depicted in Figure 4.1(a), when the Ar^+ ions impinge on the sample, they can remove adsorbates from the surface via momentum transfer. However, this process can also implant residual gas atoms into the sample and heavily damage the surface crystal structure.

To create a clean, well-reconstructed surface, the sample is subsequently annealed to heal damage caused by sputtering. The sample is typically heated from the back. In this thesis, the sample was heated using either a pyrolytic boron nitride (PBN) heater plate (in the LT-STM chamber) or a heating filament, as used in the BL11 endstation

sample holder and the room temperature scanning tunneling miscroscope (RT-STM) chamber's manipulator. When using a PBN heater plate, the sample is heated primarily by thermal radiation. If a heating filament is used instead, as depicted in Figure 4.1(b), the sample is heated by thermal radiation from the hot filament and, additionally, by electron bombardment (often termed electron beam heating (EB)). To heat via electron bombardment, a high voltage of up to 1 kV is applied between the filament and the sample, accelerating electrons emitted from the hot filament onto the back of the sample to achieve higher temperatures than with thermal radiation alone. Typically, several cycles of sputtering and annealing are required to remove most contaminants from the sample surface and achieve a clean, well-reconstructed crystal lattice.

4.2.1 Preparation of Monolayer Films

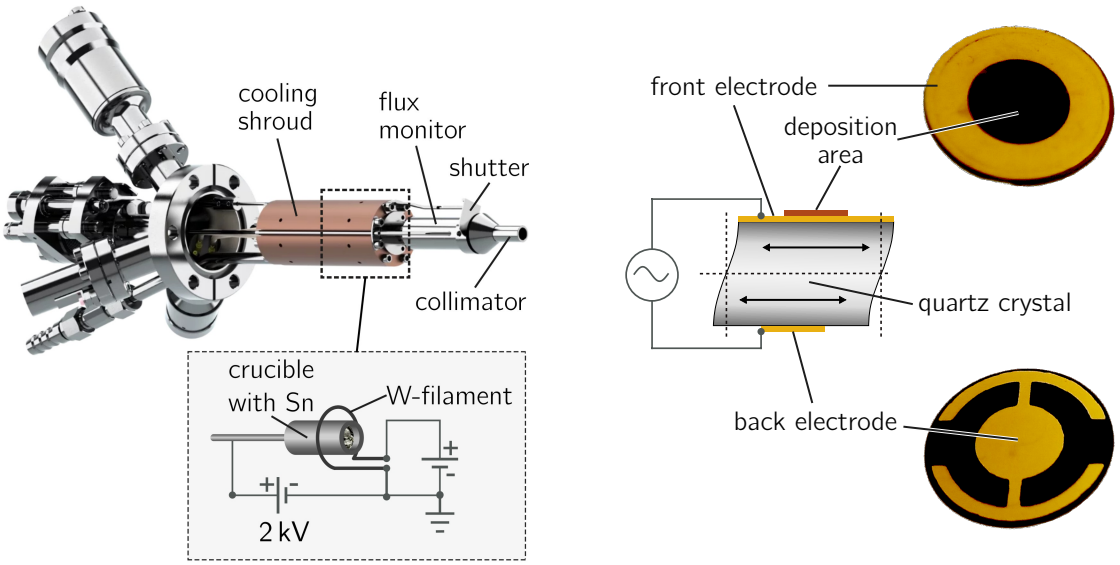

(a) EB evaporator. **(b)** quartz crystal microbalance (QCM).

Figure 4.2: (a) Electron beam evaporator used to deposit tin (Sn). The picture is adapted from [222]. (b) Schematic of the working principle of a quartz crystal microbalance.

Submonolayer Sn films were grown epitaxially on the Au(111) substrate via physical vapor deposition (PVD), using EB evaporators similar to the one shown in Figure 4.2(a). Inside the evaporator's cooling shroud, a tungsten crucible filled with Sn pellets is mounted centrally, surrounded by a circular tungsten filament. By applying a current to the filament and a high voltage of $U_{\mathrm{HV}} \approx 2\,\mathrm{kV}$ between the crucible and the filament, the crucible is heated by electron bombardment with an emission current I_{em}. This heating causes the Sn pellets to melt and subsequently evaporate at temperatures around 950 K [223]. A shutter and collimator are used to direct the resulting beam of Sn atoms onto the sample, with the shutter precisely controlling the deposition time. The heating power, given by $P_{\mathrm{em}} = U_{\mathrm{HV}} \cdot I_{\mathrm{em}}$, determines the flux of atoms and thus the deposition rate. Since Sn melts at a relatively low temperature of 500 K, well below the temperatures

required for significant evaporation, the crucible must be oriented upwards to contain the molten metal [223].

To calibrate the deposition rate as a function of heating power, a QCM is used. The QCM operates based on the piezoelectric effect. A quartz crystal, as displayed in Figure 4.2(b), is excited to oscillate at its resonant frequency $f_0 \approx 6\,\mathrm{MHz}$ by an alternating voltage. When material is deposited onto the crystal, the total oscillating mass increases, causing the resonant frequency to decrease by Δf. This frequency shift is directly proportional to the added mass Δm, allowing for the calculation of the deposited film thickness Δd via the Sauerbrey equation [224]:

$$\Delta f = -C_\mathrm{q} \cdot \Delta m = -C_\mathrm{q} \cdot \rho_\mathrm{Sn} \cdot A \cdot \Delta d\,. \tag{4.6}$$

Here, C_q is the sensitivity constant of the quartz crystal, which depends on its material properties. To determine the deposited film thickness Δd from the frequency shift, the density of the deposited material (ρ_Sn) and the active area A of the microbalance must be known.

The deposition rates and corresponding heating powers were first calibrated using the QCM in a separate test chamber and later verified by XPS film thickness measurements at the BL11 endstation. Furthermore, the high sensitivity of the Sn submonolayer's structural arrangement to coverage, particularly below $1/3\,\mathrm{ML}$, provided a precise method for *in-situ* film thickness calibration [45]. The distinct diffraction patterns observed via LEED in the low-coverage regime were used to fine-tune the preparation parameters in each experimental chamber, accounting for specific chamber geometries.

4.3 Vacuum Chambers

As described, all chambers offer similar methods for sample preparation; however, the detailed experimental setups differ, and most importantly, each chamber provides unique sample characterization methods. The following sections provide a brief description of each experimental setup.

4.3.1 RT-STM Chamber

The RT-STM chamber is the smallest chamber used in this thesis. Sample preparation and characterization are performed within the same vacuum chamber. The chamber is equipped with a rotatable manipulator, on which the sample can be heated using a filament. A voltage of up to $1\,\mathrm{kV}$ can be applied for EB-heating. For sputtering, an ion sputter gun is used. The temperatures achieved as a function of heating power were calibrated using a thermocouple mounted close to the sample [225].

In addition, the chamber is equipped with an electron beam evaporator. Unlike the evaporator presented in Figure 4.2, this one is not equipped with a flux monitor due to geometric constraints of the experimental setup. To verify successful sample preparation,

the chamber is equipped with a SPECS ErLEED 150 LEED system. STM data acquisition is performed using an Omicron RT-STM. In this setup, the sample is mounted on a piezo tube, while the tip remains grounded. Consequently, scanning is achieved by moving the sample rather than the tip, unlike most standard STM designs. The STM data at low Sn coverages, up to the formation of the Au_2Sn surface alloy (presented in Chapter 6), were acquired using this RT-STM chamber.

4.3.2 LT-STM Chamber

The Omicron LT-STM surface science facility consists of an analysis chamber and a preparation chamber, separated by a gate valve. The preparation chamber is equipped with a 4-axis manipulator (x, y, z, and rotation) and multiple stages for preparing samples and cooling them to 10 K using a flow cryostat. In this work, however, only liquid nitrogen was used to cool the sample to approximately 80 K. The preparation stage features a PBN heater plate with a thermocouple mounted next to the sample, allowing for precise temperature monitoring. Similar to the other experimental setups, the preparation chamber includes an EB evaporator and a sputter gun. This setup enables LEED measurements of the cooled sample, suppressing thermal background and sharpening the diffraction spots. Consequently, most LEED data presented in this thesis were recorded using this setup. Additionally, the preparation chamber is equipped with a high-resolution photoelectron analyzer and a He discharge lamp for photoelectron spectroscopy, though neither was used in this thesis.

The analysis chamber is equipped with an Omicron LT-STM. The STM is housed in a dual-stage cryostat, enabling data acquisition at temperatures as low as 5 K. However, it was observed that the tip easily picked up residual or Sn atoms from the sample surface during measurements at low temperatures, leading to unstable tip conditions. Since returning the tip to a sharp and stable state was challenging at low temperatures, all data presented in this thesis were recorded at room temperature. The significant influence of the tip on the sample's morphology is demonstrated in Figure F.1. All STM data for Sn film thicknesses above 0.35 ML (presented in Chapter 7) were recorded using the LT-STM chamber. Further details of the experimental setup are provided in References [226–228].

4.3.3 DELTA and Beamline 11 Endstation

Synchrotron facilities are the preferred sources for X-ray photoemission experiments. While a synchrotron facility requires significantly more complex instrumentation and infrastructure than a laboratory X-ray tube, its advantages justify the additional effort. In contrast to laboratory X-ray tubes, which emit discrete lines (typically Al $K\alpha$ and Mg $K\alpha$), synchrotron light is tunable, offering monochromatized X-rays with high brilliance and a photon flux that is orders of magnitude higher than that of X-ray tubes [229].

Initially, synchrotrons were developed to improve the performance of cyclotrons, specifically to reach higher particle energies for nuclear and high-energy physics. When a

charged particle traveling at relativistic speed undergoes radial acceleration, it emits bremsstrahlung radiation. Ironically, this synchrotron radiation was initially regarded as an unwanted energy loss, despite early synchrotrons being designed to generate X-rays by focusing high-energy electrons onto a target [230]. While at early synchrotron facilities this *unwanted* radiation was only used parasitically, today around 50 dedicated synchrotron light sources are in operation worldwide, one of which is the DELTA.

Figure 4.3 displays a simplified schematic of the DELTA facility. Electrons are generated via thermal emission in an electron gun, accelerated to 70 MeV in a linear pre-accelerator of DELTA (LINAC), and injected into a booster synchrotron ring (BoDo). The booster increases the electron energy to the final storage-ring energy of 1.5 GeV using a 3-cell 500 MHz cavity. Once the electrons reach this energy, they are injected into the storage ring in bunches.

The electron beam, with a maximum current of 130 mA, is stored with a lifetime of over 24 h. Because DELTA does not operate in top-up mode (where beam current loss is compensated by continuous electron injection), scattering processes and intra-beam scattering inevitably lead to a loss of electrons and an exponential decay of the beam current [231].

In the DELTA storage ring, electrons travel near the speed of light, maintained on a closed orbit by a magnet lattice. This lattice uses dipole magnets to steer the electrons, while quadrupole and sextupole magnets focus the beam to counteract the Coulombic repulsion that constantly defocuses it. Due to synchrotron radiation, the beam electrons continually lose energy. To prevent them from losing their orbit, a 1-cell radiofrequency cavity boosts the electrons on each pass, maintaining their energy and orbital stability [232].

Experimental endstations, known as beamlines, are located around the storage ring. They are positioned either along the straight sections, using synchrotron radiation generated at insertion devices such as the superconducting Wiggler (SCW) and the undulators (undulator 55 (U55) and undulator 250 (U250)), or tangentially at the dipole bending magnets.

In Figure 4.3, BL11, the beamline used in this thesis, is highlighted. BL11 provides soft X-ray radiation in the range of 50 eV to 1500 eV, generated by the U55 undulator. The undulator consists of two rows of alternating permanent magnets with a period length of 55 mm. When electrons pass through the undulator, the periodic alternating magnetic fields force them onto an oscillating trajectory. This motion results in the emission of highly brilliant, linearly polarized synchrotron radiation with a sharp photon energy distribution. The energy of the emitted X-rays is tuned by varying the undulator gap. Using a plane-grating monochromator (PGM), monochromatic X-ray radiation of a desired photon energy is selected by adjusting the relative alignment of a plane grating and a mirror, effectively spectrally band-pass filtering the synchrotron radiation [233, 234]. The X-ray beam is focused to a spot size of $(70 \times 30)\,\mu m^2$ at the sample, with a maximum energy resolution of $\Delta E/E = 1/30000$ achieved at $h\nu = 140\,eV$ [235].

The BL11 chamber, similar to the other experimental setups used in this thesis, is equipped with a LEED system and a sputter gun. A heating filament is integrated into the sample holder. The sample holder's design allows continuous rotation around the sample's surface

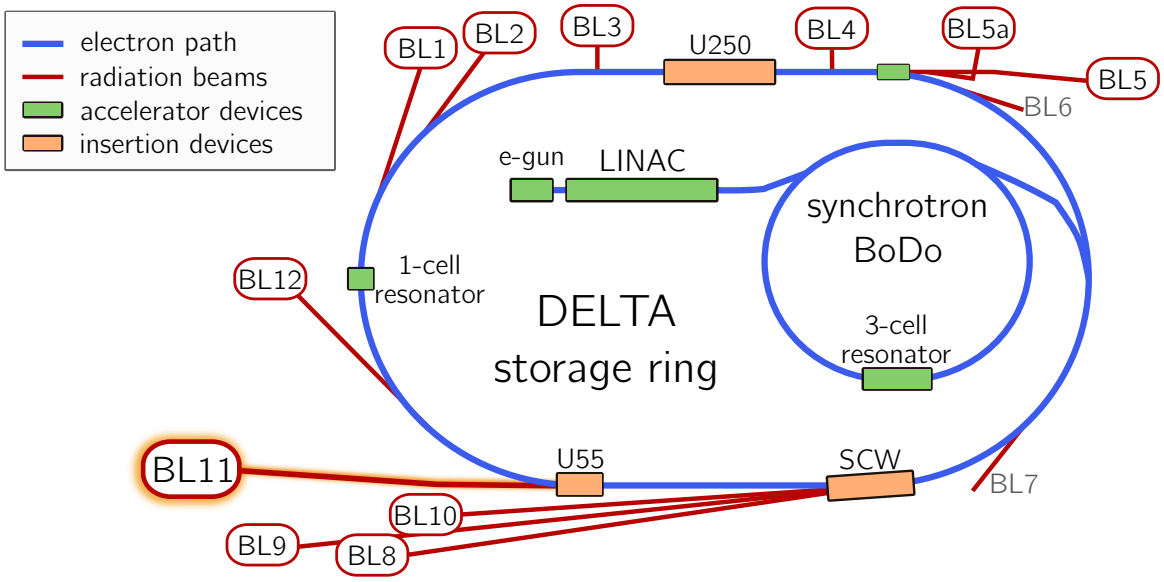

Figure 4.3: Schematic of the 1.5 GeV electron storage ring DELTA, including the main accelerator and insertion devices. Beamline 11, which was used during this thesis, is highlighted.

normal, as required for XPD measurements. All XPS and XPD data were measured with a CLAM IV hemispherical energy analyzer from VG Microtech. The analyzer is mounted at an angle of $\alpha = 55°$ with respect to the incident synchrotron radiation. This configuration is close to the *magic angle* configuration of $\alpha_m \approx 54.7°$, which minimizes intensity distortions arising from the angular distribution of photoelectrons excited by polarized radiation [236, 237]. The setup is also equipped with a SPECS dual-anode X-ray tube, which was used for calibration and test measurements. However, all spectra presented in this thesis were acquired using synchrotron radiation.

5 Sample Preparation

This chapter details the preparation of the sample system. Before submonolayer films of Sn can be prepared on the Au(111) substrate, a clean and well-ordered Au(111) surface must be prepared and characterized. Here, successful sample preparation is confirmed by combining LEED, STM, and XPS with ARXPS measurements of the valence-band region.

Following the successful preparation of the substrate, Sn is deposited onto the surface. To ensure controlled growth, the Sn deposition rates required to deposit well-defined submonolayer coverages onto the Au(111) substrate surface were measured and are presented at the end of this chapter. Parts of this chapter were previously published in:

- J. A. Hochhaus et al., *Structural analysis of Sn on Au(111) at low coverages: Towards the Au_2Sn surface alloy with alternating fcc and hcp domains*, Scientific Reports **15**, 7953 (2025)
- J. A. Hochhaus et al., *Ultraflat honeycomb stanene nanoribbons on au(111)*, Advanced Materials Interfaces **12**, e00861 (2025)

5.1 Clean Au(111)

As discussed in Section 4.1, sample preparation is performed in a UHV chamber to prevent surface contamination by residual gases and adsorbates.

In this thesis, monocrystalline Au(111) crystals with a purity of $> 99.999\%$ and an orientation accuracy of $< 0.1°$ relative to the surface normal were used. All gold crystals were supplied by *MaTecK* and *Surface Preparation Laboratory*.

To prepare a clean Au(111) surface, the standard procedure involves repeated cycles of Ar^+-ion sputtering and thermal annealing. In this work, optimal surface quality was achieved using the parameters detailed in Table 5.1.

For crystals freshly inserted into the UHV chamber, initial preparation cycles with higher sputtering currents ($I_{\mathrm{Ion}} \approx 3\,\mu\mathrm{A}$) and higher annealing temperatures ($\approx 950\,\mathrm{K}$) were applied. These higher temperatures and more intense sputtering removes contaminants from the surface and near-surface layers. In subsequent cycles, the sample was annealed at lower temperatures and sputtered more moderately. This strategy minimizes the further segregation of bulk impurities to the surface. Consequently, by reducing the sputtering intensity and annealing temperature relative to the first two cycles, a near-surface region depleted of impurities is created, yielding a well-ordered sample surface.

The successful preparation of the Au(111) surface was confirmed using LEED. As shown in Figure 5.1, a hexagonal pattern is observed, stemming from the face-centered

Table 5.1: Preparation parameters of the clean Au(111) substrate. Reprinted from [46].

Process Step	Details	Pressure (UHV)
First Two Cycles (Only if freshly inserted into UHV)		
Sputtering	Performed for 1 h using Ar^+-ions ($E = 1000\,\text{eV}$); ion current at sample: $I_{\text{Ion}} \approx 3\,\mu\text{A}$	4×10^{-6} mbar (Ar^+ atmosphere)
Annealing	Temperature ramped linearly over 10 min to $T_{\text{final}} \approx 950\,\text{K}$, held for 120 min, and cooled parabolically over 20 min	$\leq 5 \times 10^{-10}$ mbar
Repeated Cycles (> 5 times)		
Sputtering	Performed for 1 h using Ar^+-ions ($E = 1000\,\text{eV}$); ion current at sample: $I_{\text{Ion}} \approx 1.2\,\mu\text{A}$	2×10^{-6} mbar (Ar^+ atmosphere)
Annealing	Temperature ramped linearly over 10 min to $T_{\text{final}} \approx 920\,\text{K}$, held for 120 min, and cooled parabolically over 20 min	$\leq 3.5 \times 10^{-10}$ mbar

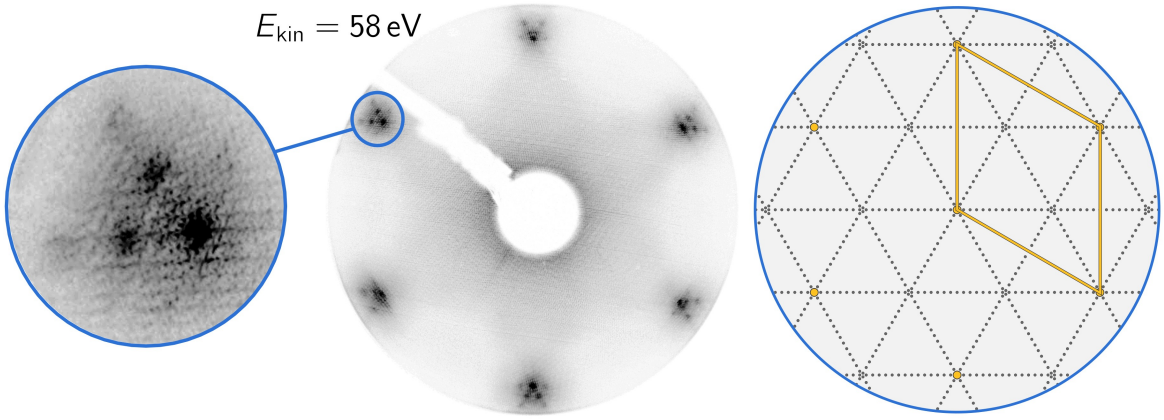

Figure 5.1: LEED pattern of the clean Au(111) showing the first Brillouin zone. The inset displays satellite spots stemming from the long-range order of the herringbone surface reconstruction. The right panel shows the simulated Rec($22 \times \sqrt{3}$)-reconstruction pattern, with the bulk spots and unit cell marked in yellow. Figure adapted from [46].

cubic symmetry of the Au(111) substrate. In addition, the zoomed-in inset reveals a superstructure surrounding the primary substrate diffraction spots. These satellite spots arise from the surface reconstruction of the Au(111). This reconstruction is described by a Rec($22 \times \sqrt{3}$) unit cell; the expected LEED pattern, calculated using LEEDPat [238], is displayed in the right panel of the figure and matches the experimental LEED pattern well.

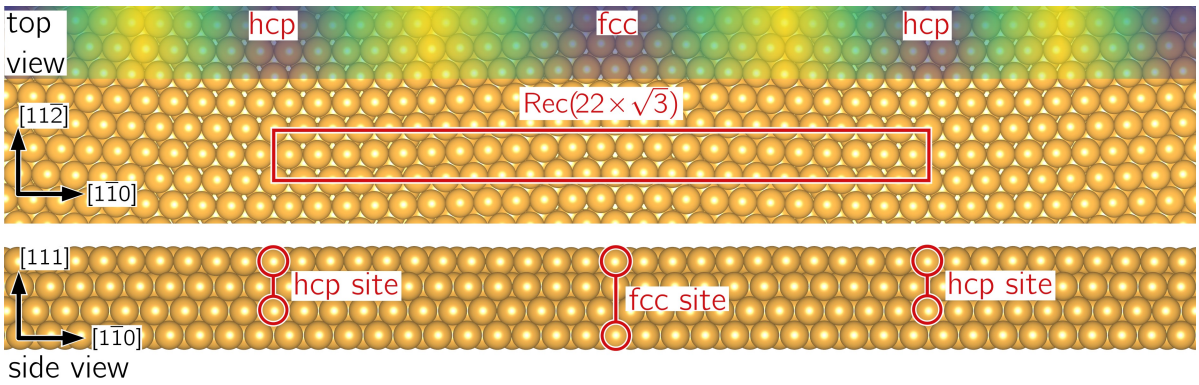

Figure 5.2: Structural model of clean Au(111). The compression of atoms in the surface layer leads to the Rec($22 \times \sqrt{3}$)-reconstruction (unit cell marked in red). The alternating hcp and fcc stacking results in variations in electron density and atomic corrugation (barely visible in the side view, as the maximum height corrugation is approx. 14 pm, 6 % of interlayer distance). The alternating stacking results in bright and dark stripes, the herringbone pattern, in STM (indicated by the top color gradient). Based on the model by Hanke and Björk [239].

The Au(111) surface reconstruction is illustrated in Figure 5.2, following the structural model of Hanke and Björk [239]. Due to its low reactivity towards residual gases [240] and the relative ease of preparing clean surfaces in UHV, Au(111) has been studied extensively using STM and other surface techniques [241–244]. As depicted in the model, the topmost surface layer experiences a uniaxial compression of $\approx 4\%$ along the [1$\bar{1}$0]-direction. This results in the stacking of 23 surface atoms onto 22 substrate lattice sites. This mismatch forces the surface atoms to form alternating stripes of fcc- and hcp-stacked regions. Additionally, the calculations by Hanke and Björk indicate a displacement along the [11$\bar{2}$]-direction, which locally optimizes the stacking so that more gold surface atoms occupy hollow positions [239]. In the transition regions between fcc and hcp stacking, atoms are forced into less favorable bridge or quasi-top sites; consequently, they are vertically lifted and appear brighter in STM measurements. This is visualized by the color gradient shown in the top third in Figure 5.2.

However, the local Rec($22 \times \sqrt{3}$) unit cell alone does not fully capture the complexity of the surface. As extensively studied by STM [241, 245, 246] and shown in Figure 5.3, these local stripe-like domains arrange into a long-range order with a periodicity of several tens of nanometers. This is the well-known herringbone reconstruction, consisting of domains of the stripe-like Rec($22 \times \sqrt{3}$)-reconstruction rotated by 120° relative to each other.

Simulating the Au(111) substrate is challenging because the local surface unit cell already contains 46 atoms. Simulations, therefore, often focused on isolated aspects, such as the local striped pattern [239, 247, 248] or the ”elbows” of the herringbone pattern [249].

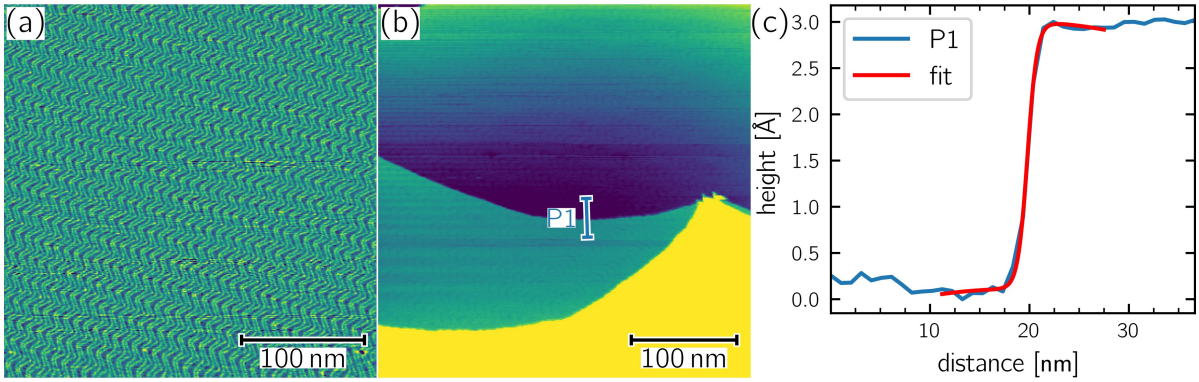

Figure 5.3: STM images of clean Au(111) recorded at $U = -1.3\,\mathrm{V}$ and $I = 23\,\mathrm{pA}$. (a) Large-scale image showing the long-range herringbone reconstruction. (b) A monoatomic step. (c) Step profile used for height calibration. Subfigure (a) reproduced from [46].

Recently, the combination of modern computing power and machine learning enabled Li and Ding to provide a unified theoretical treatment of both the local reconstruction and the long-range ordering [250]. Their approach, which closely reproduces experimental results, identified that the herringbone reconstruction involves atomic displacements extending as deep as the 10th to 30th atomic layer.

Generally, (111)-oriented metal surfaces are considered very stable. It was long believed that Au(111) was the unique exception in exhibiting a surface reconstruction, until it was discovered that Pt(111) also shows a similar high-temperature local striped phase with a long-range order when kept at 1330 K [251, 252]. Li and Ding calculated that the long-range herringbone order generates an energy gain of only $\approx 0.6\,\mathrm{eV}$ per Rec$(22 \times \sqrt{3})$ supercell compared to a simple striped reconstruction without the domain zig-zagging. They observed that the herringbone reconstruction results in atomic displacements tens of layers deep in the bulk. They argue that, for a given displacement of atoms at the surface, a lower shear modulus reduces the energy penalty for displacements in deeper layers. Since gold is a relatively soft metal with a low shear modulus, the deep relaxations required to form the herringbone pattern are energetically possible. In contrast, platinum has a shear modulus more than twice that of gold [253]; thus, the reconstruction is less favorable and appears only at elevated temperatures where the material softens [254].

These theoretical insights and experimental observations likely explain the success of the preparation recipe presented in Table 5.1. Since the herringbone pattern requires well-ordered atomic displacements tens of layers deep, the near-surface region must be exceptionally pure. This is achieved through a two-step preparation process: starting with higher annealing temperatures and high sputtering intensities, then moving to more moderate parameters. Furthermore, the parabolic reduction of the annealing temperature during each preparation step ensures the sample temperature decreases slowly immediately after annealing, giving the sample system sufficient time to reach equilibrium and arrange into the complex, long-range order of the herringbone pattern. The success of this approach is confirmed by the observation of undistorted herringbone reconstruction over terraces up to 500 nm wide, as shown in Figure 5.3.

The successful preparation of a clean Au(111) substrate is further verified by chemical analysis of the surface using XPS.

In Figure 5.4, an XPS survey spectrum of the clean Au(111) surface is shown. The spectrum was recorded at $h\nu = 700\,\text{eV}$ under grazing emission at $\Theta = 60°$ for enhanced surface sensitivity. As marked by the red boxes, the survey reveals carbon or oxygen contamination. All observed signals can be attributed to Au, confirming the preparation of a clean surface.

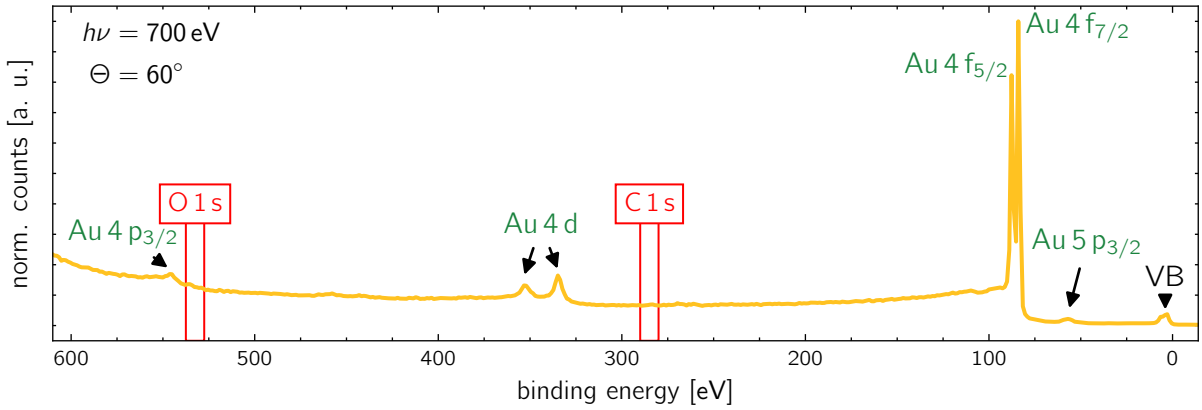

Figure 5.4: XPS survey spectrum of the clean Au(111) recorded at $h\nu = 700\,\text{eV}$ under grazing emission at $\Theta = 60°$. Figure reprinted from [45].

In addition, HighRes angle-resolved Au $4f$ spectra were measured and are presented in Figure 5.5. The binding energy axis was calibrated by fitting the Fermi edge (see Section B.1). The high-resolution spectra are best described by a two-component Doniach-Šunjić model. Comparing the spectra obtained under normal ($\Theta = 0°$) and grazing emission ($\Theta = 60°$) reveals distinct bulk and surface components. The surface component (yellow), shifted by $\approx 310\,\text{meV}$ to lower binding energy, is notably enhanced at grazing angles relative to the bulk signal at $E_{\text{bin}} = 84.00\,\text{eV}$ (dark green). The observed small peak asymmetry of $\beta = 0.03$ is linked to the electronic structure of noble metals [148, 255]. Fit parameters are summarized in Table 5.2 and agree well with the literature [138, 256–259].

Table 5.2: Fit parameters of the XPS analysis corresponding to the Au $4f$ core-level signal in Figure 5.5. The statistical fit error for the reported binding energies is typically well below 10 meV. Reprinted from [46].

Structural phase	Θ (°)	Component	E_{bin} (eV)	E_{SOC} (eV)	FWHM (eV)	asymmetry β	rel. area (%)
clean Au Figure 5.5	0	bulk	84.01	3.67	0.53	0.03	64.83
		surface	83.70	3.67	0.53	0.03	35.17
	60	bulk	84.00	3.67	0.53	0.03	53.90
		surface	83.69	3.67	0.53	0.03	46.10

In Figure 5.6, the valence band of the clean Au(111) surface, measured using $h\nu = 52.5\,\text{eV}$, is presented. Subfigure (a) displays a single cut of the valence band measured at normal emission ($\Theta = 0°$), which corresponds to a cut along the energy axis at the Γ-point. Several distinct band features are observed, labeled A-E. In addition, the Shockley surface

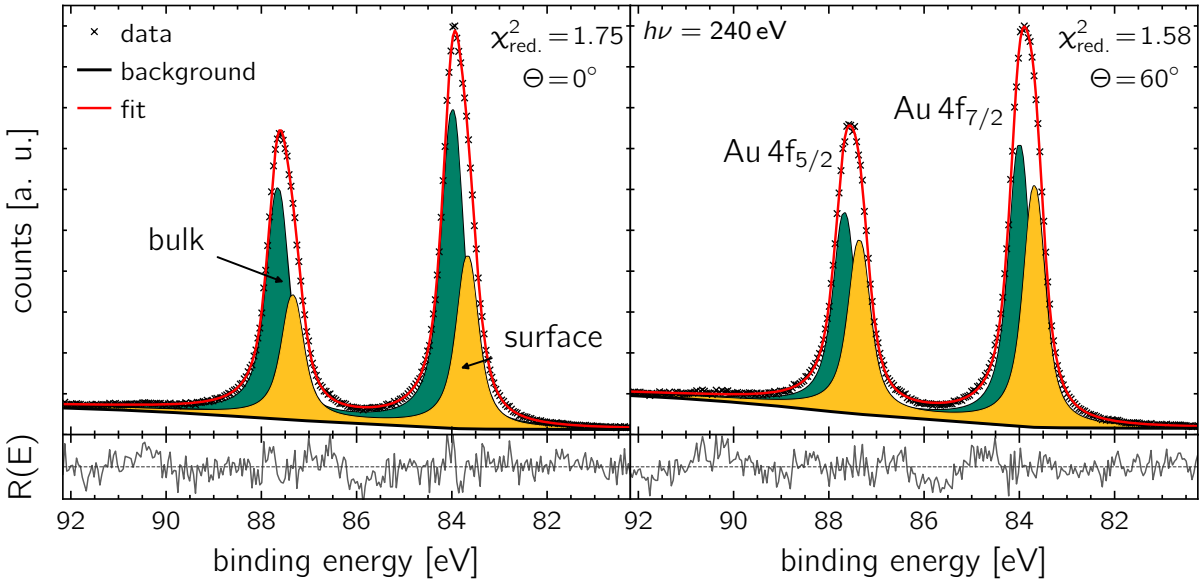

Figure 5.5: Angle-resolved Au $4f$ spectra of the clean Au(111) substrate at $\Theta = 0°$ and 60°, recorded at $h\nu = 240\,\text{eV}$. Figure modified after [46].

state (labeled S) at 480 meV below the Fermi level is observed, which is in excellent agreement with the literature [226].

The occurrence of the surface state, which shows a parabolic dispersion as shown in Figure 5.6(c), confirms a well-prepared, clean Au(111) surface [261]. Figure 5.6(c) displays the valence band dispersion around the Γ point measured along the $\Gamma - K$ and $\Gamma - M$ directions as indicated in Subfigure (b). While the left panel of (c) shows the measured valence-band spectrum, the right panel plots the second derivative of the band structure using a blue-to-red color scale, which simplifies the identification of subtle features. Superimposed on the measured band structure are calculated band spectra of the two topmost surface layers by Requist et al. [260]. Considering the photoelectron kinetic energy of $\approx 40\,\text{eV}$ to $50\,\text{eV}$, the contribution of the topmost two layers should dominate the measured spectrum. A comparison between the calculated band structure and the experimentally measured dispersion reveals good agreement.

The features labeled A to E are identified as follows: Feature B ($\approx 5.95\,\text{eV}$) and D ($\approx 3.4\,\text{eV}$) are assigned to the Au $5d_{3/2}$ and Au $5d_{5/2}$ bands, respectively [262, 263]. Feature C, observed at $\approx 4.6\,\text{eV}$, is attributed to a hybridized p–d band [264, 265], while the shoulder E at $\approx 2.5\,\text{eV}$ and feature A at $\approx 7.65\,\text{eV}$ originate from hybridized s/d-orbitals [266–269]. In the second derivative of the valence band, it is evident that features C and D disperse as two branches or are two separate features even at the Γ point; a more detailed discussion of the valence band structure can be found in the literature cited above.

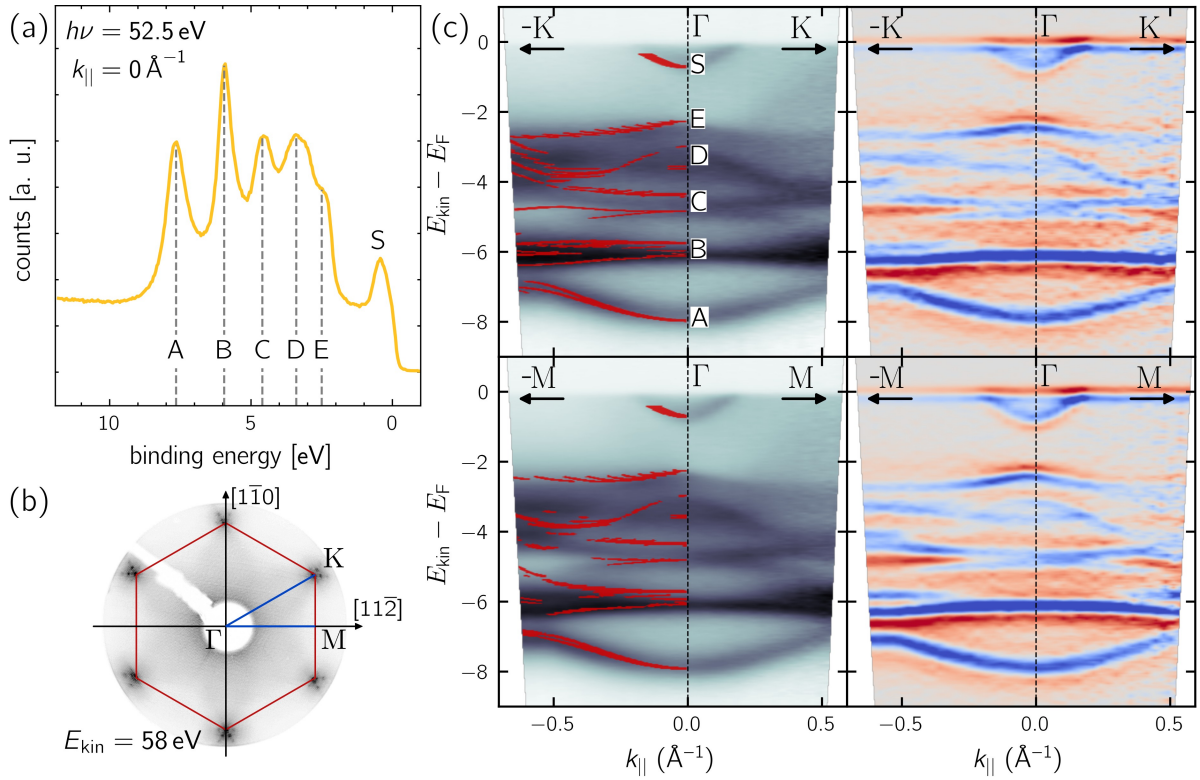

Figure 5.6: Valence band spectra of the clean Au(111). (a) An energy cut of the valence band at the Γ point, recorded under normal emission. (b) The first Brillouin zone of Au(111) (red hexagon) with symmetry points marked. (c) Cuts of the valence band structure, recorded along the $\Gamma - K$ and $\Gamma - M$ axes. The left panel of (c) shows the measured spectra, while the right panel shows the second derivative. Calculated band structures of the two topmost Au(111) layers are overlaid in red in the left panel of (c) [260]. Spectra were recorded at $h\nu = 52.5\,\mathrm{eV}$. Subfigure (a) adapted from [46]. Band structure calculations reprinted with permission from [260].

5.2 Deposition Rates of Sn

Submonolayer Sn films were prepared via PVD, as detailed in Section 4.2.1. To precisely control the submonolayer coverage, deposition rates were determined using a QCM.

The deposited Sn film thickness, Δd, was measured via QCM as a function of the heating power $P_{\mathrm{em}} = U_{\mathrm{HV}} \cdot I_{\mathrm{em}}$ applied to the Sn pellets in the evaporator's crucible. Figure 5.7 illustrates the linear increase in deposited layer thickness for two representative heating powers, $P_{\mathrm{em}} = 8.4\,\mathrm{W}$ and $10.2\,\mathrm{W}$. Instead of the thickness Δd, the corresponding coverage Λ (in ML) is shown in the figure, as this unit is more relevant for the analysis of submonolayer films.

As evident in Figure 5.7(a), the Sn coverage increases linearly with deposition time. Deposition rates can therefore be obtained by applying linear fits. The fits yielded errors below 0.1%; thus, the statistical uncertainty is negligible, as is the uncertainty arising from the $10\,\mu\mathrm{W}$ precision of the heating power supply. The dominant source of uncertainty is likely due to adsorption of residuals, which scales inversely with the vacuum pressure (see Section 4.1) and directly affects the deposition rate. At pressures exceeding $10^{-9}\,\mathrm{mbar}$, a monolayer of N_2 would be adsorbed in less than an hour, according to Equation (4.5). Consequently, to ensure reproducibility and to prepare clean Sn submonolayers, it was necessary to wait for a stable background pressure below $5 \times 10^{-10}\,\mathrm{mbar}$ before measuring deposition rates and before opening the evaporator's shutter later during sample preparation.

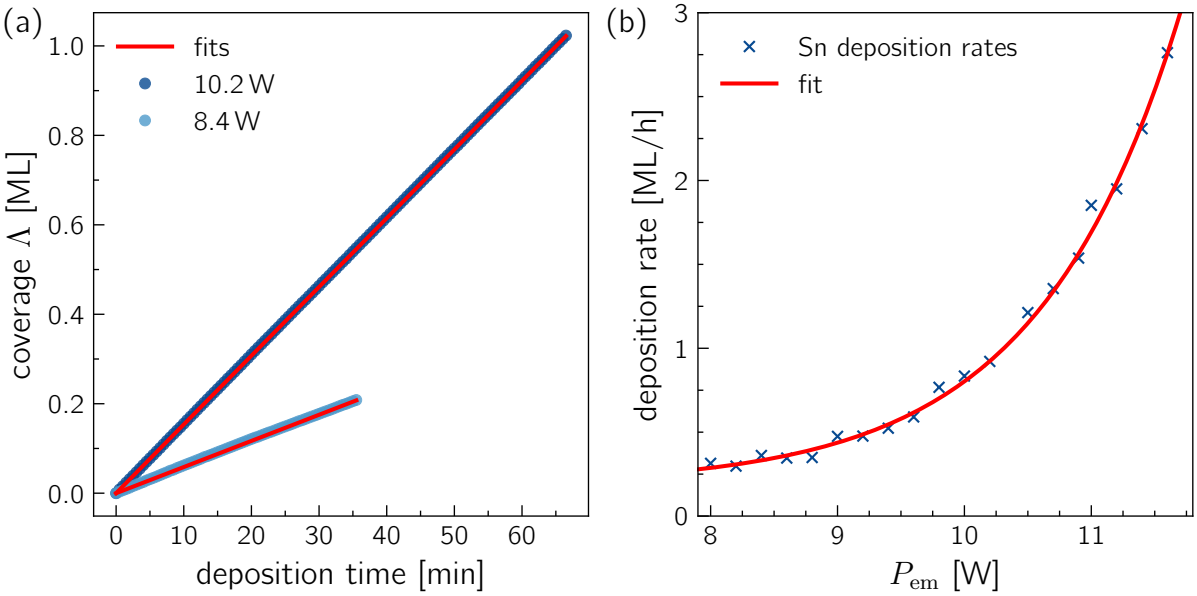

Figure 5.7: (a) Quartz crystal microbalance measurements of Sn deposition rates over time for two different heating powers. (b) Exponential dependence of the measured Sn deposition rates on the applied heating power $P_{\mathrm{em}} = U_{\mathrm{HV}} \cdot I_{\mathrm{em}}$.

Figure 5.7(b) displays the exponential dependence of the determined deposition rates on the applied heating power P_{em}. The exponential fit matches the data points well, enabling the selection of the specific heating power P_{em} required to achieve a desired coverage Λ

within a reasonable deposition time. In this thesis, a heating power of $P_{\mathrm{em}} = 10.2\,\mathrm{W}$ was typically used, corresponding to a deposition rate of 1 ML per 65 min. Additionally, for investigations of structural transitions happening at small coverage differences, requiring precise control over the deposited amount of Sn, a lower power of $P_{\mathrm{em}} = 8.4\,\mathrm{W}$ was used. This yields a rate of $\approx 0.36\,\mathrm{ML/h}$. These two specific settings correspond to the thickness measurements presented in Figure 5.7(a).

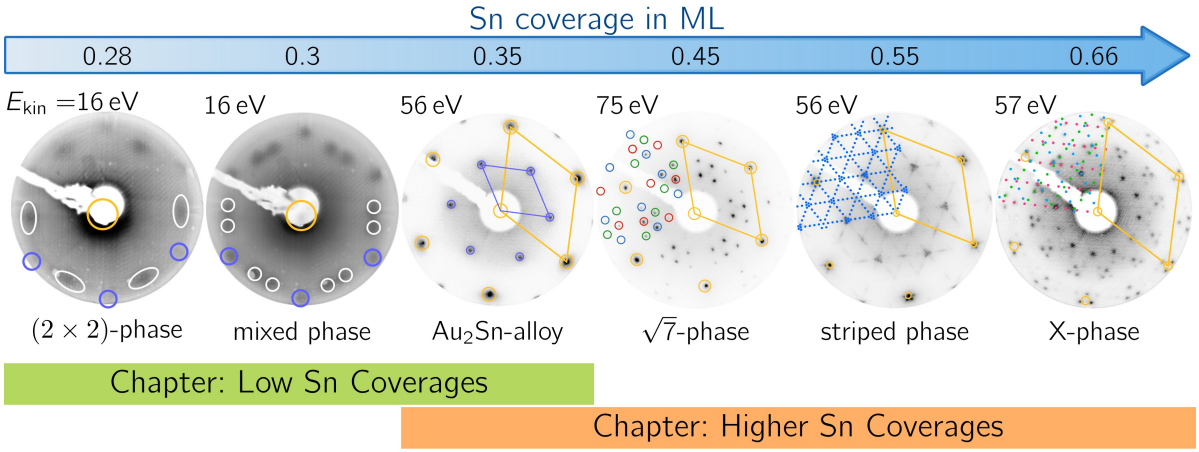

Figure 5.8: Overview of the structural evolution of submonolayer Sn films on Au(111).

Figure 5.8 provides an overview of the structural Sn arrangements on Au(111) identified in the submonolayer regime. The discussion of these structural phases is divided into two parts: Chapter 6 covers the low-coverage phases, up to the formation of the Au_2Sn surface alloy. Subsequently, Chapter 7 addresses the structural arrangements that emerge at higher coverages, specifically the $\sqrt{7}$, striped, and X-phase.

6 Low Sn Coverages

In the following two chapters, the analysis of the different structural phases of Sn on Au(111) at submonolayer coverage is discussed in detail. As will be shown, the structural arrangement of Sn and the transitions between different structural phases are highly dependent on small changes in the Sn coverage. Two different coverage regimes of interest are identified: At a coverage of 0.33 ML and slightly below, two distinct structural arrangements and a transition between them are observed and are the topic of this chapter. In contrast, structural phases at higher coverages between 0.33 ML and 0.66 ML will be discussed in the next chapter.

The main results presented in this chapter were previously published in:

- J. A. Hochhaus et al., *Structural analysis of Sn on Au(111) at low coverages: Towards the Au_2Sn surface alloy with alternating fcc and hcp domains*, Scientific Reports **15**, 7953 (2025)

6.1 Towards the Au_2Sn Surface Alloy

As will be discussed in detail in the next chapter, the Au_2Sn surface alloy serves as the starting point for the structural phases observed at higher Sn coverages. In the following, a detailed analysis of the structural phases and transitions leading towards the formation of the Au_2Sn surface alloy will be presented.

6.1.1 LEED

After verifying the successful preparation of a clean and well-reconstructed Au(111) surface, as presented in the previous chapter, submonolayer Sn films were deposited in small increments while keeping the sample at room temperature. After each deposition step of ≈ 0.02 ML, without any sample annealing, the surface reconstruction was checked using LEED. Up to a coverage of ≈ 0.25 ML, no indication of change was observed in the LEED pattern, except for an incrementally increasing background signal, which is expected for randomly arranged atoms on the surface.

However, upon surpassing a coverage of ≈ 0.25 ML Sn, a faint diffraction pattern is observed at very low kinetic LEED energies. As shown in Figure 6.1(a), a faint (2×2)-reconstruction appears, which intensifies at ≈ 0.28 ML before fading again at slightly higher coverages. Determining the periodicity of adlayers using LEED requires that both substrate and adsorbate diffraction spots are visible in the same pattern. However, the already faint spots of the (2×2)-reconstruction completely vanish when kinetic LEED energies above ≈ 28 eV are used, which is long before the substrate spots of the Au(111) appear at the border of the LEED screen at ≈ 45 eV.

Fortunately, at a coverage of ≈ 0.3 ML Sn, a mixed phase between the (2×2)-and a $(\sqrt{3} \times \sqrt{3})$R30°-reconstruction is observed, with the diffraction pattern of the latter still visible at higher kinetic LEED energies. This enables the calibration of observed distances in the LEED pattern of both reconstructions with respect to the Au(111) substrate spots and allows us to identify them as (2×2) and $(\sqrt{3} \times \sqrt{3})$R30°-reconstructions, respectively. The corresponding expected positions of LEED spots for the two reconstructions were calculated using LEEDPat [238] and are overlaid as white circles for the (2×2) and blue circles for the $(\sqrt{3} \times \sqrt{3})$R30°-reconstruction onto the LEED patterns. In Figure 6.1(a), the spot pattern of the (2×2) is marked by white ovals; its blurry appearance hints at some degree of disorder. Furthermore, as previously discussed, only the first-order spot pattern is observed, with no higher-order spots becoming visible at higher kinetic LEED energies, indicating a lack of long-range order in the reconstruction. Simultaneously, faint spots are already noticeable at the positions of the $(\sqrt{3} \times \sqrt{3})$R30°-reconstruction, which become more pronounced when slightly increasing the film thickness, as shown in Figure 6.1(b). Notably, the (2×2) spots are now significantly sharper and are identified as two separate spots, revealing the reconstruction to be a (2×2)R8°-reconstruction. This indicates that the emergence of the $(\sqrt{3} \times \sqrt{3})$R30°-reconstruction improves the ordering of the (2×2)-phase. As described before, the $(\sqrt{3} \times \sqrt{3})$R30°-phase exhibits second and third-order spots, indicating long-range order. Meanwhile, the spots corresponding to the (2×2)-reconstruction are still only observed at LEED kinetic energies below ≈ 28 eV.

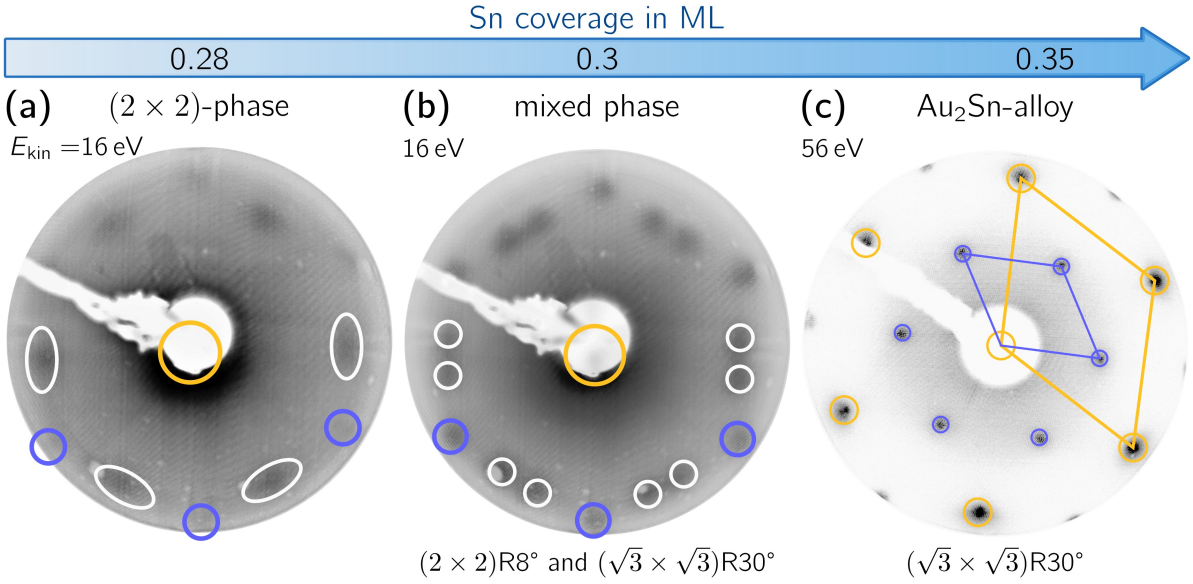

Figure 6.1: Structural evolution of Sn reconstructions up to a coverage of 0.33 ML. In yellow, the unit cell and diffraction spots of the Au substrate are marked, while in blue and white, spots corresponding to the different Sn reconstructions are marked. Figure reproduced after [45].

Upon further increasing the Sn coverage to ≈ 0.33 ML, the (2×2)-reconstruction completely vanishes, and only the sharp diffraction pattern of the $(\sqrt{3} \times \sqrt{3})$R30° remains.

In the literature, $(\sqrt{3} \times \sqrt{3})$R30°-reconstructions have been observed for various materials deposited on noble metal crystals with a (111)-orientation. These reconstructions were

identified as substitutional surface alloys, where one out of three atoms of the (111)-surface is substituted by an atom of the deposited material. Examples include Cu_2Bi [270, 271], Cu_2Sb [272], Ag_2Ge [57, 273, 274], Ag_2Sb [272], and Ag_2Pb [275, 276]. Regarding Sn, the formation of Pd_2Sn [277] and Ag_2Sn [25, 278] substitutional surface alloys has been reported. These substitutional surface alloys may play an important role in the growth of strain-free single atomic 2D layers. They allow for the creation of modified adsorption sites at the surface compared to the clean monoelemental (111)-surface, enabling the formation of strain-free 2D layers on top. In addition, the substitutional alloy layer might help to decouple the 2D layer from the substrate. Such formation of strain-free 2D layer systems has been predicted for stanene on Au_2Sn [279] and experimentally demonstrated for stanene on Pd_2Sn [26].
Notably, the clean Au(111) surface differs from other noble metal substrates due to its complex Rec($22 \times \sqrt{3}$) herringbone reconstruction, as discussed in detail in Section 5.1.

Nevertheless, several different (substitutional) alloy phases of Sn on Au(111) have been observed, though some involve more than one atomic layer. Examples are a Au_2Sn in a ($\sqrt{3} \times \sqrt{7}$)-arrangement [41], a AuSn p(3×3)R15°-reconstruction [41, 44], and $Au_{5.1}Sn$ in a ($\sqrt{3} \times \sqrt{3}$)R30°-reconstruction [54]. Additionally, the common substitutional surface alloy of Au_2Sn has been reported in the ($\sqrt{3} \times \sqrt{3}$)R30°-arrangement by Maniraj et al. [39] and Shah et al. [40].
However, the structural models proposed by these two groups differ. While Maniraj et al. suggested that the herringbone reconstruction remains unchanged during the formation of the Au_2Sn-alloy, Shah et al. identified a stripe-like order in STM images, reminiscent of the herringbone pattern but with a larger unit cell of Rec($26 \times \sqrt{3}$).

6.1.2 XPS

As shown in Figure 6.2, XPS survey spectra were measured to analyze the film thickness and chemical composition of the observed structural phases. The spectra were recorded at a grazing emission angle of $\Theta = 60°$ to enhance surface sensitivity. At the bottom of the plot, the survey spectrum of the clean Au(111) substrate is shown, with the observed structural phases stacked above with increasing Sn coverage. No residual contamination is observed following Sn deposition; the expected positions of the O 1*s* and C 1*s* signals are again marked by red boxes. The increasing Sn coverage is evident from the intensity increase of the Sn 4*d* signal at $E_{\text{bin}} \approx 24\,\text{eV}$ and the Sn 3*d* signal at $E_{\text{bin}} \approx 490\,\text{eV}$. Using XPS and assuming a non-attenuating fractional Sn adlayer, the Sn coverage was determined. For the (2×2)-phase, XPS gave a film thickness of (0.24 ± 0.02) ML; for the mixed phase, (0.27 ± 0.03) ML; and for the Au_2Sn ($\sqrt{3} \times \sqrt{3}$)R30°-reconstruction, (0.31 ± 0.02) ML. These values are slightly below the coverages determined by the QCM measurements, which resulted in (0.28±0.02) ML, (0.30±0.02) ML, and (0.33±0.02) ML, respectively.

High-resolution spectra of the Au 4*f* and the Sn 4*d* signals were used to resolve the system's interface and the internal chemical structure of the Sn layers atop. Focusing on the Sn 4*d* signal presented in Figure 6.3, spectra recorded under normal emission are displayed in the top row, while grazing emission spectra are plotted in the bottom row.

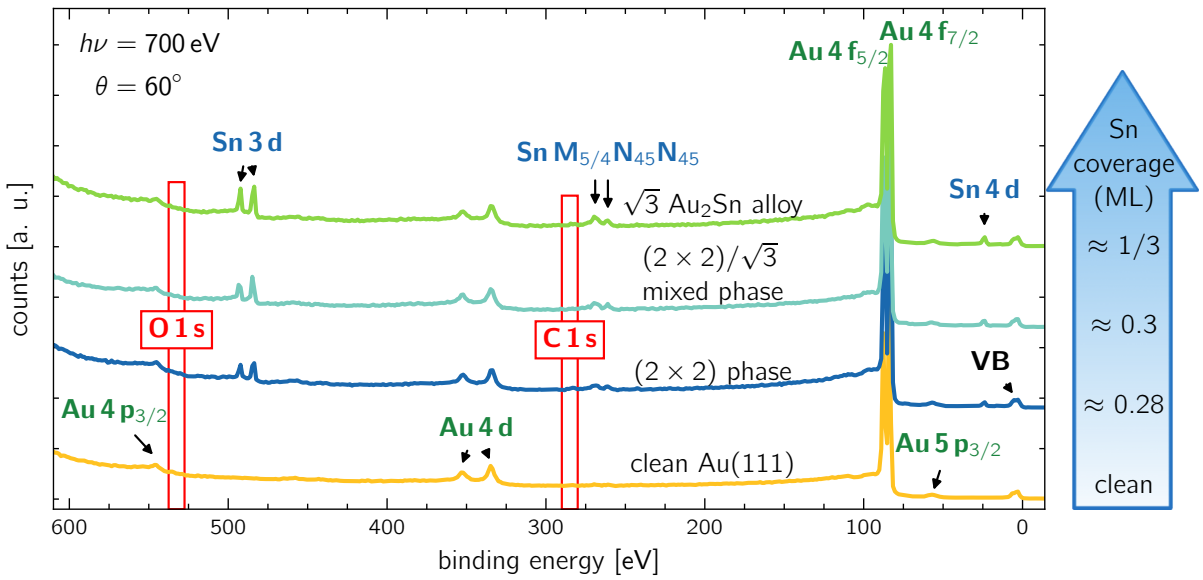

Figure 6.2: XPS survey spectra of the clean Au(111) in comparison to the different low-coverage Sn phases. The spectra were measured at $h\nu = 700\,\text{eV}$ and at $\Theta = 60°$. The binding energy of each spectrum was referenced to the Fermi edge. Figure adapted from [45].

This comparison enables angle-resolved analysis of the stacking order, as explained in Section 3.2. The fit parameters corresponding to the Sn $4d$ signal are summarized in Table 6.1.

Figure 6.3(a) shows the spectra obtained for the (2×2)-reconstruction. They are best described using a single Doniach-Šunjić doublet component with a spin-orbit splitting of $E_{\text{SOC}} = 1.03\,\text{eV}$, which is in excellent agreement with the literature [280, 281]. The binding energy of $E_{\text{bin}} = 24.03\,\text{eV}$ for the Sn $4d_{5/2}$ peak approximately matches the binding energy of pure Sn metal, which is given as 23.9 eV to 24.1 eV [282–284]. The peak asymmetry was determined to be $\beta = 0.12$, indicating the metallic character of the valence band in this phase [148, 255]. Since only a single component was identified in the high-resolution spectrum, it is directly assigned to the (2×2)-reconstruction. Forcing a second component into the fit would require reducing the FWHM of each component to unphysically small values and would decrease the overall fit quality, as confirmed by both the relatively constant residual $R(E)$ and the low $\chi^2_{\text{red.}}$ value obtained for the single component fit.

Turning to the mixed phase presented in Figure 6.3(b), the FWHM of the Sn $4d$ signal increases from 0.47 eV (obtained for the (2×2)-phase) to 0.58 eV. This increase in FWHM clearly indicates the presence of at least a second component. Additionally, the peak maxima of the Sn $4d$ signal shift by $\approx 100\,\text{meV}$ toward higher binding energies. The best fit is achieved using a two-component model. Approximately 1/3 of the signal is attributed to the previously identified (2×2)-phase. A second component is identified, shifted by 160 meV to higher binding energies. Apart from the energy position, this second component (marked in dark blue in Figure 6.3(b)) is fitted using parameters identical to those of the (2×2) component. The high peak asymmetry of $\beta = 0.12$ obtained for both

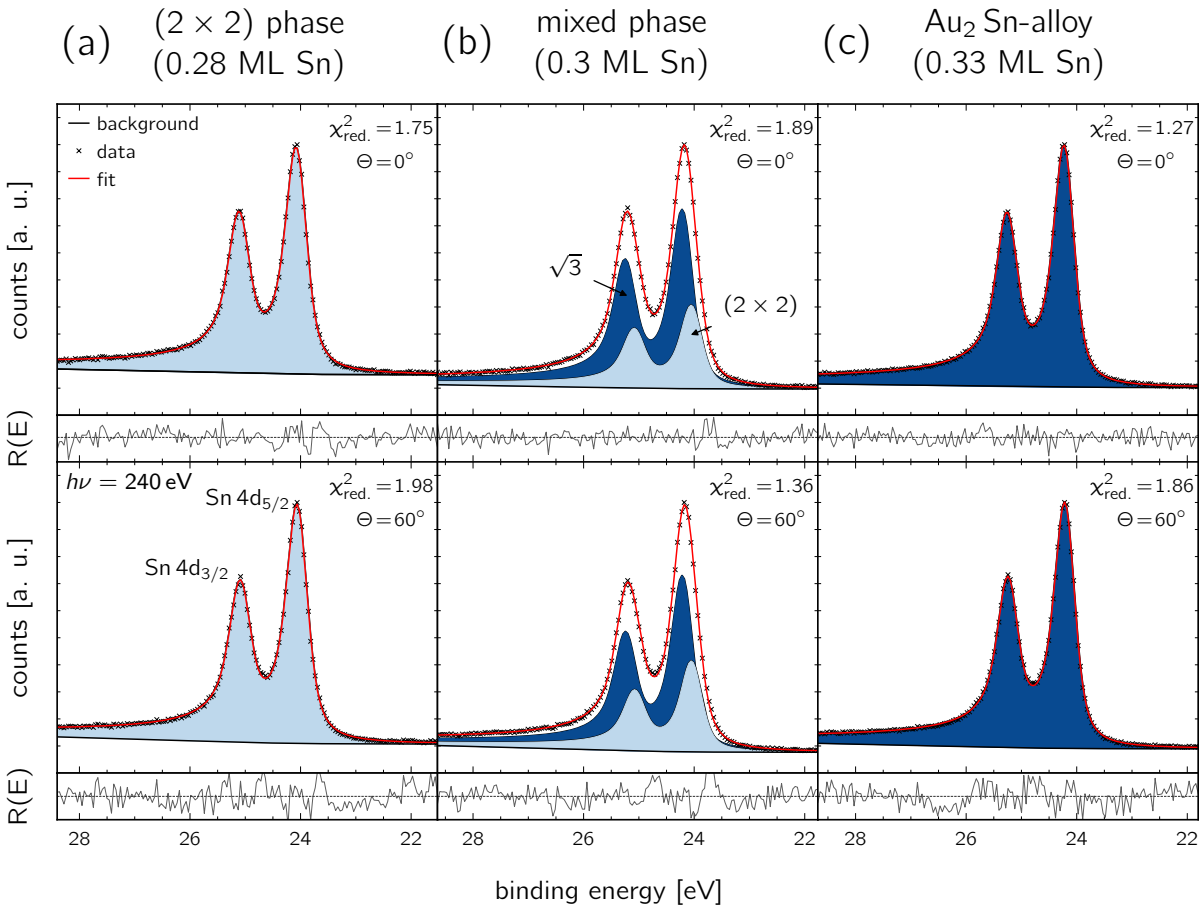

Figure 6.3: Analysis of the internal structure of the different structural phases using high-resolution XPS spectra of the Sn $4d$ core level. The spectra were taken at $h\nu = 240\,\mathrm{eV}$, using emission angles of $\Theta = 0°$ and $\Theta = 60°$, respectively. The corresponding fit parameters are given in Table 6.1. Figure modified after [45].

components again suggests the metallic character of both structural Sn arrangements [148, 255]. This second component is readily identified as the $(\sqrt{3} \times \sqrt{3})$R30°-reconstruction.

Based on the high-resolution XPS analysis, no chemical distinction can be made between the (2×2)-and the (2×2)R8°-reconstructions identified at slightly different coverages in LEED. Consequently, the two phases are likely chemically identical. The faint and diffuse LEED pattern observed at a coverage of 0.28 ML likely corresponds to a (2×2)R8° structure with a lower degree of long-range order. Comparing the composition of the normal and grazing emission spectra of the mixed phase reveals almost no difference in the respective area contributions of the two components. This indicates that both structural arrangements coexist within the same atomic layer, rather than one being stacked atop the other.

Finally, regarding the $(\sqrt{3} \times \sqrt{3})$R30°-reconstruction observed for a coverage of 0.33 ML (Figure 6.3(c)), the best fit is again achieved with a single component. This is identified as the $(\sqrt{3} \times \sqrt{3})$R30°-reconstruction, and its fit parameters match those of the previously identified component in the mixed phase.

Table 6.1: XPS analysis fit parameters to the chemical evolution of the Sn 4*d* signal shown in Figure 6.3. The statistical fit error for the reported binding energies is typically well below 10 meV. To simplify the reading and the table layout, the $(\sqrt{3} \times \sqrt{3})$R30°-table entry was simplified to $\sqrt{3}$. Reprinted from [45].

Structural phase	Θ (°)	Component	E_{bin} (eV)	E_{SOC} (eV)	FWHM (eV)	asymmetry β	rel. area (%)
(2×2) phase	0	(2×2)	24.03	1.03	0.47	0.12	100.00
figure 6.3(a)	60	(2×2)	24.04	1.03	0.47	0.12	100.00
mixed phase figure 6.3(b)	0	$\sqrt{3}$	24.19	1.03	0.48	0.12	68.03
		(2×2)	24.03	1.03	0.48	0.12	31.97
	60	$\sqrt{3}$	24.19	1.04	0.48	0.12	65.78
		(2×2)	24.03	1.04	0.48	0.12	34.22
Au_2 Sn-alloy	0	$\sqrt{3}$	24.20	1.03	0.47	0.12	100.00
figure 6.3(c)	60	$\sqrt{3}$	24.19	1.03	0.47	0.12	100.00

Turning to the analysis of the sample's interfacial chemical structure, Figure 6.4 displays the fitted angle-resolved high-resolution spectra of the Au 4*f* core level for the different structural phases. The corresponding fit parameters are given in Table 6.2.

Starting with the (2×2)-reconstruction shown in Subfigure (a), the spectrum is best described by two components, which are identical in their binding energy E_{bin}, FWHM, and asymmetry β to the fit obtained for the clean Au(111) substrate (compare with Section 5.1). Only the relative area contribution of the two components to the spectrum has changed, with the surface contribution being reduced compared to the clean Au(111). Otherwise, no evidence of alloying or influence of the formation of the (2×2)-reconstruction at the surface is identified in the Au 4*f* core-level signal. The (2×2)-phase can therefore be considered chemically decoupled from the substrate.

It could be assumed, however, that the (2×2)-reconstruction exhibits island growth, with the areas in between remaining a clean Au(111) surface, which could even explain

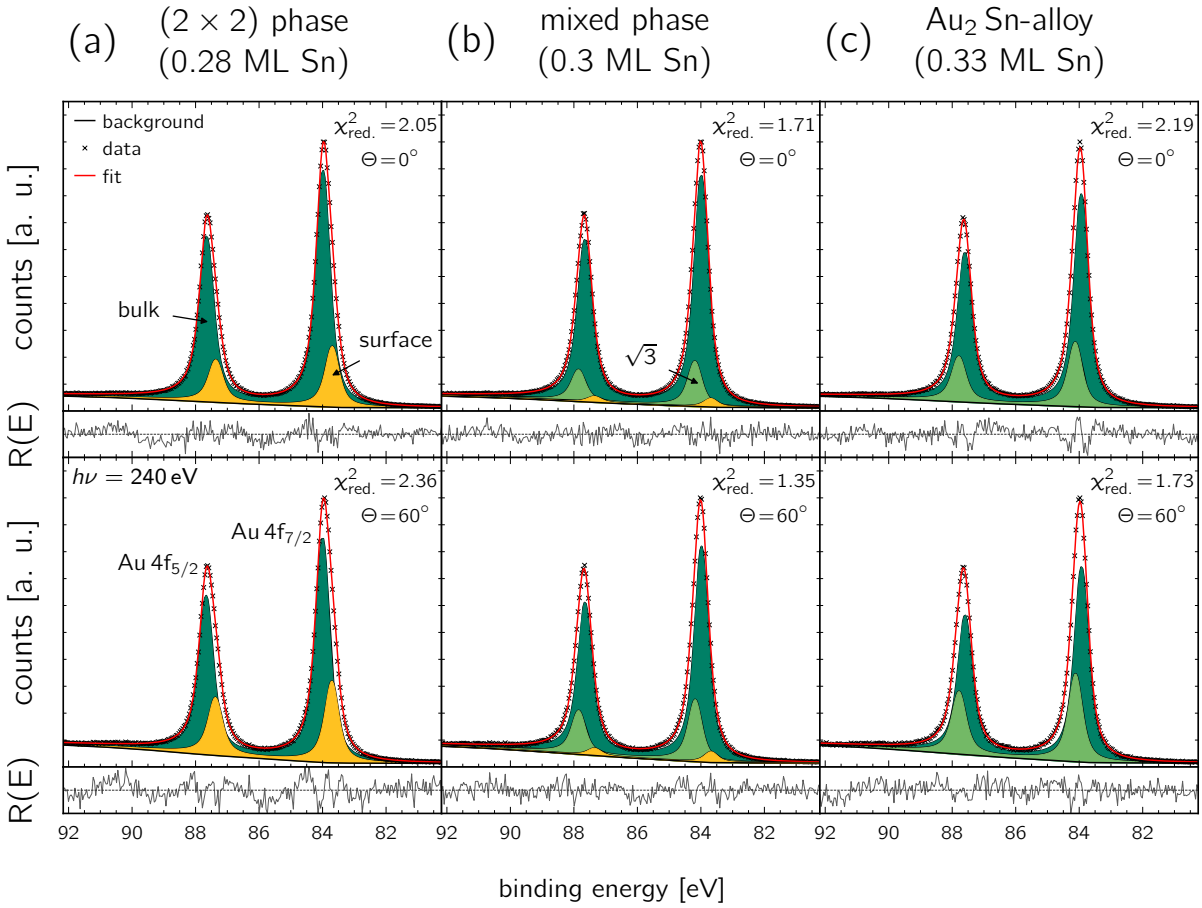

Figure 6.4: High-resolution XPS spectra of the Au $4f$ core-level signal used to analyze the interface structure of the low-coverage Sn phases. The spectra were taken at $h\nu = 240\,\mathrm{eV}$ and emission angles of $\Theta = 0°$ and $\Theta = 60°$, respectively. The corresponding fit parameters are given in Table 6.2. Figure reproduced from [45].

Table 6.2: Fit parameters of the XPS analysis corresponding to the Au $4f$ core-level signal in Figure 6.4. The statistical fit error for the reported binding energies is typically well below 10 meV. To simplify the reading and the table layout, the $(\sqrt{3} \times \sqrt{3})$R30°-table entry was simplified to $\sqrt{3}$. Reprinted from [45].

Structural phase	Θ (°)	Component	E_{bin} (eV)	E_{SOC} (eV)	FWHM (eV)	asymmetry β	rel. area (%)
(2×2) phase figure 6.4(a)	0	bulk	84.01	3.67	0.53	0.03	79.48
		surface	83.72	3.67	0.53	0.03	20.52
	60	bulk	84.00	3.67	0.53	0.03	73.27
		surface	83.71	3.67	0.53	0.03	26.73
mixed phase figure 6.4(b)	0	bulk	84.01	3.67	0.53	0.03	80.93
		surface	83.71	3.67	0.53	0.03	3.07
		$\sqrt{3}$	84.21	3.67	0.53	0.03	16.00
	60	bulk	84.01	3.67	0.52	0.03	74.64
		surface	83.71	3.67	0.52	0.03	3.74
		$\sqrt{3}$	84.21	3.67	0.52	0.03	21.63
Au_2 Sn-alloy figure 6.4(c)	0	bulk	84.00	3.67	0.52	0.03	76.63
		$\sqrt{3}$	84.19	3.67	0.53	0.03	23.37
	60	bulk	84.01	3.67	0.52	0.03	68.88
		$\sqrt{3}$	84.20	3.67	0.53	0.03	31.12

the reduced area contribution of the surface component to the spectrum. While the observed faint LEED pattern of this structural phase might support this hypothesis, the STM measurements, showing atomically flat monolayer growth (compare Figure 6.5) and the deposited Sn coverage, contradict it. The coverage of (0.28 ± 0.02) ML (QCM measurement) or (0.24 ± 0.02) ML (XPS coverage estimation) closely matches the density required for a full atomic layer arranged in a (2×2) periodicity. Since a (2×2) unit cell contains one atom per four substrate atoms, a coverage of 0.25 ML is required to cover the entire surface. Furthermore, the binding energy of the (2×2) component in the Sn $4d$ signal aligns with that of metallic Sn, and the Au $4f$ signal remains unchanged relative to the clean surface. These observations strongly suggest a weak interaction with the substrate, indicating that the phase is effectively freestanding.

Notably, the (2×2)-phase has not been reported in prior studies by Maniraj et al. [43] and Sadhukhan et al. [41, 54] of submonolayer Sn coverages on Au(111). Both described the first observed periodic Sn arrangements on Au(111) starting at a coverage of 1/3 ML, forming a $(\sqrt{3} \times \sqrt{3})$R30°-structure.
As the (2×2)-phase creates only a very faint LEED pattern at low kinetic LEED energies and only appears in a small coverage window, its existence might have been overlooked so far.

Turning to the mixed phase, with the corresponding Au $4f$ spectrum shown in Figure 6.4(b), a new component is observed at $E_{\text{bin}} = 84.21$ eV (depicted in light green). This component is directly attributed to the $(\sqrt{3} \times \sqrt{3})$R30°-reconstruction. Meanwhile, the Au(111) surface component remains visible, despite becoming smaller. Since a new component associated with the $(\sqrt{3} \times \sqrt{3})$R30°-reconstruction is found in both the Sn $4d$ and Au $4f$ signals, this phase is identified as an alloy. Notably, both $(\sqrt{3} \times \sqrt{3})$R30° components (the one in the Au $4f$ spectrum as well as the one in the Sn $4d$ spectrum)

are shifted to higher binding energies. According to the standard rule of thumb based on electronegativity, it would be expected that one component would shift to lower binding energies while the other shifts to higher energies. As Sn with 1.96 has a smaller Pauling electronegativity compared to Au with 2.54 [285], charge transfer from Sn to Au would be expected. This should decrease the binding energy of the respective components in the Au $4f$ signal and increase their binding energy in the Sn $4d$ signal. However, such shifts of both components towards higher binding energies are characteristic of $Au_x Sn$ alloy formation [286] and have also been noted in AgSn alloying [287].
As discussed in Section 3.2.2, the Au-Sn system is a well-known example that does not follow the simple predictive rule of electronegativity regarding chemical shifts.

Finally, regarding the fitted spectrum of the $(\sqrt{3} \times \sqrt{3})$R30°-reconstruction shown in Figure 6.4(c), only the alloy component remains. The alloy component shows a similar angular dependence to the Au(111) surface component identified in the fit of the clean Au(111) (see Table 5.2) as well as the surface component identified in the (2×2)-phase; in all cases the increase of the respective component is $\approx 30\%$ when comparing the area contribution at $\Theta = 60°$ to the area contribution at normal emission. This indicates that the stacking order is comparable and suggests the alloy component originates from the topmost layer. Furthermore, considering the determined Sn coverage of ≈ 0.33 ML, the alloy is identified as a Au_2Sn substitutional surface alloy. Additionally, the determined binding energies for the $(\sqrt{3} \times \sqrt{3})$R30°-reconstruction are in excellent agreement with those reported by Sadhukhan et al. [41, 54].

6.1.3 STM

Complementing the reciprocal-space analysis presented above in the LEED section 6.1.1, the structural evolution at low coverages was examined in real space using STM. The corresponding STM results are shown in Figure 6.5.

As shown in Figure 6.5(a), at 0.28 ML, a well-ordered atomic arrangement is observed. This hexagonal arrangement of Sn with one atom per unit cell, follows the (2×2) periodicity observed in LEED. As indicated by the red lines in the top left of the STM image, occasional dislocation lines with a width of $\approx a_{\mathrm{Au}} = 2.88$ Å are observed, where a_{Au} denotes the Au(111) surface lattice constant assuming no surface reconstruction. As shown in Figure 6.6(a), such dislocation lines are also observed with a width of $\approx 5a_{\mathrm{Au}}$, containing two densely packed Sn atomic rows. While for the smaller dislocation line in Figure 6.5(a), a shift of the observed structures bordering the dislocation line is observed (indicated by red guidelines), no such shift is observed for the wider dislocation line in Figure 6.6(a). Additionally, a coexistence of the (2×2)-reconstruction with areas of unordered Sn is occasionally observed; an STM image showing such coexistence is displayed in Figure 6.6(b), with the disordered region marked by the black border.

The next-neighbour distance was determined from the STM image by averaging next-neighbour distances from line profiles, such as the one shown in Figure 6.5(d). This yields a next-neighbour distance of (5.8 ± 0.2) Å. This closely matches the expected

lattice constant of a (2×2)-reconstruction with one atom per unit cell, as it matches $2 \cdot a_{\mathrm{Au}} = 5.764\,\text{Å}$.

For the mixed phase, a striped-like STM image is measured, shown in Figure 6.5(b), showing alternating stripes of a well-ordered $(\sqrt{3} \times \sqrt{3})$R30°-phase and regions of often disordered (2×2)-reconstruction. The width of the stripes ranges from approximately 5 nm to 10 nm for both types. Usually, no sharp boundary between the two regions is observed, and the stripe width varies along their length.

Fast-Fourier Transforms (FFTs) of the squares marked in both regions in Figure 6.5(b) are shown in Subfigures (e) and (f), respectively. The FFT of the $(\sqrt{3} \times \sqrt{3})$R30°-region, marked by an orange box in the STM image and shown in (e), shows a sharp hexagonal diffraction pattern. The expected spot positions of the $(\sqrt{3} \times \sqrt{3})$R30° (marked by orange circles) match the obtained FFT pattern. In addition, spots of the second and third orders are visible in the FFT. In (f), the FFT is noisier; however, the spot pattern still appears as a hexagon, but rotated by 30° to the pattern of the $(\sqrt{3} \times \sqrt{3})$R30°. This matches the expected diffraction pattern of a (2×2)-reconstruction, with the spot positions indicated by white circles.

In the mixed phase LEED pattern, a (2×2)R8°-reconstruction was observed. Due to the limited resolution of the FFT, such a small rotation would not clearly be identified in the FFT pattern. Furthermore, due to the relatively high degree of disorder, a noisy FFT pattern would be expected. The observed rotation by 30° of the two hexagonal FFT patterns perfectly matches the observation from the LEED pattern, consistent with a mixed pattern of an unrotated (2×2) (or (2×2)R8°) and the $(\sqrt{3} \times \sqrt{3})$R30°-phase, where the unit cell is rotated by 30° with respect to the substrate.

In Figure 6.5(c), an STM image similar to the mixed phase is observed for the Au_2Sn-alloy. Again, a striped STM image is measured; however, now stripes of alternating widths are observed. The observed STM image closely resembles typical STM images of the Au(111) herringbone reconstruction, except that the zig-zag pattern with the elbow-like structure is not observed; instead, the observed stripes run straight for up to 100 nm. Occasionally, single hexagons, still matching the (2×2) lattice periodicity, are observed in the regions appearing brighter in the STM image. A similar disorder in the striped STM pattern of the Au_2Sn was observed by Shah et al. [40].

As will be explained in detail in the XPD analysis below, the Au_2Sn-stripes are indeed similar to the herringbone reconstruction, as they show alternating fcc and hcp stacking as well. Specifically, there is a transition region that cannot be clearly assigned to either stacking order, but in which the atoms instead sit in energetically unfavorable positions (bridge-like or near-top). Therefore, they appear lifted in STM. This lifted domain wall is visible in Figure 6.5(g); in the line profile, the domain wall appears approximately 20 pm higher than the regions in between.

In the literature, the striped Au_2Sn alloy was already investigated using LEED and STM. While Maniraj et al. [39] proposed that the striped STM pattern stems from the herringbone reconstruction and that the alloy formation does not alter the herringbone $\mathrm{Rec}(22 \times \sqrt{3})$ unit cell, Shah et al. [40] proposed a slightly larger unit cell of $\mathrm{Rec}(26 \times \sqrt{3})$. In the STM image in 6.5(c), both unit cells are plotted, with the periodicity of the

alternating stripes being more closely matched by the Rec($26 \times \sqrt{3}$) unit cell. Indeed, the periodicity of the stripes was determined to be (7.6 ± 0.6) nm, which translates to a 26 ± 2 periodicity with respect to the Au(111) lattice.

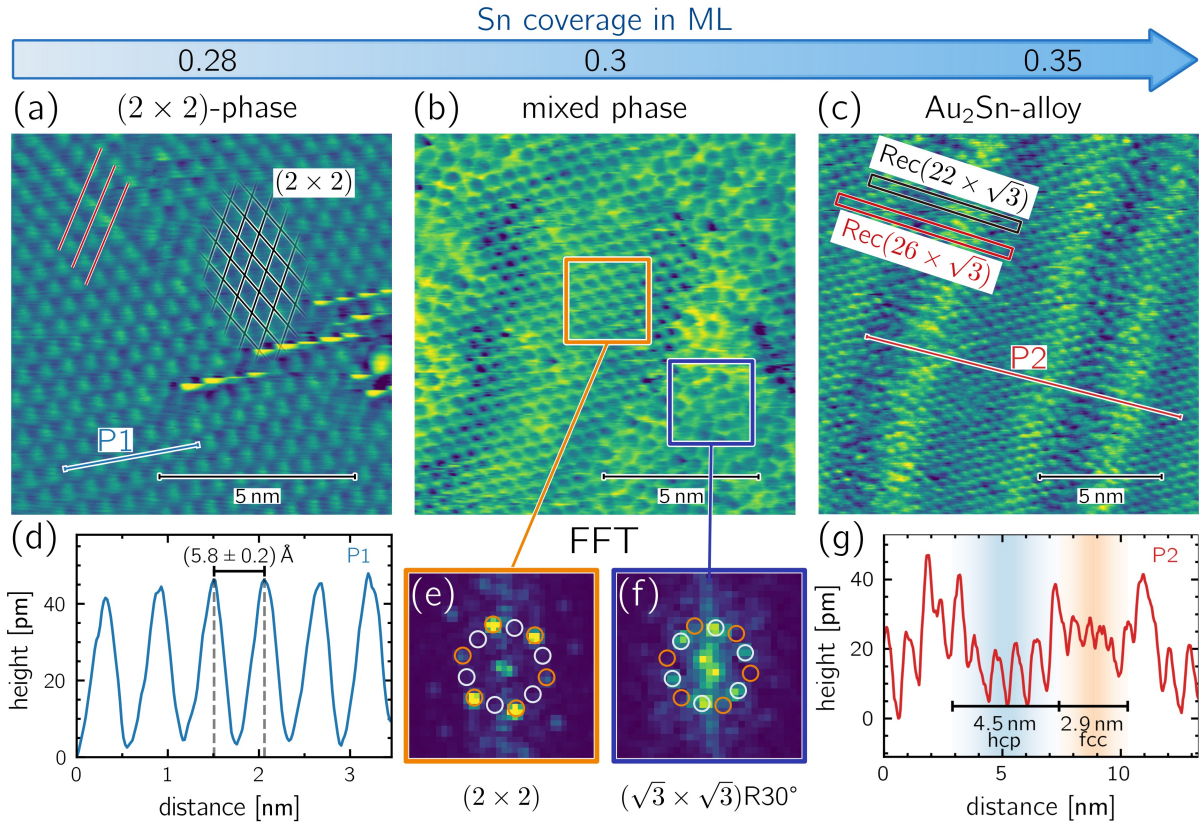

Figure 6.5: Structural evolution at low Sn coverages observed using atomically resolved STM. Shown in (a) is the (2 × 2), recorded at $U_{\text{bias}} = 0.75\,\text{V}$ and $I_{\text{tunnel}} = 176\,\text{pA}$. The mixed phase in (b) was recorded with the same bias voltage but at $I_{\text{tunnel}} = 22.3\,\text{pA}$. FFTs of the regions marked within the alternating $(\sqrt{3} \times \sqrt{3})$R30° and distorted stripes of the (2 × 2) are shown in (e) and (f), respectively. (c) The alternating stripes of the local $(\sqrt{3} \times \sqrt{3})$R30°-reconstruction, recorded with identical parameters to (b), form a Rec($26 \times \sqrt{3}$) unit cell as highlighted in red. The line profile shown in (d) corresponds to the line marked in (a) of the (2 × 2)-reconstruction. In the Fourier transforms in (e) and (f), spot positions corresponding to a $(\sqrt{3} \times \sqrt{3})$R30°-periodicity and a (2 × 2)-reconstruction are marked by orange and white circles, respectively. (g) The indicated widths of the hcp and fcc regions in the line profile of the striped Rec($26 \times \sqrt{3}$)-reconstruction are obtained from our XPD analysis. Figure modified after [45].

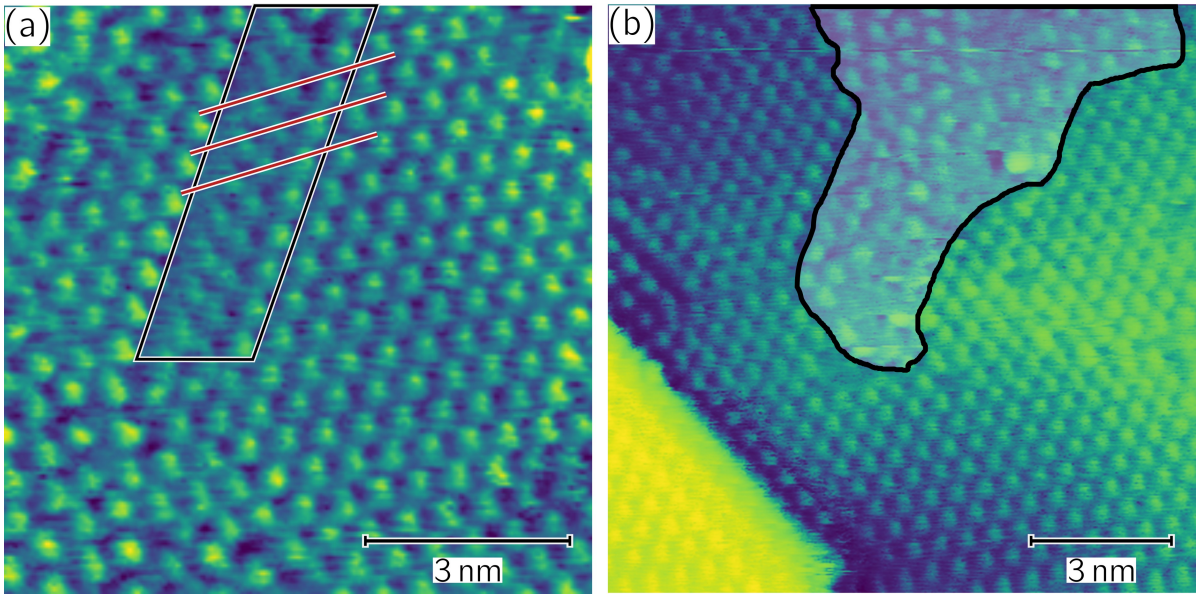

Figure 6.6: (a) Separation line in the well-ordered (2×2)-reconstruction containing two dense-packed Sn-atom rows. (b) Coexistence of the well-ordered (2×2)-reconstruction with unordered Sn in the region marked in black. Figure reprinted from [45].

6.1.4 XPD

Because the STM analysis did not yield a definitive conclusion on the structural model and periodicity of the Au_2Sn alloy, diffraction methods were used to provide deeper insights. First, Figure 6.7 shows a LEED image of the Au_2Sn $(\sqrt{3} \times \sqrt{3})$R30°-reconstruction recorded at a low electron kinetic energy of $E_{kin} = 24\,eV$. Notably, at the $\sqrt{3}$-spot position, not a single sharp 2D-Gaussian spot is observed; instead, a distinct triangular shape, stemming from an imposed superstructure, is visible. Importantly, the triangles at all corners of the hexagonal LEED pattern point outwards, as shown in the zoomed inset. It was noted that the superstructure becomes better reconstructed when the sample was slightly annealed after Sn-deposition. The best ordering was found for annealing at $\approx 550\,K$, the superstructure starts degrading if heated above $\approx 700\,K$, and the $(\sqrt{3} \times \sqrt{3})$R30°-reconstruction vanishes when annealed above $\approx 900\,K$, as the Sn is then desorbed.

Subsequently, LEED patterns for unit cells of the type Rec$(m \times \sqrt{3})$ were calculated using LEEDPat [238], where m ranged from $m = 22$ (herringbone reconstruction) to $m = 29$. This range covers the periodicity determined via STM ($m = 26 \pm 2$). Zoomed insets of the $\sqrt{3}$-spot positions for selected calculated patterns are shown in Figure 6.7. It is observed that if the condition $m \bmod 3 = 2$ is fulfilled (e.g., $m = 23$ or $m = 26$), the superstructure around the $\sqrt{3}$-spot resembles the experimental pattern, exhibiting an outward-pointing triangle. Conversely, for $m \bmod 3 = 1$ (e.g., $m = 22$ and $m = 25$), the triangular superstructure points inwards, while for $m \bmod 3 = 0$ (e.g., $m = 24$ and $m = 27$), a hexagonal superstructure is observed. Consistent with the STM periodicity analysis ($m = 26 \pm 2$), these findings strongly suggest the Rec$(26 \times \sqrt{3})$ unit cell proposed by Shah et al. [40]. The unaltered Rec$(22 \times \sqrt{3})$ herringbone unit cell proposed by Maniraj

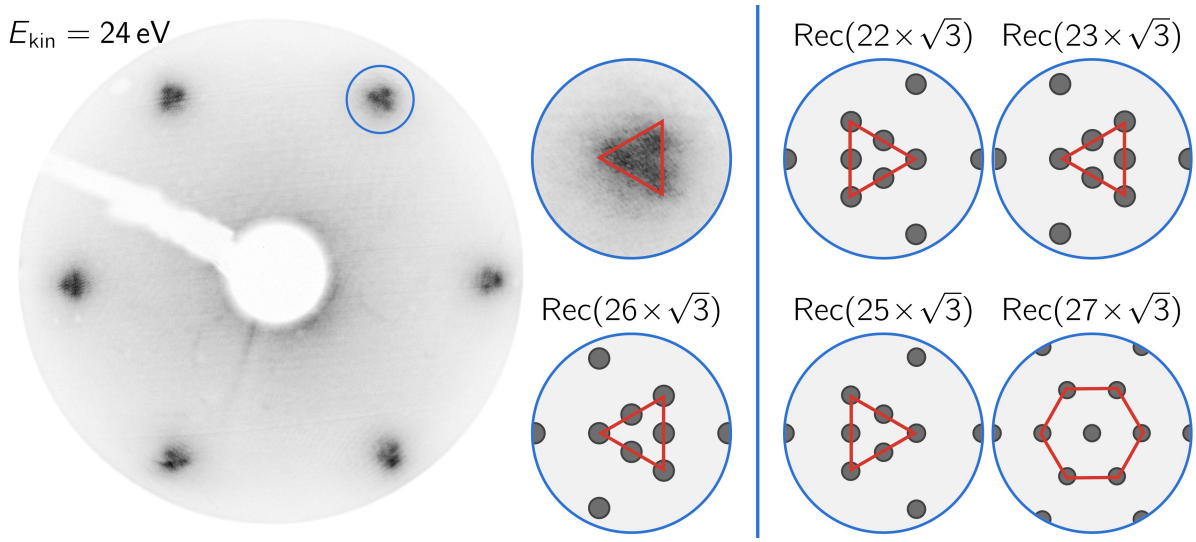

Figure 6.7: Comparison of calculated LEED patterns with the long-range order substructure observed around the $\sqrt{3}$-spot positions. Only the Rec($23 \times \sqrt{3}$) and Rec($26 \times \sqrt{3}$) reproduce the observed superstructure as indicated by the red triangle. The Rec($23 \times \sqrt{3}$)-reconstruction can be ruled out by analyzing the spot distances of the superstructure in detail. Figure reproduced in parts from [45].

et al. [39] appears unlikely, as the observed LEED superstructure does not match the experimental data.

To resolve the atomic arrangement within the unit cell and further confirm the Rec($26 \times \sqrt{3}$) model, the structure was analyzed using XPD.

XPD measurements and simulations of the Sn 4*d* and Au 4*f* core level signals were performed. The results are shown in Figure 6.8(a) and (b). Simulating a unit cell of size Rec($26 \times \sqrt{3}$) involves 54 atoms in the topmost layer per unit cell alone. Since the EDAC algorithm calculates the interference pattern of multi-diffracted photoelectron waves based on the local environment of the initial emitter atom and relies on absolute atomic positions, including only a single unit cell in the structural model is insufficient. Therefore, the structural model contained 6 atomic layers, each consisting of 4 unit cells, resulting in a total of approximately 1300 atoms (depending on the assumed periodicity and compression in the topmost layer, this number varied slightly between different assumed Rec($m \times \sqrt{3}$) starting structures). Such large structural models would result in calculation times of up to 40 h per diffraction pattern if all individual emitters in the unit cell of the topmost layer were used. Given that the genetic algorithm typically requires $\approx$ 100 generations to converge, a result could be expected after 6 months of calculation time. Therefore, tests were performed to determine the minimum number of emitters required to generate a representative XPD pattern. This approach is valid based on the following reasoning: If the photoelectron waves from two different emitter atoms propagate through and are diffracted by overlapping local clusters, the (multiply) diffraction of the photoelectron waves in the overlapping region will give an identical contribution to the diffraction pattern. Therefore, for simulating the Sn 4*d* XPD pattern, using only 8 emitter atoms in the unit cell yields almost the full diffraction pattern. For

the Au $4f$ diffraction pattern, 12 Au emitters are needed to achieve a sufficiently accurate approximation, as their respective local clusters surrounding the chosen emitters already cover all atoms of the unit cell.

This reduction decreases the calculation time per diffraction pattern to 1 h to 2 h, allowing the structural simulation to converge within several days.

As the genetic algorithm used for structural optimization varies individual atomic positions, all allowed variations must be carefully constrained to preserve the unit cell periodicity. To achieve this, custom scripts were developed to restrict the genetic algorithm, ensuring that variations do not break the system's symmetry. This resulted in up to 1250 allowed translation variations for single atoms and groups of atoms. To maintain the system's rotational symmetry during variation, up to 300 constraints were applied to enforce threefold rotational symmetry in the structural model.

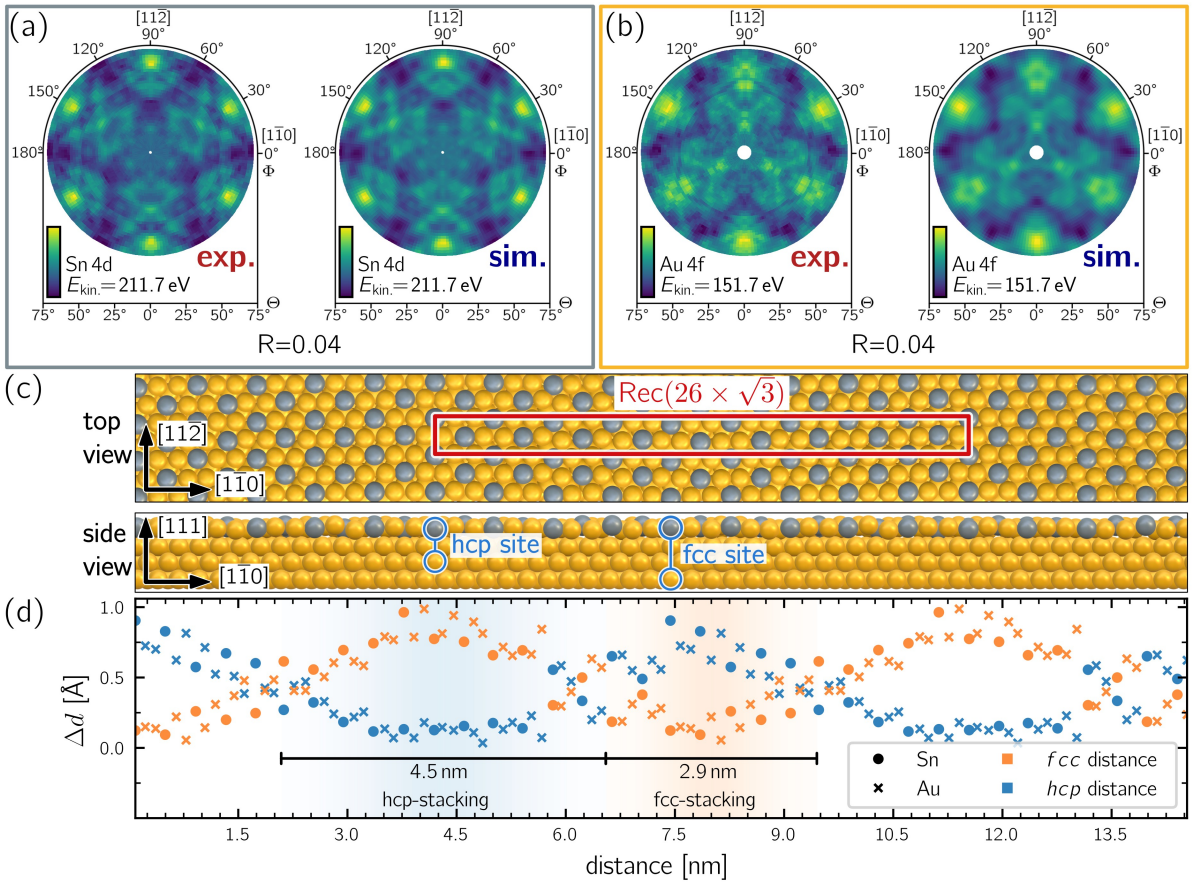

Figure 6.8: XPD analysis of the Rec(26 × √3)-phase. (a) and (b) Experimental (left) and simulated (right) XPD patterns for Sn $4d$ photoelectrons with a kinetic energy of $E_{\text{kin.}} = 211.7\,\text{eV}$ and Au $4f$ signal with $E_{\text{kin.}} = 151.6\,\text{eV}$, respectively. (c) The resulting structural model of the phase, showing alternating hcp and fcc stripes, as evident from the plot in (d). Here, the lateral distances (Δd) from the ideal fcc and hcp stacking sites for the atoms in the surface layer are shown. Figure reproduced from [45].

While all atoms in the two topmost layers were allowed to vary their position (provided symmetry was maintained), the deeper atomic layers of the structural model were only

allowed to vary their z-position as a whole layer, thereby enabling modification of the interlayer distance. The topmost layer was allowed to compress/stretch by $\pm 10\,\%$ along the $[1\bar{1}0]$-direction, effectively enabling the variation of the periodicity m of the structural model. Using this structural model, the genetic algorithm was used to optimize the structure. The optimization procedure was performed independently for the Sn $4d$ and Au $4f$ core level signals. The results are plotted in Figure 6.8(a) and (b) next to the respective experimental data. Both simulated XPD patterns match the experimental patterns excellently, as indicated by the very small Pendry R-factor (termed R-factor in the following) for both of $R = 0.04$, reflecting almost perfect agreement. Notably, both structural optimizations *independently* resulted in the same periodicity, $m = 26$. The differences between the two optimized structures obtained for the two signals are negligible. All differences in atomic positions for the full structural model along the $[1\bar{1}0]$- and $[11\bar{2}]$-directions are $\leq 5\,\mathrm{pm}$. In the z-direction ([111]), the maximum deviation in individual atomic positions is $\leq 30\,\mathrm{pm}$.

The resulting structural model obtained from the optimization of the Sn $4d$ signal is shown in Figure 6.8(c). Figure 6.8(d) plots the in-plane distance Δd of each atom to the closest ideal fcc (blue) and hcp (orange) stacking site. Clearly, an oscillation of atoms between hcp and fcc stacking sites is observed, analogous to the herringbone reconstruction of the Au(111) surface. Furthermore, atomic displacement along the $[11\bar{2}]$-direction is observed, which allows more atoms to be positioned in energetically favorable hollow sites in the unit cell.

Atoms are assigned to the hcp region if they are closer to an hcp site than to an fcc site, and vice versa. In transition regions where this assignment is ambiguous, atoms are assigned to neighboring regions using a similar approach to that used to describe the herringbone reconstruction; thus, the width of the domain walls is set to zero in this context [242, 288, 289]. The observed disorder in the transition region might be an artifact of the XPD simulations, stemming from the reduced number of representative emitters used; the contribution of atoms far away from the next emitter, so atoms close to the border of the atomic cluster around the atoms used as emitters, will be underestimated in the simulated diffraction pattern. Consequently, some regions of the unit cell may be less well-represented during optimization, and their absolute atomic position will remain ambiguous. While the hcp and fcc regions of the herringbone reconstruction have widths of $\approx 2.8\,\mathrm{nm}$ and $\approx 3.8\,\mathrm{nm}$, respectively [288], the Au_2Sn alloy exhibits a wider hcp region ($\approx 4.5\,\mathrm{nm}$) and a narrower fcc region ($\approx 2.9\,\mathrm{nm}$). These domain widths are in good agreement with the STM line profile shown in Figure 6.5(g).

Analogous to the herringbone reconstruction, where 23 surface atoms are compressed onto 22 substrate lattice sites, the $\mathrm{Rec}(26 \times \sqrt{3})$ unit cell involves 27 atoms in the surface layer compressed onto 26 substrate lattice sites. This corresponds to a compression of the surface alloy layer of $\approx 3.7\%$ along the $[1\bar{1}0]$-direction relative to the layers below.

Notably, a similar striped phase is observed for Ge on Ag(111). At a coverage of $\approx 1/3\,\mathrm{ML}$ Ge, a Ag_2Ge substitutional alloy forms with alternating hcp and fcc stripes, resulting in a $c(31 \times \sqrt{3})$ supercell [290].

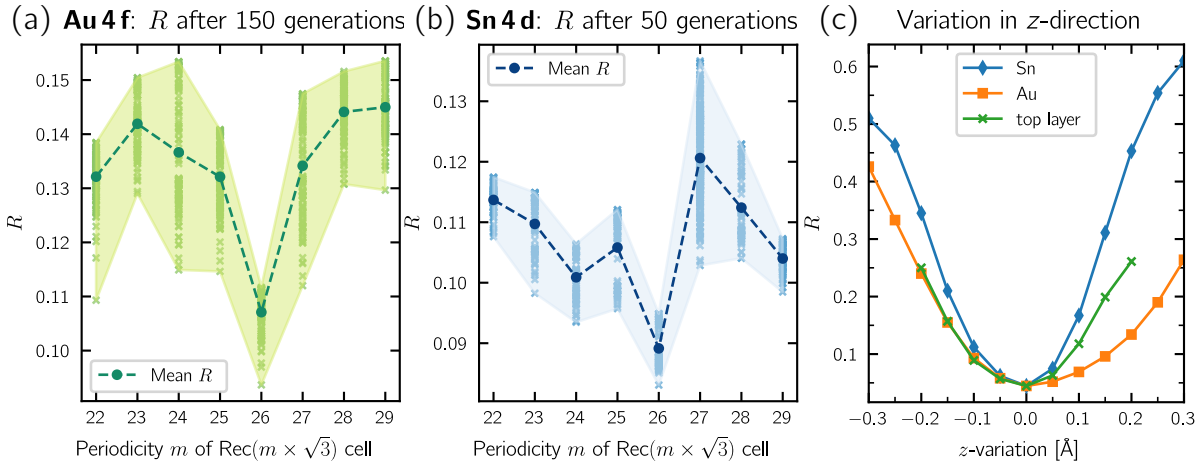

Figure 6.9: The R-factors for different periodicities m of the Rec($m \times \sqrt{3}$) rectangular unit cell were calculated for the Au $4f$ signal in (a) and the Sn $4d$ signal in (b), resulting independently in a minimum for $m = 26$. In (c), the R-factor minimum is confirmed for variations of layer positions in the direction normal to the surface (z-direction). Figure adapted from [45].

In addition, the stability of the obtained structural model was tested against modifications. As shown in Figure 6.9(a) and (b), simulating the Au $4f$ and Sn $4d$ diffraction patterns individually for a fixed periodicity m of the Rec($m \times \sqrt{3}$) unit cell results in a minimum R-factor for $m = 26$ after letting the genetic algorithm run for 150 (Au $4f$) or 50 generations (Sn $4d$), respectively.

The limit on the number of generations was chosen such that the improvement to the R-factor was smaller than $\Delta R \leq 0.01$ in the last ≈ 10 generations before termination. Importantly, the genetic algorithm was terminated after a generation with an even generation number (yielding an odd iteration index, as the index starts at 0). These generations correspond to steps in which gene combinations are used to create the next generation. In general, these generations yield greater average improvement and a more homogeneous R-factor than generations created from random modifications (mutation), which tend to be more heterogeneous and contain more outliers.

The genetic algorithm was run 3 times, with 60 individuals per generation for each m, to minimize the influence of the process's stochastic nature. This prevents a scenario where a lucky early guess allows one run of the genetic algorithm to converge significantly faster than others. To generate initial start structures and to randomize structural models during the mutation step of the genetic algorithm, a pseudo-random number generator (PRNG) was initialized using the computer clock as the seed. This approach ensures that each run of the genetic algorithm has a unique starting seed and generates a unique set of structural variations. Each small cross in Figures 6.9(a) and (b) represents the R-factor obtained for an individual within the created generation of the best set of obtained structures after the given number of generations. The lightly shaded area represents the range of R-factors obtained, while the connected dots represent the average R-factor.

In Figure 6.9(c), the interlayer distance of the entire Au_2Sn alloy layer, as well as the individual Sn and Au sublattices within it, was varied with respect to the layers below in

the z-direction ([111]-direction). For all three analyzed interlayer distance variations, the minimum of the R-factor is obtained for a variation of $z = 0$, meaning that the R-factor of the obtained structural model cannot be further improved by modifying interlayer distances.

Our combined analysis of the structural model, using STM, LEED, and XPD, therefore strongly favors the Rec($26 \times \sqrt{3}$) unit cell as proposed by Shah et al. [40], and rules out a substitution of Au atoms by Sn directly in the herringbone Rec($22 \times \sqrt{3}$) unit cell as proposed by Maniraj et al. [39]. While the results presented in the remainder of this chapter were obtained via deposition at room temperature, extensive parameter testing was conducted to ensure that the observed structure is not an artifact of a specific preparation procedure. This involved systematically screening a wide range of parameters, including post-deposition annealing of samples prepared at room temperature to temperatures ranging from 350 K up to the Sn desorption threshold of $\approx$ 800 K. Additionally, Sn deposition directly onto substrates held at elevated temperatures within the same range was tested. Remarkably, LEED measurements confirmed the formation of the identical Rec($26 \times \sqrt{3}$) structural arrangement across the entire annealing temperature range tested. This structural invariance strongly suggests that although Maniraj et al. [39] used different preparation parameters (see Table 6.3), they likely observed the same structural phase but misassigned the reconstruction. It is worth noting that while the observed periodicity remained Rec($26 \times \sqrt{3}$), the degree of ordering varied; the sharpest diffraction spots and optimal ordering were achieved using a substrate or annealing temperature of $\approx$ 520 K.

Table 6.3: Comparison of the preparation parameters used by Maniraj et al. [39], Shah et al. [40], and the tested parameter ranges in this work. Independent of the used preparation parameters, the LEED pattern always indicated a Rec($26 \times \sqrt{3}$)-periodicity as analysed in Figure 6.7. Reprinted from [47].

Parameter	Maniraj et al. [39]	Shah et al. [40]	This work
Evaporation rate	not given, Sn in crucible at 1100 K	not given	1.5 Å/h to 9 Å/h (0.33 ML deposited)
Substrate temperature	650 K	503 K	300 K to 800 K
Pressure (during evaporation)	$\leq 5 \times 10^{-10}$ mbar	not given	$\leq 3.5 \times 10^{-10}$ mbar
Base pressure	$\leq 2 \times 10^{-10}$ mbar	not given	$\leq 1 \times 10^{-10}$ mbar

6.2 Chapter Summary

In this chapter, the structural evolution of Sn on Au(111) in the low coverage regime ($\Lambda < 0.33\,\mathrm{ML}$) was characterized. Two distinct structural phases were identified. First, a chemically freestanding (2×2)-phase appears at coverages around 0.28 ML; this phase exhibits a (2×2) periodicity with respect to the substrate and could be interpreted as half a layer of α-Sn, which corresponds to buckled stanene [291, 292]. Upon slightly increasing the coverage, a mixed transition phase is observed, until the Au_2Sn substitutional surface alloy forms at $\Lambda \approx 0.33\,\mathrm{ML}$.

The central result of this chapter is the determination of the specific long-range order of the Au_2Sn alloy. While previous studies suggested an unaltered Rec$(22 \times \sqrt{3})$ herringbone reconstruction, our combined approach of LEED, STM, and XPD structural optimization conclusively identifies a larger Rec$(26 \times \sqrt{3})$ unit cell. This reconstruction features alternating hcp and fcc stacking domains, similar to the Au(111) herringbone reconstruction but with modified domain widths.

As discussed in the following chapter, the Au_2Sn surface alloy serves as the interface layer for the coverage regime between 0.33 ML and 0.66 ML. It guides the formation of complex Sn phases, such as an exotic square-like Sn arrangement and honeycomb stanene structures.

7 Higher Sn Coverages

In this chapter, the different structural arrangements of Sn observed at higher coverages between 0.33 ML and 0.66 ML are discussed. Three unique structural phases were identified and analyzed in detail: the X-phase with a local square-like Sn arrangement; the striped phase, featuring alternating stripes of square-like and honeycomb Sn arrangements that result in a nanoribbon structure; and the $\sqrt{7}$-phase, which is a stretched hexagonal structure. Before discussing the structural models for each of these phases in detail, this chapter begins with the structural and chemical evolution observed as a function of the Sn coverage.

The main results of this chapter were previously published in:

- J. A. Hochhaus et al., *Ultraflat honeycomb stanene nanoribbons on au(111)*, Advanced Materials Interfaces **12**, e00861 (2025)
- J. A. Hochhaus et al., *First evidence of a square-like Sn lattice on the Au_2Sn surface alloy on Au(111)*, Applied Surface Science **714**, 164470 (2025)

7.1 Structural and Chemical Evolution at Higher Coverages

Figure 7.1 displays the observed structural evolution after depositing 0.66 ML Sn on the clean Au(111) surface at room temperature and subsequently annealing the sample to the temperatures indicated. Before discussing the details of the different LEED patterns, it should be noted that the observed structural arrangement is not determined by the annealing temperature but rather by the Sn coverage. Annealing, however, is a precise method to reduce the Sn coverage by desorption until the desired structural phase is reached. The success of this controlled desorption approach likely stems from the specific activation energies required to break the bonds within stable structural arrangements. Furthermore, the thermal energy supplied during annealing promotes thermodynamic equilibrium, resulting in significantly better long-range order than can be achieved by direct Sn deposition at room temperature.

When ≈ 0.66 ML Sn is deposited on the clean Au(111) kept at room temperature or at slightly elevated temperatures (310 K), the so-called X-phase forms. This complex, spot-rich reconstruction was first reported by Maniraj et al. [43], who described their observation using the reconstruction matrix $\left(\begin{smallmatrix} 3.58 & 0 \\ 1.96 & 3.92 \end{smallmatrix}\right)$. They coined the name "X-phase" for the observed incommensurate LEED pattern, a term adopted in this thesis. Their description translates to a Rec(3.58 × 3.4) unit cell. Pang et al. [42] identified the X-phase as a compressed/stretched Rec($2 \times \sqrt{3}$)-reconstruction; precisely, they determined a square-like Rec(1.9 × 1.9) unit cell. As will be discussed in detail in Section 7.2, the X-phase was determined to be a Rec(7.7 × 3.85) unit cell, which consists of a

(4×2) arrangement of slightly distorted local square-like Rec(1.925×1.925) cells. The determined Rec(7.7×3.85) thereby closely matches twice the unit cell proposed by Maniraj et al., and is almost identical to the description by Pang et al. Besides, they never mention the long-range order observed and therefore can only explain the most pronounced LEED spots.

Reducing the Sn coverage to ≈ 0.55 ML by annealing the X-phase to ≈ 450 K leads to a structural phase with triangular and hexagonal superstructures as well as stripe-like features observed in the LEED pattern. The transition to this structural arrangement is irreversible; cooling the sample back to room temperature does not restore the X-phase. The structural model of this so-called striped phase is discussed in detail in Section 7.3. Desorbing more Sn by annealing to slightly higher temperatures (≈ 455 K) results in the formation of the $\sqrt{7}$-phase, described by the reconstruction matrix $\left(\begin{smallmatrix} 2 & 1 \\ 1 & 3 \end{smallmatrix}\right)$, which is a stretched $\sqrt{7} \times \sqrt{3}$ hexagonal structure. This structural arrangement was analyzed in detail by Maniraj et al. [43]. They described it as a stretched hexagonal arrangement of Sn-dimers. In addition, they observed linear dispersing bands below the Fermi level at the Γ-point with alternating spin polarization and a Fermi velocity of $v_F = 1 \times 10^6$ m/s, closely matching that of graphene. As Maniraj et al. already conducted a detailed structural analysis of the $\sqrt{7}$-phase, a short comparison of the STM and LEED results obtained in this thesis with their results is provided in Section 7.4.

When the sample is annealed above 480 K (coverage ≈ 0.35 ML), the characteristic $(\sqrt{3} \times \sqrt{3})$R30° LEED pattern of the Au_2Sn substitutional surface alloy, as described in Chapter 6, is formed. The long-range order of the Rec$(26 \times \sqrt{3})$-reconstruction of the Au_2Sn alloy is observed until annealing temperatures of ≈ 750 K. Above this temperature, the superstructure and long-range order start to degrade, and at ≈ 900 K, the Sn fully desorbs from the surface. As mentioned, the observed structural phases and transitions are coverage-dependent, and the annealing temperature is only used to desorb Sn in a controlled manner. All observed structural phases could be prepared directly by depositing the necessary amount of Sn onto the clean Au(111) surface. However, this often results in a mixture of structural phases or worse long-range order. Step-by-step preparation is also possible. The $\sqrt{7}$-phase, for example, can be obtained by preparing the X-phase, annealing to 450 K (striped phase), and then annealing to ≈ 455 K. It was noted that the Au_2Sn surface alloy serves as a universal starting point for preparing the other structural phases. For example, by depositing ≈ 0.3 ML on the preformed Au_2Sn surface alloy, the X-phase is obtained. No difference in behavior was observed between the Au_2Sn-alloy prepared by direct deposition of ≈ 0.33 ML or by annealing higher amounts of Sn.

In general, the preparation of the striped phase and the $\sqrt{7}$-phase is very challenging, as the required parameter window is narrow. The preparation method via annealing provides one decisive advantage over direct deposition: The chamber geometry allows live monitoring of the sample during annealing via LEED, enabling precise observation of structural transitions. Live monitoring via LEED, however, is not possible during Sn deposition.

XPS survey spectra of all structural phases described above were recorded and are shown in Figure 7.2. Besides analyzing the chemical composition, this allowed the determination

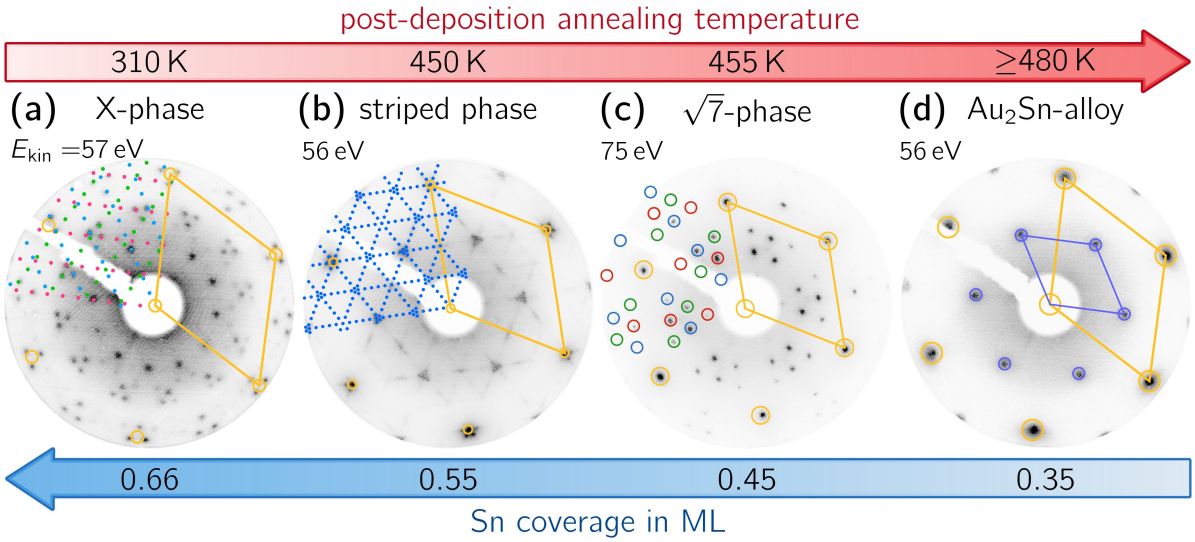

Figure 7.1: LEED patterns illustrating the structural evolution driven by post-deposition annealing to control Sn coverage. The Au(111) substrate unit cell and diffraction spots are marked in yellow. (a) The Rec(7.7 × 3.85)-reconstruction associated with the X-phase obtained after deposition of approximately 0.66 ML Sn on the surface kept at room temperature. (b) The LEED pattern of the striped phase. (c) The three unique subpatterns created by the rotational domains of the $\begin{pmatrix} 2 & 1 \\ 1 & 3 \end{pmatrix}$-reconstruction (also referred to as the $\sqrt{7}$-reconstruction). (d) The unit cell and $(\sqrt{3} \times \sqrt{3})$R30° pattern of the Au_2Sn surface alloy indicated in blue. Adapted from [46].

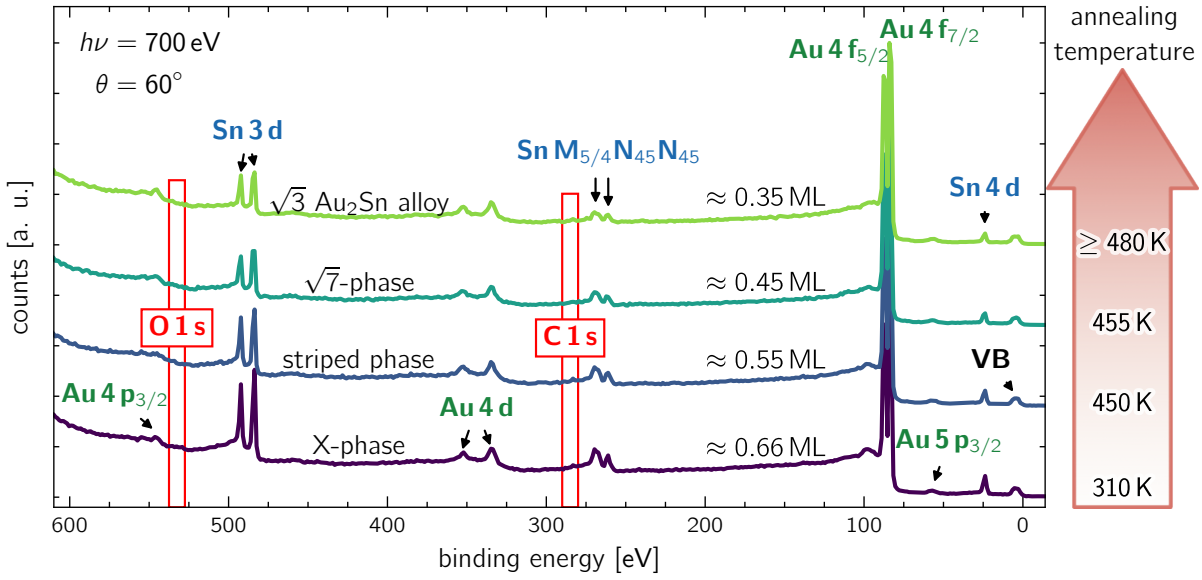

Figure 7.2: XPS survey spectra of the Sn phases in the coverage range of 0.33 ML to 0.66 ML, obtained via post-deposition annealing of 0.66 ML Sn. All spectra were recorded using a photon energy of $h\nu = 700$ eV and an emission angle of $\Theta = 60°$. Binding energies are referenced to the Fermi level. The reduction of the Sn signals with increasing post-deposition annealing temperature confirms the Sn coverage reduction via desorption of Sn. Modified after [46].

of the Sn coverage. Figure 7.2 shows survey spectra recorded with $h\nu = 700\,\mathrm{eV}$ at a grazing emission angle of $\Theta = 60°$. The spectra are stacked, starting with the X-phase (highest coverage) at the bottom. As marked by red boxes, signals of common contaminants like oxygen and carbon are absent. As clearly evident, with increasing annealing temperature, Sn-related features, e.g. the Sn $4d$ and Sn $3d$ signals, decrease. This behavior is reflected in the estimated Sn coverages: For the X-phase, a coverage of $(0.63 \pm 0.05)\,\mathrm{ML}$ was obtained, matching the QCM result ($(0.66 \pm 0.02)\,\mathrm{ML}$). For the Au_2Sn-alloy, $(0.33 \pm 0.03)\,\mathrm{ML}$ was obtained (QCM: $(0.33 \pm 0.02)\,\mathrm{ML}$). For the striped and $\sqrt{7}$-phases, which are best prepared by controlled desorption via sample annealing, the coverages were estimated via XPS to be $(0.55 \pm 0.02)\,\mathrm{ML}$ and $(0.46 \pm 0.03)\,\mathrm{ML}$, respectively.

Next, the chemical structure in the Sn layer and at the Au-Sn interface was analyzed using high-resolution XPS. Starting with the Sn $4d$ signal of the X-phase, shown in Figure 7.3(a), the best fit is achieved using a two-component Doniach-Šunjić doublet model. All fit parameters are given in Table 7.1. The dominating component (white) is observed at $E_{\mathrm{bin}} = 23.92\,\mathrm{eV}$, which is close to metallic Sn, while the second component (dark blue) is observed at $\approx 370\,\mathrm{meV}$ higher binding energy. Comparing the spectra recorded at normal and grazing emission, the higher binding energy component reduces by more than 33%, whereas the dominating component increases under grazing emission. Thus, the stacking order is determined as follows: The white component sits atop, while the dark blue component corresponds to the interface. It is identified as an Au_2Sn-alloy at the interface. It shifts to slightly higher binding energies ($\approx 90\,\mathrm{meV}$) compared to the respective component observed in the Sn $4d$ signal of the surface Au_2Sn-alloy, discussed in Chapter 6.

The observed shifts can be explained by the presence of the X-phase layer stacked above the Au_2Sn-alloy interface. As discussed, the simple electronegativity rule fails for Au-Sn alloys. The observed shifting to higher binding energies of the alloy component in the Au $4f$ signal is counterintuitive. However, as explained by Egelhoff [136], the expected shift to lower binding energies of the alloy component in the Au $4f$ signal, stemming from the Pauling electronegativity prediction of component shifting, is compensated and even inverted by intra-atomic charge transfer from the Au $5d$ to the $6s$ level. If the local atomic environment and bonding change, the alloy component in both the Au $4f$ and the Sn $4d$ signals may shift. This can be understood as follows: As will be discussed in Section 7.2, the Au_2Sn interface layer is likely stretched by approximately 11 % in the $[11\overline{2}]$-direction compared to the substitutional alloy. This results in a decreased packing density of the Au_2Sn-layer, effectively reducing the screening of the core by valence electrons (again for both, the Au $4f$ and the Sn $4d$ signal), leading to stronger binding of core electrons. A second argument considers the local environment: With increased Sn coverage, the local environment of each Au atom becomes Sn-richer. Considering that the 1:1 distribution of Au to Sn in the top two layers (of the X-phase) represents an increase in Sn contribution compared to the 2:1 distribution in the Au_2Sn-alloy, it is plausible that the higher Sn concentration enhances the Au $5d$ to the $6s$ intra-atomic charge transfer. This could explain the observed shift to even higher binding energies of the alloy component in the Au $4f$ signal (compare Figure 7.4(a)) as well as the observed shift of the Au_2Sn interface alloy component in the Sn $4d$ signal.

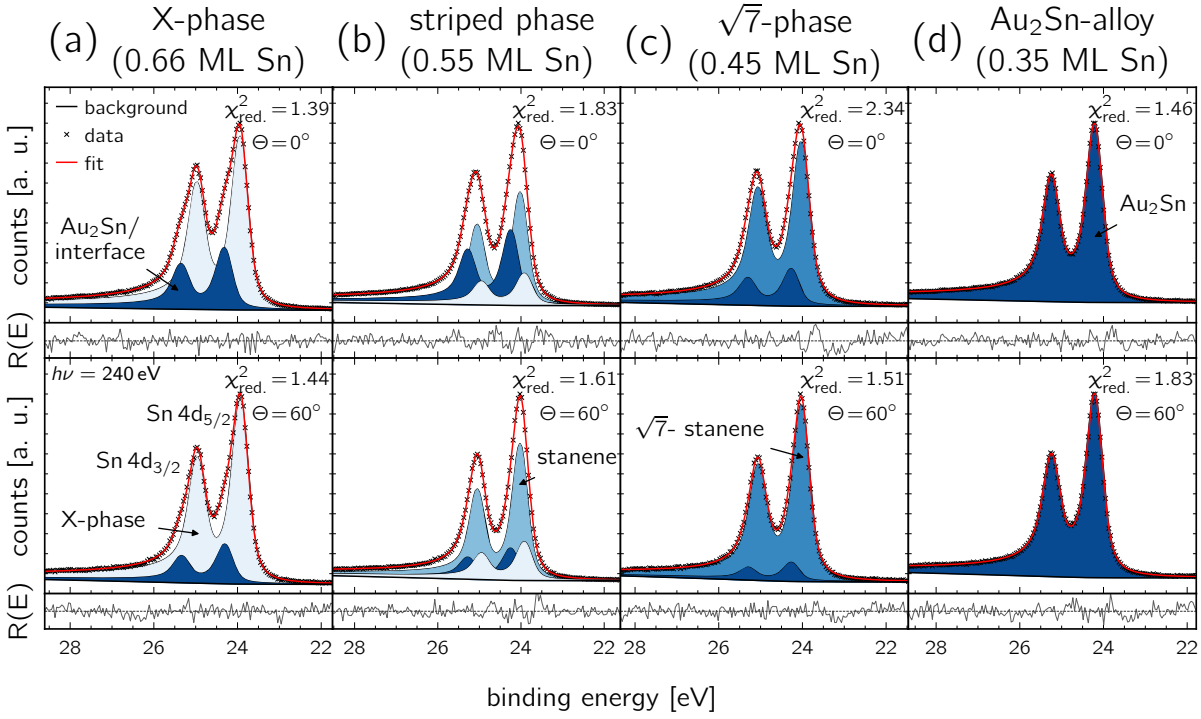

Figure 7.3: High-resolution XPS spectra of the Sn 4*d* core level, used to investigate the internal chemical composition of the topmost Sn layer(s) for coverages between 0.33 ML and 0.66 ML Sn. Recorded at a photon energy of $h\nu = 240\,\text{eV}$ with emission angles of $\Theta = 0°$ (top row) and $\Theta = 60°$ (bottom row). The corresponding fit parameters are listed in Table 7.1. Adapted from [46].

Table 7.1: Fit parameters from the XPS analysis of the chemical evolution of the Sn $4d$ signal shown in Figure 7.3. The statistical fit error for the reported binding energies is typically well below 10 meV. Reprinted from [46].

Structural phase	Θ (°)	Component	E_{bin} (eV)	E_{SOC} (eV)	FWHM (eV)	asymmetry β	rel. area (%)
X-phase Figure 7.3(a)	0	X-Phase	23.92	1.04	0.48	0.12	73.88
		Au_2 Sn	24.29	1.04	0.48	0.12	26.12
	60	X-Phase	23.91	1.04	0.48	0.12	82.39
		Au_2 Sn	24.28	1.04	0.48	0.12	17.61
striped phase Figure 7.3(b)	0	X-Phase	23.92	1.04	0.47	0.12	15.44
		Au_2 Sn	24.25	1.04	0.47	0.12	36.10
		stanene	24.02	1.04	0.44	0.09	48.46
	60	X-Phase	23.91	1.03	0.47	0.12	20.16
		Au_2 Sn	24.25	1.03	0.47	0.12	16.60
		stanene	24.02	1.03	0.44	0.09	63.25
$\sqrt{7}$ phase Figure 7.3(c)	0	Au_2 Sn	24.25	1.04	0.47	0.12	18.03
		$\sqrt{7}$-stanene	24.01	1.04	0.49	0.10	81.97
	60	Au_2 Sn	24.25	1.03	0.47	0.11	9.67
		$\sqrt{7}$-stanene	24.01	1.03	0.48	0.09	90.33
Au_2 Sn-alloy Figure 7.3(d)	0	Au_2 Sn	24.19	1.04	0.49	0.11	100.00
	60	Au_2 Sn	24.19	1.03	0.49	0.11	100.00

Comparing the Sn $4d$ fits of the X-phase with literature, they agree well with the two-component model reported by Sadhukhan et al. [41]. However, their fit of the Au $4f$ signal uses only two components, which disagrees with the analysis presented below. Moreover, their assignment of the X-phase to an AuSn-alloy contradicts in some aspects the structural model presented in Section 7.2. In contrast, Pang et al. [42] applied a three-component model. While their approach yields a reasonable fit, the third component contributes only about 4% to the total peak area. Given this small contribution, the two-component model provides a more straightforward yet equally robust description, especially because it agrees well with the structural model derived from atomically resolved STM measurements.

Turning to the striped phase, three components are identified. While components matching the X-phase and the Au_2Sn interface are still present, the spectrum is now dominated by a new component, plotted in light blue at $E_{\mathrm{bin}} = 24.02$ eV, which is assigned to the honeycomb arrangement of Sn (detailed in Section 7.3). In the following, this component will therefore be referred to as the stanene component. The Au_2Sn-interface component is observed at a slightly lower binding energy compared to the X-phase. This can be explained by the reduced Sn coverage, which reverses some of the effects discussed above.

The stanene component is shifted by about 230 meV towards lower binding energies relative to the Au_2Sn interface component. A similar behavior was reported for atomically flat honeycomb stanene on Ag_2Sn/Ag(111) [25]. While other components exhibit a FWHM of ≈ 480 meV and $\beta = 0.12$, the stanene component exhibits a significantly reduced asymmetry of $\beta = 0.09$ and narrower FWHM of ≈ 440 meV. The reduced asymmetry indicates a less metallic character [293, 294] and points to predominant sp^2 bonding rather than the sp^2/sp^3 hybridization of freestanding stanene [17]. As evident from STM, an atomically flat honeycomb structure is observed, which likely favors sp^2

bonding due to the lack of buckling. Similar to the (2×2) component, the binding energy of the stanene component ($\approx 24.02\,\mathrm{eV}$) closely matches bulk tin values [282–284].

While the Au_2Sn-component decreases significantly under grazing emission, the X-phase and stanene components increase. In addition, the ratio of the stanene component area to that of the X-phase remains roughly constant at 3.1:1 for both emission angles. Due to their similar angular dependence, the X-phase and stanene components must originate from the same stacking layer (the topmost surface layer). As will be shown in Section 7.3, the surface unit cell contains 34 Sn atoms: 8 in a square-like configuration and 26 in a honeycomb structure. This yields an atomic ratio of 3.25:1, which is in excellent agreement with the measured XPS area ratio of 3.1:1.

For the $\sqrt{7}$-phase (Figure 7.3(c)), the best fit is achieved using a two-component model. A small Au_2Sn component is identified, but the spectrum is mainly dominated by the second component, fitted with parameters very similar to the stanene component of the striped phase. As this phase corresponds to a stretched dimer hexagonal structure with exotic electronic properties, it is referred to as $\sqrt{7}$-stanene [43]. Remarkably, the stanene component in the striped phase and the $\sqrt{7}$-stanene component are indistinguishable by XPS alone; only structural analysis reveals their distinct origins. Comparing the structural models, only a stretch of approximately 15 % along $[11\bar{2}]$ is needed to transform the honeycomb arrangement into the $\sqrt{7}$-phase (which is a stretched hexagonal Sn-dimer arrangement, in Section 7.4, more details are found). While the Lorentzian contribution to the FWHM of the Au_2Sn component is $\Gamma_\mathrm{L} \approx 260\,\mathrm{meV}$, an increased Lorentzian contribution ($\Gamma_\mathrm{L} \approx 310\,\mathrm{meV}$) is observed for the $\sqrt{7}$-stanene, yielding core-hole lifetimes of $\tau \approx 2.5\,\mathrm{fs}$ and $\tau \approx 2.1\,\mathrm{fs}$, respectively. However, both values match typical values given for Sn and Sn-alloy components given in the literature [295, 296]. The small Au_2Sn-alloy component needed to fit the spectrum could be explained by either residual regions of the striped phase or the onset of $\sqrt{3}$-phase formation, as the parameter window for preparing the $\sqrt{7}$-phase is narrow. As discussed in Section 7.4 and shown in Figure 7.23, both types of mixed phases are observed in the experimental data.

As shown in Figure 7.3(d), when the sample is annealed above 480 K ($\approx 0.35\,\mathrm{ML}$), the spectrum can be fitted with a single component, identified as Au_2Sn-component, with fit parameters in perfect agreement with the substitutional alloy discussed in Chapter 6.

Turning to the analysis of the Au-Sn interface, the evolution of the Au $4f$ signal is presented in Figure 7.4, with the fit parameter being presented in Table 7.2. Starting with the X-phase, the fit consists of three components: bulk ($E_\mathrm{bin} = 84.00\,\mathrm{eV}$), interface ($E_\mathrm{bin} = 84.30\,\mathrm{eV}$), and X-phase ($E_\mathrm{bin} \approx 84.62\,\mathrm{eV}$). The interface component is identified as similar to the Au_2Sn substitutional alloy but shifted by $\approx 100\,\mathrm{meV}$ to higher binding energy likely due to the higher effective Sn concentration from the X-phase layer above, as already discussed in the analysis of the Sn $4d$ signal. Applying a two-component model (like Sadhukhan et al. did) required FWHMs larger by 25 % than clean Au(111) and shifted the bulk component by $\approx 60\,\mathrm{meV}$. Additionally, their assignment of the X-phase to a two-layer AuSn system does not match either the STM data or the angular-resolved XPS data presented here. Applying the four-component model of Pang et al. generates a reasonable fit, but their fourth component contributes only 2 %. Combining the results from Sadhukhan et al., regarding their reported Au_XSn shifts [41, 54], with

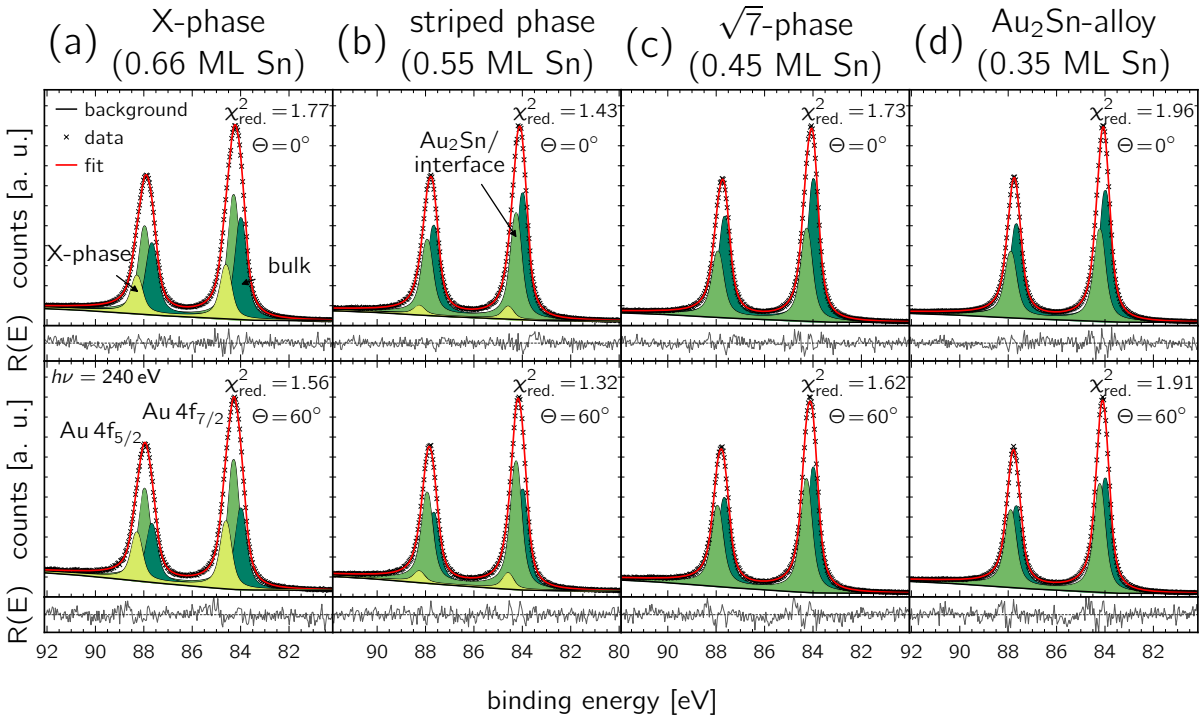

Figure 7.4: High-resolution XPS spectra of the Au $4f$ core level used to analyze the interface structure of the different Sn phases observed for coverages between 0.33 ML and 0.66 ML Sn. Recorded at a photon energy of $h\nu = 240\,\mathrm{eV}$ with emission angles of $\Theta = 0°$ (top row) and $\Theta = 60°$ (bottom row). Fit parameters corresponding to these spectra are provided in Table 7.2. Reproduced from [46].

Table 7.2: XPS analysis fit parameters to the chemical evolution of the Au $4f$ signal shown in Figure 7.4. The statistical fit error for the reported binding energies is typically well below 10 meV. Reprinted from [46].

Structural phase	Θ (°)	Component	E_{bin} (eV)	E_{SOC} (eV)	FWHM (eV)	asymmetry β	rel. area (%)
X-phase figure 7.4(a)	0	bulk	84.00	3.68	0.54	0.03	36.32
		interface	84.30	3.68	0.54	0.03	44.40
		X-phase	84.62	3.68	0.54	0.03	19.28
	60	bulk	84.00	3.68	0.54	0.03	29.24
		interface	84.30	3.68	0.54	0.03	46.54
		X-phase	84.62	3.68	0.54	0.03	24.22
striped phase figure 7.4(b)	0	bulk	84.00	3.67	0.53	0.03	51.49
		interface	84.27	3.67	0.53	0.03	43.26
		X-Phase	84.59	3.67	0.53	0.03	5.25
	60	bulk	84.00	3.67	0.53	0.04	41.05
		interface	84.27	3.67	0.53	0.04	52.42
		X-Phase	84.59	3.67	0.53	0.04	6.53
$\sqrt{7}$ phase figure 7.4(c)	0	bulk	83.99	3.67	0.54	0.03	60.61
		interface	84.27	3.67	0.54	0.03	39.39
	60	bulk	84.00	3.67	0.54	0.03	52.53
		interface	84.28	3.67	0.54	0.03	47.47
Au_2 Sn-alloy figure 7.4(d)	0	bulk	84.00	3.68	0.54	0.03	58.66
		Au_2 Sn	84.23	3.68	0.54	0.03	41.34
	60	bulk	84.00	3.68	0.53	0.03	51.31
		Au_2 Sn	84.23	3.68	0.53	0.03	48.69

the data presented here allows the following conclusion: The packing density in the two topmost layers corresponds to a 1:1 Au:Sn ratio, where Au atoms in the Au_2Sn interface alloy experience a local environment similar to a AuSn alloy, as the Au_2Sn interface is covered by the X-phase Sn layer. Therefore, the Au_2Sn/interface component of the X-phase is actually measured closer to the expected binding energies observed for an AuSn alloy, which explains the proposed explanation of the X-phase being an AuSn alloy by Sadhukhan et al. [41].

For the striped phase, the same components are observed, but the X-phase component contribution is significantly reduced. Combined with the observed reduction of the Au_2Sn interface component, this indicates dealloying during the structural transition from X-phase to striped phase. In the X-phase, the square-like layer grows atop a Au_2Sn interface. During the structural transformation to the striped phase, stripes of honeycomb Sn (growing directly on Au(111)) alternate with remaining X-phase regions (still atop Au_2Sn). Since the honeycomb arrangement requires a higher Sn packing density, the surplus Sn likely originates from the dealloying of the Au_2Sn interface. Vice versa, the transition from striped to X-phase results from the Sn packing density becoming too large for a single layer, favoring two-layer growth.

Heading to the $\sqrt{7}$-phase (Figure 7.4(c)), the fit is virtually identical to the striped phase, with the exception that the X-phase component has now entirely vanished. This indicates that the Au-Sn bonding at the interface is very similar between the stanene honeycomb-arrangement of the striped phase and the $\sqrt{7}$-stanene. For both arrangements, an atomically flat Sn arrangement is observed with the Sn sitting at identical adsorption sites (compare Section 7.3 and 7.4).

Finally, analyzing the Au_2Sn-alloy phase, shown in Figure 7.4(d) obtained after annealing the sample above 480 K yields a similar fit to that of the substitutional alloy obtained after depositing 0.33 ML at room temperature (see Chapter 6). Comparing the details, the Au_2Sn component is observed at a slightly higher binding energy of $E_{\text{bin}} = 84.23\,\text{eV}$ compared to the room-temperature preparation.

It was observed, that annealing the sample at 480 K initiates the structural transition from the $\sqrt{7}$-phase to the $(\sqrt{3} \times \sqrt{3})$R30°-reconstruction observed in LEED. However, only annealing at 480 K does not fully remove the $\sqrt{7}$-stanene component contribution from the Sn $4d$ core-level spectrum. The spectra presented here were measured after annealing to $\approx 650\,\text{K}$, which is precisely the annealing temperature needed to remove the $\sqrt{7}$-stanene component contribution completely from the Sn $4d$ signal. In the Au $4f$ signal, the binding energy of the Au_2Sn-alloy component appears at $E_{\text{bin}} = 84.23\,\text{eV}$ (after annealing to $\approx 650\,\text{K}$). It gradually shifts toward this value as the $\sqrt{7}$-stanene contribution decreases with increasing annealing temperature. Annealing to $\approx 750\,\text{K}$ finally yields the binding energy observed for the Au_2Sn room-temperature preparation of $E_{\text{bin}} = 84.20\,\text{eV}$. Notably, in the annealing temperature range of 480 K to 750 K, the Sn coverage, determined using XPS, is only slightly reduced, going from (0.33 ± 0.03) ML to (0.31 ± 0.02) ML, which is, however, within the margin of error.

The similarity of the interface component observed for the striped and $\sqrt{7}$-phases to the Au_2Sn alloy phase can be understood as follows: Au atoms at the interface experience a similar local Sn environment when covered by the honeycomb or $\sqrt{7}$-stanene, as in both cases the atomic ratio of Au:Sn is $\approx 2:1$, matching the Au_2Sn-alloy. Considering the complex electronic behavior of Au-Sn compounds [136], the interface Au atoms likely experience similar hybridization and inter-atomic charge transfer.

Overall, the observed chemical evolution can be summarized as follows: Starting with the two-layer system of the X-phase (consisting of the Au_2Sn alloy interface and the square-like Sn arrangement), annealing leads to partial dealloying and the formation of the striped phase. This phase features alternating regions similar to the X-phase and regions where a honeycomb stanene arrangement sits directly atop the Au(111) surface. Further annealing continues the dealloying, leading to the formation of the Sn-dimer hexagonal arrangement of the $\sqrt{7}$-phase, directly atop the Au(111) surface. Finally, further annealing leads to realloying and the formation of the substitutional Au_2Sn surface alloy.

Alternatively, the sequence can be viewed with Sn coverage as the driving factor: Starting from the substitutional surface alloy, increasing the coverage to 0.45 ML leads to dealloying, as the $\sqrt{7}$ arrangement becomes energetically favorable. Further increasing the coverage to 0.55 ML starts the realloying, as the Sn packing density becomes too high for a single atomic layer. Increasing the coverage to 0.66 ML further drives the realloying process, resulting in two-layered growth with the formation of the square-like X-phase atop the Au_2Sn interface alloy. Increasing the film thickness to 1.33 ML does not significantly alter the X-phase LEED pattern, likely indicating that multi-layer growth of the square-like arrangement begins, showing similarities to the bcc β-Sn allotrope. Notably, monolayers of the α-Sn allotrope would correspond to a honeycomb stanene

phase, but its thermal instability limits multilayer growth at room temperature [20, 21]. However, Sn coverages above 0.66 ML were not analyzed in detail in this thesis.

7.1.1 Valence band analysis

In addition to the core-level analysis, the valence band evolution across the different structural phases was observed as shown in Figure 7.5(a). Since Features A to E were already discussed for clean Au(111) in Chapter 5, the following discussion focuses on the changes observed during the structural evolution of the Sn phases. Upon formation of the Au_2Sn surface alloy, all features (except C) shift by approximately 200 meV to higher binding energies with respect to clean Au(111), and the Shockley surface state S completely vanishes. Progressing to higher Sn coverages in the $\sqrt{7}$-phase and the striped phase, Feature E becomes less pronounced, while all other features shift slightly further to higher binding energies (except Feature C, which remains constant). Features A and B weaken in the Au_2Sn and $\sqrt{7}$-phases. In the subsequent striped and X-phase, the intensity of Feature B recovers, while Feature A continues to vanish.

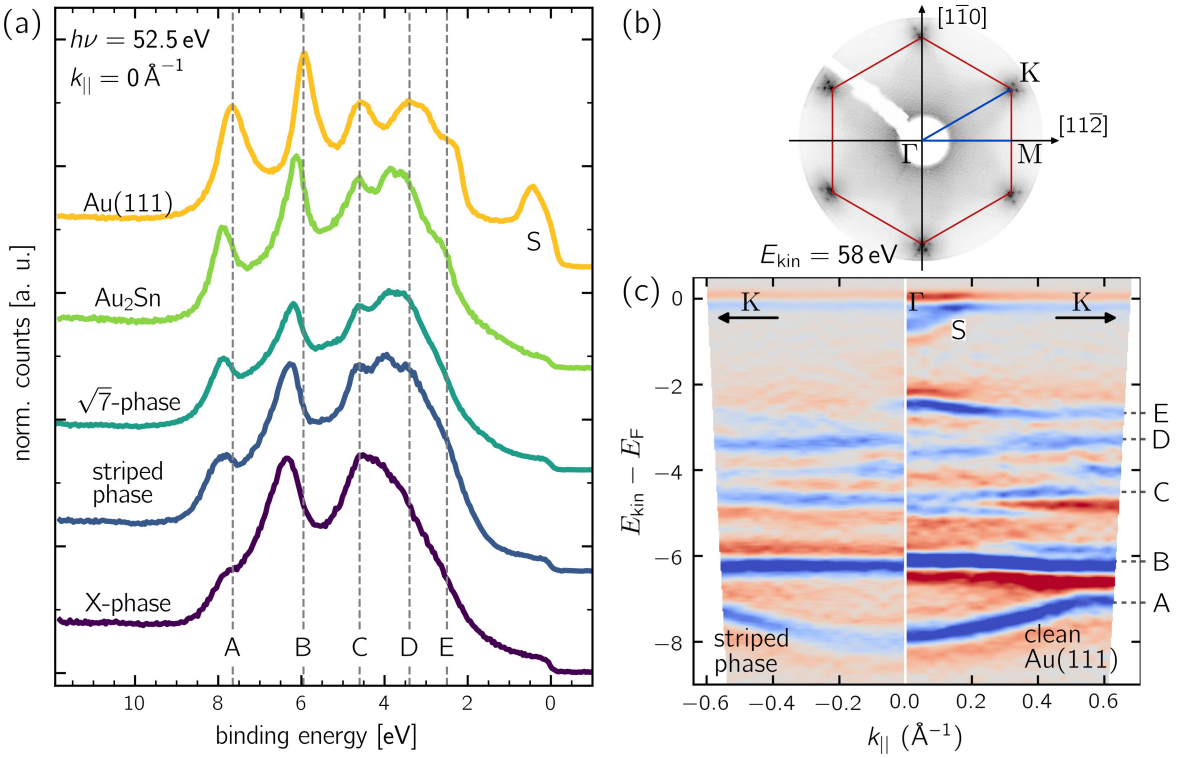

Figure 7.5: (a) Comparison of the valence band spectra of clean Au(111) and the different structural phases observed at Sn coverages between 0.33 ML and 0.66 ML, recorded at $h\nu = 52.5$ eV under normal emission (at Γ). The dashed lines labeled **A**–**E** correspond to the band maxima identified for the clean Au(111), while the surface state is labeled **S**. (b) Symmetry points of the Brillouin zone marked in a LEED image. (c) Band structures along $\Gamma - K$ of the clean Au(111) and the striped phase plotted for comparison. Subfigure (a) reprinted from [46].

In the valence band region of $E_{\text{bin}} = 2\,\text{eV}$ to $5\,\text{eV}$, a new feature appears to arise at $E_{\text{bin}} \approx 4\,\text{eV}$ for the striped phase. Figure 7.5(c) presents a side-by-side comparison of the valence band structure of clean Au(111) and the striped phase along $\Gamma - K$. The most evident change here is the shift of the two deep valence band features A and B ($E_{\text{bin}} = 6\,\text{eV}$ to $8\,\text{eV}$) to higher binding energies by $\approx 200\,\text{meV}$ in the striped phase. Feature B appears to flatten out, and the splitting into two distinct bands observed for clean Au(111) around $\left|k_{||}\right| \approx 0.5/\text{Å}$ is not visible. Instead, a new, weak feature appears at $E_{\text{bin}} \approx 5.3\,\text{eV}$, between the positions of Features B and C.

The most significant differences occur in the region $E_{\text{bin}} = 2\,\text{eV}$ to $5\,\text{eV}$. While both spectra show Feature C at $\approx 4.6\,\text{eV}$, the splitting into two distinct bands away from Γ is only observed for clean Au(111). Additionally, Feature E ($\approx 2.5\,\text{eV}$) is highly suppressed in the striped phase. Feature D ($\approx 3.4\,\text{eV}$) shows complex behavior in the striped phase; it appears to split into two bands when going away from Γ. The new band feature observed shifts toward lower binding energies as $\left|k_{||}\right|$ increases.

Returning to Figure 7.5(a), for the X-phase no distinct features are observed between $E_{\text{bin}} = 2\,\text{eV}$ to $5\,\text{eV}$, besides one very broad feature indicating strong band hybridization. Feature A appears only as a shoulder on the high-binding-energy side ($E_{\text{bin}} \approx 7.9\,\text{eV}$), and the heavily shifted Feature B ($E_{\text{bin}} \approx 6.3\,\text{eV}$) is observed.

Considering that the IMFP of photoelectrons with $E_{\text{kin}} \approx 40\,\text{eV}$ is $\approx 5\,\text{Å}$ (which is approximately two atomic layers), the suppression of certain features likely indicates that they are originating from the bulk gold. Consequently, this allows assigning features dominating the spectrum at higher Sn coverages (specifically Features B and C/D) to the interface and surface regions. These observations, consistent with the XPS results, confirm the presence of chemical bonding between Au and Sn for all phases. In general, the strong modification of features between $E_{\text{bin}} = 2\,\text{eV}$ to $5\,\text{eV}$ matches the general behavior of Au-Sn alloying [54, 286].

Calculations from theory of crystalline Au-Sn-alloys predicts high densities of states (DOS) near $E_{\text{bin}} \approx 4\,\text{eV}$, attributed to hybridization between Au d-orbitals and Sn p/s-orbitals [297]. The dominant presence of Feature B likely arises from hybridization between Au d and Sn s states [298, 299]. While freestanding stanene is assumed to be heavily buckled and sp^2/sp^3 hybridized, the experimental observation of atomically flat arrangements, as in the $\sqrt{7}$ and the honeycomb region of the striped phase, suggests a different intra-and interlayer bonding and hybridization. The hybridization of Au d states with Sn s/p states likely favors the formation of flat, sp^2-like Sn arrangements, a hypothesis supported by the reduced asymmetry β observed for the corresponding component in the XPS Sn $4d$ signal [293, 294].

Although the goal in 2D material preparation is often to reduce adsorbate-substrate interaction to create freestanding structures, a stronger interaction appears necessary in the case of Sn on Au(111) to stabilize the atomically flat honeycomb arrangement. Furthermore, linear dispersion features measured for the $\sqrt{7}$-phase confirm this significant substrate interaction [41, 43].

7.2 X-Phase

Having established the chemical and structural evolution of Sn on Au(111) in the coverage range of 0.33 ML to 0.66 ML, the following sections will focus on discussing the structural models, starting here with the X-phase, which is formed if 0.66 ML is deposited on the Au(111) surface at room temperature. Combining LEED and STM, the structural model of the X-phase will be derived. The results from this section were previously published in [47].

The analysis of the LEED pattern of the X-phase (Figure 7.6(a)) starts with the assumption of a square Rec(1.925 × 1.925) unit cell; this closely matches the one proposed by Pang et al. [42]. However, comparing the overlaid LEEDPat simulation (marked by black circles) reveals that while the assumed periodicity well explains some spots, it cannot account for all observed diffraction spots. Doubling the periodicity to a Rec(3.85 × 3.85) unit cell (Subfigure (b), blue circles) accounts for most of the dominant spots that were not matched by the Rec(1.925 × 1.925).

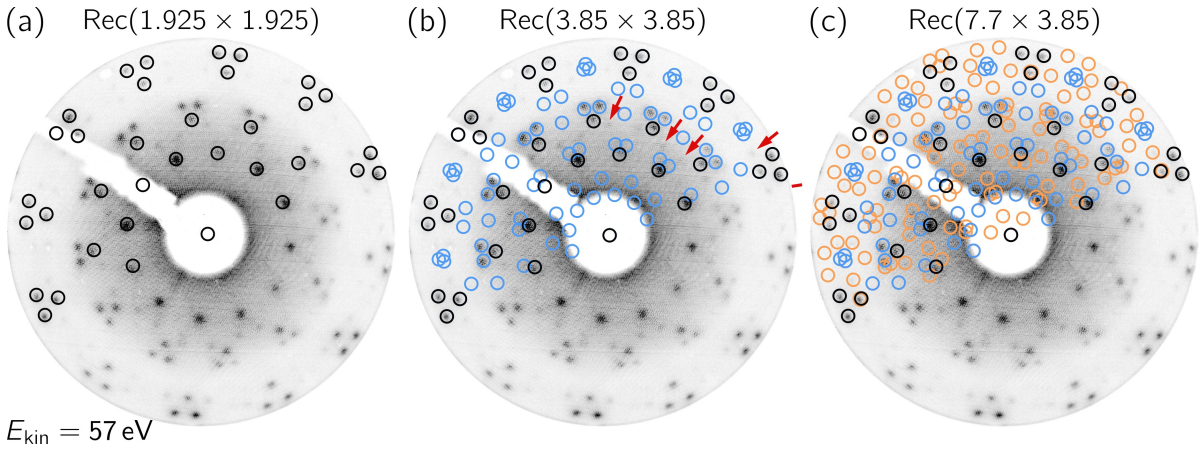

Figure 7.6: Analysis of the LEED diffraction pattern of the X-phase. Black circles indicate the diffraction spots of a Rec(1.925 × 1.925) reconstruction. As shown in (a), the Rec(1.925 × 1.925) cannot explain all observed spots. Doubling the size of the unit cell to a Rec(3.85 × 3.85) (additional spots marked in blue in (b)) already matches most of the spots. As marked by red arrows, some faint spots are still not reproduced; they could be described by a Rec(7.7 × 3.85) unit cell, with the additional expected spot positions marked orange in (c). Reproduced after [47].

However, as indicated by the red arrows, some faint spots remain unexplained. Only a Rec(7.7 × 3.85) unit cell, with the additional spots marked in orange, can describe all observed spots in the experimental LEED pattern. To further confirm that the Rec(7.7 × 3.85) unit cell indeed captures the observed periodicity, Figure 7.7 shows a zoomed region of the details of the LEED pattern. In addition, the zoomed-in LEED pattern is shown with a LEEDPat simulation of the same region for comparison.

As a next step, STM data was recorded to analyse the structure of the X-phase in real space. Figure 7.8(a) presents a large area scan of the clean Au(111) surface, showing the herringbone reconstruction. In (b), a large area scan of the X-phase, typically showing

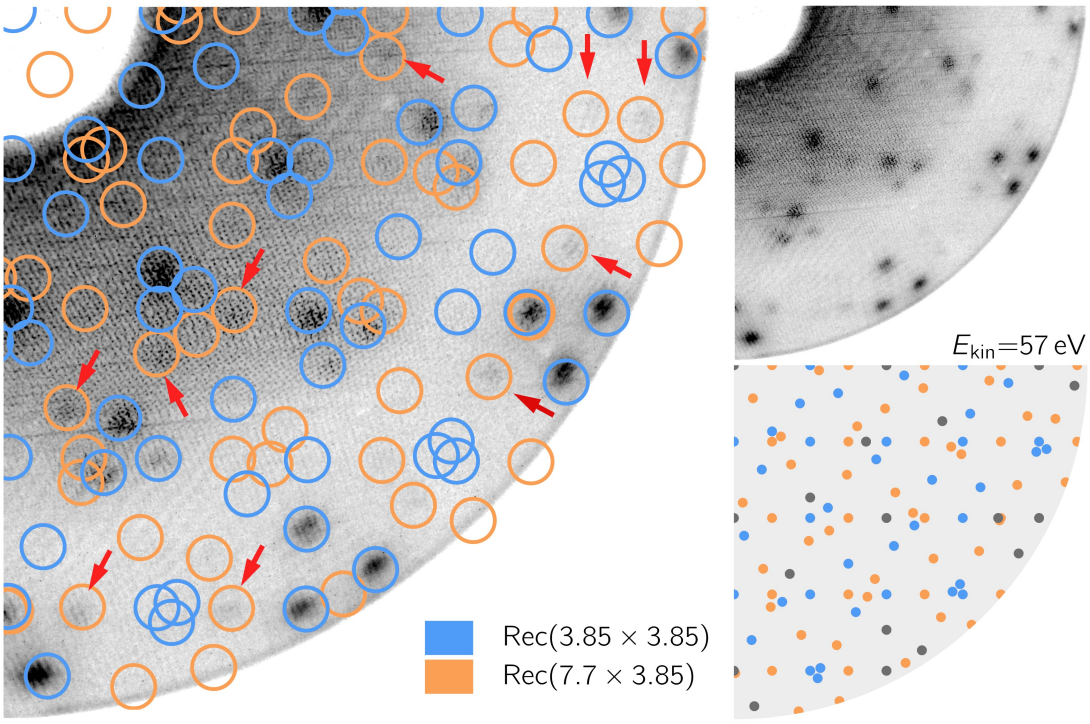

Figure 7.7: Details of the LEED pattern of the X-phase. In the left panel, some of the most pronounced spots corresponding to the Rec(7.7 × 3.85) unit cell are marked by red arrows. In addition, the simulated LEED pattern [238] and the measured LEED pattern without the overlay are shown on the right. In the simulated pattern, white circles correspond to the Rec(1.925 × 1.925), while blue and orange circles represent the additional spots stemming from the Rec(3.85 × 3.85) and Rec(7.7 × 3.85), respectively. Reprinted from [47].

planar terrace growth with islands atop, is observed, which matches the growth behaviour of Sn on Au(111) observed in the literature [42, 43]. Line profiles were extracted from both STM images, which are shown in Figure 7.8(c). Both islands and step heights of the X-phase were measured at (2.6 ± 0.1) Å, which is higher than step heights measured on the clean Au(111). However, after Sn deposition, clean Au(111) steps are no longer observed; therefore, the STM cannot be height-calibrated using the gold step height. For Sn on Al(111), it has been reported that differing step heights are measured, depending on the tunneling voltage [36], however, to analyze such a behaviour, a clean Au(111) step is necessary for comparison to check the STM height-calibration. It was noted that the STM tip strongly influences the sample's morphology, often displacing small islands and altering the structure at step edges. This indicates that the topmost Sn layer of the X-phase is only weakly bound to the substrate. In the Appendix in Section F, continuously scanned STM images of the same region are presented, showing the influence of the STM tip on the sample's morphology.

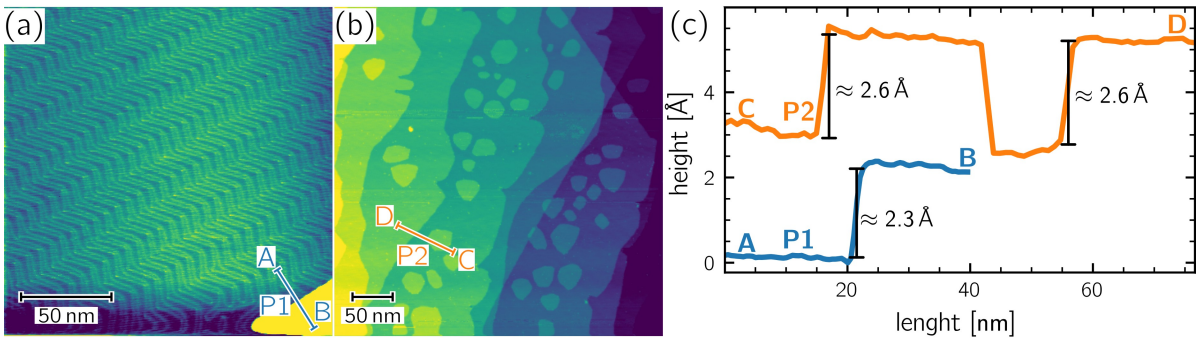

Figure 7.8: Comparison of large-scale STM images of the bare Au(111) surface in a well-ordered herringbone reconstruction, shown in (a) and after the deposition of 0.66 ML of Sn, depicted in (b). The STM images were measured at $U = 1.15$ V and $I = 102$ pA (a) and $U = 40$ mV and $I = 1$ nA (b). In (c), the profiles of the lines at step edges marked in (a) and (b) are plotted. Adapted from [47].

To analyze the local atomic arrangement of Sn in the X-phase, high-resolution STM images (Figure 7.9 and Figure 7.10) were used. A local, square-like Sn-arrangement is observed. Extracting line profiles of the STM image in Figure 7.9(a), shown in Figure 7.9(b), allowed the determination of an average next-neighbour distance of (5.5 ± 0.3) Å for the square-like structure. This matches a Rec(1.925×1.925) with respect to the Au(111) surface, as $1.925 \cdot a_{\mathrm{Au}} \approx 5.55$ Å. The line profiles confirm the periodic atomic arrangement along both the $[1\bar{1}0]$ and the $[11\bar{2}]$ direction. The FFTs of the STM image (Figure 7.9(c) and (d)) again show a higher periodicity, similar to the LEED pattern, beside the Rec(1.925×1.925) square-like unit cell marked by white circles. Some spots corresponding to the Rec(3.85×3.85), as well as two spots close to the center corresponding to the Rec(7.7×3.85), are observed, matching the periodicity obtained from LEED. The difference in the appearance of the FFT compared to the LEED pattern is explained by the LEED averaging over the three rotational domains of the X-phase. In contrast, in the Fourier-transformed STM frame, only one domain is present.

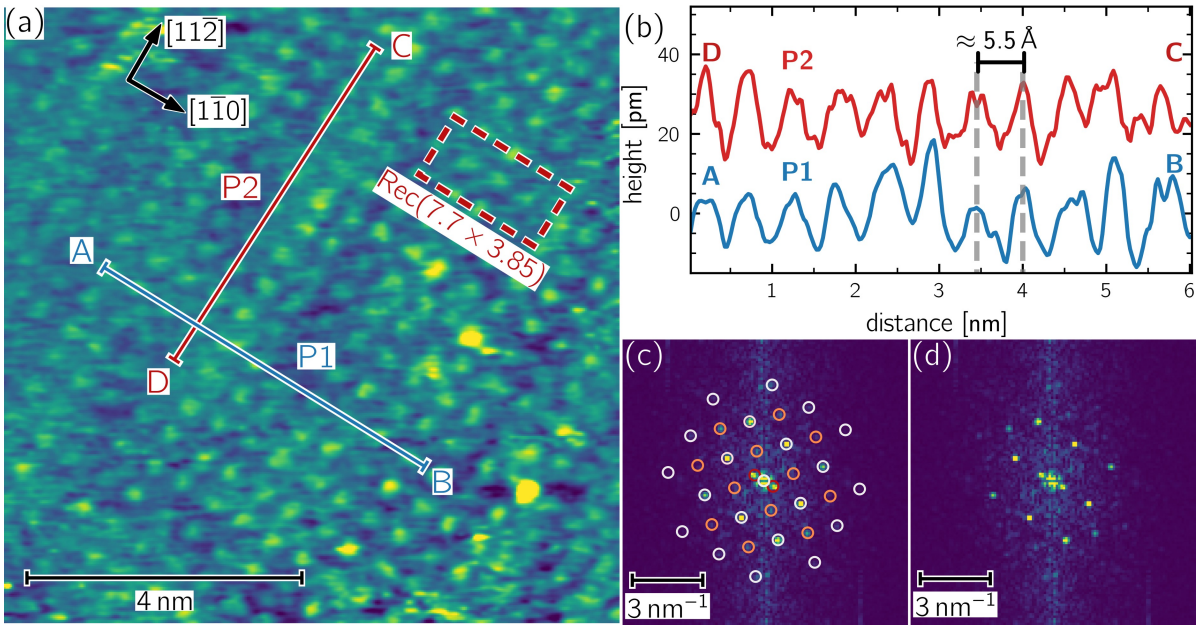

Figure 7.9: Shown in (a) is an atomically resolved STM image of the X-phase, showing a local square arrangement of Sn atoms, measured at $U = 3\,\mathrm{mV}$ and $I = 325\,\mathrm{pA}$. Corresponding line profiles are plotted in (b). (c) and (d) depict identical FFTs of the STM image in (a). In (c), the reconstruction pattern of one domain of the Rec(7.7 × 3.85) is depicted as circles atop the FFT. White circles match a Rec(1.925 × 1.925)-reconstruction, orange circles correspond to the higher-order Rec(3.85 × 3.85) spots, and the red circles, near the center, only match the Rec(7.7 × 3.85)-reconstruction. Reproduced after [47].

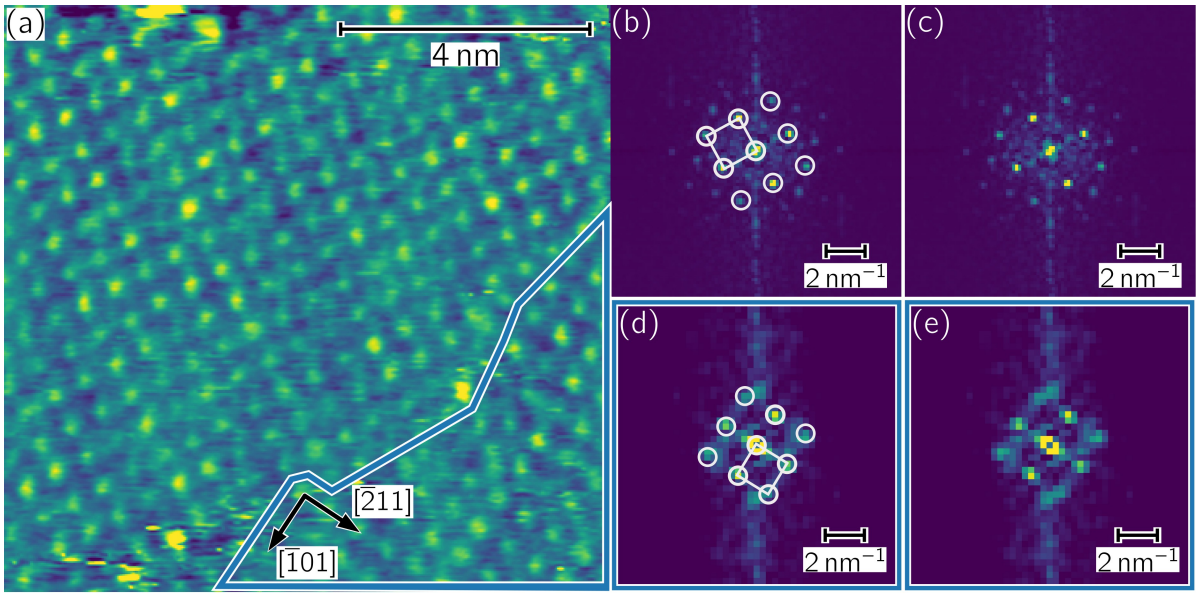

Figure 7.10: Two domains of the X-phase measured on the same terrace. The STM image in (a) was recorded with $U = 3\,\mathrm{mV}$ and $I = 325\,\mathrm{pA}$. In the bottom right corner, a second, rotated domain is marked. FFTs are shown in (b)/(c) and (d)/(e) for the two different domains. White circles in (b) and (d) mark the intensity maxima corresponding to the local Rec(1.925 × 1.925) square-like lattice. The FFTs confirm that the two domains are rotated by 120° to each other. Reprinted from [47].

In Figure 7.10(a), an STM frame showing two of the three rotational domains of the X-phase is presented. As evident from the FFTs calculated for both domains separately, shown in Figure 7.10(b)-(e), the two domains are rotated by 120° to each other, which matches the rotational symmetry of the Au(111) substrate. Especially in the FFTs of the larger domain, shown in (b) and (c), the higher-order periodicities are evident, as the observed spot pattern could not be fully explained by the Rec(1.925×1.925) marked in white.

As the higher-order periodicity is visible in the FFTs as well as in the LEED pattern, there has to be a periodic modulation in the topmost, square-like arranged Sn layer, which is not easily detectable by eye. Therefore, a total of 58 line profiles along the $[1\bar{1}0]$-axis and 45 line profiles along the $[11\bar{2}]$-axis were extracted and analyzed for variations in their next-neighbour distances, primarily focusing on periodic patterns which could match the (4×2) periodicity of the local Rec(1.925×1.925), resulting in the Rec(7.7×3.85) observed in LEED. In the extracted line profiles, maxima and minima were fitted within each line profile, and the next-neighbour distances were extracted. Then, a four-fold periodicity of the form $ABCDABCD...$ was assumed; the resulting extracted next-neighbour distances are given in Table 7.3. A distinct structural modulation is found.

Table 7.3: Analysis of lattice variations of the square-like Sn lattice. Each obtained maximum in the line profile was fitted using a Gaussian profile to determine the atoms' site and respective next-neighbour distances. The given uncertainty results from averaging the determined respective next-neighbour distances. Reprinted from [47].

	$[11\bar{2}]$	$[1\bar{1}0]$
A	(5.2 ± 0.4) Å	(5.4 ± 0.2) Å
B	(5.8 ± 0.3) Å	(5.9 ± 0.4) Å
C	(5.1 ± 0.4) Å	(5.1 ± 0.4) Å
D	(5.8 ± 0.4) Å	(5.7 ± 0.3) Å

Along the $[11\bar{2}]$-axis, evidence for a two-fold periodicity with alternating lattice constants (compressed/stretched compared to the average) of $a \approx 5.2$ Å and $b \approx 5.8$ Å is observed. Along the $[1\bar{1}0]$-axis, in contrast, a four-fold periodicity is observed. These periodicities agree well with the observed (4×2) periodicity of the Rec(1.925×1.925) local square cell, resulting in the Rec(7.7×3.85) periodicity observed in the FFTs and in LEED.

Taking into account that the LEED pattern does not change when higher amounts of Sn are deposited, the square-like structure could be interpreted as the onset of β-Sn(001) layer growth. Bulk β-Sn, which crystallizes in a body-centered tetragonal structure, has a square (001) surface lattice with a constant of approximately 5.82 Å [35], closely matching the 5.55 Å average lattice constant observed for the square-like phase. However, a complete β-Sn(001) layer contains two atoms per unit cell due to its body-centered symmetry, resulting in a thickness twice that of the single atomic layer observed in the STM measurements. Likely, in the X-phase, therefore, only half a β-Sn(001) layer has formed, and depositing higher amounts of Sn then completes the β-Sn(001) structure, which would not alter the LEED pattern. Since higher coverages have not been studied extensively, the proposed growth mode is merely an assumption.

For the topmost, square-like arrangement observed in STM, the packing density can be determined to be ≈ 0.27 ML. Since the coverage estimate from the QCM measurements as well as from XPS are both ≈ 0.66 ML, two-layer growth is needed to explain the measured coverage. Based on the XPS analysis presented in Section 7.1, likely, two-layer growth with an Au_2Sn-interface alloy layer with a Sn contribution of 0.35 ML explains the observed film thickness. The deviation of the Sn contribution from 0.33 ML in the substitutional alloy thereby stems from the $\approx 3.7\,\%$ compression of the Rec$(26 \times \sqrt{3})Au_2Sn$-alloy along the $[1\bar{1}0]$-direction. However, one crucial question remains: Why are neither distinct spots from the Au(111) substrate nor from the proposed Au_2Sn-interface alloy observed in the LEED patterns of the X-phase?

Assuming the Rec$(26 \times \sqrt{3})$-reconstruction of the Au_2Sn substitutional alloy layer, where 27 atoms in the alloy align with 26 atoms of the underlying Au(111) substrate, a compression of $\approx 3.7\,\%$ along the $[1\bar{1}0]$ direction is obtained, which gives a lattice constant of $0.963 \cdot a_{\mathrm{Au}}$. Given this compression, the $1.925\times$ local periodicity of the square-like Sn layer, when referenced to the uncompressed Au(111) substrate, corresponds to a $\approx 2\times$ periodicity relative to the compressed Au_2Sn-alloy along the $[1\bar{1}0]$ direction. Effectively, the Sn overlayer and the Au_2Sn-alloy are commensurate in this direction. Therefore, no additional LEED diffraction features, neither from the alloy nor from a superposition of both layers, are expected along $[1\bar{1}0]$, as long as only the two topmost layers are considered.

The situation is different along the $[11\bar{2}]$ direction, as a lattice mismatch is present here: the Au_2Sn-alloy has a periodicity of $\sqrt{3} \cdot a_{\mathrm{Au}} \approx 1.73 \cdot a_{\mathrm{Au}}$, while the square-like Sn overlayer has an average periodicity of approximately $1.925 \cdot a_{\mathrm{Au}}$. Assuming no modification of the Au_2Sn-interface alloy, additional spots in the LEED pattern would therefore be expected. As indicated by the XPS coverage analysis, the XPS high-resolution analysis, and the structural evolution observed, it is highly likely that an interface close to the Au_2Sn-alloy is present below the square-like Sn arrangement. To match the observed LEED pattern, the Au_2Sn-alloy at the interface is likely stretched by $\approx 11\,\%$ along the $[11\bar{2}]$ direction. Thus, the observed Rec(7.7×3.85)-reconstruction corresponds to the periodicity of the combined two topmost layers: the square-like arrangement in the top layer and the stretched Au_2Sn-layer below. In addition, stretching of the Au_2Sn-layer could potentially explain the observed binding energy shift to higher binding energies of the respective component in the Au $4f$ XPS spectrum as discussed in Section 7.1.

To prove that no additional LEED spots stemming from the Rec$(26 \times \sqrt{3})$-reconstruction of the Au_2Sn alloy are observed, Figure 7.11 shows LEED patterns of the X-phase with expected spot positions of a $(\sqrt{3} \times \sqrt{3})$R30° marked in blue. As is evident, the Au(111) spots are not visible in the LEED pattern either. Analyzing LEED patterns at higher kinetic energies, as shown in Figure 7.12, reveals that LEED features from the substrate are not yet visible at $E_{\mathrm{kin}} = 155$ eV but are clearly visible at $E_{\mathrm{kin}} = 170$ eV. Assuming that the square-like Sn phase grows atop the Au_2Sn surface alloy, diffracted electrons from the underlying Au(111) substrate must traverse both overlaying layers, corresponding to a combined thickness of approximately 5 Å. Using the TPP-2M formula [81], it is estimated that electrons with a kinetic energy of $E_{\mathrm{kin}} = 155$ eV have an inelastic mean free path (IMFP) of approximately 5.5 Å in Au_2Sn, 7 Å in Sn, and only about 4 Å in Au.

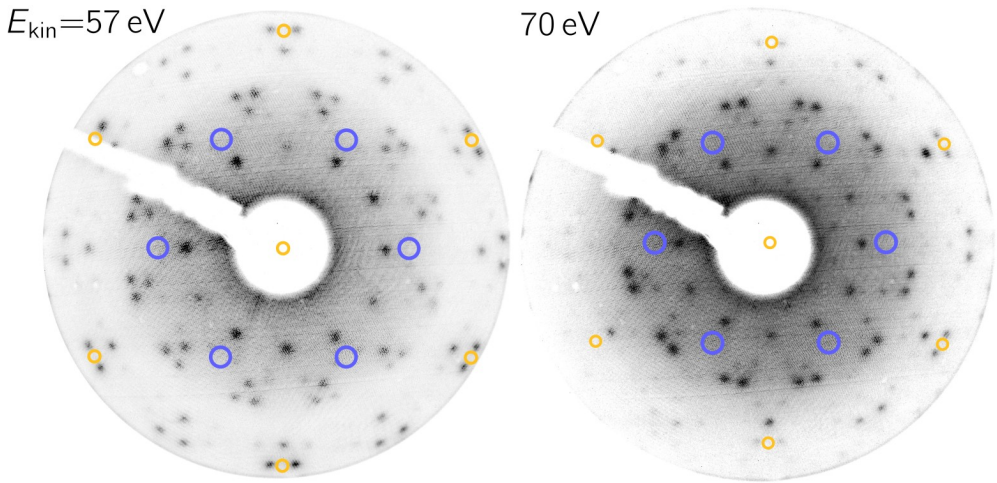

Figure 7.11: LEED patterns of the Rec(7.7 × 3.85) X-phase recorded at $E_{min} = 57\,eV$ and 70 eV. The diffraction pattern of the Au(111) substrate is marked in yellow. Expected spot positions for a $(\sqrt{3} \times \sqrt{3})$R30°-reconstruction are indicated by blue circles, showing that no corresponding spots are observed. Modified reprint from [47].

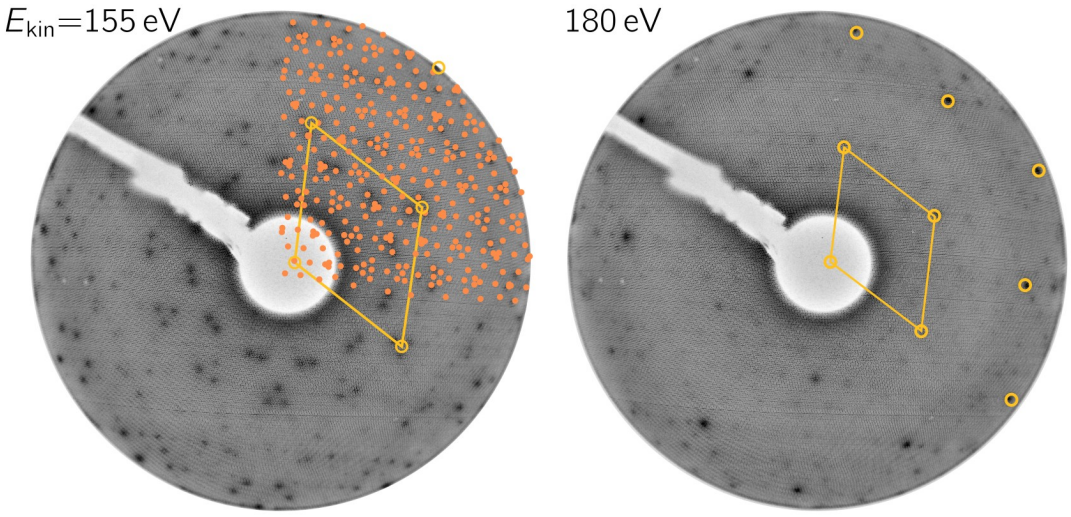

Figure 7.12: LEED diffraction pattern of the X-phase at higher kinetic energies. The complex Rec(7.7 × 3.85)-reconstruction pattern is marked by orange dots in **(a)**. The diffraction pattern and unit cell of the Au(111) substrate are marked in yellow. Substrate spots only become visible at electron energies above ≈ 160 eV. Reproduced after [47].

All obtained IMFPs are therefore within the range of the thickness of two atomic layers and would only exceed this value at higher kinetic energies. Thus, contributions from the third atomic layer (the first Au(111) substrate layer) would be expected to become visible in the LEED pattern recorded with $E_{\mathrm{kin}} \geq 160\,\mathrm{eV}$, which matches the observed behaviour in LEED, indicating two-layered growth atop, in full accordance with all other methods used. Nevertheless, while the observed LEED patterns indicate that the Au_2Sn interface alloy is stretched along the $[11\bar{2}]$ axis (in addition to the stretch of the Rec($26 \times \sqrt{3}$) along the $[1\bar{1}0]$ axis), the detailed relative arrangement of the square-like Sn arrangement in the topmost layer relative to the Au_2Sn-interface alloy layer below remains ambiguous to some degree based on the presented experimental data. A full structural simulation combining the Rec(7.7×3.85) periodicity of the top Sn layer with the Rec($26 \times \sqrt{3}$) periodicity of the alloy would involve giant unit cells, making such simulations highly computationally demanding.

Based on the analysis presented, the structural model shown in Figure 7.13(a) is proposed. In the model, the interface alloy layer is assumed to maintain its Rec($26 \times \sqrt{3}$) periodicity with a 3.7 % compression along $[1\bar{1}0]$, forming alternating hcp and fcc stacking regions similar to the Au herringbone reconstruction [40, 45], and experiencing an approximately 11 % stretch along the $[11\bar{2}]$ direction. Following the Rec(7.7×3.85), small variations of the ideal square-like positions, as extracted from the STM analysis, are assumed for the atoms in the square-like top layer. The Rec(7.7×3.85) unit cell, as well as associated lattice constant variations, are indicated in the figure. The red arrows in the top view mark the atoms' displacements relative to an ideal square lattice. The displacements create a zigzag pattern, producing an alternating row arrangement along the $[11\bar{2}]$ direction: For every second atomic row, the nearest-neighbour spacing pattern ($ABCD$) starts with identical displacement. In contrast, the periodicity observed for the rows in between is laterally shifted by one lattice constant along $[1\bar{1}0]$. This periodicity pattern matches the observed 3.85× periodicity along $[11\bar{2}]$ and is shown in the bottom right of Figure 7.13(b). It is noted that often small modulations in the measured electron density, visible as faint background intensity variations in the STM images, are observed, as marked by the red-white lines in Figure 7.13(b). These faint modulations display a 3× periodicity of the square-like lattice along the $[1\bar{1}0]$ direction. The modulations seem uncorrelated to the observed periodicity and lattice variations of the square-like Sn arrangement observed in STM. However, as evident from the structural model, it corresponds to differing relative stacking of Sn atoms in the topmost layer with respect to those in the underlying Au_2Sn-alloy. Precisely, every fourth Sn atom along the $[1\bar{1}0]$ direction is located similarly to the atoms in the alloy layer. This stacking variation may account for the observed modulation in electron density. Moreover, this observation indicates that the structural arrangement of the square-like top layer is only weakly influenced by that of the Au_2Sn-alloy layer below, suggesting some degree of decoupling.

Indeed, from a geometrical point of view, the observation of a square-like arrangement atop a hexagonal (111) surface is very counterintuitive. The structural versatility of bulk tin with a well-known bulk phase transition at 285 K between semiconducting α-Sn (diamond structure) and metallic β-Sn (body-centered tetragonal structure) might help explain the observed behaviour. In addition, while monolayer α-Sn corresponds to the honeycomb stanene phase, its thermal instability limits multilayer growth at elevated

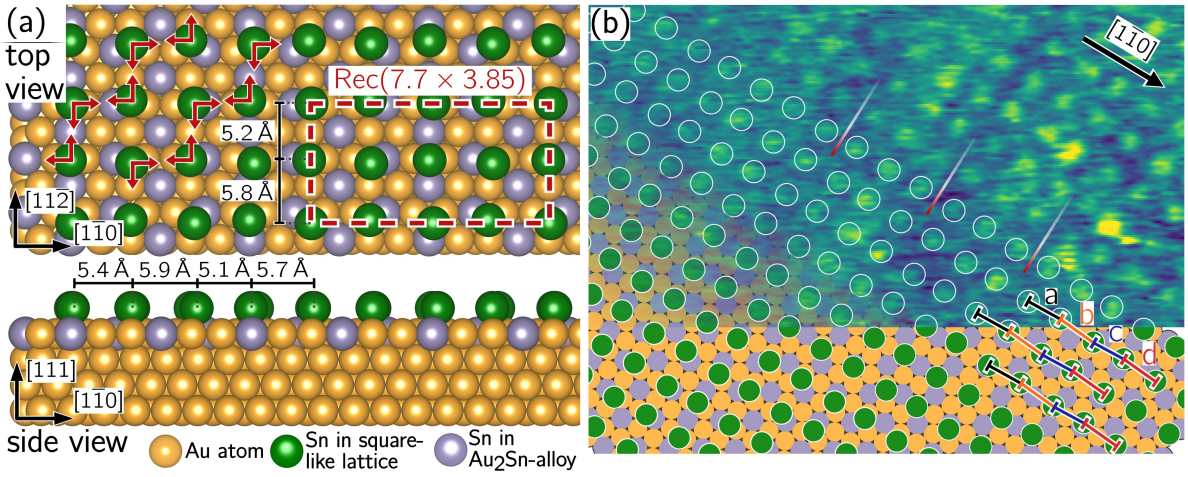

Figure 7.13: (a) Proposed structural model of the X-phase with a Rec(7.7 × 3.85) surface reconstruction grown atop the Au_2Sn surface alloy. The red arrows indicate the directions of small distortions in the local square lattice of the topmost layer, leading to the formation of the Rec(7.7 × 3.85) superstructure. (b) The structural model overlaid on an STM image measured at $U = 3\,\mathrm{mV}$ and $I = 325\,\mathrm{pA}$ of the X-phase. Alternating next-neighbor distances are shown in the bottom right. The red-white lines indicate a subtle modulation observed in the electron density showing a 3× periodicity of the square-like lattice along the [1$\bar{1}$0] direction. Modified from [47].

temperatures [20, 21]. As already discussed, the observed square-like Sn arrangement could be interpreted as the onset of β-Sn(001) layer growth, as the square-like unit cell closely matches half a layer of β-Sn [35]. The Au_2Sn interface alloy likely stabilizes the observed square-like Sn arrangement, especially considering that honeycomb and hexagonal Sn arrangements are observed when the Sn coverage is decreased, as in the striped and $\sqrt{7}$-phase discussed in the following two sections. Square-like Sn lattices have been reported on Al(111), which further highlights the structural diversity of 2D Sn phases [36] and shows similarities to the substrate-symmetry breaking behaviour of the square-like arrangement of the X-phase. The β-Sn bulk allotrope is known to be one of the earliest superconductors ($T_c = 3.72\,\mathrm{K}$) [300, 301], and full single-layer β-Sn grown on Cu(111) has been shown to exhibit a nearly freestanding electronic structure [37], and theoretical studies are proposing ultrathin β-Sn(001) as a platform for realizing topological superconductivity [22]. These promising results and predictions make the square-like Sn arrangement of the X-phase a promising candidate for further investigations.

7.3 Striped Phase

In the following, a structural model of the striped phase will be derived from LEED and STM measurements. The striped phase forms when depositing 0.55 ML on Au(111) at room temperature, or by annealing a 0.66 ML Sn coverage at 450 K. The results presented in this section were already published in [46].

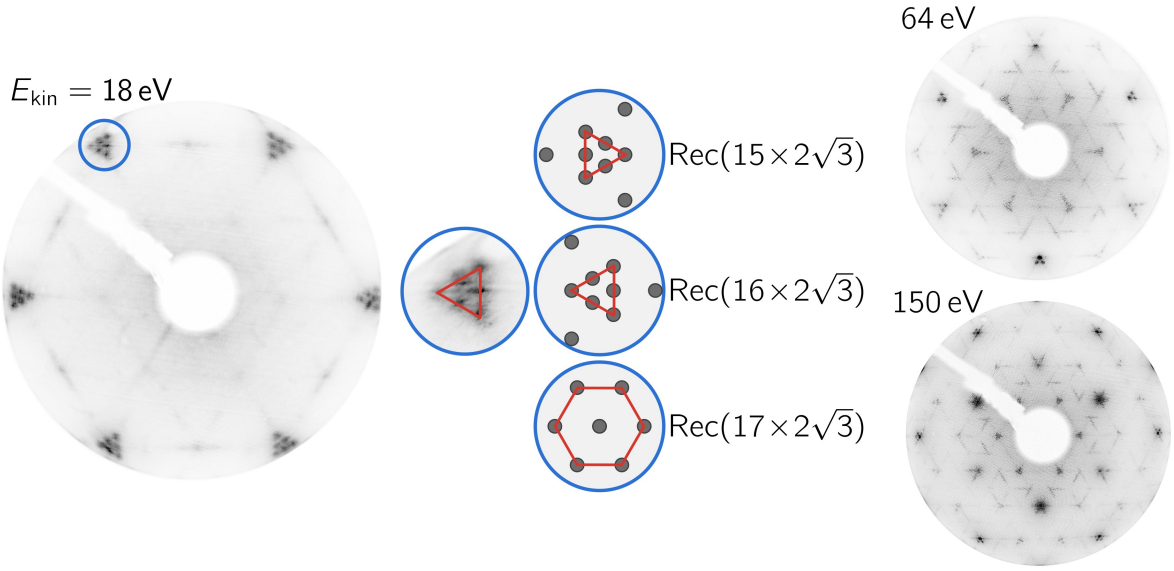

Figure 7.14: LEED patterns of the striped phase, recorded at different kinetic energies show triangular and striped-like patterns. Analysis of the substructure in the LEED pattern recorded at $E_{\text{kin.}} = 18\,\text{eV}$ reveals a Rec($16 \times 2\sqrt{3}$) supercell. Reproduced after [46].

First, the periodicity of the striped LEED pattern was determined. A clear triangular spot superstructure, in addition to stripe-like and triangular/hexagonal features, is observed. The local superstructure around the most intense spots was then analyzed using LEEDPat, as for the superstructure of the Au_2Sn-alloy (compare Figure 6.7). Measuring the distance of the superstructure spots relative to the Au(111) substrate spots yields an average periodicity of 16.2 ± 0.8 along the $[1\bar{1}0]$ direction and $3.5 \pm 0.2 \approx 2 \times \sqrt{3}$ along $[11\bar{2}]$. To verify these periodicities, the superstructure surrounding the $\sqrt{3}$-spot in the LEED pattern recorded at $E_{\text{kin.}} = 18\,\text{eV}$ was calculated using LEEDPat [238] and compared to the experimental LEED pattern. Specifically, the characteristic features of the experimental pattern, such as the inward-pointing triangular shape of the superstructure, match well with a Rec($16 \times 2\sqrt{3}$). In contrast, simulating a Rec($15 \times 2\sqrt{3}$) produces a triangle pointing outward, and Rec($17 \times 2\sqrt{3}$) results in a hexagonal configuration inconsistent with the measured LEED pattern. Thus, only the Rec($16 \times 2\sqrt{3}$) periodicity reproduces the observed spot arrangement. The next matching shapes are realized by Rec($13 \times 2\sqrt{3}$) and Rec($19 \times 2\sqrt{3}$) periodicities, which are considered unlikely as they do not agree with the determined periodicity. Consequently, the observed striped LEED pattern can be assigned to a Rec($16 \times 2\sqrt{3}$) supercell.

As the next step, the real-space structure of the striped phase is analyzed using STM. In the large-scale STM image of the striped phase (Figure 7.15(a)), alternating bright

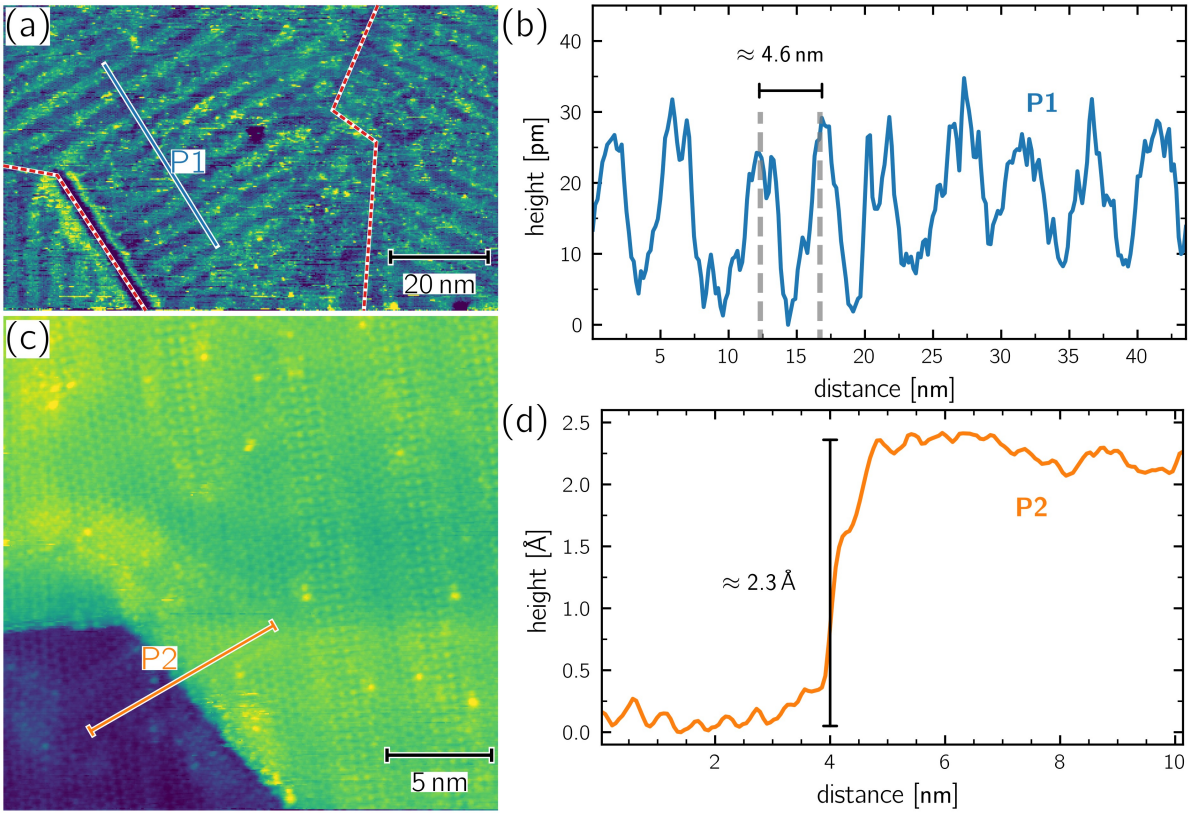

Figure 7.15: (a) Large-scale STM image measured at $U = 4\,\mathrm{mV}$ and $I = 310\,\mathrm{pA}$, displaying alternating stripes of square-like and honeycomb arrangements of Sn atoms. The dashed red lines mark the borders of the three rotational domains. (b) Line profile corresponding to the path marked in (a). The average distance between neighboring stripes is approximately 4.6 nm. (c) Step edge of the striped phase measured at $U = 3\,\mathrm{mV}$ and $I = 400\,\mathrm{pA}$, with the atomic structure being visible on both terraces. (d) Line profile corresponding to the step edge marked in (c). Modified from [46].

and dark stripes with three rotational domains are observed. The domains are rotated by 120° with respect to one another, consistent with the threefold symmetry of the underlying Au(111) substrate. The longest region of stripes measured approximately $\approx 120\,\text{nm}$ in length. The periodicity of the stripes was quantified by extracting 27 line profiles across different STM images. In Figure 7.15(b), a representative line profile is shown. An average stripe distance of $(4.6 \pm 0.4)\,\text{nm}$ is determined, which corresponds to a 16.1 ± 1.5-fold multiple of the Au lattice constant $a_{\text{Au}} = 2.88\,\text{Å}$. Therefore, the periodicity of the dark/bright-striped structure observed in STM matches that observed in LEED well.

An STM image of an atomic step edge of the striped phase is shown in Figure 7.15(c). The corresponding line profile (Figure 7.15(d)) gives a step height of $(2.3 \pm 0.2)\,\text{Å}$, matching the clean Au(111) step height [302, 303]. Notably, the striped phase is observed on both terraces, with the reconstruction beginning directly at the step edge. To determine the precise local atomic arrangement in the unit cell, line profiles of atomically resolved STM images were extracted (Figure 7.16(a) and (b)). In the atomically resolved STM images, the darker stripes can be identified as a square-like atomic arrangement. In contrast, the brighter stripes are resolved as a honeycomb arrangement.

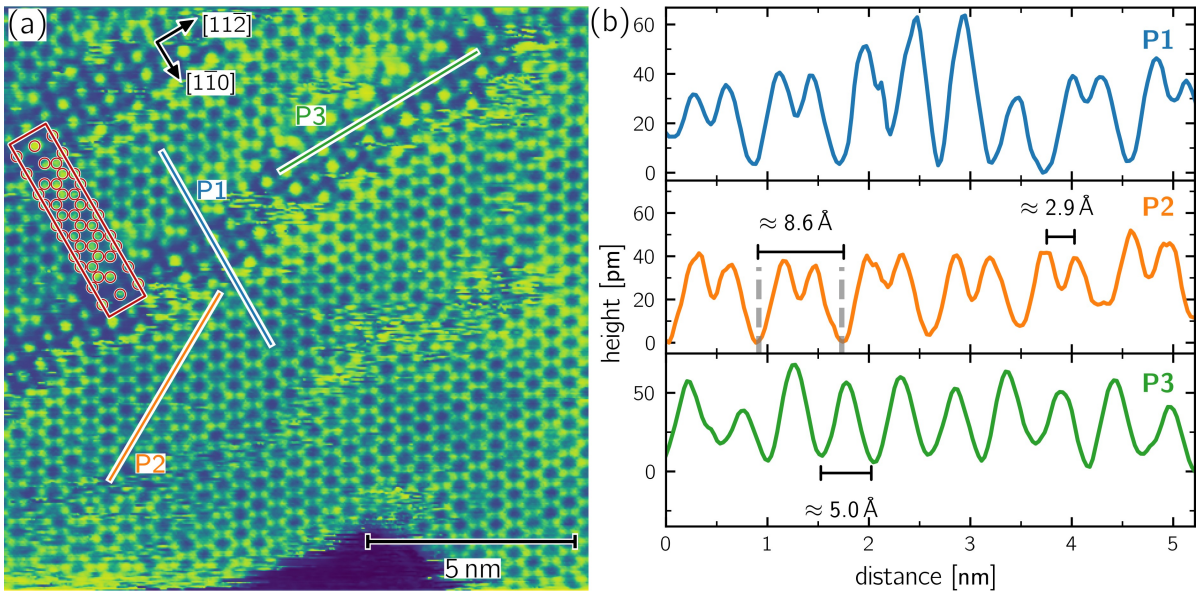

Figure 7.16: High-resolution STM analysis of the striped phase. (a) Atomically resolved STM image showing an atomically flat honeycomb arrangement of Sn atoms, separated by Sn atoms in a square-like arrangement. A Rec($16 \times 2\sqrt{3}$) building block is overlaid in red. The image was acquired at $U = 3\,\text{mV}$ and $I = 360\,\text{pA}$. (b) Line profiles corresponding to the marked lines in (a). Reproduced after [46].

Analyzing the detailed local arrangement, line profile P1 (blue), taken across both the square-like and honeycomb regions, shows that the striped phase is atomically flat. A small height difference of about 20 pm is observed between the square-like and honeycomb stripes. It has been observed (e.g., in Figure 7.15(a)) that the height difference can appear to vanish or even reverse. This small height variation is likely an artifact of the STM tip state and does not reflect an actual topographic height difference.

Line profile P2 (orange), taken within the honeycomb region, shows an atomically flat arrangement with a nearest-neighbor distance of ≈ 2.9 Å, which matches the Au(111) lattice constant. The distance between two minima in the profile is determined to be ≈ 8.6 Å, which equals $3a_{\mathrm{Au}}$. Therefore, the diagonal of the honeycomb hexagon matches $2a_{\mathrm{Au}}$, and Sn atoms occupy equivalent adsorption sites on the Au(111) substrate, consistent with previous reports on the $\sqrt{7}$-phase [43] and with DFT results [38]. Line profile P3 (green), within the square-like stripe, shows an atomically flat arrangement with minimal height variation. The nearest-neighbor distance of ≈ 5 Å corresponds to a $\sqrt{3}$ periodicity relative to the Au(111) substrate, allowing all Sn atoms in the square-like region to occupy hcp hollow sites. In addition, this square-like arrangement closely matches the X-phase, with the lattice constant being approximately 10 % smaller than observed in the X-phase. As similar components were identified in the XPS analysis for both phases, these two square-like arrangements are likely closely related.

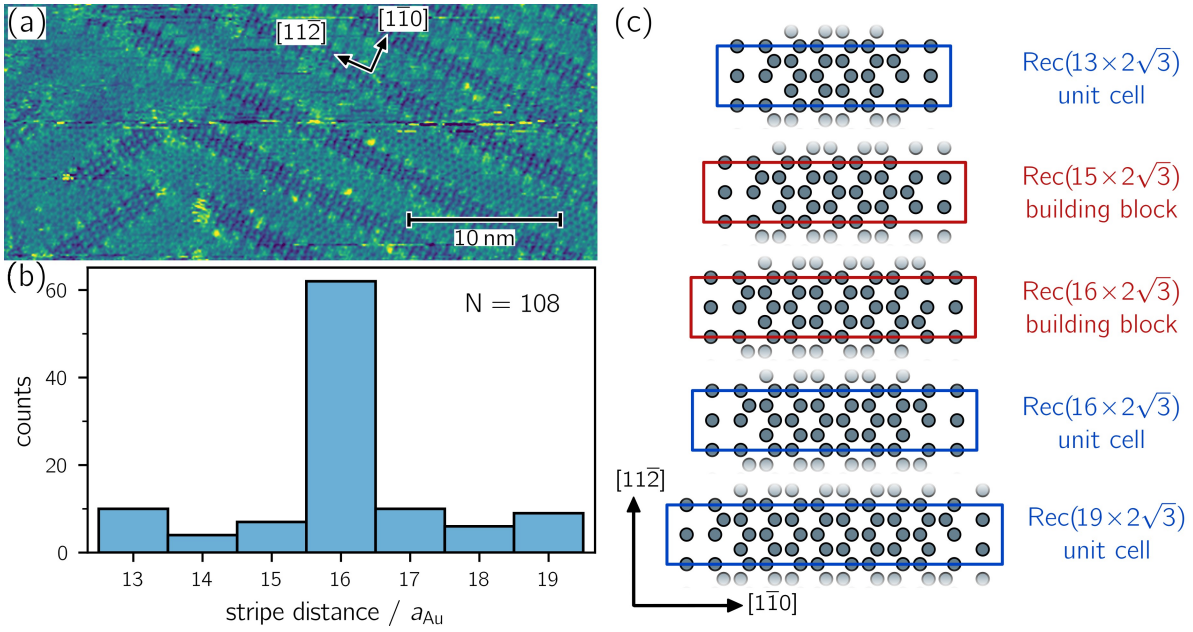

Figure 7.17: (a) High-resolution image of the striped structure showing variation in the width of the honeycomb stripe. The image was measured using $U = 3\,\mathrm{mV}$ and $I = 360\,\mathrm{pA}$. (b) The distribution of the periodicity length, which was measured as the distance between the centers of the square-like stripes in seven different STM images. Examples of building blocks and unit cells observed in the high-resolution STM images are shown in (c). The Rec($16 \times 2\sqrt{3}$) periodicity is thereby the most common motif. Modified after [46].

As evident from the atomically-resolved STM image in Figure 7.15(a), the honeycomb region appears to be of varying width, while the square-like region has a fixed width. The varying width of the honeycomb stripes is also evident from Figure 7.17(a). To analyze this variation, a total of 108 individual distances between neighbouring stripes were measured. Figure 7.17(b) shows the resulting distribution of stripe distances in units of the Au(111) lattice constant. Most frequently, a $16 \cdot a_{\mathrm{Au}}$ distance is observed. However, distances ranging from $13 \cdot a_{\mathrm{Au}}$ to $19 \cdot a_{\mathrm{Au}}$ were also observed. This translates to honeycomb stripe widths ranging from ≈ 1.5 nm to ≈ 3.2 nm, with ≈ 2.4 nm being the most common, as the width of the square-like region remains fixed at ≈ 14.6 Å.

This results in numerous possible unit cells and building blocks, as shown in Figure 7.17(c), which can be combined to tile the observed structure. To clarify the terminology, the different cells are classified based on their symmetry: *Unit cells* (marked in blue) have a mirror symmetry plane, while *building blocks* (red) are defined as a small variation of the unit cell that lacks this mirror symmetry. The difference is shown in Figure 7.18. Unit cells are fully symmetric across the σ_1 plane, which is required to match the symmetry of the square-like region (symmetric across σ_2). In contrast, for building blocks, this symmetry is broken: the missing atom in the border hexagon is shifted by one atomic site upward or downward on one side, breaking the mirror symmetry. The structural difference is marked in green. This type of cell, therefore, lacks σ_1 symmetry and cannot tile the observed structure of the striped phase on its own. However, tiling the observed structure is perfectly possible using a mixed set of building blocks and unit cells, or obviously as well by only using unit cells.

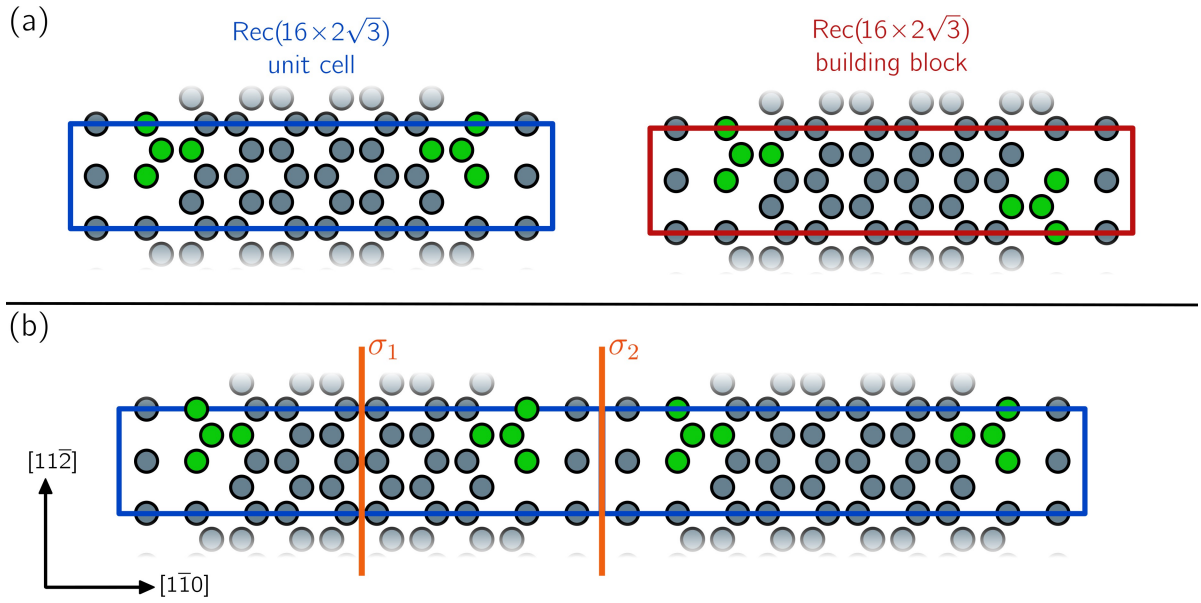

Figure 7.18: Comparison of the Rec($16 \times 2\sqrt{3}$) **(a)** unit cell (blue) and building block (red). Atoms in the border region between the honeycomb and square-like region are marked in green. The unit cell is fully symmetric when mirrored at the σ_1 plane, which matches the symmetry of the square-like region (which is symmetric when mirrored at the σ_2 plane). The atomic arrangement in the border region of the building block breaks this mirror symmetry at σ_2, required to tile the observed structure on its own. Reprinted from [46].

For reference, a Rec($16 \times 2\sqrt{3}$) building block is marked in red in Figure 7.16(a). Based on the LEED and STM analysis, no strong preference for one cell type is observed. In all atomically resolved STM images, unit cells and building blocks appear with roughly equal frequency, suggesting that the small structural difference does not lead to a strong energetic preference. However, the Rec($16 \times 2\sqrt{3}$) periodicity is clearly identified as the most common periodicity. The observed faint stripe-like features in the LEED pattern could likely be explained by the observation that $\approx 43\,\%$ of the observed cells show a different periodicity along the [1$\bar{1}$0]-direction. This would create superstructure spots lying on the faint lines observed in Figure 7.14.

Figure 7.19(c) shows the Fast-Fourier Transform (FFT) of the STM image in Figure 7.19(a). The stripe-like, spot-rich pattern matches well with the features of a single domain of the LEED pattern. The zoomed-in STM image of the square-like region (Figure 7.19(b)) reveals a substructure beneath the square-like atoms. Assuming that the square-like region is similar to the X-phase, it likely grows atop an Au_2Sn-region. Therefore, expected positions of Sn atoms in an Au_2Sn-alloy are marked by orange circles, while atoms of the striped top layer are marked in white. The marked positions match the observed substructure, at least in part.

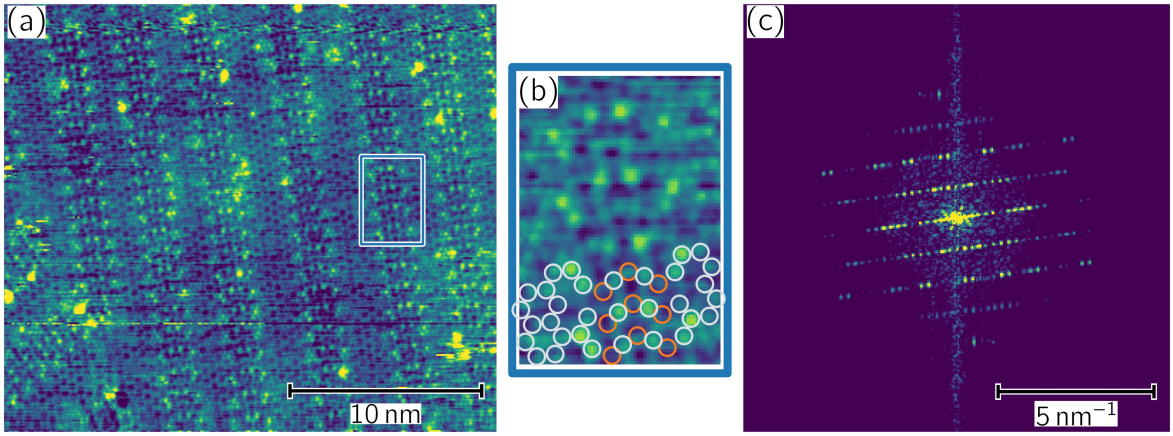

Figure 7.19: High-resolution STM image of the striped phase, recorded with a different tip state compared to the other STM images. (a) Image measured at $U = 3\,\mathrm{mV}$ and $I = 290\,\mathrm{pA}$. The zoom-in shown in (b) of the region marked in (a), reveals a substructure beneath the atoms in the square-like region of the striped phase. Expected positions of Sn atoms in a Au_2Sn-alloy are marked by orange cycles while atoms of the striped top layer are marked in white. Shown in (c) is the FFT of (a), showing excellent agreement with a single domain of the LEED pattern of the striped phase. Reprinted from [46].

Based on these results, which identified a Rec($16 \times 2\sqrt{3}$) cell as the most likely, and combined with the XPS analysis (Section 7.1), the structural model shown in Figure 7.20 is proposed. The model assumes only a Rec($16 \times 2\sqrt{3}$) unit cell for simplicity. In the model, the honeycomb-like region forms directly on the Au(111) surface, with Sn atoms occupying equivalent hcp hollow sites, consistent with DFT predictions [38].

In analogy with the X-phase, it is proposed that the square-like stripe regions grow on top of stripes of an Au_2Sn-alloy. This interpretation is supported by the following observations: (i) Counting Sn atoms visible in the topmost layer from STM images results in slightly smaller coverages compared to those determined by XPS. The difference corresponds approximately to the atomic density needed to form a stripe of Au_2Sn-alloy beneath the square-like region. (ii) In the XPS analysis (compare Figure 7.4), the fit of the Au $4f$ signal gives very similar components for both the striped phase and the X-phase. Additionally, the measured intensity ratio of the two components in Sn $4d$ signal is 3.1:1 (stanene:square-like). This is in excellent agreement with the atomic ratio obtained from STM, with 26 honeycomb atoms vs. 8 square-like atoms, yielding a ratio of 3.25:1. (iii) According to the structural and chemical evolution, a dealloying process occurs with decreasing Sn coverage. Starting with the X-phase and its square-like Sn growing atop the

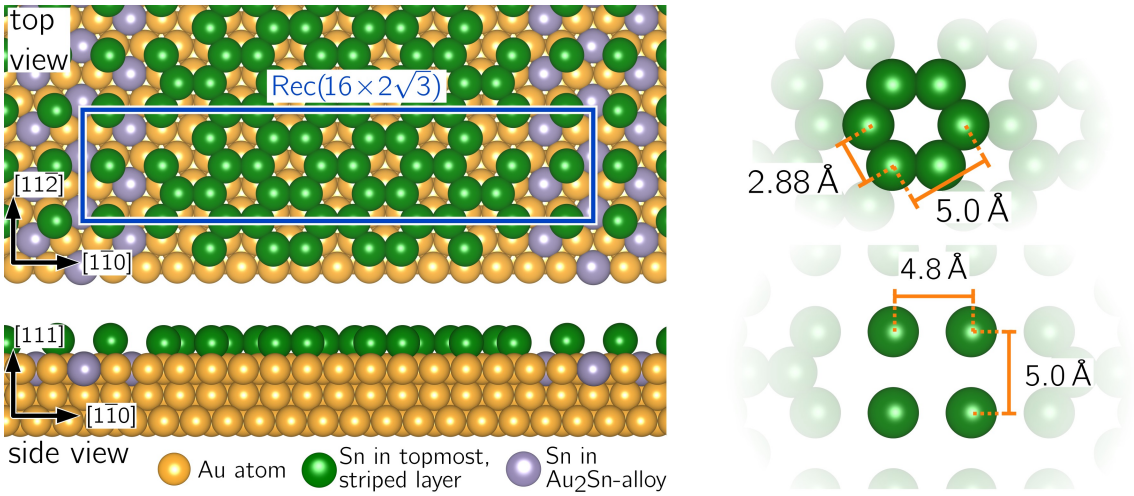

Figure 7.20: Proposed structural model of the Rec($16 \times 2\sqrt{3}$) Sn honeycomb striped phase. Sn atoms in the topmost layer are shown in green, while Sn atoms in the Au_2Sn-alloy beneath the regions of square-like ordered Sn atoms are shown in grey. Adapted from [46].

Au_2Sn alloy, and ending with the $\sqrt{7}$-phase, which consists of Sn-dimers growing directly on the Au(111) surface, the striped phase represents a partially dealloyed configuration in between. (iv) As shown in the inset of Figure 7.19(b), depending on the STM tip state, the substructure in the square-like region is resolved. The assignment of Au_2Sn atomic positions closely resembles parts of the observed substructure. In Figure 7.20, the Rec($16 \times 2\sqrt{3}$) unit cell is marked in blue. In addition, the next-neighbour distances in the honeycomb and the square-like region are given.

To summarize, the striped phase was determined to be a complex superstructure composed of different unit cells and building blocks with periodicities ranging from Rec($13 \times 2\sqrt{3}$) to Rec($19 \times 2\sqrt{3}$), with Rec($16 \times 2\sqrt{3}$) being the most common. The phase consists of alternating honeycomb-like and square-like Sn regions, arranged in stripes with three rotational domains consistent with the Au(111) substrate symmetry. The honeycomb regions are atomically flat, and the determined Sn-Sn bond length matches well with predictions for freestanding stanene as well as reports of flat stanene on Pd_2Sn(111) and Cu(111) [17, 24, 26]. Considering the distinct structural and chemical characteristics of the square-like and honeycomb-like stripes, the striped phase can be interpreted as zigzag-terminated stanene nanoribbons. In addition, the STM measurements presented here provide the first evidence of ultraflat regular honeycomb stanene on Au(111). Stanene nanoribbons are predicted to offer QSH-edge states [304], optical spin-filter properties [305], and edge magnetization [306] with the structural properties like width and length highly influencing its electrical properties [307]. These predictions make stanene nanoribbons and the striped phase a promising candidate for future topological device applications.

7.4 $\sqrt{7}$-Phase

A detailed structural and electronic analysis of the $\sqrt{7}$-phase was already published by Maniraj et al. [43]. Therefore, the $\sqrt{7}$-phase is not discussed in detail here; instead, the experimental LEED and STM measurements are compared with the results of Maniraj et al. Specifically, the time-consuming STM measurements were not optimized for maximum resolution but instead only to allow a reliable comparison with the literature.

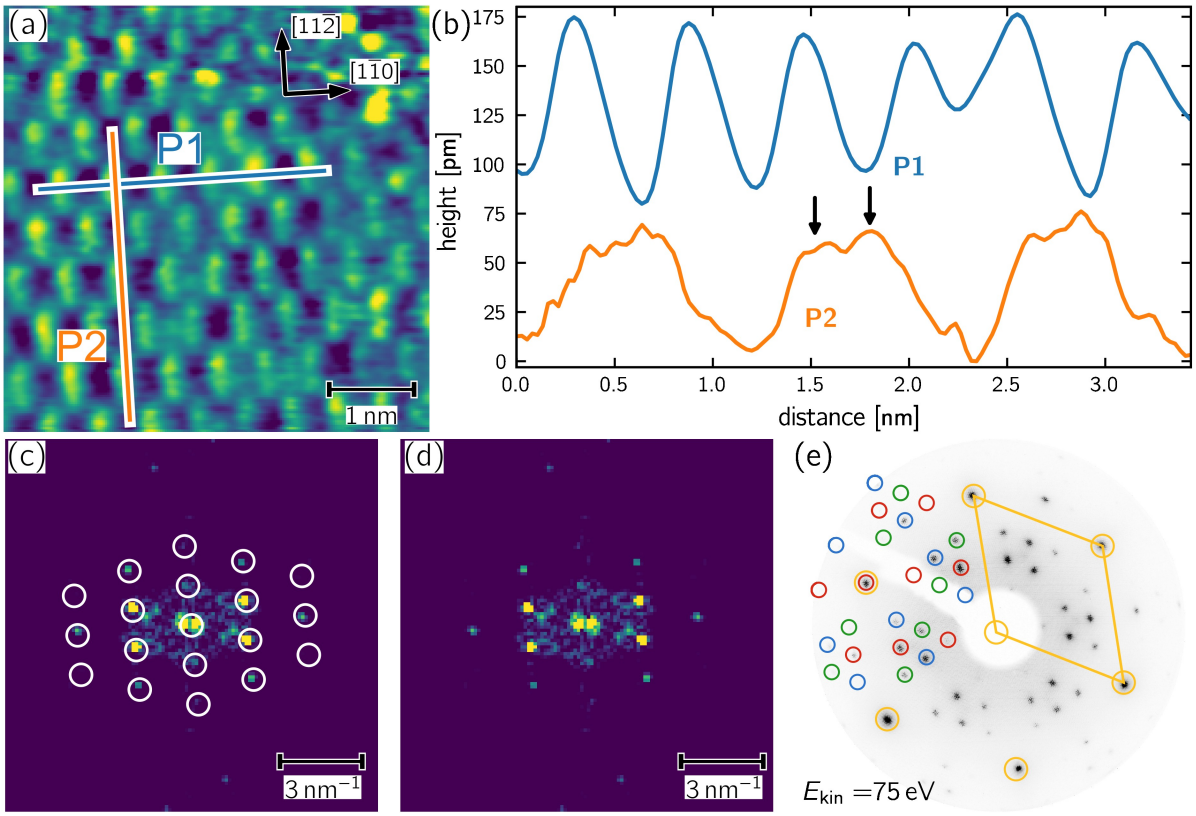

Figure 7.21: High-resolution STM and LEED data of the $\sqrt{7}$-phase. The STM image in (a) was recorded at $U = 5\,\text{mV}$ and $I = 300\,\text{pA}$. A stretched hexagonal arrangement of Sn-dimers is observed; the corresponding marked line profiles are shown in (b). (c) and (d) are the FFT of the STM image in (a), which matches a single domain of the $\begin{pmatrix} 2 & 1 \\ 1 & 3 \end{pmatrix}$-reconstruction as marked by white circles in (c). All three rotational domains of the reconstruction are marked in the LEED pattern of the $\sqrt{7}$-phase displayed in (e). The colored circles correspond to spots of the $\sqrt{7}$-reconstruction, while the unit cell and diffraction spots corresponding to the Au(111) substrate are marked in yellow. Subfigures (a), (b), and (e) reprinted from [46].

In Figure 7.21(a), an atomically resolved region of the $\sqrt{7}$-phase is shown. In the extracted line profiles as shown in (b), a periodic atomic arrangement is observed along both directions. Along the [1$\bar{1}$0]-direction (profile P1, plotted in blue), sharp peaks are observed, separated by $(5.2 \pm 0.3)\,\text{Å}$, which corresponds approximately to $\sqrt{3} \cdot a_{\text{Au}} \approx 5\,\text{Å}$. Along [11$\bar{2}$] (profile P2, plotted in orange), broad peaks are visible, separated by $(13.6 \pm 0.5)\,\text{Å}$, matching approximately $4.5 \cdot a_{\text{Au}} \approx 13\,\text{Å}$. In addition, a substructure with two distinct maxima is sometimes observed in the broad peaks

(indicated by black arrows), separated by $\approx 2.8\,\text{Å}$, matching the Au(111) lattice constant. This indicates the formation of Sn-dimers, with a Sn-dimer bond length of approx. 2.9 Å matching that of gas phase Sn dimers [38]. Figure 7.21(c) and (d) show the FFT of the $\sqrt{7}$-phase, with one domain of the $\left(\begin{smallmatrix} 2 & 1 \\ 1 & 3 \end{smallmatrix}\right)$ (named here $\sqrt{7}$) reconstruction marked by white circles. This matches the reconstruction observed in LEED (shown in (e)) with three rotational domains.

As demonstrated in Figure 7.22, the present STM measurements (a) match the results of Maniraj et al. (b). Their structural model, displayed in panel (c), consists of a stretched hexagonal arrangement of Sn-dimers corresponding to the $\sqrt{7}$-reconstruction. The inter-dimer distances of $\sqrt{3} \cdot a_{\text{Au}}$ along $[1\bar{1}0]$ and $4.5 \cdot a_{\text{Au}}$ along $[11\bar{2}]$ align with the line profiles discussed earlier, confirming that the model matches both the STM and LEED measurements. In addition, their proposed structural model agrees well with the XPS analysis presented in Section 7.1, which identified the Sn $4d$-signal to consist mainly of a single dominating component (besides some Au_2Sn-residuals as discussed in detail there). In the Au $4f$ XPS signal, one component of the fit was identified as corresponding to the Au atoms at the interface interacting with the Sn atoms of the $\sqrt{7}$-stanene above.

Using ARPES, Maniraj et al. observed a linearly dispersing band below the Fermi level with an exceptionally high Fermi velocity of $v_{\text{F}} \approx 1 \times 10^6\,\text{m/s}$, being at the upper end of reported Fermi velocities of graphene [15, 58]. In contrast to graphene, the linearly dispersing band was, however, observed at the Γ point. They attributed their observation of the flat Sn arrangement to strong lateral chemical bonding between Sn atoms, hence, resulting in the inhomogeneous Sn distribution and the formation of the Sn-dimers, as well as to a bonding of the Sn π-orbitals to the Au substrate, which would match the observed component in the XPS analysis of the Au $4f$ signal. To conclude, the results reported by Maniraj et al. agree well with those obtained in this thesis and expand on them through XPS analysis and by discussing the structural and chemical evolution towards the $\sqrt{7}$-phase. Regarding the structural evolution, as already mentioned, the striped and the $\sqrt{7}$-phase are often challenging to prepare, as they appear in a very small parameter window.

As shown in Figure 7.23(a), occasionally a mix of honeycomb Sn arrangement (as known from the striped phase) and the Sn dimer-arrangement of the $\sqrt{7}$-phase is observed in STM measurements. In the figure, the honeycomb regions are marked in red. As the honeycomb arrangement would be transformed into the $\sqrt{7}$-phase by stretching it along the $[11\bar{2}]$ direction, and the parameter window separating the two phases is small, such coexistence is not surprising. The stretch of the structure, or the phase transition, is triggered by reducing the Sn coverage. Interestingly, in the honeycomb arrangement, the Sn bond length matches the Sn-dimer gas phase bond length as well. Following the argument of Maniraj et al. that strong lateral bonding between neighboring Sn atoms leads to the formation of the Sn-dimer structure, it looks pretty plausible that Sn favors dimer formation when the coverage becomes too sparse to form a complete atomic layer with neighbour-bonding lengths of $\approx 2.8\,\text{Å}$. In Figure 7.23(b), a mix of the $\sqrt{7}$ and the $\sqrt{3}$-periodicity is observed at a coverage of $\approx 0.4\,\text{ML}$. Likely, some regions of the sample surface are too sparsely covered to trigger the formation of the Sn-dimer layer of the

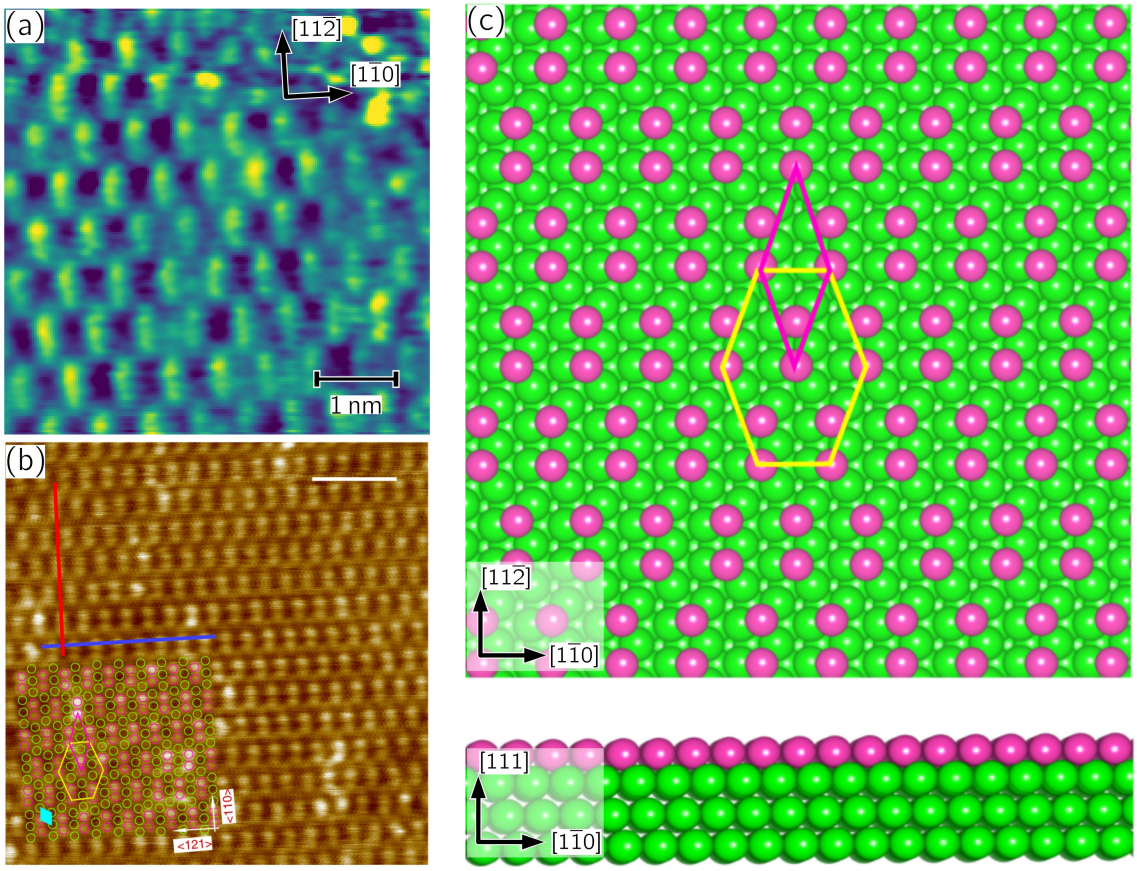

Figure 7.22: Comparison of the measured STM data to the results of Maniraj et al. [43]. While (a) is the STM image already shown in Figure 7.21, in (b) the STM image measured by Maniraj et al. is shown. In both STM images, the same Sn-dimer arrangement is observed. In (c), the structural model as proposed by Maniraj et al., with a stretched hexagonal arrangement of Sn dimers, is shown. Subfigure (a) reprinted from [46]. Subfigures (b) and (c) reprinted with permission from Maniraj et al. [43].

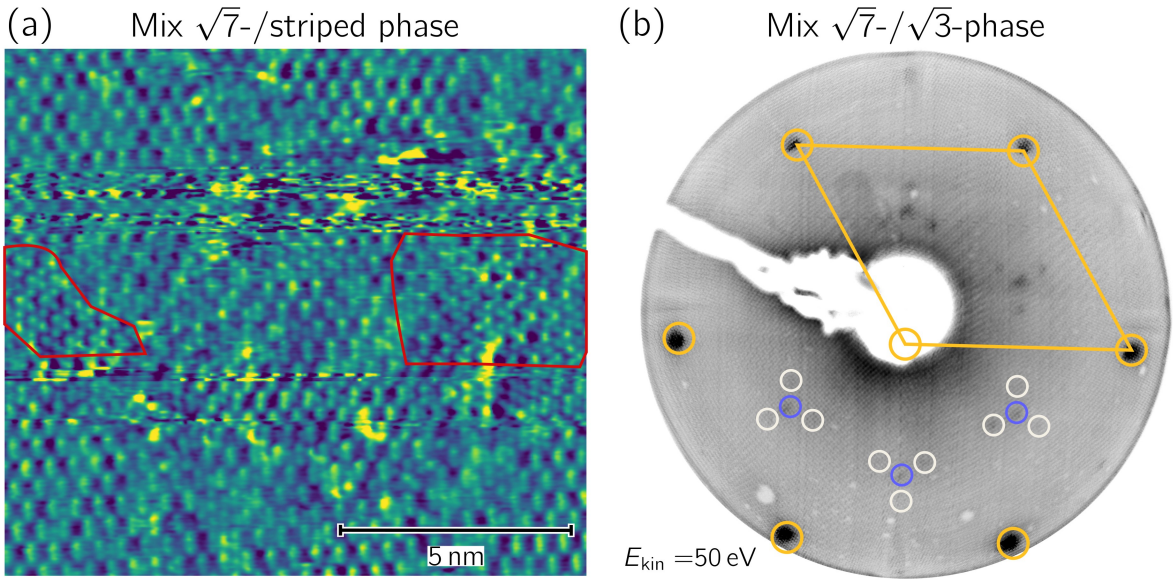

Figure 7.23: Mix of other structural phases with the $\sqrt{7}$-phase. In (a), a high-resolution STM image showing both the honeycomb-like Sn arrangement, as in the striped phase, and the stretched hexagonal Sn-dimer structure of the $\sqrt{7}$-phase, is presented. The honeycomb regions are marked in red. Image recorded at $U = 5\,\mathrm{mV}$ and $I = 300\,\mathrm{pA}$. (b) shows a LEED pattern of a mix of the $\sqrt{3}/\sqrt{7}$-phases. Marked in yellow are the diffraction spots and unit cell of the Au(111) substrate. Blue circles mark spots corresponding to the $(\sqrt{3} \times \sqrt{3})$R30°-reconstruction, while white circles indicate spots of the $\sqrt{7}$-phase. Adapted from [46].

$\sqrt{7}$-phase. This matches the XPS analysis in Section 7.1 of the $\sqrt{7}$-phase as well, where a small contribution of the Au_2Sn-alloy, which reconstructs as $\mathrm{Rec}(26 \times \sqrt{3})$ as discussed in Chapter 6, was observed. To summarize, the results presented confirm the structural model of the stretched hexagonal Sn-dimer structure proposed by Maniraj et al. [43].

7.5 Chapter Summary

In this chapter, the structural evolution of Sn on Au(111) in the higher coverage regime ($0.33\,\mathrm{ML} \leq \Lambda \leq 0.66\,\mathrm{ML}$) was characterized. Three distinct structural phases were identified, with the structural transitions driven by Sn coverage, which is most easily controlled by Sn desorption via sample annealing.

Starting with the highest investigated coverage (0.66 ML), the X-phase forms. In contrast to previous reports in the literature [41, 42], this phase is identified as an uncommon local square-like Sn arrangement growing atop the Au_2Sn substitutional alloy with a Rec(7.7×3.85) unit cell.

At a coverage of $\approx 0.55\,\mathrm{ML}$, the striped phase forms. It is identified as alternating square-like and honeycomb arranged Sn stripes with a Rec($16 \times 2\sqrt{3}$)-reconstruction. The striped phase is interpreted as zigzag stanene nanoribbons. Observations indicate that dealloying occurs upon thermal annealing, reducing the Sn coverage and triggering the transition from the X-phase to the striped phase. The square-like stripes of the striped phase resemble the structure observed for the X-phase, as they likely also grow on stripes of the Au_2Sn substitutional interface alloy. The presented analysis provides the first successful preparation of atomically flat honeycomb stanene on Au(111). In addition, the striped arrangement potentially provides the first successful preparation of atomically flat honeycomb stanene nanoribbons.

At a coverage of $\approx 0.45\,\mathrm{ML}$, the $\sqrt{7}$-phase forms, which was analyzed in detail in the literature by Maniraj et al. [43]. This phase is a fully dealloyed single atomic Sn layer growing atop the Au(111) substrate. The structure is identified as a stretched arrangement of Sn-dimers, which shows extraordinary electronic properties [43]. The results presented here fully support the analysis of Maniraj et al. and extend it with a XPS-based chemical analysis. If the Sn coverage is finally reduced to 0.33 ML, a realloying process occurs, leading to the reformation of the Au_2Sn substitutional alloy discussed in detail in the previous chapter.

8 Conclusion and Outlook

This thesis establishes a comprehensive framework for the structural and chemical evolution of Sn on Au(111) in the submonolayer regime. By combining LEED, XPS, STM, and XPD, the complex interplay between surface ordering and interface alloying has been resolved up to a coverage of 0.66 ML. This work clarifies longstanding discrepancies in the literature regarding the Au_2Sn surface alloy and the X-phase, while identifying novel structural phases, including the freestanding (2×2)-reconstruction and the ultraflat stanene nanoribbons of the striped phase.

The evolution of Sn on Au(111) can be categorized into two distinct regimes. At coverages below 0.33 ML, Sn adsorption is characterized by weak substrate interactions. A previously unreported, chemically freestanding (2×2)-phase was identified at 0.28 ML. This phase corresponds to half a layer of α-Sn and might act as a precursor for buckled stanene growth [291, 292]. Increasing the coverage triggers the formation of a mixed phase and, subsequently, a long-range-ordered Au_2Sn substitutional surface alloy at 0.33 ML. Using XPD combined with genetic algorithm structural optimization, this structure was identified as a substitutional alloy described by a Rec$(26 \times \sqrt{3})$ unit cell [45], resolving conflicting structural models proposed in the literature [39, 40].

Increasing the coverage beyond the alloy phase triggers transitions driven by the interplay between the Au_2Sn interface alloy and the Sn adlayer. At ≈ 0.66 ML, the X-phase forms. Contrary to previous reports suggesting AuSn alloys [41] or honeycomb stanene [42], this work identifies the X-phase as a bilayer system: a local square-like Sn arrangement growing atop the Au_2Sn alloy. Small distortions to the square-like arrangement result in the formation of a Rec(7.7×3.85) supercell. The X-phase breaks the hexagonal symmetry of the substrate and is interpreted as the onset of β-Sn(001)-like growth stabilized by the underlying alloy [47]. Upon thermal annealing, a dealloying process leads to the formation of the striped phase at 0.55 ML. Structurally, this phase consists of alternating stripes of the square-like arrangement, supported by the Au_2Sn interface alloy, and stripes of honeycomb stanene formed directly on the Au(111) substrate. STM reveals that these honeycomb regions are atomically flat, representing the first experimental realization of ultraflat stanene nanoribbon-like structures and providing the first realization of honeycomb stanene on Au(111) [46]. Further dealloying results in the formation of the $\sqrt{7}$-phase at 0.45 ML, consisting of a single layer of stretched Sn-dimers. The detailed structural and chemical analysis demonstrated that the structural transitions observed for Sn are driven by alloying and dealloying processes at the interface and identified Sn coverage as the decisive parameter triggering these transitions.

The presented structural analysis of Sn/Au(111) provides several promising pathways for future research, particularly regarding the electronic and topological properties of these phases. The discovery of ultraflat honeycomb nanoribbon-like regions in the striped phase offers a unique platform for studying 1D topological physics. As theory predicts extraordinary edge states and transport properties in stanene nanoribbons [304–307],

a detailed analysis of their electronic structure using ARPES or scanning tunneling spectroscopy (STS) is the next logical step to investigate their topological character.

Furthermore, the identification of the X-phase as a precursor to β-Sn(001) growth opens the way to realize exotic low-dimensional topological applications. Since ultrathin β-Sn(001) films are predicted to host topological superconductivity [22], investigating the growth of thicker films is a promising direction; in this thesis, the X-phase was observed to remain intact up to at least 1.33 ML. Additionally, since the current study focused on room-temperature deposition, the formation energy and low-temperature stability of the X-phase remain open questions. Deposition onto cooled Au(111) substrates could determine the onset temperature of X-phase formation and potentially stabilize additional structural Sn phases, which are not stable at room temperature. Similarly, the freestanding (2×2)-phase observed at low coverage warrants low-temperature investigation. Given its potential as a precursor to buckled α-stanene [291, 292], cooling the sample might stabilize the long-range order of this phase, preventing alloying and enabling the controlled growth of freestanding stanene layers.

In summary, this thesis frames the Sn/Au(111) system as a versatile playground for realizing diverse 1D/2D structures, ranging from surface alloys to substrate-symmetry-breaking square-like Sn lattices and honeycomb nanoribbons. By resolving the complex structural landscape at submonolayer coverage, this work provides a solid framework for future studies investigating the exotic electronic properties of low-dimensional Sn phases.

Appendix

A Quantum Numbers

Since a full motivation of quantum numbers and their relation to the Schrödinger equation would be lengthy and is discussed in detail in the literature (e.g., see [126]), the primary focus of this chapter is to explain how the quantum numbers of an electron translate to its orbitals and how these quantum numbers are expressed in the X-ray and spectroscopic notations.

A.1 Introduction to Quantum Numbers

The one-dimensional Bohr model, which primarily describes the size of an electron's orbit, can be characterized by a single quantum number, n. Schrödinger's model, however, allows the electron to occupy a three-dimensional space, hence requiring three quantum numbers. These three quantum numbers, the principal quantum number n, the angular quantum number l, and the magnetic quantum number m_l, describe the shell (size/energy, n), the subshell (shape, l), and the specific orbital (orientation of the shape, m_l), respectively [128].

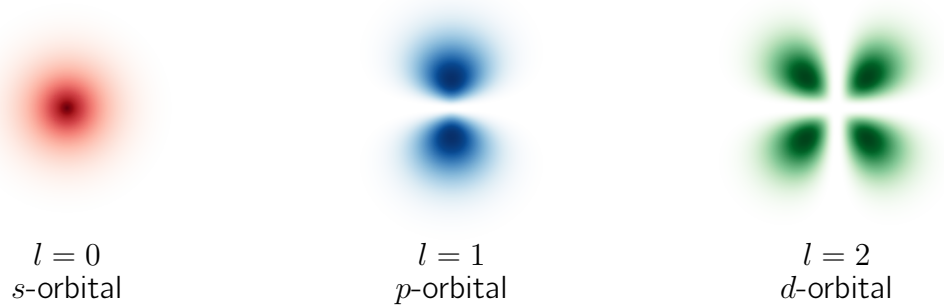

Figure A.1: Sketch of the characteristic shapes of electron orbitals within different subshells.

The principal quantum number can take integer values $n = 1, 2, 3, ...$, describing the size and therefore the primary energy level of an electronic shell. Orbitals with $n = 2$ are larger than those with $n = 1$. To excite an electron from the $n = 1$ shell to the $n = 2$ shell, energy must be absorbed, as electrons closer to the nucleus (i.e., with $n = 1$) are attracted more strongly by the nucleus.

The angular quantum number l can have integer values $l = 0, 1, ..., n-1$ and defines the subshell. This quantum number determines the shape of the orbitals within that subshell. These shapes become more complex as l becomes larger, as shown in Figure A.1.

While an s-orbital ($l = 0$) has a spherical shape with only one possible orientation in space, the dumbbell-shaped p-orbitals ($l = 1$) and more complex "cloverleaf" shaped d-orbitals ($l = 2$) can be oriented in different directions. More precisely, the orbital angular momentum is a vector, $\boldsymbol{L}$. The magnetic quantum number m_l specifies the quantized projection of this vector onto an arbitrary axis (conventionally the z-axis), such that $L_z = m_l\hbar$. The factor $\hbar$ arises because angular momentum is quantized in quantum mechanics, and its eigenvalues are integer multiples of $\hbar$. The value of m_l can be any integer from $-l$ to $+l$, including zero [128].

To fully describe an electron, the spin quantum number s (or m_s) is also required. Each orbital (defined by n, l, m_l) can be occupied by a maximum of two electrons with opposing spins. This quantum number takes the values $s_\uparrow = +1/2$ and $s_\downarrow = -1/2$ to indicate the two possible spin orientations.

A.2 Spin-Orbit Coupling (SOC)

An electron with an orbital angular momentum ($l > 0$) moving through the electrostatic field of the nucleus experiences a relativistic effect. In the electron's rest frame, the moving nucleus generates a magnetic field. The electron's intrinsic magnetic moment (its spin) then interacts with this induced magnetic field. This interaction is called spin-orbit coupling (SOC) [130].

This interaction couples the electron's spin angular momentum, s, with its orbital angular momentum, l. This coupling is described by the total angular momentum quantum number, j, defined as $j = l + s$, which can take values of $j = l \pm 1/2$. Similar to the magnetic quantum number m_l, the total angular momentum vector $\boldsymbol{J}$ has a component along the z-axis described by m_j, which runs in integer steps from $-j$ to $+j$. The number of possible m_j values for a given j is called the degeneracy of that state, and it is equal to $2j + 1$. This degeneracy determines the intensity ratio observed for each doublet in XPS spectra.

For the Au $4f$ subshell ($l = 3$), the two possible states are $j = 3 + 1/2 = 7/2$ and $j = 3 - 1/2 = 5/2$.

- For the Au $4f_{7/2}$ state, the degeneracy is $2j + 1 = 2 \cdot 7/2 + 1 = 8$. The possible m_j values are $-7/2, -5/2, ..., 7/2$.
- For the Au $4f_{5/2}$ state, the degeneracy is $2j + 1 = 2 \cdot 5/2 + 1 = 6$. The possible m_j values are $-5/2, -3/2, ..., 5/2$.

The ratio of the number of available states is $8 : 6$, which simplifies to $4 : 3$. This determines the expected area ratio of the photoemission peaks, $A_{7/2} : A_{5/2} = 4 : 3$. Table A.1 lists the theoretical area ratios for other common doublets. For the Sn $4d$ subshell ($l = 2$), which is analyzed in detail in this thesis as well, possible j-values are $j = 5/2$ and $j = 3/2$, with an electron ratio of $6 : 4$ or, simplified, a resulting area ratio of $3 : 2$. It is important to note that according to the Pauli exclusion principle, no two electrons in the same atom can have an identical set of all four quantum numbers (n, l, m_l, m_s) [129].

Table A.1: Theoretical area ratios for spin-orbit doublets in XPS from different subshells

Subshell	doublet components	area ratio
s	-	-
p	$p_{3/2}$, $p_{1/2}$	2:1
d	$d_{5/2}$, $d_{3/2}$	3:2
f	$f_{7/2}$, $f_{5/2}$	4:3

A.3 Different Nomenclatures for Quantum Numbers

The use of two different notations has historical reasons and is not meant to confuse the reader. Chemists primarily developed the spectroscopic notation, while physicists developed the X-ray notation. As the XPS technique was established with input from chemistry and physicists developed AES, both nomenclatures are often used together when discussing survey XPS spectra, which contain both XPS core-level signals (labeled using spectroscopic notation) and Auger signals (labeled using X-ray notation). The spectroscopic notation uses an integer (for n) followed by a letter that relates to the angular quantum number l. The following convention is used [127]:

- The s-subshell (sharp) contains orbitals with $l = 0$.
- The p-subshell (principal) contains orbitals with $l = 1$.
- The d-subshell (diffuse) contains orbitals with $l = 2$.
- The f-subshell (fundamental) contains orbitals with $l = 3$.

To account for spin-orbit splitting, the total angular momentum quantum number j is given as a subscript. For example, the $4f$ subshell ($n = 4$, $l = 3$) splits into two distinct energy levels due to spin-orbit coupling, with $j = 7/2$ and $j = 5/2$. These are denoted in spectroscopic notation as $4f_{7/2}$ and $4f_{5/2}$, respectively. To note the number of electrons within a subshell, a superscript is used in the spectroscopic notation; for example, $4f^{14}$ denotes that 14 electrons are present in the $4f$ subshell.

The X-ray notation uses capital letters K, L, M, N, ... to denote the principal quantum number n (the shell), starting with K for $n = 1$ and proceeding alphabetically for higher n. The reason this convention starts in the middle of the alphabet is that when Charles Barkla first established the notation in 1911, he was unsure if the K line he had discovered was the innermost (lowest-energy) one. He therefore left space in the alphabet for other, yet-undiscovered, lower-energy shells that might be found later [308]. It was later confirmed that his K-shell was, in fact, the $n = 1$ shell. The sublevels, distinguished by their l and j quantum numbers, are designated by an integer subscript, starting from 1 for the lowest-energy sublevel within that shell. The sublevels are counted consecutively up to the highest-energy sublevel within the shell. For example, the $1s$ level ($n = 1$, $l = 0$) is denoted as K_1. The $2s$ level ($n = 2$, $l = 0$) is L_1, while the $2p_{1/2}$ ($n = 2$, $l = 1$, $j = 1/2$) and $2p_{3/2}$ ($n = 2$, $l = 1$, $j = 3/2$) levels are denoted as L_2 and

Table A.2: Conversion between spectroscopic and X-ray notation

n	l	s	j	spectroscopic notation	X-ray notation
1	0	1/2	1/2	$1s$	K
2	0	1/2	1/2	$2s$	L_1
	1	1/2	1/2	$2p_{1/2}$	L_2
			3/2	$2p_{3/2}$	L_3
3	0	1/2	1/2	$3s$	M_1
	1	1/2	1/2	$3p_{1/2}$	M_2
			3/2	$3p_{3/2}$	M_3
	2	1/2	3/2	$3d_{3/2}$	M_4
			5/2	$3d_{5/2}$	M_5
4	0	1/2	1/2	$4s$	N_1
	1	1/2	1/2	$4p_{1/2}$	N_2
			3/2	$4p_{3/2}$	N_3
	2	1/2	3/2	$4d_{3/2}$	N_4
			5/2	$4d_{5/2}$	N_5
	3	1/2	5/2	$4f_{5/2}$	N_6
			7/2	$4f_{7/2}$	N_7

L_3, respectively [127]. Further examples to convert between the two nomenclatures are given in Table A.2.

To describe transitions between different stationary states, either notation can be used. For example, to describe the creation of a $1s$ core hole in a gold atom (Step I), followed by the transition of a $2p_{3/2}$ electron to fill this core hole (Step II), the following description would be used in spectroscopic notation:

$$\text{Step I: } 1s^2 2s^2 2p^6 3s^2 3p^6 3d^{10} 4s^2 4p^6 4d^{10} 4f^{14} 5s^2 5p^6 5d^{10} 6s^1 \rightarrow 1s^1 2s^2 2p^6 3s^2 3p^6 3d^{10} 4s^2 4p^6 4d^{10} 4f^{14} 5s^2 5p^6 5d^{10} 6s^1$$

$$\text{Step II: } 1s^1 2s^2 2p^6 3s^2 3p^6 3d^{10} 4s^2 4p^6 4d^{10} 4f^{14} 5s^2 5p^6 5d^{10} 6s^1 \rightarrow 1s^2 2s^2 2p^5 3s^2 3p^6 3d^{10} 4s^2 4p^6 4d^{10} 4f^{14} 5s^2 5p^6 5d^{10} 6s^1$$

Since it is confusing and redundant to write out the full configuration, the notation is usually reduced to only the subshells involved:

$$\text{Step I: } 1s^2 2p^6 \rightarrow 1s^1 2p^6$$
$$\text{Step II: } 1s^1 2p^6 \rightarrow 1s^2 2p^5$$

In X-ray notation, this would be noted as:

$$\text{Step I: } K\text{-shell ionization}$$
$$\text{Step II: } KL_3 \text{ transition}$$

Auger transitions are denoted by all subshells involved. Assuming a third step to the process explained above, where an Auger electron is emitted, with the energy from the $2p_{3/2}$ electron filling the $1s$ core hole being transferred to a $2p_{1/2}$ electron, the emitted Auger electron would be denoted as KL_3L_2 [127].

There is a third system, the Siegbahn notation, which is used in conjunction with the X-ray (IUPAC) notation, particularly for labeling characteristic X-ray emission lines [309]. This notation uses Greek letters $(\alpha, \beta, \gamma, ...)$ to designate the specific transitions that fill a core hole in a given shell.

For example, transitions from the L-shell ($n = 2$) to fill a K-shell ($n = 1$) hole are labeled as $K\alpha$ lines. Transitions from the M-shell ($n = 3$) to the K-shell are labeled as $K\beta$ lines. This Siegbahn notation is still the standard for naming X-ray sources used in lab-based XPS, such as the common Al$K\alpha$ and Mg$K\alpha$ anodes. These labels specify that the X-rays are generated by the $K\alpha$ emission line within aluminum or magnesium atoms, respectively.

B XPS Measurement Resolution

Observed XPS linewidths result from a convolution of extrinsic and intrinsic broadening mechanisms. Extrinsic contributions arise from the energy distribution of the excitation source and the instrumental resolution of the spectrometer. Intrinsic sources, in contrast, depend on the sample material and the photoemission process itself, such as the finite lifetime of the core hole and interactions with the sample's electrons (particle-hole excitations) and lattice vibrations (phonons).

For unmonochromatized Mg or Al $K\alpha$ X-ray sources, the photon flux has a FWHM of approximately 1 eV [310]. In contrast, synchrotron radiation is far more monochromatic, with a typical broadening of only 100 meV to 200 meV [311]. For BL11, as used in this thesis, the theoretical resolution limit in high-flux mode at $h\nu = 240$ eV is $\frac{\Delta E}{E} \approx \frac{1}{2500}$ [235], which gives a photon energy broadening of $\text{FWHM}_{h\nu} \approx 96$ meV. Given that the beamline was optimized for high photon flux rather than maximum energy resolution in recent years, realistically, the photon energy broadening is larger.

The measured spectrum is also broadened by the contribution of the analyzer [145, 294]. As discussed in Section 3.2, the energy resolution limit of the analyzer is given by:

$$\Delta E_{\mathrm{ana}} = E_{\mathrm{pass}}\left(\frac{w_1 + w_2}{4r_0} + \frac{\alpha^2}{2}\right), \tag{B.1}$$

with w_1 and w_2 being the widths of the entry and exit slits, respectively, α half the acceptance angle of the electron cone at the entry slit, and r_0 the radius of the central path through the hemispherical analyzer [113–115, 312].

For the CLAM IV hemispherical analyzer used in this work, this results in a lower limit of the FWHM of $\mathrm{FWHM}_{\mathrm{ana}} \approx 125\,\mathrm{meV}$, using $w_1 = w_2 = 5\,\mathrm{mm}$ to maximize the count rate. This calculation assumes that the Kuyatt-Simpson criterion

$$\frac{\alpha^2}{2} \leq 0.5\frac{w_1 + w_2}{4r_0}, \tag{B.2}$$

is fulfilled [114].

Intrinsic broadening arises from several sources. The dominant contribution to the broadening of core-level spectra is the finite lifetime of the core-hole created during photoemission. This lifetime broadening does not affect the Fermi edge, however. Other effects, like Franck-Condon vibrational broadening or coupling to phonon modes, may contribute to the broadening of core levels as well as of the Fermi edge, typically accounting for a few tens of meV [145, 313]. Thermal broadening, however, is the dominant intrinsic contribution to the broadening of the Fermi edge [314, 315]. At 300 K, the thermal energy is $k_{\mathrm{B}}T \approx 26\,\mathrm{meV}$, which gives a thermal broadening of $\mathrm{FWHM}_{\mathrm{thermal}} \approx 90\,\mathrm{meV}$ [316].

Taking all estimated contributions into account, the lower limit of the FWHM of the Fermi edge can be calculated:

$$\begin{aligned}
\mathrm{FWHM}_{\mathrm{total}} &= \sqrt{\mathrm{FWHM}_{\mathrm{h}\nu}^2 + \mathrm{FWHM}_{\mathrm{ana}}^2 + \mathrm{FWHM}_{\mathrm{thermal}}^2} \\
&= \sqrt{(96\,\mathrm{meV})^2 + (125\,\mathrm{meV})^2 + (90\,\mathrm{meV})^2} \\
&\approx 182\,\mathrm{meV}
\end{aligned}$$

The extrinsic (instrumental) broadening alone would be:

$$\begin{aligned}
\mathrm{FWHM}_{\mathrm{instr}} &= \sqrt{\mathrm{FWHM}_{\mathrm{h}\nu}^2 + \mathrm{FWHM}_{\mathrm{Ana}}^2} \\
&= \sqrt{(96\,\mathrm{meV})^2 + (125\,\mathrm{meV})^2} \approx 158\,\mathrm{meV}
\end{aligned}$$

It is evident that the instrumental broadening still dominates the thermal broadening at room temperature. As shown in Figure B.1(a), the measured Fermi edge is a convolution of a Fermi-Dirac distribution at 300 K with a Gaussian function representing the total extrinsic broadening. The resulting curve shows excellent agreement with the measured Fermi edge in Figure B.1(b).

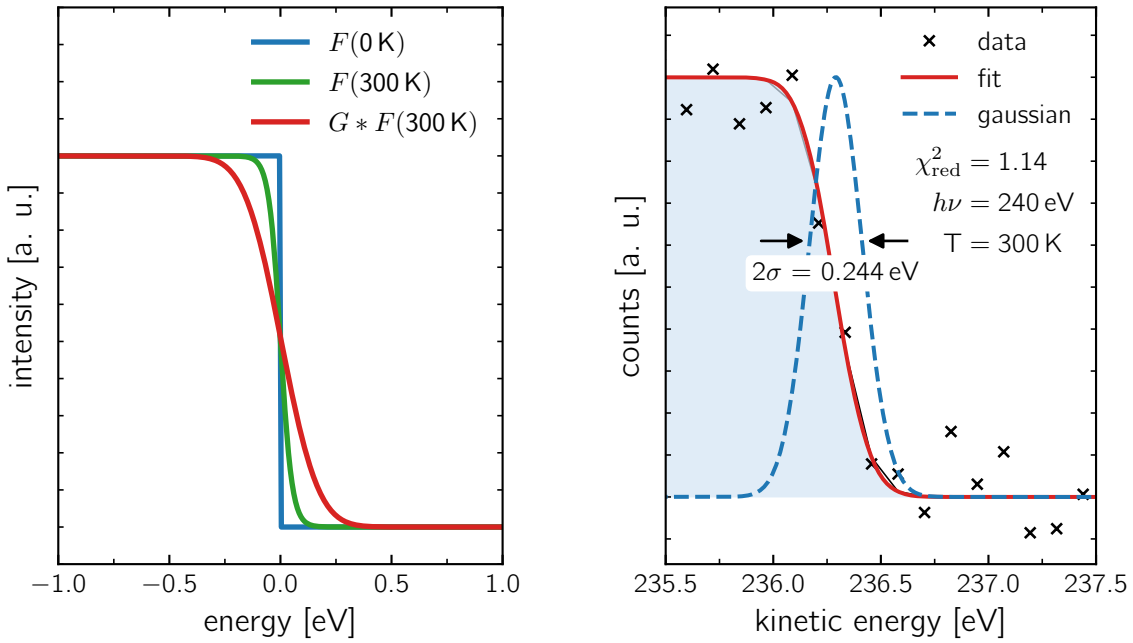

(a) Convolution of a Fermi edge with a Gaussian. **(b)** Gaussian contribution to the Fermi edge.

Figure B.1: (a) Illustration of the measured Fermi edge modeled as a convolution of the Fermi-Dirac distribution $F(T)$ with a Gaussian instrument function G. (b) Determination of the Gaussian contribution to the broadening. The broadened Fermi edges (dark red) are identical in both plots.

In both plots, the sum curve is a convolution of a Fermi-Dirac function at $T = 300\,\mathrm{K}$ with a Gaussian with $\sigma_\mathrm{G} = 123\,\mathrm{meV}$, which gives the best fit result. This corresponds to a fitted Gaussian FWHM of $\mathrm{FWHM}_\mathrm{fit} = 2\sigma_\mathrm{G}\sqrt{2\ln 2} \approx 290\,\mathrm{meV}$. This fitted value is well above the lower limit estimate for the instrumental broadening of 158 meV; the discrepancy can be attributed to the idealizations made in the estimate. Specifically, the theoretical analyzer resolution is a lower limit that neglects non-ideal effects such as space-charge broadening within the electron beam, mechanical imperfections of the spectrometer, and aberrations in the lens system [114, 317–319]. Moreover, the fitted resolution of the experimental setup at BL11 likely falls short of the theoretical limit in high-flux mode at $h\nu = 240\,\mathrm{eV}$ ($\Delta E/E \approx 1/2500$ [235]), as the beamline has not been optimized and calibrated for high resolution in recent years. It should be noted that in the discussion above, since the sample temperature is known to be $T \approx 300\,\mathrm{K}$, the thermal broadening was explicitly accounted for in the Fermi-Dirac distribution. Therefore, the fitted $\mathrm{FWHM}_\mathrm{fit}$ describes only the extrinsic Gaussian broadening contributions and should be compared directly with $\mathrm{FWHM}_\mathrm{instr}$.

Experimentally, the contributions to signal broadening can have either a Gaussian or a Lorentzian character. The extrinsic contributions (photon source and analyzer) as well as the thermal broadening are Gaussian in nature [145]. The finite core-hole lifetime, however, causes a Lorentzian broadening. Other intrinsic contributions are typically negligibly small [313]. The total experimental lineshape is a convolution of these components. Since the convolution of multiple Gaussians is itself a Gaussian, the instrumental and thermal broadening can be treated as a single effective Gaussian

function. Consequently, core-level signals in XPS are best described by a Voigt profile, which is a convolution of a Gaussian and a Lorentzian [294], or as a convolution of the Doniach-Šunjić-lineshape with a Gaussian for asymmetric peak signals.

In this thesis, the Gaussian contribution used in fitting core-level spectra was always constrained to the total Gaussian broadening determined from the Fermi edge fit. Only a minor adjustment of $\pm 5\%$ was allowed during the fitting procedure.

However, for defining the measurement resolution, the FWHM is often not the metric of choice. Instead, 2σ or the *16-84 rule* is applied, which typically results in a smaller numerical value than the FWHM [320, 321].

B.1 The 2σ Resolution Criterion

As mentioned, 2σ is often used to define the experimental energy resolution. This has a practical, intuitive basis and explains why the energy difference between the 16% and 84% intensity points on the Fermi edge (the 16-84 rule) is often used as a resolution metric [322].

The measured Fermi edge at non-zero temperature is a Fermi-Dirac distribution convoluted with the instrumental Gaussian broadening. At $T = 0\,\mathrm{K}$, the Fermi-Dirac distribution becomes a Heaviside step function. The convolution of a Heaviside step function with a Gaussian is equivalent to the integral of that Gaussian, which is the Gaussian error function. Since the thermal broadening of the Fermi edge itself is Gaussian, and the convolution of two Gaussians is a Gaussian itself, the measured Fermi edge has the shape of the corresponding Gaussian error function of the Gaussian of the convolution of instrumental and thermal broadening Gaussians. The integral of a Gaussian reaches approximately 16% and 84% of its total height at a distance of $\pm\sigma$ from its center, as shown in Figure B.2(a). These positions correspond to the inflection points of the Gaussian function itself. The ability to resolve two adjacent peaks depends on their separation relative to their widths. If a distance greater than 2σ separates two identical Gaussian peaks, a distinct minimum appears between them, as shown in Figure B.2(b). This is analogous to the Rayleigh criterion in optics [323]. Two ideal, delta-function-like spectral lines would be just resolvable as two distinct peaks after being broadened by the instrument if they are separated by more than 2σ. Therefore, using the 16-84 rule or extracting 2σ by fitting the Fermi edge is a physically meaningful definition of the instrumental resolution. For our setup, this gives a resolution of $2\sigma = 246\,\mathrm{meV}$, as shown in Figure B.1(b).

This resolution value defines the minimum separation required to distinguish two sharp features as separate peaks. It does not, however, prevent the fitting of components that are closer together, provided a robust fitting model with physically meaningful constraints is used. Once the total Gaussian broadening is determined from the Fermi edge, this value can be used as a primary constraint in subsequent core-level fitting. If the core-level spectra are measured with the same excitation energy, analyzer settings, and sample temperature as the Fermi edge, the Gaussian contribution to their broadening can be treated as a fixed parameter.

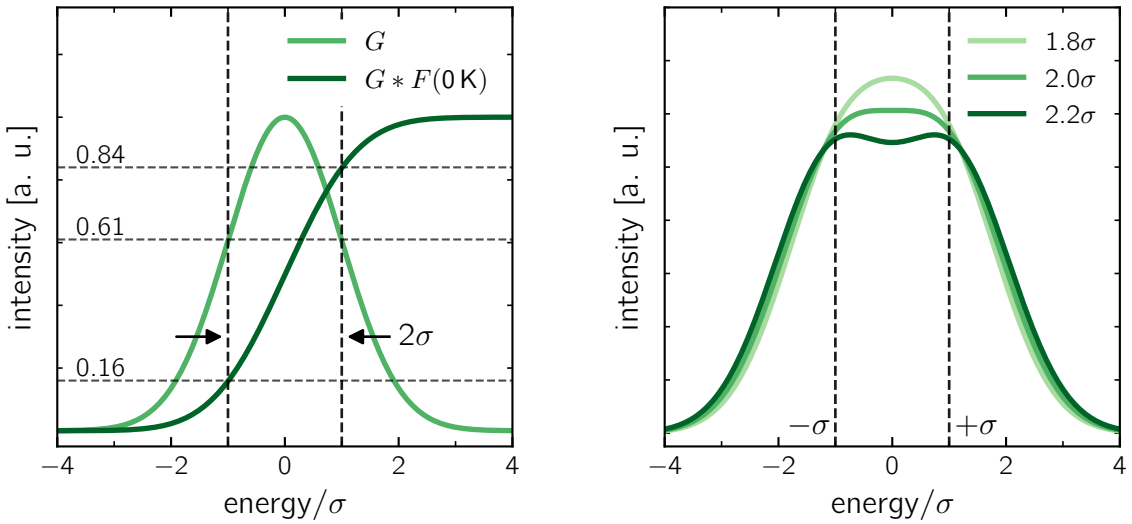

(a) The 2σ environment

(b) Two Gaussians shifted and added.

Figure B.2: (a) Plot of a Gaussian G and its integral, which is equal to the convolution of a Gaussian and the Fermi edge for $T = 0\,\mathrm{K}$ (b) Plot of two Gaussians with different relative shifts of their centers.

For the core-hole lifetime, databases provide reliable initial estimates for the Lorentzian broadening of many elements [324, 325]. By combining these constraints, a fixed Gaussian width from the Fermi edge and a literature-based Lorentzian width, it is possible to successfully deconvolve spectral components separated by energies as small as 50 meV, depending on their relative intensities and the signal-to-noise ratio.

C XPS Coverage Determination

In this work, the Sn coverage was determined by analyzing peak intensities in the X-ray photoelectron survey spectra. To determine the thickness of adsorbate layers consisting of several atomic monolayers, the attenuation of peak intensities originating from the substrate is typically used [124]. The intensity of the substrate peak scales according to:

$$N_{\mathrm{sub}}(\Theta) = N_{\mathrm{sub},0}(\Theta) \cdot \exp\left(\frac{-t}{\Lambda_e^{\mathrm{overl}}(E_{\mathrm{sub}})\cos(\Theta)}\right), \tag{C.1}$$

where $N_{\mathrm{sub},0}(\Theta)$ is the intensity measured for the substrate peak in the absence of an overlayer, t is the thickness of the overlayer, $\Lambda_e^{\mathrm{overl}}(E_{\mathrm{sub}})$ is the attenuation length for substrate photoelectrons in the adlayer, and Θ is the photoelectron emission angle.

However, when analyzing coverages of a small number of atomic monolayers or even less than a single atomic monolayer, the attenuation of the substrate photoelectron intensity by the adlayer becomes negligible. Therefore, the adlayer can be assumed to be non-attenuating. It has been demonstrated that this assumption yields high precision for submonolayer coverages ranging from 0.02 ML to 3 ML [125, 326, 327]. The coverage is defined here as the ratio between the number of Sn atoms forming the overlayer and

the number of Au atoms in a single atomic layer of the unreconstructed Au(111) surface. One monolayer is therefore defined by an atomic density of 1.391×10^{15} atoms/cm^2, which corresponds to the packing density of the unreconstructed Au(111) surface.

Assuming a non-attenuating submonolayer adlayer, the coverage $C(\Theta)$ can be expressed as [124]:

$$C(\Theta) = \frac{N_{\mathrm{Sn3d}}(\Theta)}{N_{\mathrm{Au4f}}(\Theta)} \cdot \frac{\Omega_0(E_{\mathrm{Au4f}}) \cdot A_0(E_{\mathrm{Au4f}})}{\Omega_0(E_{\mathrm{Sn3d}}) \cdot A_0(E_{\mathrm{Sn3d}})} \frac{\frac{\mathrm{d}\sigma_{\mathrm{Au4f}}}{\mathrm{d}\Omega}}{\frac{\mathrm{d}\sigma_{\mathrm{Sn3d}}}{\mathrm{d}\Omega}} \cdot \frac{\Lambda_e^{\mathrm{Au}}(E_{\mathrm{Au4f}}) \cdot \cos(\Theta)}{d_{\mathrm{Au}}} . \tag{C.2}$$

Here, $N_{\mathrm{Sn3d}}(\Theta)$ and $N_{\mathrm{Au4f}}(\Theta)$ are the photoemission peak areas of the adlayer (Sn $3d$) and the substrate (Au $4f$) at a given photoemission angle, Θ, with respect to the surface normal.

The factor $\frac{\Omega_0(E_{\mathrm{Au4f}}) \cdot A_0(E_{\mathrm{Au4f}})}{\Omega_0(E_{\mathrm{Sn3d}}) \cdot A_0(E_{\mathrm{Sn3d}})}$ represents the ratio of the acceptance solid angle Ω_0 and the effective specimen area A_0 for the different photoelectron signals emerging from Au $4f$ and Sn $3d$. This term cancels out, as the spectrometer was set to uniform angular and spatial acceptance, and the area illuminated by the photon flux from the synchrotron beamline is smaller than the analyzer's field of view.

Since the spectrometer axis and the incident beam in the experimental setup at BL11 are in the "magic angle" configuration ($\alpha \approx 54.7°$), the angular and Reilmann asymmetry dependency of the differential cross-section becomes unity [124]. Consequently, the differential cross-section becomes independent of the asymmetry parameter β and simplifies to $\frac{\mathrm{d}\sigma_k}{\mathrm{d}\Omega} = \frac{\sigma(E_k)}{4\pi}$, where $\sigma(E_k)$ is the tabulated Scofield cross-section [328].

The EAL, $\Lambda_e^{\mathrm{Au}}(E_{\mathrm{Au4f}})$, is the attenuation length for Au 4f photoelectrons in the Au substrate. As mentioned above, the Sn adlayer is assumed to be non-attenuating. The EAL was calculated using NIST SRD-82 [329]. d_{Au} is the mean separation between Au(111) layers. All parameters used for the calculation of $C(\Theta)$ are listed in Table C.1.

To determine Sn coverages, peak intensities of the Sn $3d$ and Au $4f$ signals were obtained by fitting the respective signals in the survey spectra. As survey spectra were measured for multiple emission angles (at least $\Theta = 0°$ and $\Theta = 60°$), the reported coverage value is the average of these measurements, and the reported error corresponds to the standard deviation of the determined coverages across the different emission angles.

Table C.1: XPS quantification parameters for the coverage calculation. For the spectra, $h\nu = 700$ eV was used and emission angles were in the range $\Theta = 0°$ to $60°$.

Parameter	Au	Sn
Analyzed photoelectron signal	Au 4f	Sn 3d
Kinetic energy [eV]	615.5	212.4
Scofield cross-section σ [Mb]	1.993	2.4805
EAL [Å]	8.77	–
d_{Au} [Å]	2.36	–

D Tight-Binding Hamiltonian for Honeycomb Structures

This section derives the Hamiltonian for graphene within the nearest-neighbor tight-binding approximation. This model captures the low-energy electronic properties of honeycomb lattices, including the characteristic Dirac cones.

D.1 Tight-Binding Hamiltonians

The Schrödinger equation for an electron in the periodic potential of a lattice of ions is

$$\left(-\frac{\hbar^2}{2m}\nabla^2 + V_{\text{ion}}(\boldsymbol{r})\right)\psi(\boldsymbol{r}) = E\psi(\boldsymbol{r})\,, \tag{D.1}$$

where $V_{\text{ion}}(\boldsymbol{r}) = \sum_{\boldsymbol{R}} V_{\text{i}}(\boldsymbol{r}-\boldsymbol{R})$. Here, $V_{\text{i}}(\boldsymbol{r}-\boldsymbol{R})$ is the potential from a single ion at position $\boldsymbol{R}$ [330].

In the tight-binding limit, electrons are tightly localized at individual ions, and localized atomic orbitals well approximate their wavefunctions. All other ions are, from the electron's perspective, negligible, so the single-particle states approximately solve

$$\left(-\frac{\hbar^2}{2m}\nabla^2 + V_{\text{i}}(\boldsymbol{r})\right)\varphi_n(\boldsymbol{r}) = E_n\varphi_n(\boldsymbol{r})\,. \tag{D.2}$$

When $\varphi_n(\boldsymbol{r})$ extends to neighboring ions, the electron is influenced by more than just its parent ion [330]. In the tight-binding approach, a correction term is introduced, which describes the coupling between different localized states by matrix elements:

$$\langle\varphi_n(\boldsymbol{r}-\boldsymbol{R})|H|\varphi_n(\boldsymbol{r})\rangle := -t_n(\boldsymbol{R})\,, \tag{D.3}$$

where $t_n(\boldsymbol{R})$ is the hopping amplitude between sites separated by $\boldsymbol{R}$ [330]. In 2D honeycomb lattices, often, uniform nearest-neighbor hopping is assumed, so that $-t_n(\boldsymbol{R}) \approx -t$ can be approximated [68].

In second quantization, the Hamiltonian becomes:

$$H = -\sum_{n,\,\boldsymbol{R},\,\boldsymbol{R}'} t_n(\boldsymbol{R}-\boldsymbol{R}')\, c_n^\dagger(\boldsymbol{R})\, c_n(\boldsymbol{R}')\,, \tag{D.4}$$

where $c_n^\dagger(\boldsymbol{R})$ creates an electron in state $\varphi_n(\boldsymbol{r}-\boldsymbol{R})$, and $c_n(\boldsymbol{R}')$ annihilates one in $\varphi_n(\boldsymbol{r}-\boldsymbol{R}')$ [68].

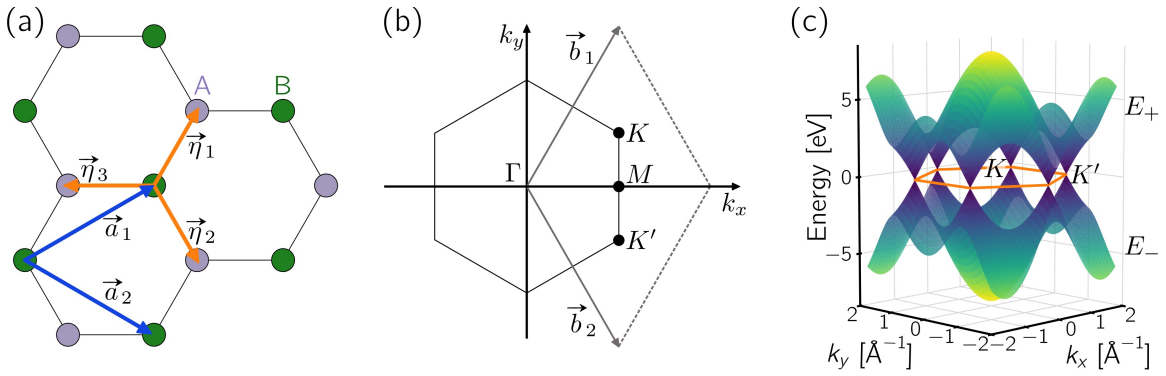

Figure D.1: (a) Graphene's real-space unit cell showing the A and B sublattices. The lattice vectors $\boldsymbol{a}_i$ and next-neighbour vectors $\boldsymbol{\eta}_i$ are shown as well. (b) Hexagonal Brillouin zone in reciprocal space, highlighting high-symmetry points. (c) Band structure calculated using a tight-binding model, assuming next-neighbor hopping with $t = 2.8\,\text{eV}$ [50], showing Dirac cones at K and K' points. A similar band structure, taking into account in addition next-nearest neighbour hopping, is shown in Figure 2.3.

D.2 Graphene in the Tight-Binding Model

Graphene consists of carbon atoms arranged in a single-layer honeycomb structure, as shown in Figure D.1(a). The lattice vectors [50] are:

$$\boldsymbol{a}_1 = \frac{d}{2}\big(3,\ \sqrt{3}\big)\,, \qquad \boldsymbol{a}_2 = \frac{d}{2}\big(3,\ -\sqrt{3}\big)\,, \tag{D.5}$$

where $d = |\boldsymbol{\eta}_1| = |\boldsymbol{\eta}_2| = |\boldsymbol{\eta}_3|$ is the nearest-neighbor C–C distance and the nearest-neighbor vectors [50] are given by:

$$\boldsymbol{\eta}_1 = \frac{d}{2}\big(1,\ \sqrt{3}\big)\,, \qquad \boldsymbol{\eta}_2 = \frac{d}{2}\big(1,\ -\sqrt{3}\big)\,, \qquad \boldsymbol{\eta}_3 = d(-1,\ 0)\,. \tag{D.6}$$

The reciprocal lattice vectors [50] are:

$$\boldsymbol{b}_1 = \frac{2\pi}{3d}\big(1,\ \sqrt{3}\big)\,, \qquad \boldsymbol{b}_2 = \frac{2\pi}{3d}\big(1,\ -\sqrt{3}\big)\,. \tag{D.7}$$

The first Brillouin zone, as shown in Figure D.1(b), reflects the hexagonal symmetry. The Dirac points K, K' are located at

$$K = \frac{2\pi}{3d}\left(1,\ \frac{1}{\sqrt{3}}\right)\,, \qquad K' = \frac{2\pi}{3d}\left(1,\ -\frac{1}{\sqrt{3}}\right)\,. \tag{D.8}$$

Due to the bipartite lattice, electrons only hop from an atom on sublattice A to an atom on B and vice versa as long as only nearest-neighbor hopping is taken into account [50, 64]. The corresponding creation and annihilation operators are $A^\dagger(\boldsymbol{R})$, $B^\dagger(\boldsymbol{R})$ and $A(\boldsymbol{R})$, $B(\boldsymbol{R})$, respectively.

The tight-binding Hamiltonian (D.4), considering only the relevant p_z orbitals and a single nearest-neighbor hopping parameter t (hopping between different sublattices), becomes:

$$H_{\mathrm{nn}} = -t \sum_{\boldsymbol{R},\, n=1}^{3} \left[A^{\dagger}(\boldsymbol{R})\, B(\boldsymbol{R} + \boldsymbol{\eta}_n) + B^{\dagger}(\boldsymbol{R} + \boldsymbol{\eta}_n)\, A(\boldsymbol{R}) \right]. \tag{D.9}$$

This can be written more compactly as:

$$H_{\mathrm{nn}} = -t \sum_{\boldsymbol{R},\, n=1}^{3} \left[A^{\dagger}(\boldsymbol{R})\, B(\boldsymbol{R} + \boldsymbol{\eta}_n) \right] + \mathrm{h.c.}\,, \tag{D.10}$$

where h.c. denotes the Hermitian conjugate, reflecting that hopping from B to A is also included [50, 68].

To diagonalize the Hamiltonian, it is expressed in momentum space:

$$A(\boldsymbol{R}) = \frac{1}{\sqrt{N}} \sum_{\boldsymbol{k}} A(\boldsymbol{k})\, \exp\{i\boldsymbol{k} \cdot \boldsymbol{R}\}\,, \qquad B(\boldsymbol{R}) = \frac{1}{\sqrt{N}} \sum_{\boldsymbol{k}} B(\boldsymbol{k})\, \exp\{i\boldsymbol{k} \cdot \boldsymbol{R}\}\,, \tag{D.11}$$

where N is the number of unit cells [49, 68]. Substituting these into the Hamiltonian yields:

$$H_{\mathrm{nn}} = \sum_{\boldsymbol{k}} \left[-t \sum_{n=1}^{3} \exp\left(i\boldsymbol{k} \cdot \boldsymbol{\eta}_n\right) A^{\dagger}(\boldsymbol{k})\, B(\boldsymbol{k}) + \mathrm{h.c.} \right]. \tag{D.12}$$

Because the Hamiltonian couples the A and B sublattices, it is convenient to define the *spinor*, containing the two operators $A(\boldsymbol{k})$ and $B(\boldsymbol{k})$:

$$\psi(\boldsymbol{k}) = \begin{pmatrix} A(\boldsymbol{k}) \\ B(\boldsymbol{k}) \end{pmatrix} \quad \text{and} \quad \psi^{\dagger}(\boldsymbol{k}) = \left(A^{\dagger}(\boldsymbol{k}),\, B^{\dagger}(\boldsymbol{k}) \right). \tag{D.13}$$

The spinor behaves similarly to an electron spin, as will be explained later in (D.25) [50]. Using this spinor notation, the Hamiltonian can be written compactly as:

$$H = \sum_{\boldsymbol{k}} \psi^{\dagger}(\boldsymbol{k})\, H_{\mathrm{B}}(\boldsymbol{k})\, \psi(\boldsymbol{k})\,, \tag{D.14}$$

where $H_{\mathrm{B}}(\boldsymbol{k})$ is the Bloch Hamiltonian:

$$H_{\mathrm{B}}(\boldsymbol{k}) = \begin{pmatrix} 0 & \xi(\boldsymbol{k}) \\ \xi^{*}(\boldsymbol{k}) & 0 \end{pmatrix}, \tag{D.15}$$

and

$$\xi(\boldsymbol{k}) = -t \sum_{j=1}^{3} \exp\left\{ i\boldsymbol{k} \cdot \boldsymbol{\eta}_j \right\}, \tag{D.16}$$

where t is the hopping energy or hopping amplitude [50]. Diagonalizing $H_{\mathrm{B}}(\boldsymbol{k})$ [50, 64, 66], yields the energy dispersion:

$$E_{\pm}(\boldsymbol{k}) = \pm t\sqrt{3 + 2\cos\left(\sqrt{3}k_y d\right) + 4\cos\left(\frac{\sqrt{3}}{2}k_y d\right)\cos\left(\frac{3}{2}k_x d\right)}\,. \tag{D.17}$$

The resulting spectrum consists of two bands touching at the K and K' points, as shown in Figure D.1(c).

If next-nearest-neighbor hopping (hopping within the same sublattice) is additionally taken into account, the energy bands are modified to:

$$E_{\pm}(\boldsymbol{k}) = \pm t\sqrt{3 + f(\boldsymbol{k})} - t' f(\boldsymbol{k})\,, \tag{D.18}$$

where

$$f(\boldsymbol{k}) = 2\cos\left(\sqrt{3}k_y d\right) + 4\cos\left(\frac{\sqrt{3}}{2}k_y d\right)\cos\left(\frac{3}{2}k_x d\right), \tag{D.19}$$

and t' is the next-nearest-neighbor hopping amplitude [50]. The value of t' is not precisely known but is estimated [66] to lie in the range $0.02t \leq t' \leq 0.2t$. The energy bands of graphene, taking into account the next-nearest-neighbor hopping with $t' = 0.2\,\mathrm{eV}$, are plotted in the main manuscript in Figure 2.3.

D.3 Dirac Physics

The two bands in Equation (D.17) touch at the K and K' points and are otherwise well separated. To analyze the low-energy excitations of graphene, it is therefore appropriate to expand the Hamiltonian around, e.g., the K' point (expanding around K yields an identical result). For a small momentum deviation $\boldsymbol{q}$ from K', the structure factor becomes:

$$\xi(\boldsymbol{K}' + \boldsymbol{q}) \approx -\frac{3td}{2}\exp\left\{-\frac{2\pi i}{3}\right\}(q_y + iq_x)\,, \tag{D.20}$$

where $\boldsymbol{q}$ is small compared to the reciprocal lattice vectors [50, 64].

Substituting this expansion for $\xi(\boldsymbol{K}' + \boldsymbol{q})$ [67] back into the Bloch Hamiltonian matrix (D.15) yields the Hamiltonian near the K' point:

$$H_{\mathrm{B}}(\boldsymbol{K}' + \boldsymbol{q}) \approx -\frac{3td}{2}\begin{pmatrix} 0 & \exp\{-\frac{2\pi i}{3}\}(q_y + iq_x) \\ \exp\{\frac{2\pi i}{3}\}(q_y - iq_x) & 0 \end{pmatrix}. \tag{D.21}$$

The complex phase factor can be removed by applying a suitable unitary transformation (gauge transformation) to the spinor basis. Using the Pauli matrices

$$\sigma_x = \begin{pmatrix} 0 & 1 \\ 1 & 0 \end{pmatrix}, \qquad \sigma_y = \begin{pmatrix} 0 & -i \\ i & 0 \end{pmatrix}, \tag{D.22}$$

and defining the Fermi velocity $v_{\mathrm{F}} = \frac{3td}{2\hbar}$, which represents the group velocity of the electrons near the Dirac points, the effective Hamiltonian takes the form:

$$H_{\mathrm{D}}(\boldsymbol{K}' + \boldsymbol{q}) = v_{\mathrm{F}}\hbar\big(\sigma_x q_x + \sigma_y q_y\big)\,. \tag{D.23}$$

This is known as the Dirac Hamiltonian. The corresponding eigenvalues are linear in momentum:

$$E_{\mathrm{D}} = \pm\hbar v_{\mathrm{F}}|\boldsymbol{q}|\,, \tag{D.24}$$

and the eigenfunctions are given by:

$$\psi_{\pm} = \frac{1}{\sqrt{2}}\left(\exp\left(\frac{i\vartheta_q}{2}\right),\ \pm\exp\left(-\frac{i\vartheta_q}{2}\right)\right)^{\mathrm{T}}, \tag{D.25}$$

where $\vartheta_q = \arctan\left(\frac{q_y}{q_x}\right)$ is the angle of the momentum vector $\boldsymbol{q}$ relative to the x-axis [49, 64, 68].

Since $\boldsymbol{q}$ originates from K', the eigenfunctions describe a circular winding around the Dirac point. Notably, a full 2π rotation of $\boldsymbol{q}$ results in a phase shift of π (a Berry phase of π) for the wavefunction. Only after two full rotations (4π) does the wavefunction return to its initial value. This behavior is characteristic of a spinor. Here, the spinor $\psi(\boldsymbol{k}) = (A(\boldsymbol{k}), B(\boldsymbol{k}))^{\mathrm{T}}$ represents the amplitudes on the A and B sublattices, and the sublattice degree of freedom behaves like a spin-$\frac{1}{2}$ particle, referred to as *pseudospin*. The sublattice symmetry protects this topological Berry phase π and is responsible for many of graphene's unique electronic properties, such as the suppression of backscattering [67].

A similar derivation around K yields $H(\boldsymbol{K} + \boldsymbol{q}) = H^*(\boldsymbol{K}' + \boldsymbol{q})$, leading to an identical energy spectrum as in Equation (D.24). These two contributions are combined to form the low-energy Hamiltonian presented in Equation (2.2) of the main text.

The behavior of the spinor $\psi(\boldsymbol{k})$ is directly tied to the bipartite sublattice symmetry. If a mass term is introduced (e.g., via spin-orbit coupling) that breaks this symmetry or couples the sublattices to open a gap, the honeycomb lattice can exhibit topological phases. For advanced discussions on topological insulators and edge states in this system, see Refs. [64, 67, 69, 331].

E Valence Band Spectra of Sn/Au(111)

This section presents the complete set of recorded valence band spectra for the clean Au(111) substrate, the Au_2Sn-alloy, the striped phase, and the X-phase. For these structural phases, valence band dispersion cuts were recorded along both the $\Gamma - K$ and $\Gamma - M$ directions. However, for the $\sqrt{7}$-phase, only a cut along $\Gamma - M$ was recorded due to limited beam time.

Due to limited experimental resolution, particularly near the Fermi edge, which is especially crucial for characterizing 2D electronic properties, no detailed analysis of the

valence band region is done besides the comparison presented in Chapter 7 and the analysis of the clean Au(111) band structure, presented in Section 5.1. Consequently, the data are presented here primarily for reference and without further discussion.

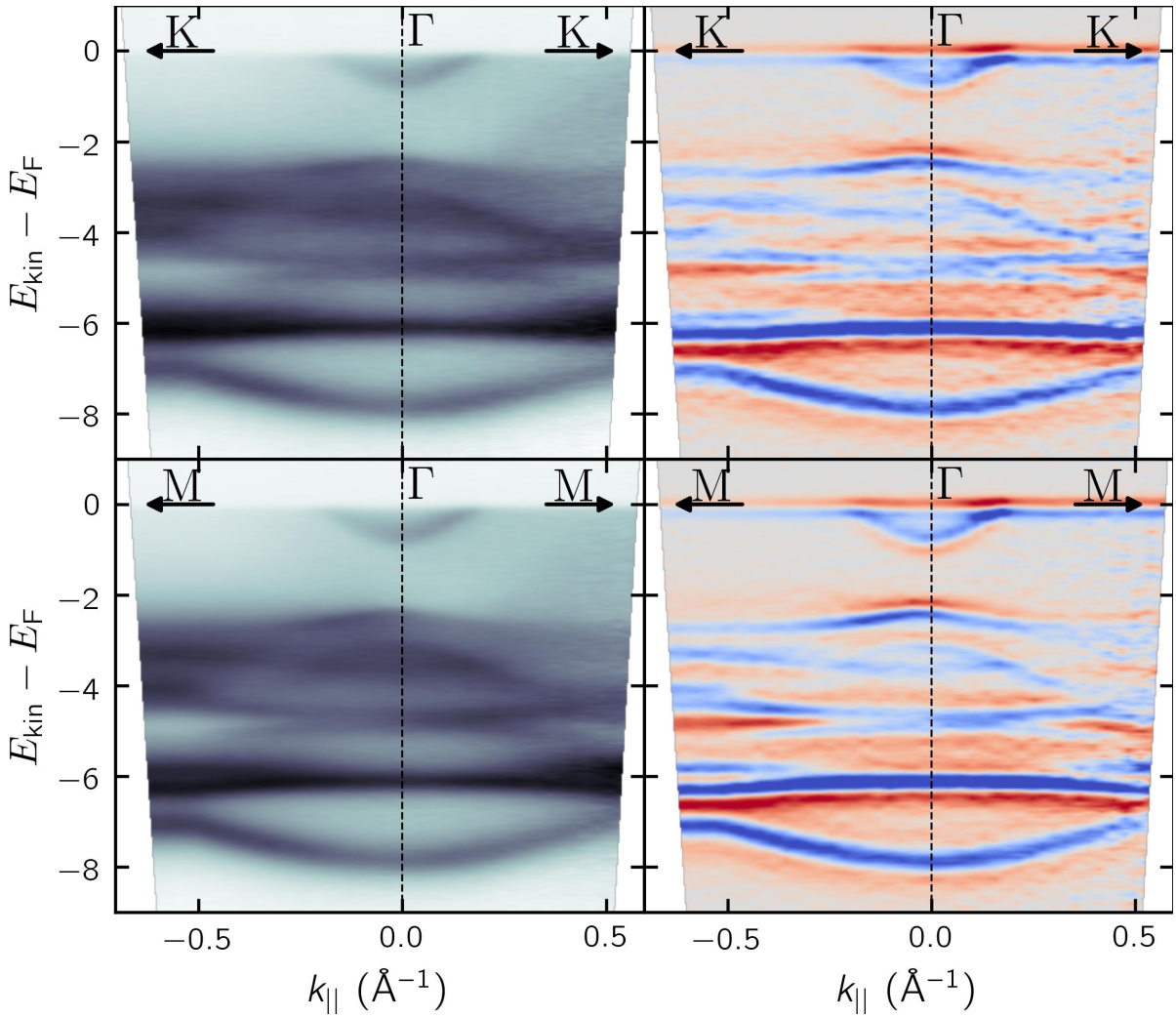

Figure E.1: Valence band measurements of the clean Au(111). Cuts along $\Gamma - K$ and $\Gamma - M$ are shown on the left, with the second derivative being shown on the right.

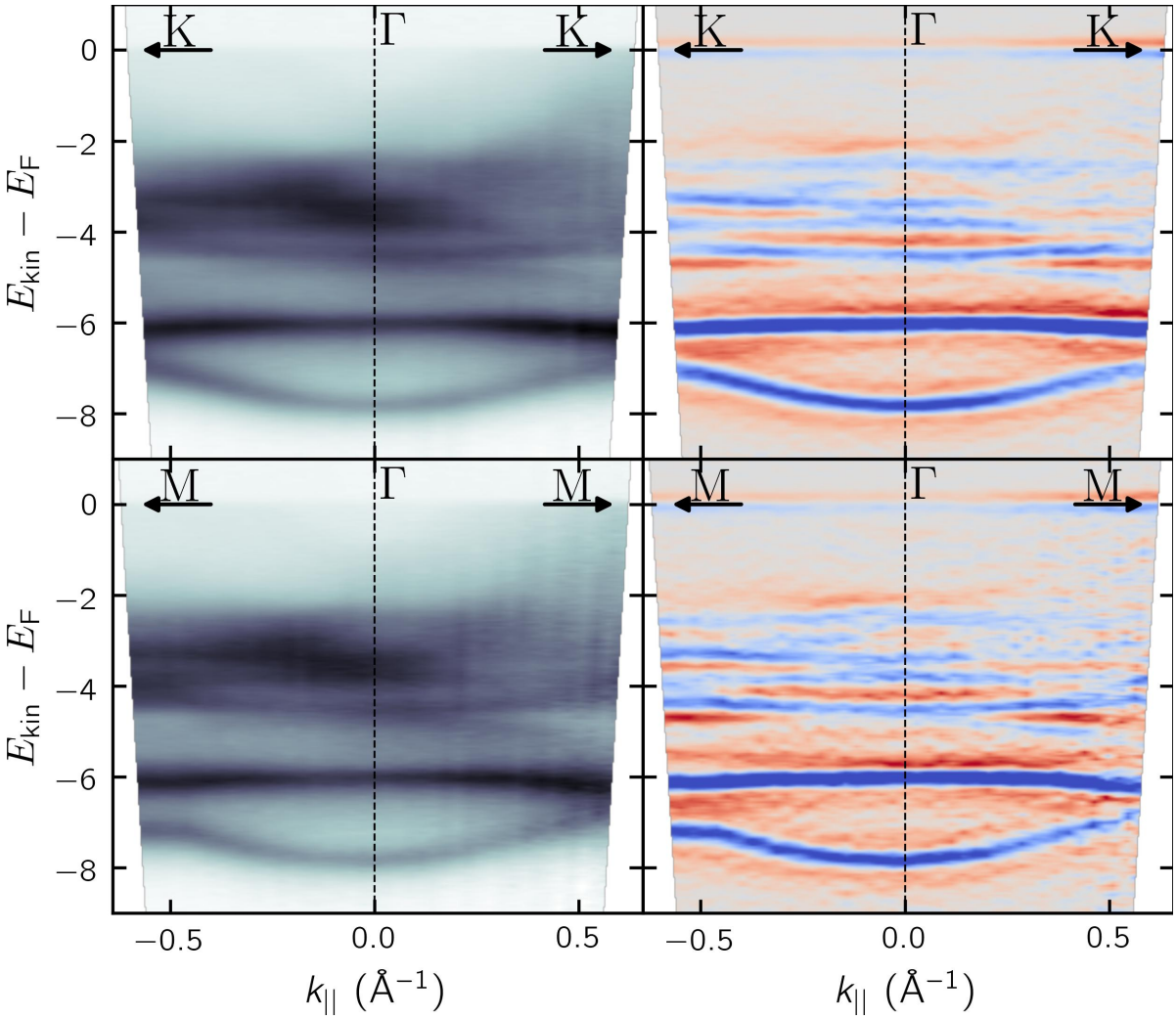

Figure E.2: Valence band measurements of the Au_2Sn substitutional surface alloy observed at 0.33 ML. Cuts along $\Gamma - K$ and $\Gamma - M$ are shown on the left, with the second derivative being shown on the right.

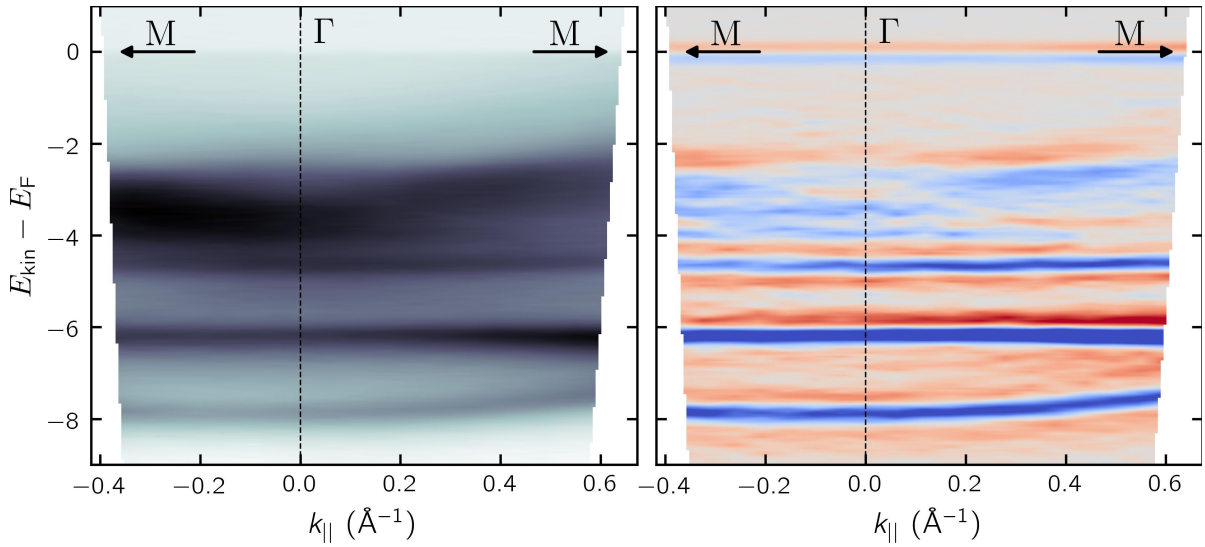

Figure E.3: Valence band measurements of the $\sqrt{7}$-phase observed at 0.45 ML. Only a cut along $\Gamma - M$ is shown on the left, with the second derivative being shown on the right.

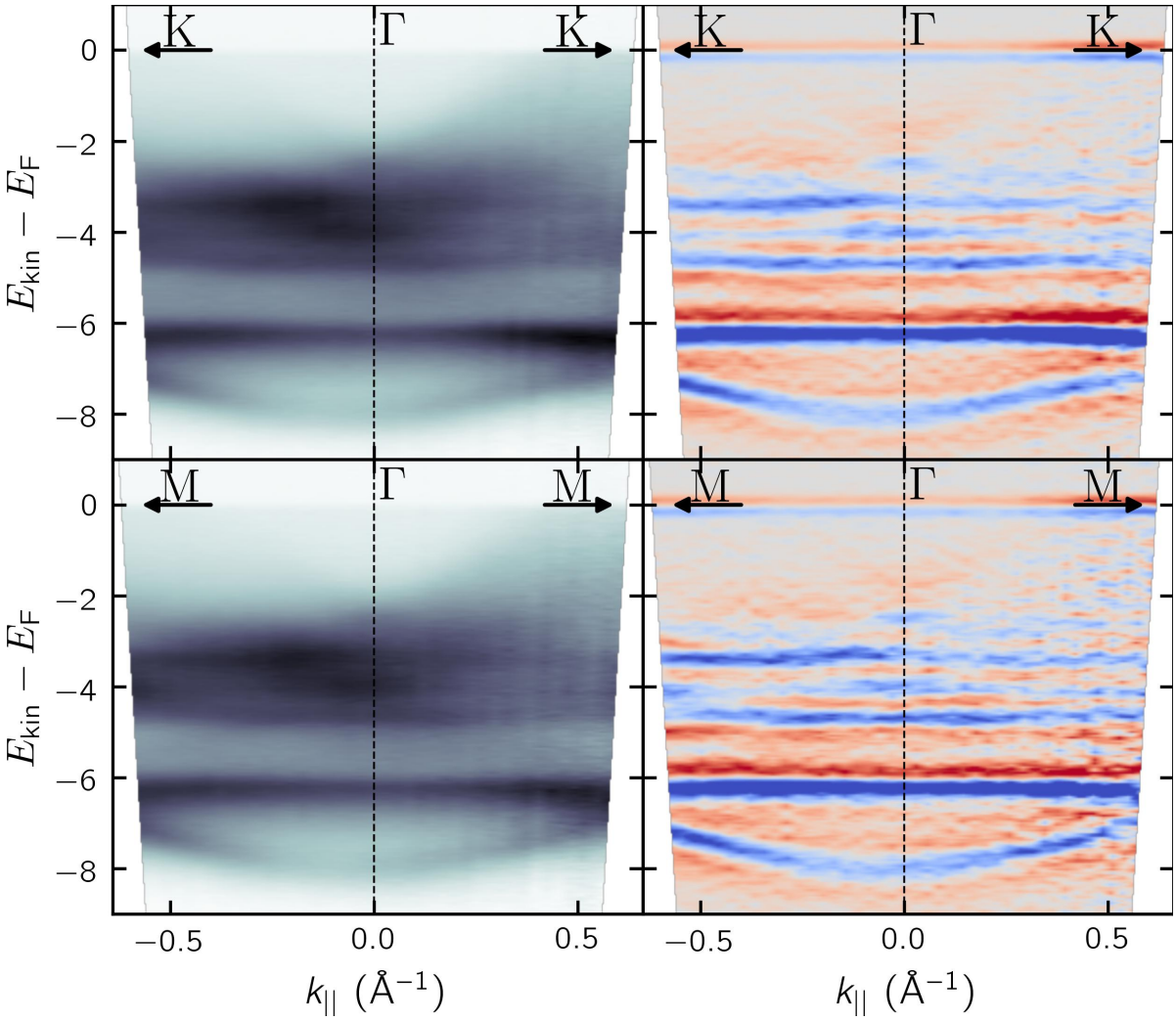

Figure E.4: Valence band measurements of the striped phase observed at 0.55 ML. Cuts along $\Gamma - K$ and $\Gamma - M$ are shown on the left, with the second derivative being shown on the right.

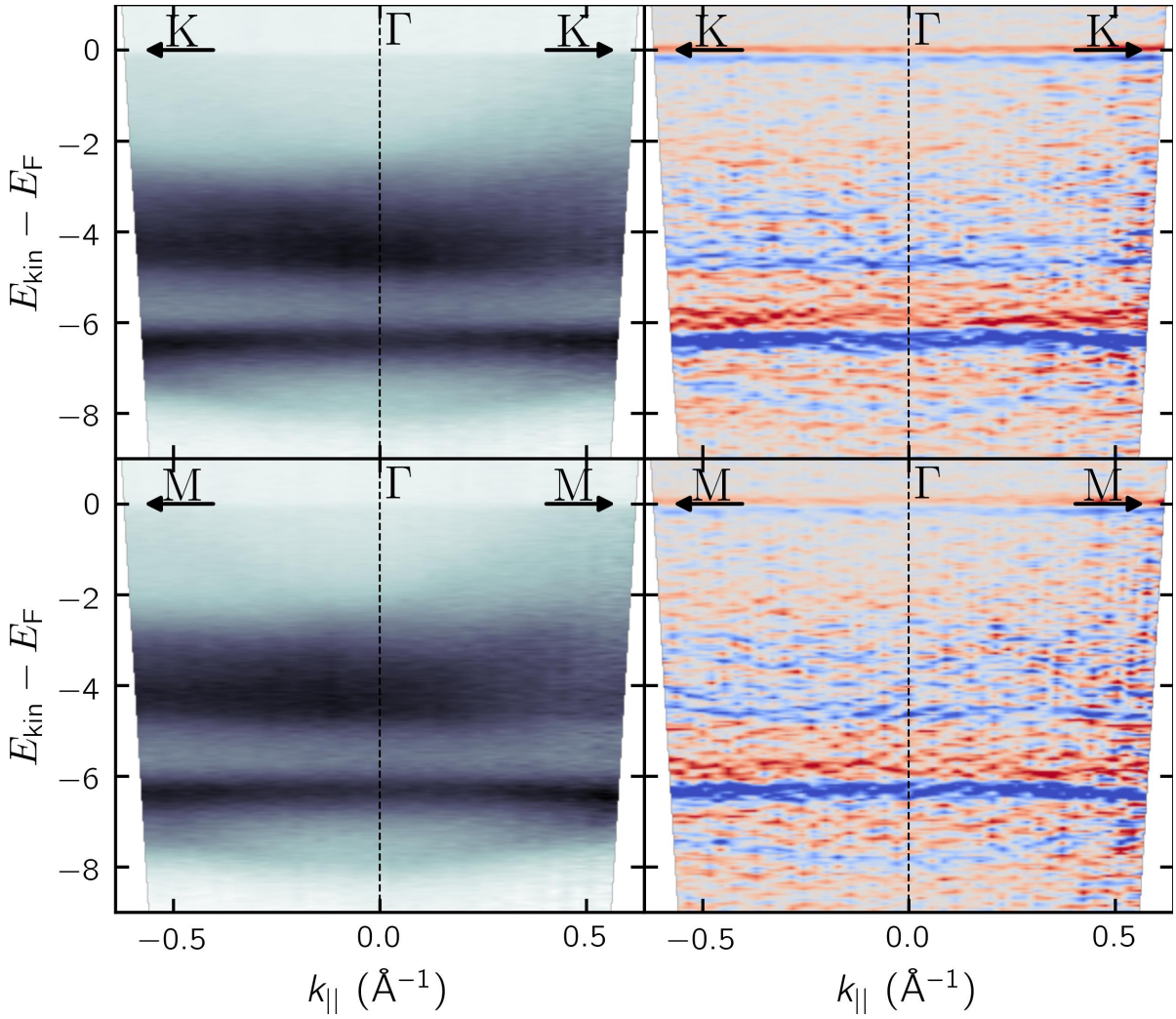

Figure E.5: Valence band measurements of the X-phase observed at 0.66 ML. Cuts along $\Gamma - K$ and $\Gamma - M$ are shown on the left, with the second derivative being shown on the right.

F Influence of the STM Tip on the X-phase

As shown in Figure F.1, the STM tip appears to significantly influence the structural arrangement of the topmost Sn layer in the X-phase. A sequence of STM images obtained during continuous scans is presented in Figure F.1(a)–(c), where all images correspond to downward scan directions. To determine whether the STM tip is the primary driver of the observed rearrangements or if spontaneous diffusion of atoms at room temperature causes the structural changes, the scanning was paused for 260 min before recording the frame shown in Figure F.1(d).

Comparing Figure F.1(c) and (d), some structural modifications are still evident, suggesting that limited spontaneous reorganization may occur over longer timescales. However, the extent of these changes is relatively small compared to the pronounced modifications observed during continuous scanning. Between Figure F.1(a) and (c), acquired over 140 min of continuous rastering, the morphology undergoes significant modification, supporting the conclusion that the STM tip actively induces rearrangement in the weakly bound topmost Sn layer.

Notably, regions near the right edges of each frame, where the tip changes direction, show fewer modifications than the central scanning region. Additionally, near the scan reversal edge, a ”wall” of disordered Sn atoms appears with an increased number of scans, suggesting that the tip may be displacing and redepositing Sn adatoms during rastering.

Strong tip-adsorbate interactions frequently destabilized tunneling conditions during measurements of the X-phase. Achieving atomic resolution for Sn overlayers on Au(111) has proven generally challenging in the literature: Sadhukhan et al. [41] and Maniraj et al. [43] reported comparable resolution for the $\sqrt{7}$-phase, whereas Pang et al. [42] did not achieve clear atomic resolution of the X-phase at all.

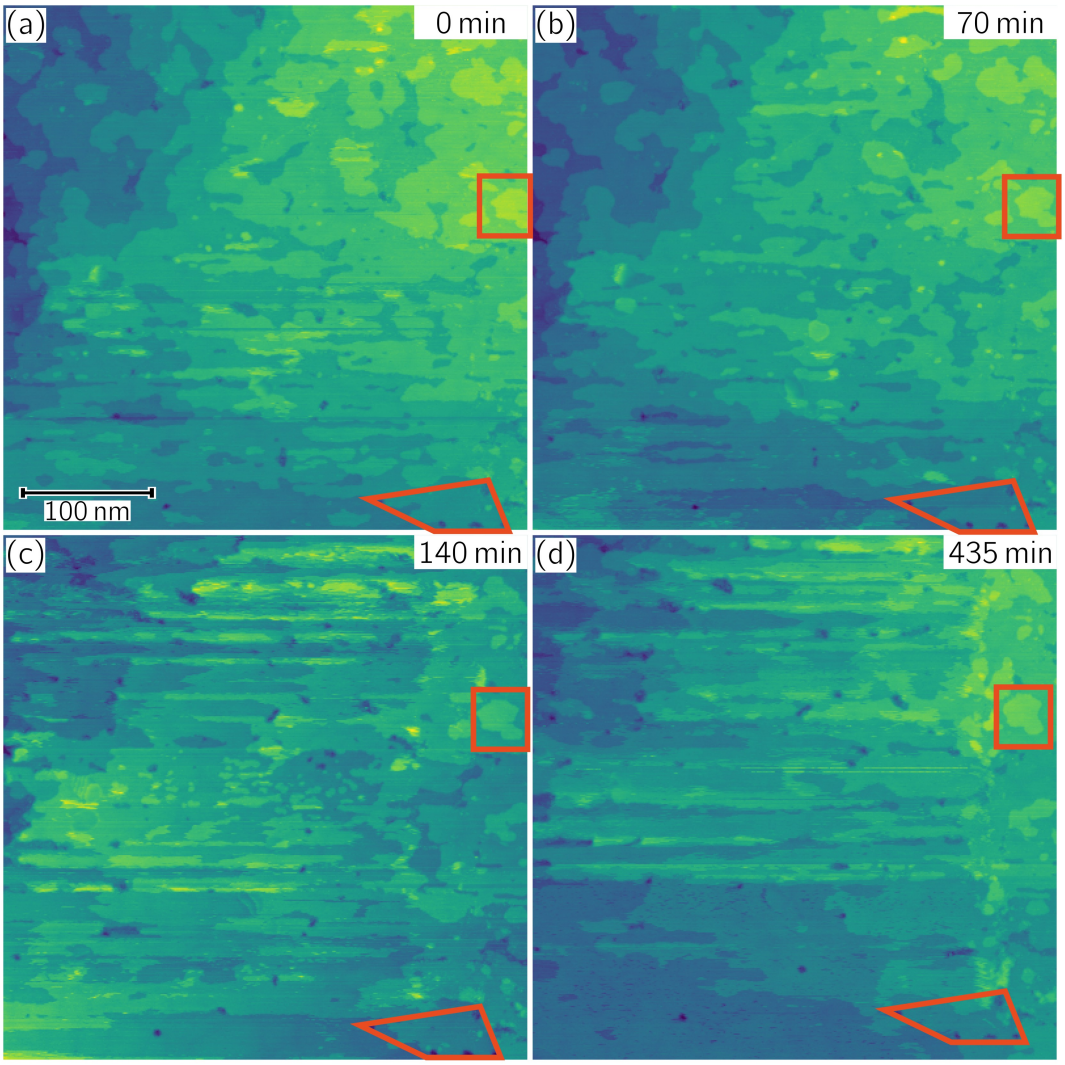

Figure F.1: Influence of the STM tip on the sample morphology. Frames (a)-(c) were recorded consecutively. The recording of each frame took 35 min. One additional frame (not shown) was scanned between (a) and (b), and another between (b) and (c). Thus, 140 min elapsed between the first frame shown in (a) and the last frame (c). Between frames (c) and (d), the sample area was not scanned, and the measurement was paused. Frame (d) was recorded 260 min after finishing frame (c). The red-marked areas indicate regions with no or only minor changes during data recording. All frames were measured at $U = 30\,\mathrm{mV}$ and $I = 200\,\mathrm{pA}$. Reprinted from [47].

Bibliography

[1] W. Brinkman, D. Haggan, and W. Troutman, *A history of the invention of the transistor and where it will lead us*, IEEE Journal of Solid-State Circuits **32**, 1858 (1997).

[2] G. E. Moore, *Cramming more components onto integrated circuits, Reprinted from Electronics, volume 38, number 8, April 19, 1965, pp.114 ff.* IEEE Solid-State Circuits Society Newsletter **11**, 33 (2006).

[3] R. S. Williams, *What's Next? The end of Moore's law*, Computing in Science & Engineering **19**, 7 (2017).

[4] T. N. Theis and H.-S. P. Wong, *The End of Moore's Law: A New Beginning for Information Technology*, Computing in Science & Engineering **19**, 41 (2017).

[5] J. Manner, *Black software — the energy unsustainability of software systems in the 21st century*, Oxf Open Energy **2**, oiac011 (2023).

[6] M. S. Lundstrom and M. A. Alam, *Moore's law: The journey ahead*, Science **378**, 722 (2022).

[7] S. Das, A. Sebastian, E. Pop, C. J. McClellan, A. D. Franklin, T. Grasser, T. Knobloch, Y. Illarionov, A. V. Penumatcha, J. Appenzeller, Z. Chen, W. Zhu, I. Asselberghs, L.-J. Li, U. E. Avci, N. Bhat, T. D. Anthopoulos, and R. Singh, *Transistors based on two-dimensional materials for future integrated circuits*, Nat Electron **4**, 786 (2021).

[8] Y. Liu, X. Duan, H.-J. Shin, S. Park, Y. Huang, and X. Duan, *Promises and prospects of two-dimensional transistors*, Nature **591**, 43 (2021).

[9] K. S. Novoselov, A. K. Geim, S. V. Morozov, D. Jiang, Y. Zhang, S. V. Dubonos, I. V. Grigorieva, and A. A. Firsov, *Electric field effect in atomically thin carbon films*, Science **306**, 666 (2004).

[10] A. K. Geim and K. S. Novoselov, *The rise of graphene*, Nature Mater **6**, 183 (2007).

[11] P. Vogt, P. De Padova, C. Quaresima, J. Avila, E. Frantzeskakis, M. C. Asensio, A. Resta, B. Ealet, and G. Le Lay, *Silicene: compelling experimental evidence for graphenelike two-dimensional silicon*, Physical Review Letters **108**, 155501 (2012).

[12] M. E. Dávila, L. Xian, S. Cahangirov, A. Rubio, and G. Le Lay, *Germanene: a novel two-dimensional germanium allotrope akin to graphene and silicene*, New Journal of Physics **16**, 95002 (2014).

[13] F. Zhu, W. Chen, Y. Xu, C. Gao, D. Guan, C. Liu, D. Qian, S.-C. Zhang, and J. Jia, *Epitaxial growth of two-dimensional stanene*, Nature Materials **14**, 1020 (2015).

[14] J. Yuhara, B. He, N. Matsunami, M. Nakatake, and G. Le Lay, *Graphene's latest cousin: plumbene epitaxial growth on a "nano WaterCube"*, Advanced Materials **31**, 1901017 (2019).

[15] A. Molle, J. Goldberger, M. Houssa, Y. Xu, S.-C. Zhang, and D. Akinwande, *Buckled two-dimensional xene sheets*, Nature Materials **16**, 163 (2017).

[16] S. Rachel and M. Ezawa, *Giant magnetoresistance and perfect spin filter in silicene, germanene, and stanene*, Physical Review B **89**, 195303 (2014).

[17] Y. Xu, B. Yan, H.-J. Zhang, J. Wang, G. Xu, P. Tang, W. Duan, and S.-C. Zhang, *Large-gap quantum spin hall insulators in tin films*, Physical Review Letters **111**, 136804 (2013).

[18] Y. Fang, Z.-Q. Huang, C.-H. Hsu, X. Li, Y. Xu, Y. Zhou, S. Wu, F.-C. Chuang, and Z.-Z. Zhu, *Quantum spin hall states in stanene/Ge(111)*, Scientific Reports **5**, 14196 (2015).

[19] J. Wang, Y. Xu, and S.-C. Zhang, *Two-dimensional time-reversal-invariant topological superconductivity in a doped quantum spin-hall insulator*, Physical Review B **90**, 54503 (2014).

[20] K. Houben, J. K. Jochum, D. P. Lozano, M. Bisht, E. Menéndez, D. G. Merkel, R. Rüffer, A. I. Chumakov, S. Roelants, B. Partoens, M. V. Milošević, F. M. Peeters, S. Couet, A. Vantomme, K. Temst, and M. J. Van Bael, In situ *study of the α -Sn to β -Sn phase transition in low-dimensional systems: phonon behavior and thermodynamic properties*, Physical Review B **100**, 75408 (2019).

[21] L. L. Wang, X. C. Ma, S. H. Ji, Y. S. Fu, Q. T. Shen, J. F. Jia, K. F. Kelly, and Q. K. Xue, *Epitaxial growth and quantum well states study of Sn thin films on Sn induced Si(111)- $(2\sqrt{3} \times 2\sqrt{3})R30^\circ$ surface*, Physical Review B **77**, 205410 (2008).

[22] C. Lei, H. Chen, and A. H. MacDonald, *Ultrathin films of superconducting metals as a platform for topological superconductivity*, Physical Review Letters **121**, 227701 (2018).

[23] C.-Z. Xu, Y.-H. Chan, Y. Chen, P. Chen, X. Wang, C. Dejoie, M.-H. Wong, J. A. Hlevyack, H. Ryu, H.-Y. Kee, N. Tamura, M.-Y. Chou, Z. Hussain, S.-K. Mo, and T.-C. Chiang, *Elemental topological dirac semimetal: α -Sn on InSb(111)*, Physical Review Letters **118**, 146402 (2017).

[24] J. Deng, B. Xia, X. Ma, H. Chen, H. Shan, X. Zhai, B. Li, A. Zhao, Y. Xu, W. Duan, S.-C. Zhang, B. Wang, and J. G. Hou, *Epitaxial growth of ultraflat stanene with topological band inversion*, Nature Materials **17**, 1081 (2018).

[25] J. Yuhara, Y. Fujii, K. Nishino, N. Isobe, M. Nakatake, L. Xian, A. Rubio, and G. Le Lay, *Large area planar stanene epitaxially grown on Ag(111)*, 2D Materials **5**, 25002 (2018).

[26] J. Yuhara, T. Ogikubo, M. Araidai, S.-i. Takakura, M. Nakatake, and G. Le Lay, *In-plane strain-free stanene on a Pd_2Sn (111) surface alloy*, Physical Review Materials **5**, 53403 (2021).

[27] P. Tang, P. Chen, W. Cao, H. Huang, S. Cahangirov, L. Xian, Y. Xu, S.-C. Zhang, W. Duan, and A. Rubio, *Stable two-dimensional dumbbell stanene: a quantum spin hall insulator*, Physical Review B **90**, 121408 (2014).

[28] W. Cao, P. Tang, S.-C. Zhang, W. Duan, and A. Rubio, *Stable dirac semimetal in the allotropes of group-IV elements*, Physical Review B **93**, 241117 (2016).

[29] D. Zhou, N. Si, B. Jiang, X. Song, H. Huang, Q. Ji, and T. Niu, *Interfacial effects on the growth of atomically thin film: group VA elements on Au(111)*, Advanced Materials Interfaces **6**, 1901050 (2019).

[30] P. Borlido, A. W. Huran, M. A. L. Marques, and S. Botti, *Structural prediction of stabilized atomically thin tin layers*, npj 2D Materials and Applications **3**, 21 (2019).

[31] W. Quan, C. Hong, S. Pan, J. Hu, Q. Wu, Z. Zhang, F. Zhou, F. Zheng, Z. Zhu, and Y. Zhang, *Rectangular-phase tellurene on Ni(111) from monolayer films to periodic striped patterns*, ACS Applied Materials & Interfaces **15**, 16144 (2023).

[32] Z. Zhang, A. J. Mannix, Z. Hu, B. Kiraly, N. P. Guisinger, M. C. Hersam, and B. I. Yakobson, *Substrate-induced nanoscale undulations of borophene on silver*, Nano Letters **16**, 6622 (2016).

[33] T. Niu, W. Zhou, D. Zhou, X. Hu, S. Zhang, K. Zhang, M. Zhou, H. Fuchs, and H. Zeng, *Modulating epitaxial atomic structure of antimonene through interface design*, Advanced Materials **31**, 1902606 (2019).

[34] D. Zhou, Q. Meng, N. Si, X. Zhou, S. Zhai, Q. Tang, Q. Ji, M. Zhou, T. Niu, and H. Fuchs, *Epitaxial growth of flat, metallic monolayer phosphorene on metal oxide*, ACS Nano **14**, 2385 (2020).

[35] L. Lei, F. Cao, S. Xing, H. Dong, J. Guo, S. Gu, Y. Geng, S. Mi, H. Wu, F. Pang, R. Xu, W. Ji, and Z. Cheng, *Phase transition-induced superstructures of β-Sn films with atomic-scale thickness*, Chinese Physics B **30**, 96804 (2021).

[36] H. Feng, X. Xu, Y. Liu, J. Zhuang, W. Hao, Y. Du, and S. X. Dou, *Microstructural constructing 2D tin allotropes on Al(111): from quasi-periodic lattice to square-like lattice*, Microstructures **3**, `10.20517/microstructures.2023.01` (2023).

[37] Y.-S. Lan, C.-J. Chen, S.-H. Kuo, Y.-H. Lin, A. Huang, J.-Y. Huang, P.-J. Hsu, C.-M. Cheng, and H.-T. Jeng, *Dual Dirac Nodal Line in Nearly Freestanding Electronic Structure of β-Sn Monolayer*, ACS Nano **18**, 20990 (2024).

[38] S. Nigam, S. Gupta, D. Banyai, R. Pandey, and C. Majumder, *Evidence of a graphene-like Sn-sheet on a Au(111) substrate: electronic structure and transport properties from first principles calculations*, Physical Chemistry Chemical Physics **17**, 6705 (2015).

[39] M. Maniraj, D. Jungkenn, W. Shi, S. Emmerich, L. Lyu, J. Kollamana, Z. Wei, B. Yan, M. Cinchetti, S. Mathias, B. Stadtmüller, and M. Aeschlimann, *Structure and electronic properties of the* $(\sqrt{3} \times \sqrt{3})R30^{\circ}$ $SnAu_2/Au(111)$ *surface alloy*, Physical Review B **98**, 205419 (2018).

[40] J. Shah, W. Wang, H. M. Sohail, and R. I. G. Uhrberg, *Atomic and electronic structures of the* Au_2Sn *surface alloy on Au(111)*, Physical Review B **104**, 125408 (2021).

[41] P. Sadhukhan, D. Pandey, V. K. Singh, S. Sarkar, A. Rai, K. Bhattacharya, A. Chakrabarti, and S. Roy Barman, *Electronic structure and morphology of thin surface alloy layers formed by deposition of Sn on Au(111)*, Applied Surface Science **506**, 144606 (2020).

[42] W. Pang, K. Nishino, T. Ogikubo, M. Araidai, M. Nakatake, G. Le Lay, and J. Yuhara, *Epitaxial growth of honeycomb-like stanene on Au(111)*, Applied Surface Science **517**, 146224 (2020).

[43] M. Maniraj, B. Stadtmüller, D. Jungkenn, M. Düvel, S. Emmerich, W. Shi, J. Stöckl, L. Lyu, J. Kollamana, Z. Wei, A. Jurenkow, S. Jakobs, B. Yan, S. Steil, M. Cinchetti, S. Mathias, and M. Aeschlimann, *A case study for the formation of stanene on a metal surface*, Communications Physics **2**, 12 (2019).

[44] M.-G. Barthès and C. Pariset, *A low energy electron diffraction-auger electron spectroscopy study of alloy formation during the adsorption of tin on (100) and (111) Au*, Thin Solid Films **77**, 305 (1981).

[45] J. A. Hochhaus, S. Hilgers, M. Schmitz, L. Kesper, U. Berges, and C. Westphal, *Structural analysis of Sn on Au(111) at low coverages: Towards the Au_2Sn surface alloy with alternating fcc and hcp domains*, Scientific Reports **15**, 7953 (2025).

[46] J. A. Hochhaus, S. Hilgers, A. Kononov, P. Weinert, U. Berges, H. Hövel, and C. Westphal, *Ultraflat honeycomb stanene nanoribbons on au(111)*, Advanced Materials Interfaces **12**, e00861 (2025).

[47] J. A. Hochhaus, S. Hilgers, A. Kononov, L. Kesper, M. Schmitz, U. Berges, H. Hövel, and C. Westphal, *First evidence of a square-like Sn lattice on the Au_2Sn surface alloy on Au(111)*, Applied Surface Science **714**, 164470 (2025).

[48] K. Takeda and K. Shiraishi, *Theoretical possibility of stage corrugation in Si and Ge analogs of graphite*, Physical Review B **50**, 14916 (1994).

[49] G. Yang, L. Li, W. B. Lee, and M. C. Ng, *Structure of graphene and its disorders: a review*, Science and Technology of Advanced Materials **19**, 613 (2018).

[50] A. H. Castro Neto, F. Guinea, N. M. R. Peres, K. S. Novoselov, and A. K. Geim, *The electronic properties of graphene*, Reviews of Modern Physics **81**, 109 (2009).

[51] J. Proctor, *Graphene is thin, but not infinitely so*, Physics **12**, 104 (2019).

[52] F. Bechstedt, P. Gori, and O. Pulci, *Beyond graphene: clean, hydrogenated and halogenated silicene, germanene, stanene, and plumbene*, Progress in Surface Science **96**, 100615 (2021).

[53] Y. Xu, Z. Gan, and S.-C. Zhang, *Enhanced thermoelectric performance and anomalous seebeck effects in topological insulators*, Physical Review Letters **112**, 226801 (2014).

[54] P. Sadhukhan, S. Barman, T. Roy, V. K. Singh, S. Sarkar, A. Chakrabarti, and S. R. Barman, *Electronic structure of Au-Sn compounds grown on Au(111)*, Physical Review B **100**, 235404 (2019).

[55] Y. Liu, N. Gao, J. Zhuang, C. Liu, J. Wang, W. Hao, S. X. Dou, J. Zhao, and Y. Du, *Realization of strained stanene by interface engineering*, Journal of Physical Chemistry Letters **10**, 1558 (2019).

[56] J. Gou, L. Kong, H. Li, Q. Zhong, W. Li, P. Cheng, L. Chen, and K. Wu, *Strain-induced band engineering in monolayer stanene on Sb(111)*, Physical Review Materials **1**, 54004 (2017).

[57] W. Wang, H. M. Sohail, J. R. Osiecki, and R. I. G. Uhrberg, *Broken symmetry induced band splitting in the Ag_2Ge surface alloy on Ag(111)*, Physical Review B **89**, 125410 (2014).

[58] J. Wintterlin and M.-L. Bocquet, *Graphene on metal surfaces*, Surface Science **603**, 1841 (2009).

[59] M. Houssa, A. Dimoulas, and A. Molle, *Silicene: a review of recent experimental and theoretical investigations*, Journal of Physics: Condensed Matter **27**, 253002 (2015).

[60] L. C. Lew Yan Voon, E. Sandberg, R. S. Aga, and A. A. Farajian, *Hydrogen compounds of group-IV nanosheets*, Applied Physics Letters **97**, 163114 (2010).

[61] L. Matthes, O. Pulci, and F. Bechstedt, *Massive dirac quasiparticles in the optical absorbance of graphene, silicene, germanene, and tinene*, Journal of Physics: Condensed Matter **25**, 395305 (2013).

[62] X.-L. Yu, L. Huang, and J. Wu, *From a normal insulator to a topological insulator in plumbene*, Physical Review B **95**, 125113 (2017).

[63] S. Cahangirov, M. Topsakal, E. Aktürk, H. Şahin, and S. Ciraci, *Two- and one-dimensional honeycomb structures of silicon and germanium*, Physical Review Letters **102**, 236804 (2009).

[64] M. Ezawa, *Monolayer topological insulators: silicene, germanene, and stanene*, Journal of the Physical Society of Japan **84**, 121003 (2015).

[65] G. Le Lay, E. Salomon, and T. Angot, *Silicene, germanene, and stanene*, edited by P. Avouris, T. F. Heinz, and T. Low, 1st ed. (Cambridge University Press, June 2017), pp. 458–471.

[66] S. Reich, J. Maultzsch, C. Thomsen, and P. Ordejón, *Tight-binding description of graphene*, Physical Review B **66**, 35412 (2002).

[67] T. Wehling, A. Black-Schaffer, and A. Balatsky, *Dirac materials*, Advances in Physics **63**, 1 (2014).

[68] C. Bena and G. Montambaux, *Remarks on the tight-binding model of graphene*, New Journal of Physics **11**, 95003 (2009).

[69] C. L. Kane and E. J. Mele, *Quantum spin hall effect in graphene*, Physical Review Letters **95**, 226801 (2005).

[70] M. Kurpas, P. E. Faria Junior, M. Gmitra, and J. Fabian, *Spin-orbit coupling in elemental two-dimensional materials*, Physical Review B **100**, 125422 (2019).

[71] Y. Ren, Z. Qiao, and Q. Niu, *Topological phases in two-dimensional materials: a review*, Reports on Progress in Physics **79**, 66501 (2016).

[72] W. Xiong, C. Xia, Y. Peng, J. Du, T. Wang, J. Zhang, and Y. Jia, *Spin–orbit coupling effects on electronic structures in stanene nanoribbons*, Physical Chemistry Chemical Physics **18**, 6534 (2016).

[73] B. Fu, M. Abid, and C.-C. Liu, *Systematic study on stanene bulk states and the edge states of its zigzag nanoribbon*, New Journal of Physics **19**, 103040 (2017).

[74] M. Miller and F. J. Owens, *On the possibility of zigzag and armchair silicon nanoribbons having the graphene structure*, Chemical Physics **381**, 1 (2011).

[75] M. M. Monshi, S. M. Aghaei, and I. Calizo, *Edge functionalized germanene nanoribbons: impact on electronic and magnetic properties*, RSC Advances **7**, 18900 (2017).

[76] M. A. Van Hove, W. H. Weinberg, and C.-M. Chan, *Low-energy electron diffraction: experiment, theory and surface structure determination*, Vol. 6, Springer Series in Surface Sciences (Springer Berlin Heidelberg, Berlin, Heidelberg, 1986).

[77] C. J. Powell, *Practical guide for inelastic mean free paths, effective attenuation lengths, mean escape depths, and information depths in x-ray photoelectron spectroscopy*, Journal of Vacuum Science & Technology, A: Vacuum, Surfaces, and Films **38**, 23209 (2020).

[78] A. Jablonski and C. Powell, *Relationships between electron inelastic mean free paths, effective attenuation lengths, and mean escape depths*, Journal of Electron Spectroscopy and Related Phenomena **100**, 137 (1999).

[79] S. Tanuma, C. J. Powell, and D. R. Penn, *Calculation of electron inelastic mean free paths (IMFPs) VII. Reliability of the TPP-2M IMFP predictive equation*, Surface and Interface Analysis **35**, 268 (2003).

[80] Z.-J. Ding and R. Shimizu, *A monte carlo modeling of electron interaction with solids including cascade secondary electron production*, Scanning **18**, 92 (1996).

[81] H. Shinotsuka, S. Tanuma, C. J. Powell, and D. R. Penn, *Calculations of electron inelastic mean free paths. X. Data for 41 elemental solids over the 50 eV to 200 keV range with the relativistic full penn algorithm*, Surface and Interface Analysis **47**, 871 (2015).

[82] M. P. Seah and W. A. Dench, *Quantitative electron spectroscopy of surfaces: a standard data base for electron inelastic mean free paths in solids*, Surface and Interface Analysis **1**, 2 (1979).

[83] J. Ashley, *Energy loss rate and inelastic mean free path of low-energy electrons and positrons in condensed matter*, Journal of Electron Spectroscopy and Related Phenomena **50**, 323 (1990).

[84] T. Fauster, L. Hammer, K. Heinz, and M. A. Schneider, *Oberflächenphysik: Grundlagen und Methoden* (Oldenbourg Wissenschaftsverlag, Oct. 2013).

[85] J. Szajman, J. Liesegang, J. Jenkin, and R. Leckey, *Is there a universal mean-free-path curve for electron inelastic scattering in solids?* Journal of Electron Spectroscopy and Related Phenomena **23**, 97 (1981).

[86] S. Vogelgesang, *Ultrafast low-energy electron diffraction at surfaces*, PhD thesis, Georg-August-Universität Göttingen, Göttingen (2018).

[87] D. Geelen, J. Jobst, E. E. Krasovskii, S. J. Van Der Molen, and R. M. Tromp, *Nonuniversal transverse electron mean free path through few-layer graphene*, Physical Review Letters **123**, 86802 (2019).

[88] S. Tanuma, C. J. Powell, and D. R. Penn, *Calculations of electron inelastic mean free paths for 31 materials*, Surface and Interface Analysis **11**, 577 (1988).

[89] H. Hertz, *Ueber einen Einfluss des ultravioletten Lichtes auf die electrische Entladung*, Annalen der Physik **267**, 983 (1887).

[90] W. Hallwachs, *Ueber den Einfluss des Lichtes auf electrostatisch geladene Körper*, Annalen der Physik **269**, 301 (1888).

[91] A. Einstein, *Über einen die Erzeugung und Verwandlung des Lichtes betreffenden heuristischen Gesichtspunkt*, Annalen der Physik **322**, 132 (1905).

[92] K. Siegbahn and K. Edvarson, *β-ray spectroscopy in the precision range of* $1 : 10^5$, Nuclear Physics **1**, 137 (1956).

[93] C. Nordling, E. Sokolowski, and K. Siegbahn, *Precision method for obtaining absolute values of atomic binding energies*, Physical Review **105**, 1676 (1957).

[94] E. Sokolowski, C. Nordling, and K. Siegbahn, *Chemical shift effect in inner electronic levels of Cu due to oxidation*, Physical Review **110**, 776 (1958).

[95] J. Osterwalder, *Electron based methods: photoelectron spectroscopy and diffraction*, 1st ed. (Wiley, Nov. 2013), pp. 151–214.

[96] J. Pendry, *Theory of photoemission*, Surface Science **57**, 679 (1976).

[97] S. Hüfner, *Photoelectron spectroscopy: principles and applications*, Advanced Texts in Physics (Springer, Berlin Heidelberg, 2003).

[98] P. S. Bagus, *Self-consistent-field wave functions for hole states of some Ne-like and Ar-like ions*, Physical Review **139**, A619 (1965).

[99] W. Schattke, *Photoemission within and beyond the one-step model*, Progress in Surface Science **54**, 211 (1997).

[100] T. Åberg, *Theory of X-ray satellites*, Physical Review **156**, 35 (1967).

[101] L. Sangaletti, F. Parmigiani, and P. S. Bagus, *Sum rule to evaluate the exchange energy in core-level photoemission*, Physical Review B **66**, 115106 (2002).

[102] C. Fadley, *Photoelectric cross sections and multi-electron transitions in the sudden approximation*, Chemical Physics Letters **25**, 225 (1974).

[103] L. Hedin, J. Michiels, and J. Inglesfield, *Transition from the adiabatic to the sudden limit in core-electron photoemission*, Physical Review B **58**, 15565 (1998).

[104] P. Auger, *Sur l'effet photoélectrique composé*, Journal de Physique et le Radium **6**, 205 (1925).

[105] L. Meitner, *Über die β-Strahl-Spektra und ihren Zusammenhang mit der γ-strahlung*, Zeitschrift Für Physik **11**, 35 (1922).

[106] D. Roy and D. Tremblay, *Design of electron spectrometers*, Reports on Progress in Physics **53**, 1621 (1990).

[107] D. Roy and J. D. Carette, in *Electron spectroscopy for surface analysis*, Vol. 4, edited by H. Ibach (Springer Berlin Heidelberg, Berlin, Heidelberg, 1977), pp. 13–58.

[108] B. P. Reed, *Developments in the Catalytic Graphitisation of Diamond and Silicon Carbide Surfaces*, PhD thesis, Aberystwyth University, Aberystwyth, Wales (2020).

[109] L. Kesper, *On the structural evolution towards germanene*, PhD thesis, TU Dortmund University, Dortmund (2022).

[110] M. Schmitz, *XPS and XPD Investigations of Low-dimensional Silicon-based Surface-structures*, PhD thesis, TU Dortmund University, Dortmund (2021).

[111] G. Greczynski and L. Hultman, *A step-by-step guide to perform x-ray photoelectron spectroscopy*, Journal of Applied Physics **132**, 11101 (2022).

[112] F. Mangolini, J. Åhlund, G. E. Wabiszewski, V. P. Adiga, P. Egberts, F. Streller, K. Backlund, P. G. Karlsson, B. Wannberg, and R. W. Carpick, *Angle-resolved environmental X-ray photoelectron spectroscopy: a new laboratory setup for photoemission studies at pressures up to 0.4 torr*, Review of Scientific Instruments **83**, 93112 (2012).

[113] R. E. Imhof, A. Adams, and G. C. King, *Energy and time resolution of the 180 degrees hemispherical electrostatic analyser*, Journal of Physics E: Scientific Instruments **9**, 138 (1976).

[114] C. E. Kuyatt and J. A. Simpson, *Electron monochromator design*, Review of Scientific Instruments **38**, 103 (1967).

[115] G. Schönhense, S. Babenkov, D. Vasilyev, H.-J. Elmers, and K. Medjanik, *Single-hemisphere photoelectron momentum microscope with time-of-flight recording*, Review of Scientific Instruments **91**, 123110 (2020).

[116] Dr. Sjuts Optotechnik GmbH, *Channel electron multipliers: principles of operation*, `http://www.sjuts.com/Introduction_Principles.html` (visited on 10/11/2025).

[117] D. Son, S. Cho, J. Nam, H. Lee, and M. Kim, *X-ray-based spectroscopic techniques for characterization of polymer nanocomposite materials at a molecular level*, Polymers **12**, 1053 (2020).

[118] C. Brundle, G. Conti, and P. Mack, *XPS and angle resolved XPS, in the semiconductor industry: characterization and metrology control of ultra-thin films*, Journal of Electron Spectroscopy and Related Phenomena, Trends in X-ray Photoelectron Spectroscopy of Solids (Theory, Techniques and Applications) **178–179**, 433 (2010).

[119] S. Oswald, M. Zier, R. Reiche, and K. Wetzig, *Angle-resolved XPS: a critical evaluation for various applications*, Surface and Interface Analysis **38**, 590 (2006).

[120] J. Gorham, *NIST X-ray Photoelectron Spectroscopy Database - SRD 20*, (2012).

[121] J. Walton, M. R. Alexander, N. Fairley, P. Roach, and A. G. Shard, *Film thickness measurement and contamination layer correction for quantitative XPS*, Surface and Interface Analysis **48**, 164 (2016).

[122] S. A. Chambers, L. Wang, and D. R. Baer, *Introductory guide to the application of XPS to epitaxial films and heterostructures*, Journal of Vacuum Science and Technology A **38**, 61201 (2020).

[123] P. J. Cumpson, *The thickogram: a method for easy film thickness measurement in XPS*, Surface and Interface Analysis **29**, 403 (2000).

[124] C. S. Fadley, in *Electron spectroscopy: theory, techniques and applications*, Vol. 2 (Academic Press, New York, 1978), pp. 1–156.

[125] D. Y. Zemlyanov, M. Jespersen, D. N. Zakharov, J. Hu, R. Paul, A. Kumar, S. Pacley, N. Glavin, D. Saenz, K. C. Smith, T. S. Fisher, and A. A. Voevodin, *Versatile technique for assessing thickness of 2D layered materials by XPS*, Nanotechnology **29**, 115705 (2018).

[126] D. J. Griffiths, *Introduction to quantum mechanics*, 3rd ed. (Cambridge University Press, Cambridge, 2018).

[127] P. Van Der Heide, *X-ray photoelectron spectroscopy: an introduction to principles and practices*, 1st ed. (Wiley, Nov. 2011).

[128] G. M. Bodner, *Quantum numbers and electron configurations*, `https://chemed.chem.purdue.edu/genchem/topicreview/bp/ch6/quantum.html` (visited on 10/13/2025).

[129] W. Pauli, *Über den Zusammenhang des Abschlusses der Elektronengruppen im Atom mit der Komplexstruktur der Spektren*, Zeitschrift für Physik **31**, 765 (1925).

[130] G. Spavieri and M. Mansuripur, *Origin of the spin–orbit interaction*, Physica Scripta **90**, 85501 (2015).

[131] K. Siegbahn, *Electron spectroscopy for atoms, molecules, and condensed matter*, Reviews of Modern Physics **54**, 709 (1982).

[132] U. Gelius, E. Basilier, S. Svensson, T. Bergmark, and K. Siegbahn, *A high resolution ESCA instrument with X-ray monochromator for gases and solids*, Journal of Electron Spectroscopy and Related Phenomena **2**, 405 (1973).

[133] U. Gelius, P. F. Hedén, J. Hedman, B. J. Lindberg, R. Manne, R. Nordberg, C. Nordling, and K. Siegbahn, *Molecular spectroscopy by means of ESCA III.* Carbon compounds, Physica Scripta **2**, 70 (1970).

[134] K. Kim and N. Winograd, *X-ray photoelectron spectroscopic binding energy shifts due to matrix in alloys and small supported metal particles*, Chemical Physics Letters **30**, 91 (1975).

[135] S. Kowalczyk, G. Apai, G. Kaindl, F. McFeely, L. Ley, and D. Shirley, *An X-ray photoemission investigation of the density of states of β' -NiAl*, Solid State Communications **25**, 847 (1978).

[136] W. Egelhoff, *Core-level binding-energy shifts at surfaces and in solids*, Surface Science Reports **6**, 253 (1987).

[137] D. Spanjaard, C. Guillot, M.-C. Desjonquères, G. Tréglia, and J. Lecante, *Surface core level spectroscopy of transition metals: a new tool for the determination of their surface structure*, Surface Science Reports **5**, 1 (1985).

[138] P. H. Citrin, G. K. Wertheim, and Y. Baer, *Core-level binding energy and density of states from the surface atoms of gold*, Physical Review Letters **41**, 1425 (1978).

[139] D. A. Shirley, *High-resolution X-ray photoemission spectrum of the valence bands of gold*, Physical Review B **5**, 4709 (1972).

[140] R. Hesse, M. Weiß, R. Szargan, P. Streubel, and R. Denecke, *Comparative study of the modelling of the spectral background of photoelectron spectra with the shirley and improved tougaard methods*, Journal of Electron Spectroscopy and Related Phenomena **186**, 44 (2013).

[141] S. Tougaard, *Background removal in x-ray photoelectron spectroscopy: relative importance of intrinsic and extrinsic processes*, Physical Review B **34**, 6779 (1986).

[142] R. Hesse and R. Denecke, *Improved tougaard background calculation by introduction of fittable parameters for the inelastic electron scattering cross-section in the peak fit of photoelectron spectra with UNIFIT 2011*, Surface and Interface Analysis **43**, 1514 (2011).

[143] S. Tougaard, *Practical guide to the use of backgrounds in quantitative XPS*, Journal of Vacuum Science and Technology A **39**, 11201 (2021).

[144] V. Jain, M. C. Biesinger, and M. R. Linford, *The Gaussian-Lorentzian Sum, Product, and Convolution (Voigt) functions in the context of peak fitting X-ray photoelectron spectroscopy (XPS) narrow scans*, Applied Surface Science **447**, 548 (2018).

[145] G. H. Major, N. Fairley, P. M. A. Sherwood, M. R. Linford, J. Terry, V. Fernandez, and K. Artyushkova, *Practical guide for curve fitting in x-ray photoelectron spectroscopy*, Journal of Vacuum Science and Technology A **38**, 61203 (2020).

[146] R. Hesse, P. Streubel, and R. Szargan, *Product or sum: comparative tests of Voigt, and product or sum of Gaussian and Lorentzian functions in the fitting of synthetic Voigt-based X-ray photoelectron spectra*, Surface and Interface Analysis **39**, 381 (2007).

[147] R. Wells, *Rapid approximation to the voigt/faddeeva function and its derivatives*, Journal of Quantitative Spectroscopy & Radiative Transfer **62**, 29 (1999).

[148] S. Hüfner and G. K. Wertheim, *Core-line asymmetries in the x-ray-photoemission spectra of metals*, Physical Review B **11**, 678 (1975).

[149] S. Doniach and M. Šunjić, *Many-electron singularity in X-ray photoemission and X-ray line spectra from metals*, Journal of Physics C: Solid State Physics **3**, 285 (1970).

[150] J. A. Hochhaus, *lmfitxps: Python package for XPS data analysis*, Software, Zenodo (2023).

[151] N. Fairley, P. Bargiela, A. Roberts, V. Fernandez, and J. Baltrusaitis, *Practical guide to understanding goodness-of-fit metrics used in chemical state modeling of x-ray photoelectron spectroscopy data by synthetic line shapes using nylon as an example*, Journal of Vacuum Science and Technology A **41**, 13203 (2023).

[152] K. Harrison and L. B. Hazell, *The determination of uncertainties in quantitative XPS/AES and its impact on data acquisition strategy*, Surface and Interface Analysis **18**, 368 (1992).

[153] K. Levenberg, *A method for the solution of certain non-linear problems in least squares*, Quarterly of Applied Mathematics **2**, 164 (1944).

[154] D. W. Marquardt, *An algorithm for least-squares estimation of nonlinear parameters*, Journal of the Society for Industrial and Applied Mathematics **11**, 431 (1963).

[155] N. Fairley, *Casaxps: processing software for XPS, AES, SIMS and more* (Casa Software Ltd., 2009).

[156] Thermo Scientific, *Avantage data system* (Thermo Fisher Scientific Inc., 2023).

[157] R. Hesse, T. Chassé, and R. Szargan, *Peak shape analysis of core level photoelectron spectra using UNIFIT for WINDOWS*, Fresenius Journal of Analytical Chemistry **365**, 48 (1999).

[158] B. V. Crist, *The "spectral data processor" for Windows 3.1*, Journal of Surface Analysis **6** (1999).

[159] R. W. M. Kwok, *XPS Peak Fitting Program for WIN95/98 XPSPEAK, ver. 4.1*, (2000).

[160] XPSOasis, *AAnalyzer: A peak-fitting program for photoemission data*, `https://xpsoasis.org`.

[161] M. Newville, R. Otten, A. Nelson, T. Stensitzki, A. Ingargiola, D. Allan, A. Fox, F. Carter, and M. Rawlik, *LMFIT: Non-Linear Least-Squares Minimization and Curve-Fitting for Python*, (2025).

[162] J. A. Hochhaus and H. Nakajima, *LG4X-V2: A GUI for XPS data analysis with LMFIT/lmfitxps*, Software, Zenodo (2022).

[163] H. Nakajima, *LG4X*, (2024).

[164] G. Kerherve, W. S. J. Skinner, J. A. Hochhaus, A. Graf, D. J. Morgan, M. A. Isaacs, B. P. Reed, H. Nakajima, and D. J. Payne, *KherveFitting: An Open Source Software for Fitting X-Ray Photoelectron Spectroscopy Data*, Surface & Interface Analysis **58**, 54 (2026).

[165] B. Singh, R. Hesse, and M. Linford, *Good practices for XPS (and other types of) peak fitting*, Vacuum Technology & Coating **25**, 25 (2015).

[166] S. Watanabe, *A Widely Applicable Bayesian Information Criterion*, (2012).

[167] H. Bozdogan, *Model selection and akaike's information criterion (AIC): the general theory and its analytical extensions*, Psychometrika **52**, 345 (1987).

[168] S. Portet, *A primer on model selection using the akaike information criterion*, Infectious Disease Modelling **5**, 111 (2020).

[169] M. P. Seah, I. S. Gilmore, and G. Beamson, *XPS: binding energy calibration of electron spectrometers 5–Re-Evaluation of the reference energies*, Surface and Interface Analysis **26**, 642 (1998).

[170] G. Greczynski and L. Hultman, *X-ray photoelectron spectroscopy: towards reliable binding energy referencing*, Progress in Materials Science **107**, 100591 (2020).

[171] B. V. Crist, *XPS in industry—Problems with binding energies in journals and binding energy databases*, Journal of Electron Spectroscopy and Related Phenomena, Applications of XPS in Industry **231**, 75 (2019).

[172] L. De Broglie, *Recherches sur la théorie des quanta*, Annales de Physique **10**, 22 (1925).

[173] K. Siegbahn, U. Gelius, H. Siegbahn, and E. Olson, *Angular distribution of electrons in ESCA spectra from a single crystal*, Physica Scripta **1**, 272 (1970).

[174] C. Fadley and S. Bergström, *Angular distribution of photoelectrons from a metal single crystal*, Physics Letters A **35**, 375 (1971).

[175] C. S. Fadley, *Diffraction and holography with photoelectrons and auger electrons: some new directions*, Surface Science Reports **19**, 231 (1993).

[176] C. S. Fadley, *Angle-resolved x-ray photoelectron spectroscopy*, Progress in Surface Science **16**, 275 (1984).

[177] C. Westphal, *The study of the local atomic structure by means of X-ray photoelectron diffraction*, Surface Science Reports **50**, 1 (2003).

[178] M.-L. Xu, J. J. Barton, and M. A. Van Hove, *Electron scattering by atomic chains: multiple-scattering effects*, Physical Review B **39**, 8275 (1989).

[179] M. Scheffler, K. Kambe, and F. Forstmann, *Angle resolved photoemission from adsorbates: theoretical considerations of polarization effects and symmetry*, Solid State Communications **25**, 93 (1978).

[180] C. S. Fadley, *Photoelectron diffraction*, Physica Scripta **T17**, 39 (1987).

[181] S. Chambers, I. Vitomirov, S. Anderson, H. Chen, T. Wagener, and J. Weaver, *High-energy auger and medium-energy backscattered electron diffraction as a probe of ultra-thin epitaxial overlayers, sandwiches and superlattices*, Superlattices and Microstructures **3**, 563 (1987).

[182] S. Kono, S. M. Goldberg, N. F. T. Hall, and C. S. Fadley, *Azimuthal anisotropy in core-level X-ray photoemission from $c(2 \times 2)$ oxygen on Cu(001): experiment and single-scattering theory*, Physical Review Letters **41**, 1831 (1978).

[183] Y. Chen, F. J. García De Abajo, A. Chassé, R. X. Ynzunza, A. P. Kaduwela, M. A. Van Hove, and C. S. Fadley, *Convergence and reliability of the rehr-albers formalism in multiple-scattering calculations of photoelectron diffraction*, Physical Review B **58**, 13121 (1998).

[184] D. P. Woodruff and A. M. Bradshaw, *Adsorbate structure determination on surfaces using photoelectron diffraction*, Reports on Progress in Physics **57**, 1029 (1994).

[185] J. B. Pendry, *Reliability factors for LEED calculations*, J. Phys. Condens. Matter **13**, 937 (1980).

[186] F. J. García De Abajo, M. A. Van Hove, and C. S. Fadley, *Multiple scattering of electrons in solids and molecules: a cluster-model approach*, Physical Review B **63**, 75404 (2001).

[187] J. C. Slater, *Wave functions in a periodic potential*, Physical Review **51**, 846 (1937).

[188] R. Döll and M. Van Hove, *Global optimization in LEED structure determination using genetic algorithms*, Surface Science **355**, L393 (1996).

[189] M. L. Viana, R. Díez Muiño, E. A. Soares, M. A. Van Hove, and V. E. De Carvalho, *Global search in photoelectron diffraction structure determination using genetic algorithms*, Journal of Physics: Condensed Matter **19**, 446002 (2007).

[190] C. Davisson and L. H. Germer, *Diffraction of electrons by a crystal of nickel*, Physical Review **30**, 705 (1927).

[191] G. P. Thomson and A. Reid, *Diffraction of cathode rays by a thin film*, Nature **119**, 890 (1927).

[192] J. B. Pendry, in *Interaction of atoms and molecules with solid surfaces*, edited by V. Bortolani, N. H. March, and M. P. Tosi (Springer US, Boston, MA, 1990), pp. 201–211.

[193] J. B. Pendry and G. P. Alldredge, *Low Energy Electron Diffraction: The Theory and Its Application to Determination of Surface Structure*, Physics Today **30**, 57 (1977).

[194] K. Oura, M. Katayama, A. V. Zotov, V. G. Lifshits, and A. A. Saranin, *Surface science* (Springer, Berlin, Heidelberg, 2003).

[195] E. McRae, *Self-consistent multiple-scattering approach to the interpretation of low-energy electron diffraction*, Surface Science **8**, 14 (1967).

[196] M. A. Van Hove and S. Y. Tong, *Surface crystallography by LEED: Theory, computation and structural results*, Springer Series in Chemical Physics 2 (Springer, Berlin Heidelberg, 1979).

[197] G. Binnig and H. Rohrer, *Scanning tunneling microscopy*, Surface Science **126**, 236 (1983).

[198] NobelPrize.org, *Press Release: The 1986 Nobel Prize in Physics*,

[199] G. Binnig, H. Rohrer, C. Gerber, and E. Weibel, *Tunneling through a controllable vacuum gap*, Applied Physics Letters **40**, 178 (1982).

[200] J. Tersoff and D. R. Hamann, *Theory and application for the scanning tunneling microscope*, Physical Review Letters **50**, 1998 (1983).

[201] J. G. Simmons, *Generalized formula for the electric tunnel effect between similar electrodes separated by a thin insulating film*, Journal of Applied Physics **34**, 1793 (1963).

[202] G. Binnig and D. P. E. Smith, *Single-tube three-dimensional scanner for scanning tunneling microscopy*, Review of Scientific Instruments **57**, 1688 (1986).

[203] M. G. H. Schulte, *Structural analysis of 1,3,7-trimethylxanthine formations on Au(111)*, PhD thesis, TU Dortmund University, Dortmund (2021).

[204] R. H. Fowler and L. Nordheim, *Electron emission in intense electric fields*, Proceedings of the Royal Society of London. Series A, Containing Papers of a Mathematical and Physical Character **119**, 173 (1928).

[205] J. B. Pendry, A. B. Pretre, and B. C. H. Krutzen, *Theory of the scanning tunnelling microscope*, Journal of Physics: Condensed Matter **3**, 4313 (1991).

[206] J. Bardeen, *Tunnelling from a many-particle point of view*, Physical Review Letters **6**, 57 (1961).

[207] J. Tersoff and D. R. Hamann, *Theory of the scanning tunneling microscope*, Physical Review B **31**, 805 (1985).

[208] H. Neddermeyer, *Scanning tunnelling microscopy of semiconductor surfaces*, Reports on Progress in Physics **59**, 701 (1996).

[209] C. J. Chen, *Tunneling matrix elements in three-dimensional space: the derivative rule and the sum rule*, Physical Review B **42**, 8841 (1990).

[210] K. Kobayashi and M. Tsukada, *Simulation of scanning tunneling microscope image based on electronic states of surface/tip system*, Journal of Vacuum Science & Technology, A: Vacuum, Surfaces, and Films **8**, 170 (1990).

[211] S. Ohnishi and M. Tsukada, *Molecular orbital theory for the scanning tunneling microscopy*, Solid State Communications **71**, 391 (1989).

[212] D. Nečas and P. Klapetek, *Gwyddion: an open-source software for SPM data analysis*, en, Open Physics **10**, Publisher: De Gruyter Open Access, 181 (2012).

[213] F. Marinello, M. Balcon, P. Schiavuta, S. Carmignato, and E. Savio, *Thermal drift study on different commercial scanning probe microscopes during the initial warming-up phase*, Measurement Science and Technology **22**, 94016 (2011).

[214] J. F. J/orgensen, L. L. Madsen, J. Garnaes, K. Carneiro, and K. Schaumburg, *Calibration, drift elimination, and molecular structure analysis*, Journal of Vacuum Science & Technology B: Microelectronics and Nanometer Structures Processing, Measurement, and Phenomena **12**, 1698 (1994).

[215] G. Dai, L. Koenders, F. Pohlenz, T. Dziomba, and H.-U. Danzebrink, *Accurate and traceable calibration of one-dimensional gratings*, Measurement Science and Technology **16**, 1241 (2005).

[216] D. Nečas, A. Yacoot, M. Valtr, and P. Klapetek, *Demystifying data evaluation in the measurement of periodic structures*, Measurement Science and Technology **34**, 55015 (2023).

[217] E. Al-Dmour, *Fundamentals of Vacuum Physics and Technology*, (2020).

[218] A. Krönig, *Grundzüge einer Theorie der Gase*, Annalen der Physik **175**, 315 (1856).

[219] G. B. Arfken, D. F. Griffing, D. C. Kelly, and J. Priest, *KINETIC THEORY* (Elsevier, 1984), pp. 460–473.

[220] J. C. Maxwell, *IV. On the dynamical theory of gases*, Phil. Trans. R. Soc., 49 (1867).

[221] E. Al-Dmour, *Fundamentals of Vacuum Physics and Technology*, arXiv, `10.48550/ARXIV.2006.01464` (2020).

[222] SPECS Surface Nano Analysis GmbH (BU Focus), *Electron Beam Evaporator with Flux Monitor*, (2023) https://www.focus-gmbh.com/efm-evaporators/ (visited on 09/29/2025).

[223] VEM: Vacuum Engineering & Materials, *Thin Film Evaporation Guide*, https://www.vem-co.com/product-docs/thin-film-evaporation-guide/ (visited on 09/29/2025).

[224] G. Sauerbrey, *Verwendung von Schwingquarzen zur Wägung dünner Schichten und zur Mikrowägung*, Zeitschrift Für Physik **155**, 206 (1959).

[225] A. Reinold, *Präparation und Charakterisierung monoatomarer Pb-Schichten auf Pd(111)*, Master's thesis, TU Dortmund University, Dortmund (2021).

[226] T. Andreev, I. Barke, and H. Hövel, *Adsorbed rare-gas layers on Au(111): Shift of the Shockley surface state studied with ultraviolet photoelectron spectroscopy and scanning tunneling spectroscopy*, Physical Review B **70**, 205426 (2004).

[227] A. Kononov, *Fullerene and bismuth clusters on nanostructured oxide films: Influence of nearest neighbors and surface contribution on charging energy*, PhD thesis, TU Dortmund University, Dortmund (2024).

[228] T. Becker, H. Hövel, M. Tschudy, and B. Reihl, *Applications with a new low-temperature UHV STM at 5 K*, Applied Physics A: Materials Science & Processing **66**, S27 (1998).

[229] J. B. Parise and G. E. Brown, *New opportunities at emerging facilities*, Elements **2**, 37 (2006).

[230] E. M. McMillan, *A history of the synchrotron*, Physics Today **37**, 31 (1984).

[231] M. Tolan, T. Weis, C. Westphal, and K. Wille, *DELTA: Synchrotron Light in Nordrhein-Westfalen*, Synchrotron Radiation News **16**, 9 (2003).

[232] R. G. Heine, P. Hartmann, and T. Weis, *Characterisation of the EU-HOM-damped normal conducting 500 MHz cavity from the beam power spectrum at DELTA*, (2006).

[233] A. Hofmann, *Quasi-monochromatic synchrotron radiation from undulators*, Nuclear Instruments and Methods **152**, 17 (1978).

[234] H. Winick, G. Brown, K. Halbach, and J. Harris, *Wiggler and undulator magnets*, Physics Today **34**, 50 (1981).

[235] C. Westphal, U. Berges, S. Dreiner, R. Follath, M. Krause, F. Schäfers, D. Schirmer, and M. Schürmann, *The plane-grating monochromator beamline at the U55 undulator for surface and interface studies at DELTA*, Journal of Electron Spectroscopy and Related Phenomena, Proceeding of the Fourteenth International Conference on Vacuum Ultraviolet Radiation Physics **144–147**, 1117 (2005).

[236] D. J. Cant, B. P. Reed, B. F. Spencer, W. R. Flavell, and A. G. Shard, *Magic angle HAXPES*, Journal of Electron Spectroscopy and Related Phenomena **264**, 147311 (2023).

[237] A. G. Shard and B. P. Reed, *AlKα XPS reference spectra of polyethylene for all instrument geometries*, Journal of Vacuum Science & Technology, A: Vacuum, Surfaces, and Films **38**, 63209 (2020).

[238] K. Hermann, *LEEDpat Download Package*, (2022).

[239] F. Hanke and J. Björk, *Structure and local reactivity of the Au(111) surface reconstruction*, Physical Review B **87**, 235422 (2013).

[240] B. Hammer and J. K. Norskov, *Why gold is the noblest of all the metals*, Nature **376**, 238 (1995).

[241] J. V. Barth, H. Brune, G. Ertl, and R. J. Behm, *Scanning tunneling microscopy observations on the reconstructed Au(111) surface: atomic structure, long-range superstructure, rotational domains, and surface defects*, Physical Review B **42**, 9307 (1990).

[242] M. Van Hove, R. Koestner, P. Stair, J. Bibérian, L. Kesmodel, I. BartoŠ, and G. Somorjai, *The surface reconstructions of the (100) crystal faces of iridium, platinum and gold*, Surface Science **103**, 189 (1981).

[243] A. R. Sandy, S. G. J. Mochrie, D. M. Zehner, K. G. Huang, and D. Gibbs, *Structure and phases of the Au(111) surface: X-ray-scattering measurements*, Phys. Rev. B **43**, 4667 (1991).

[244] Y. Hasegawa and P. Avouris, *Manipulation of the Reconstruction of the Au(111) Surface with the STM*, Science **258**, 1763 (1992).

[245] Y. Hasegawa and P. Avouris, *Manipulation of the Reconstruction of the Au(111) Surface with the STM*, Science **258**, 1763 (1992).

[246] R. C. Jaklevic and L. Elie, *Scanning-Tunneling-Microscope Observation of Surface Diffusion on an Atomic Scale: Au on Au(111)*, Phys. Rev. Lett. **60**, 120 (1988).

[247] Y. Wang, N. S. Hush, and J. R. Reimers, *Simulation of the Au (111) - (22 × 3) surface reconstruction*, Phys. Rev. B **75**, 233416 (2007).

[248] M. Mansfield and R. J. Needs, *Application of the Frenkel-Kontorova model to surface reconstructions*, J. Phys.: Condens. Matter **2**, 2361 (1990).

[249] H. Bulou and C. Goyhenex, *Local strain analysis of the herringbone reconstruction of Au(111) through atomistic simulations*, Phys. Rev. B **65**, 045407 (2002).

[250] P. Li and F. Ding, *Origin of the herringbone reconstruction of Au(111) surface at the atomic scale*, Science Advances **8**, eabq2900 (2022).

[251] A. R. Sandy, S. G. J. Mochrie, D. M. Zehner, G. Grübel, K. G. Huang, and D. Gibbs, *Reconstruction of the Pt(111) surface*, Phys. Rev. Lett. **68**, 2192 (1992).

[252] M. Bott, M. Hohage, T. Michely, and G. Comsa, *Pt(111) reconstruction induced by enhanced Pt gas-phase chemical potential*, Phys. Rev. Lett. **70**, 1489 (1993).

[253] F. Cardarelli, *Less Common Nonferrous Metals* (Springer, London, 2008), pp. 213–454.

[254] R. Farraro and R. B. Mclellan, *Temperature dependence of the Young's modulus and shear modulus of pure nickel, platinum, and molybdenum*, Metallurgical Transactions A **8**, 1563 (1977).

[255] S. Hüfner, G. Wertheim, and J. Wernick, *XPS core line asymmetries in metals*, Solid State Communications **17**, 417 (1975).

[256] P. H. Citrin, G. K. Wertheim, and Y. Baer, *Surface-atom x-ray photoemission from clean metals: Cu, Ag, and Au*, Physical Review B **27**, 3160 (1983).

[257] P. Heimann, J. Van Der Veen, and D. Eastman, *Structure-dependent surface core level shifts for the Au(111), (100), and (110) surfaces*, Solid State Communications **38**, 595 (1981).

[258] T. C. Hsieh, A. P. Shapiro, and T.-C. Chiang, *Core-level shifts for Au epitaxial overlayers on Ag*, Physical Review B **31**, 2541 (1985).

[259] K. Heister, M. Zharnikov, M. Grunze, and L. S. O. Johansson, *Adsorption of alkanethiols and biphenylthiols on Au and Ag substrates: a high-resolution X-ray photoelectron spectroscopy study*, Journal of Physical Chemistry B **105**, 4058 (2001).

[260] R. Requist, P. M. Sheverdyaeva, P. Moras, S. K. Mahatha, C. Carbone, and E. Tosatti, *Spin-orbit interaction and Dirac cones in d-orbital noble metal surface states*, Phys. Rev. B **91**, 045432 (2015).

[261] P. Kowalczyk, M. Puchalski, W. Kozłowski, P. Dąbrowski, Z. Klusek, and W. Olejniczak, *Investigation of the shockley surface state on clean and air-exposed Au (111)*, Applied Surface Science **254**, 4572 (2008).

[262] H. Eckardt, L. Fritsche, and J. Noffke, *Self-consistent relativistic band structure of the noble metals*, Journal of Physics F: Metal Physics **14**, 97 (1984).

[263] R. Courths, H. Zimmer, A. Goldmann, and H. Saalfeld, *Electronic structure of gold: an angle-resolved photoemission study along the Λ line*, Physical Review B **34**, 3577 (1986).

[264] N. E. Christensen and B. O. Seraphin, *Relativistic band calculation and the optical properties of gold*, Physical Review B **4**, 3321 (1971).

[265] P. M. Sheverdyaeva, R. Requist, P. Moras, S. K. Mahatha, M. Papagno, L. Ferrari, E. Tosatti, and C. Carbone, *Energy-momentum mapping of d -derived Au(111) states in a thin film*, Phys. Rev. B **93**, 035113 (2016).

[266] P. Heimann and H. Neddermeyer, *Ultraviolet photoemission from single crystals and the bandstructure of gold*, Journal of Physics F: Metal Physics **7**, L37 (1977).

[267] P. Heimann, H. Neddermeyer, and H. F. Roloff, *Photoemission from (110) faces of noble metals: observation of one-dimensional density of states*, Physical Review Letters **37**, 775 (1976).

[268] K. A. Mills, R. F. Davis, S. D. Kevan, G. Thornton, and D. A. Shirley, *Angle-resolved photoemission determination of Λ -line valence bands in Pt and Au using synchrotron radiation*, Physical Review B **22**, 581 (1980).

[269] R. Mazzarello, A. D. Corso, and E. Tosatti, *Spin-orbit modifications and splittings of deep surface states on clean Au(111)*, Surface Science **602**, 893 (2008).

[270] D. Kaminski, P. Poodt, E. Aret, N. Radenovic, and E. Vlieg, *Surface alloys, overlayer and incommensurate structures of Bi on Cu(111)*, Surface Science **575**, 233 (2005).

[271] Y. Girard, C. Chacon, G. De Abreu, J. Lagoute, V. Repain, and S. Rousset, *Growth of Bi on Cu(111): alloying and dealloying transitions*, Surface Science **617**, 118 (2013).

[272] L. Moreschini, A. Bendounan, I. Gierz, C. R. Ast, H. Mirhosseini, H. Höchst, K. Kern, J. Henk, A. Ernst, S. Ostanin, F. Reinert, and M. Grioni, *Assessing the atomic contribution to the rashba spin-orbit splitting in surface alloys: Sb/Ag(111)*, Physical Review B **79**, 75424 (2009).

[273] L. Kesper, J. A. Hochhaus, M. Schmitz, M. G. H. Schulte, U. Berges, and C. Westphal, *Tracing the structural evolution of quasi-freestanding germanene on Ag(111)*, Scientific Reports **12**, 7559 (2022).

[274] E. Golias, E. Xenogiannopoulou, D. Tsoutsou, P. Tsipas, S. A. Giamini, and A. Dimoulas, *Surface electronic bands of submonolayer Ge on Ag(111)*, Physical Review B **88**, 75403 (2013).

[275] D. Pacilé, C. R. Ast, M. Papagno, C. Da Silva, L. Moreschini, M. Falub, A. P. Seitsonen, and M. Grioni, *Electronic structure of an ordered Pb/Ag(111) surface alloy: theory and experiment*, Physical Review B **73**, 245429 (2006).

[276] J. Dalmas, H. Oughaddou, C. Léandri, J.-M. Gay, G. Le Lay, G. Tréglia, B. Aufray, O. Bunk, and R. L. Johnson, *Ordered surface alloy formation of immiscible metals: the case of Pb deposited on Ag(111)*, Physical Review B **72**, 155424 (2005).

[277] C. Tayran and M. Çakmak, *Electronic structure of the Pd2Sn surface alloy on Pd(111)-*$(\sqrt{3} \times \sqrt{3})R30^{\circ}$, The European Physical Journal B **92**, 240 (2019).

[278] J. R. Osiecki and R. I. G. Uhrberg, *Alloying of Sn in the surface layer of Ag(111)*, Physical Review B **87**, 75441 (2013).

[279] D. Zhou, H. Li, S. Bu, B. Xin, Y. Jiang, N. Si, J. Sun, Q. Ji, H. Huang, H. Li, and T. Niu, *Phase engineering of epitaxial stanene on a surface alloy*, Journal of Physical Chemistry Letters **12**, 211 (2021).

[280] G. Cabailh, J. W. Wells, I. T. McGovern, V. R. Dhanak, A. R. Vearey-Roberts, A. Bushell, and D. A. Evans, *Soft x-ray photoelectron spectroscopy of tin-phthalocyanine/ GaAs(001)-* (1×6) *interface formation*, Journal of Physics: Condensed Matter **15**, S2741 (2003).

[281] M. Fondell, M. Gorgoi, M. Boman, and A. Lindblad, *An HAXPES study of Sn, SnS, SnO and SnO2*, Journal of Electron Spectroscopy and Related Phenomena **195**, 195 (2014).

[282] P. De Padova, M. Fanfoni, R. Larciprete, M. Mangiantini, S. Priori, and P. Perfetti, *A synchrotron radiation photoemission study of the oxidation of tin*, Surface Science **313**, 379 (1994).

[283] R. B. Shalvoy, G. B. Fisher, and P. J. Stiles, *Bond ionicity and structural stability of some average-valence-five materials studied by x-ray photoemission*, Physical Review B **15**, 1680 (1977).

[284] J. A. Bearden and A. F. Burr, *Reevaluation of X-ray atomic energy levels*, Reviews of Modern Physics **39**, 125 (1967).

[285] National Center for Biotechnology Information, *Electronegativity in the periodic table of elements*, `https://pubchem.ncbi.nlm.nih.gov/periodic-table/electronegativity` (visited on 10/15/2025).

[286] R. M. Friedman, J. Hudis, M. L. Perlman, and R. E. Watson, *Electronic behavior in alloys: Au-Sn*, Physical Review B **8**, 2433 (1973).

[287] S. Chakraborty and K. S. R. Menon, *Growth and structural evolution of Sn on Ag(001): epitaxial monolayer to thick alloy film*, Journal of Vacuum Science & Technology, A: Vacuum, Surfaces, and Films **34**, 41513 (2016).

[288] F. Hanke and J. Björk, *Structure and local reactivity of the Au(111) surface reconstruction*, Phys. Rev. B **87**, 235422 (2013).

[289] J. V. Barth, H. Brune, G. Ertl, and R. J. Behm, *Scanning tunneling microscopy observations on the reconstructed Au(111) surface: Atomic structure, long-range superstructure, rotational domains, and surface defects*, Phys. Rev. B **42**, 9307 (1990).

[290] K. Zhang, D. Sciacca, A. Coati, R. Bernard, Y. Borensztein, P. Diener, B. Grandidier, I. Lefebvre, M. Derivaz, C. Pirri, and G. Prévot, *Resolving the structure of the striped Ge layer on Ag(111) : Ag 2 Ge surface alloy with alternate fcc and hcp domains*, Physical Review B **104**, 155403 (2021).

[291] T. Osaka, H. Omi, K. Yamamoto, and A. Ohtake, *Surface phase transition and interface interaction in the α-Sn/InSb(111) system*, Phys. Rev. B **50**, 7567 (1994).

[292] C.-Z. Xu, Y.-H. Chan, P. Chen, X. Wang, D. Flötotto, J. A. Hlevyack, G. Bian, S.-K. Mo, M.-Y. Chou, and T.-C. Chiang, *Gapped electronic structure of epitaxial stanene on InSb(111)*, Phys. Rev. B **97**, 035122 (2018).

[293] F. Sette, G. K. Wertheim, Y. Ma, G. Meigs, S. Modesti, and C. T. Chen, *Lifetime and screening of the C1*s *photoemission in graphite*, Physical Review B **41**, 9766 (1990).

[294] P. S. Bagus, E. S. Ilton, and C. J. Nelin, *The interpretation of XPS spectra: Insights into materials properties*, Surface Science Reports **68**, 273 (2013).

[295] G. Le Lay, J. Kanski, P. O. Nilsson, and U. O. Karlsson, *Core-level spectroscopy study of the initial formation of tin-germanium interfaces*, Applied Surface Science **56–58**, 178 (1992).

[296] S. B. DiCenzo, P. A. Bennett, D. Tribula, P. Thiry, G. K. Wertheim, and J. E. Rowe, *Structure of Sn/Ge(111) from low-energy electron-diffraction and photoemission studies*, Phys. Rev. B **31**, 2330 (1985).

[297] Y. Tian, W. Zhou, and P. Wu, *A density functional investigation of the structural, elastic and thermodynamic properties of the Au–Sn intermetallics*, Journal of Electronic Materials **45**, 639 (2016).

[298] K. Osada, S. Yamaguchi, and M. Hirabayashi, *An ordered structure of Au_5Sn*, Transactions of the Japan Institute of Metals **15**, 256 (1974).

[299] Hu Jie-Qiong, Xie Ming, Zhang Ji-Ming, Liu Man-Men, Yang You-Cai, and Chen Yong-Tai, *First principles study of Au-Sn intermetallic compounds*, Acta Physica Sinica **62**, 247102 (2013).

[300] Y. Zhang, C. H. Wong, J. Shen, S. T. Sze, B. Zhang, H. Zhang, Y. Dong, H. Xu, Z. Yan, Y. Li, X. Hu, and R. Lortz, *Dramatic enhancement of superconductivity in single-crystalline nanowire arrays of Sn*, Scientific Reports **6**, 32963 (2016).

[301] K. J. Chang and M. L. Cohen, *Electron-phonon interactions and superconductivity in Si, Ge, and Sn*, Physical Review B **34**, 4552 (1986).

[302] H. Walen, D.-J. Liu, J. Oh, H. Lim, J. W. Evans, Y. Kim, and P. A. Thiel, *Self-organization of S adatoms on Au(111):* $\sqrt{3}R30^\circ$ *rows at low coverage*, Journal of Chemical Physics **143**, 14704 (2015).

[303] P. M. Spurgeon, K. C. Lai, Y. Han, J. W. Evans, and P. A. Thiel, *Fundamentals of Au(111) surface dynamics: coarsening of two-dimensional Au islands*, Journal of Physical Chemistry C **124**, 7492 (2020).

[304] Y. Li, Z. Chen, X. Su, X. Cheng, Y. Wang, G. Xu, and W.-M. Liu, *Edge-passivation modulation of the transport properties in zigzag stanene nanoribbons*, Physical Review B **109**, 235414 (2024).

[305] F. Rahimi and A. Phirouznia, *High optical spin-filtering in antiferromagnetic stanene nanoribbons induced by band bending and uniaxial strain*, Scientific Reports **13**, 12874 (2023).

[306] J. Qi, K. Hu, and X. Li, *Electric control of the edge magnetization in zigzag stanene nanoribbons from first principles*, Physical Review Applied **10**, 34048 (2018).

[307] M. A. R. Faisal, Y. Wong, N. E. Alias, T. S. Tan, C. S. Lim, and M. L. P. Tan, *Electronic properties of stanene nanoribbon using tight binding method*, Journal of Nanotechnology **2025**, edited by V. Khanna, 5108226 (2025).

[308] C. G. Barkla, *The spectra of the fluorescent Röntgen radiations*, The London, Edinburgh, and Dublin Philosophical Magazine and Journal of Science **22**, 396 (1911).

[309] M. Siegbahn, *Relations between the* K *and* L *Series of the High-Frequency Spectra*, Nature **96**, 676 (1916).

[310] D. Briggs and M. P. Seah, *Practical surface analysis. Auger and X-ray photoelectron spectroscopy*, 2. ed., repr (Wiley, Chichester, 1996).

[311] C. Papp and H.-P. Steinrück, *In situ high-resolution X-ray photoelectron spectroscopy – Fundamental insights in surface reactions*, Surface Science Reports **68**, 446 (2013).

[312] C. Tusche, Y.-J. Chen, C. M. Schneider, and J. Kirschner, *Imaging properties of hemispherical electrostatic energy analyzers for high resolution momentum microscopy*, Ultramicroscopy **206**, 112815 (2019).

[313] T. Nishida, I. Kinoshita, and J. Ishii, *Temperature-dependent broadening of the ultraviolet photoelectron spectrum of Au(110)*, Sensors **21**, 5969 (2021).

[314] J. Kröger, T. Greber, T. Kreutz, and J. Osterwalder, *The photoemission Fermi edge as a sample thermometer?* Journal of Electron Spectroscopy and Related Phenomena **113**, 241 (2001).

[315] T. J. Kreutz, T. Greber, P. Aebi, and J. Osterwalder, *Temperature-dependent electronic structure of nickel metal*, Physical Review B **58**, 1300 (1998).

[316] S. Mähl, M. Neumann, S. Dieckhoff, V. Schlett, and A. Baalmann, *Characterisation of the VG ESCALAB instrumental broadening functions by XPS measurements at the Fermi edge of silver*, Journal of Electron Spectroscopy and Related Phenomena **85**, 197 (1997).

[317] O. Sise, *Simulation of electron energy spectra of a biased paracentric hemispherical deflection analyzer as a function of entry bias: Effects of misalignments*, Journal of Spectroscopy **2014**, 1 (2014).

[318] B. Wannberg, *Effects of mechanical imperfections in a hemispherical electron spectrometer*, Nuclear Instruments and Methods in Physics Research Section A: Accelerators, Spectrometers, Detectors and Associated Equipment **239**, 269 (1985).

[319] P. Tiemeijer, *Measurement of Coulomb interactions in an electron beam monochromator*, Ultramicroscopy **78**, 53 (1999).

[320] J. W. Pinder, G. H. Major, D. R. Baer, J. Terry, J. E. Whitten, J. Čechal, J. D. Crossman, A. J. Lizarbe, S. Jafari, C. D. Easton, J. Baltrusaitis, M. A. Van Spronsen, and M. R. Linford, *Avoiding common errors in X-ray photoelectron spectroscopy data collection and analysis, and properly reporting instrument parameters*, Applied Surface Science Advances **19**, 100534 (2024).

[321] F. A. Stevie and C. L. Donley, *Introduction to x-ray photoelectron spectroscopy*, Journal of Vacuum Science & Technology, A: Vacuum, Surfaces, and Films **38**, 63204 (2020).

[322] H. Hövel, Private Communication, TU Dortmund University (2023).

[323] Rayleigh, *XXXI.* Investigations in Optics, with Special Reference to the Spectroscope, The London, Edinburgh, and Dublin Philosophical Magazine and Journal of Science **8**, 261 (1879).

[324] M. O. Krause and J. H. Oliver, *Natural widths of atomic* K *and* L *levels,* Kα *X-ray lines and several* KLL *auger lines*, Journal of Physical and Chemical Reference Data **8**, 329 (1979).

[325] J. C. Fuggle and S. F. Alvarado, *Core-level lifetimes as determined by x-ray photoelectron spectroscopy measurements*, Physical Review A **22**, 1615 (1980).

[326] R. Paul, R. G. Reifenberger, T. S. Fisher, and D. Y. Zemlyanov, *Atomic layer deposition of FeO on Pt(111) by ferrocene adsorption and oxidation*, Chem. Mater. **27**, 5915 (2015).

[327] A. Gharachorlou, M. D. Detwiler, A. V. Nartova, Y. Lei, J. Lu, J. W. Elam, W. N. Delgass, F. H. Ribeiro, and D. Y. Zemlyanov, *Palladium nanoparticle formation on TiO2(110) by thermal decomposition of palladium(II) hexafluoroacetylacetonate*, ACS Appl. Mater. Interfaces **6**, 14702 (2014).

[328] J. J. Yeh and I. Lindau, *Atomic subshell photoionization cross sections and asymmetry parameters:* $1 \leqslant Z \leqslant 103$, Atomic Data and Nuclear Data Tables **32**, 1 (1985).

[329] C. Powell and A. Jablonski, *The NIST electron effective-attenuation-length database*, Journal of Surface Analysis **9**, 322 (2002).

[330] W. M. C. Foulkes and R. Haydock, *Tight-binding models and density-functional theory*, Phys. Rev. B **39**, 12520 (1989).

[331] F. D. M. Haldane, *Model for a Quantum Hall Effect without Landau Levels: Condensed-Matter Realization of the "Parity Anomaly"*, Physical Review Letters **61**, 2015 (1988).

Publications

Articles

[A1] S. Hilgers, J. A. Hochhaus, L. Hammer, U. Berges, H. Hövel, and C. Westphal, *Structural and chemical analysis of antimony nanoribbons on Ag(110)*, Submitted, (2026).

[A2] G. Kerherve, W. S. J. Skinner, J. A. Hochhaus, A. Graf, D. J. Morgan, M. A. Isaacs, B. P. Reed, H. Nakajima, and D. J. Payne, *KherveFitting: An Open Source Software for Fitting X-Ray Photoelectron Spectroscopy Data*, Surface & Interface Analysis **58**, 54 (2026).

[A3] M. Salarinasab, J. A. Hochhaus, A. Akhtar, K. Tschulik, C. Westphal, Z. Wang, and A. Ghalgaoui, *Methanol photodecomposition on TiO_2(110) under UV illumination studied with vibrational SFG spectroscopy in ambient conditions*, In preparation, (2026).

[A4] J. A. Hochhaus, S. Hilgers, M. Schmitz, L. Kesper, U. Berges, and C. Westphal, *Structural analysis of Sn on Au(111) at low coverages: Towards the Au_2Sn surface alloy with alternating fcc and hcp domains*, Scientific Reports **15**, 7953 (2025).

[A5] J. A. Hochhaus, S. Hilgers, A. Kononov, L. Kesper, M. Schmitz, U. Berges, H. Hövel, and C. Westphal, *First evidence of a square-like Sn lattice on the Au_2Sn surface alloy on Au(111)*, Applied Surface Science **714**, 164470 (2025).

[A6] J. A. Hochhaus, S. Hilgers, A. Kononov, P. Weinert, U. Berges, H. Hövel, and C. Westphal, *Ultraflat honeycomb stanene nanoribbons on au(111)*, Advanced Materials Interfaces **12**, e00861 (2025).

[A7] P. Weinert, J. A. Hochhaus, L. Kesper, R. Appel, S. Hilgers, M. Schmitz, M. G. H. Schulte, R. Hönig, F. Kronast, S. Valencia, M. Kruskopf, A. Chatterjee, U. Berges, and C. Westphal, *Structural, chemical, and magnetic investigation of a graphene/cobalt/platinum multilayer system on silicon carbide*, Nanotechnology **35**, 165702 (2024).

[A8] L. Kesper, J. A. Hochhaus, M. Schmitz, M. G. H. Schulte, U. Berges, and C. Westphal, *Tracing the structural evolution of quasi-freestanding germanene on Ag(111)*, Scientific Reports **12**, 7559 (2022).

Conference Contributions

[C1] J. A. Hochhaus, S. Hilgers, U. Berges, and C. Westphal, *Structural analysis of Sn on Au(111) at low coverages*, ECSCD-16/ICSOS-14, Vienna, Austria (2025).

[C2] J. A. Hochhaus, S. Hilgers, U. Berges, and C. Westphal, *Investigating the chemical and structural evolution of submonolayer Sn on Au(111)*, ROCAM: 10th International Conference on Advanced Materials, Bucharest, Romania (2024).

[C3] J. A. Hochhaus, S. Hilgers, U. Berges, and C. Westphal, *Investigating the chemical and structural evolution of sub-monolayer Sn on Au(111)*, Flatlands beyond graphene, Prague, Czechia (2023).

[C4] J. A. Hochhaus, L. Kesper, U. Berges, S. Hilgers, and C. Westphal, *Tracing the structural evolution of sub-monolayer Sn phases on Au(111)*, International Workshop on Advanced Quantum Materials, Marseille, France (2023).

[C5] J. A. Hochhaus, L. Kesper, S. Hilgers, U. Berges, and C. Westphal, *Investigation of sub-monolayer Sn phases on Au(111)*, DPG-Tagung der Sektion Kondensierte Materie, Regensburg, Germany (2022).

[C6] M. G. H. Schulte, A. Jeindl, J. A. Hochhaus, I. Baltaci, M. Schmitz, U. Berges, O. T. Hofmann, and C. Westphal, *Structural Investigation of Caffeine Monolayers on Au(111)*, DPG-Frühjahrstagung, (2021).

Supervised Theses

[T1] P. A. Kohnke, *Analyse von Röntgenphotoelektronen-Spektren von Übergangsmetall-Dichalkogeniden Monolagen*, Bachelor's thesis, TU Dortmund University, Dortmund (2026).

[T2] B. Hoffmann, *Präparation und Charakterisierung eines Metal Organic Frameworks aus Kupfer/Nickel und DCA-Molekülen auf Au(111)*, Bachelor's thesis, TU Dortmund University, Dortmund (2025).

[T3] T. Honermann, *Energie- und winkelabhängige Untersuchung der Flächenverhältnisse der Spin-Bahn-Aufspaltung des Au4f-Signals mittels Photoelektronenspektroskopie*, Master's thesis, TU Dortmund University, Dortmund (2022).

[T4] S. Hilgers, *Strukturaufklärung von Antimon-Monolagen auf Ag(111)*, Master's thesis, TU Dortmund University, Dortmund (2021).

[T5] A. Reinold, *Präparation und Charakterisierung monoatomarer Pb-Schichten auf Pd(111)*, Master's thesis, TU Dortmund University, Dortmund (2021).

Other Publications

[O1] J. A. Hochhaus, *lmfitxps: Python package for XPS data analysis*, Software, Zenodo (2023).

[O2] J. A. Hochhaus, L. Kesper, U. Berges, and C. Westphal, *Comparison of two different sub-monolayer Sn* $\sqrt{3}$*−phases on Au(111)*, DELTA Annual Report, TU Dortmund University (2022).

[O3] J. A. Hochhaus and H. Nakajima, *LG4X-V2: A GUI for XPS data analysis with LMFIT/lmfitxps*, Software, Zenodo (2022).

[O4] J. A. Hochhaus, L. Kesper, U. Berges, and C. Westphal, *Investigation of sub-monolayer Sn phases on Au(111) by means of XPS and LEED*, DELTA Annual Report, TU Dortmund University (2021).

Acknowledgements

At the end of this dissertation, I would like to thank those who have stood by my side over the last few years. While I cannot possibly name everyone who deserves it, I want to express my heartfelt thanks to everyone who accompanied and supported me on this journey!

First and foremost, I would like to thank Prof. Dr. Carsten Westphal. Thank you not only for supervising my PhD but for providing a supportive environment ever since my Bachelor thesis. I am deeply grateful for the trust you placed in me and for helping me overcome every obstacle in my scientific career. And I cannot help but mention: thank you for the constant supply of snacks and "nerve food," especially during stressful writing phases!

My sincere thanks go to Prof. Dr. Mirko Cinchetti for agreeing to be the second reviewer and for offering me a broader scientific exchange. I truly appreciated being part of your group's discussions and workshops. A big thank you also goes to all members of the AG Cinchetti for warmly welcoming and supporting me.

A huge thank you goes to all active and former members of the AG Westphal. I want to emphasize how much I value the support I received from alumni even after their time at the chair—that is not something I take for granted! In particular, I thank Dr. Malte Schulte for being an excellent mentor during my early studies and for always having good advice at hand.

I am equally grateful to Dr. Marie Schmitz, Dr. Lukas Kesper, and Dr. Philipp Weinert. You supported me not only during beamtimes but also with valuable ideas for data analysis and publications. I am especially honored that you so willingly sacrificed your free time to support me even after leaving the university.

I would also like to thank Dr. Ismail Baltaci, Anneke Reinold, Celine Wassenberg, Björn Hoffmann, and Thomas Honermann for the pleasant teamwork in the laboratory.

My thanks go to the technical staff of the university, particularly the DELTA team and the mechanical and electronic workshops, for their rapid solutions to all kinds of laboratory needs. Specifically, I would like to thank Dirk Schemionek for his constant support in the preparation lab, and Dr. Ulf Berges for his help with the beamline and vacuum components.

A significant part of this work's success is due to the STM measurements at the AG Hövel. I thank Prof. Dr. Heinz Hövel for providing his lab and for his thoughtful feedback on my manuscripts—my biggest thanks for that, Heinz! I also thank Dr. Alexander Kononov, not only for his support with measurements but especially for his infectiously good mood and creative, unconventional solutions to everyday lab problems. It was always motivating and entertaining to work with you!

Regarding the software used in this work, I express my sincere gratitude to Hideki Nakajima for his pioneering open-source efforts, which inspired me to continue his

work. I am also thankful to Kavin Teenakul and Gwilherm Kerherve for their valuable collaboration, feedback, and support in making XPS analysis tools accessible to the community. I would like to thank every single user who provided input and hunted bugs.

Additionally, I thank all my colleagues at scientific conferences for helpful discussions and valuable input. In particular, I thank Lutz Hammer for the in-depth feedback regarding the structural model of the X-phase.

My biggest thanks go to Stefanie Hilgers. You have supported me in every aspect of this dissertation, from measurements and debugging to proofreading. Thank you for motivating me and, above all, for bearing with me even in frustrating moments.

I also want to thank the proofreaders of this manuscript, especially for their feedback on the scientific content: Dr. Matthias Gianfelice, Dr. Malte Schulte, Dr. Marie Schmitz, and Stefanie Hilgers. Thank you for your time and effort! In addition, thanks to Sarah and Felix for looking over the language and giving me the peace of mind that my English was on the right track. Finally, thanks to Celine Wassenberg for proofreading the manuscript for typos and inconsistencies.

Finally, my thanks go to my friends and my family. For every kind of support, for keeping my back free, and for always believing in me—my greatest thanks to you all!

Thank you all for your support!